

Design and Analysis of a Broadband SIS-Mixer for the Heterodyne Instrument for the Far Infrared (HIFI) on the Herschel Space Observatory

Inaugural-Dissertation
zur
Erlangung des Doktorgrades
der Mathematisch-Naturwissenschaftlichen Fakultät
der Universität zu Köln



vorgelegt von
Rafael Theodor Alfred Teipen
aus Münster

Köln 2006

Berichterstatter: Prof. Dr. J. Stutzki
Prof. Dr. P. Reiter

Tag der mündlichen Prüfung: 3. November 2006

SOLI DEO GLORIA

Contents

1	Introduction	1
1.1	The HIFI instrument on the Herschel Space Observatory . . .	2
1.2	Mixer development for the HIFI frequency band 2	5
1.3	Organization of this thesis	6
2	The SIS tunnel-junction as mixing element in a heterodyne receiver	9
2.1	The heterodyne receiver	9
2.2	The SIS tunnel-junction	14
2.3	Summary of characteristic SIS-junction DC-parameters . . .	23
2.4	Quantum mixer performance analysis	25
3	Broad-band matching circuits for SIS-mixers	35
3.1	HIFI band 2 mixer overview	36
3.2	RF-impedance of the SIS-junction	38
3.3	Waveguide and waveguide probe	39
3.4	Micro-strip impedances for the relevant materials	43
3.5	Band-pass calculation for the matching circuit designs . . .	51
3.6	HIFI band 2 lithography mask design	59
4	Device and mixer characterization for the selection of flight-mixers	75
4.1	The HIFI band 2 performance baseline	75
4.2	Experimental device and mixer characterization methods . .	78
4.3	RF-performance results for fabricated wafers	85
4.4	Detailed comparison of three selected wafers	98

5	Noise analysis of the device design and the fabricated mixers	117
5.1	Influence of device fabrication parameters on the calculated noise	117
5.2	Noise analysis of the optimum measured mixer performance	128
6	Summary and Outlook	139
6.1	Summary	139
6.2	Outlook	141
A	Details regarding the mixer noise calculation	143
A.1	Shot-noise calculation for an unpumped SIS-device	143
A.2	Truncation of Bessel series in large signal analysis	144
A.3	Calculation of the noise band-pass	146
B	Microstrip impedances	149
B.1	Effective microstrip width and dielectric constant	149
B.2	Anomalous skin effect	150
C	Specification of the optics contribution to the measured receiver noise	153
C.1	Consistent calculation of optics noise contribution	153
C.2	Transmission measurements of the Mylar beam-splitter	154
C.3	Transmission coefficients of the Teflon dewar window	156
C.4	Transmission measurements of the radiation shield at 77 K-stage	158
D	DC- and RF-characterization of devices and wafers	161
D.1	Tabular overview of RF-characterized devices	161
D.2	Measured noise temperatures for all characterized mixers	162
D.3	Selection process of devices for the flight mixers	167
	Bibliography	171

Chapter 1

Introduction

The studies and results presented in this thesis have been generated as a contribution to the development of the Heterodyne Instrument for the Far Infrared (HIFI) [1, 2]. HIFI is one of three focal plane instruments on the astrophysical ESA satellite mission Herschel¹ [3, 4]. Herschel provides imaging photometry and spectroscopy facilities in the frequency range of 480 GHz to 5.3 THz.

Herschel has been designed to study the “cold” universe. The continuous spectra for bodies with temperatures between 5 and 50 K show their maxima in the covered frequency range. The most common broadband thermal radiation in this band is emitted from small dust grains. The other species to be observed by Herschel are the molecular and atomic emission lines of gases with temperatures between 10 and a few hundred K. Herschel’s main research objectives are the formation and evolution of galaxies, and the formation of stars and their interrelationship with the interstellar medium [4].

¹The Herschel Space Observatory is called after the astronomer W. Herschel: “*Sir William Herschel discovered, in addition to the planet Uranus, many new nebulae, clusters of stars and binary stars. He was the first person to correctly describe the form of our Galaxy, The Milky Way. In 1800, the German-born British astronomer and musician described that the differently colored filters through which he observed the Sun allowed different levels of heat to pass. He performed a simple experiment to study the 'heating powers of colored rays': he split the sunlight with a glass prism into its different constituent rainbow colors and measured the temperature of each color. He observed an increase in temperature as he moved a thermometer from the violet to the red part of the 'rainbow'. Out of curiosity Herschel also measured temperatures in the region just beyond the red color, where no light was visible, and to his surprise, he recorded the highest temperature there. He deduced the presence of invisible 'calorific rays' ”.* From <http://sci.esa.int>; copyright: Royal Astronomical Observatory

1.1 The HIFI instrument on the Herschel Space Observatory

In this section a few characteristic data of the Herschel Space Observatory and its instruments are presented. Then a short overview of the HIFI instrument is given. The SIS-mixers, studied and characterized within this thesis, are the sensitive radiation detectors for one frequency band of this instrument.

1.1.1 The Herschel Space Observatory

Herschel is scheduled to be launched by an Ariane 5 in 2008 and then transferred to its operational orbit around the Earth-Sun L2 point. A picture of the satellite observatory as designed is given in Fig. 1.1. The telescope is a

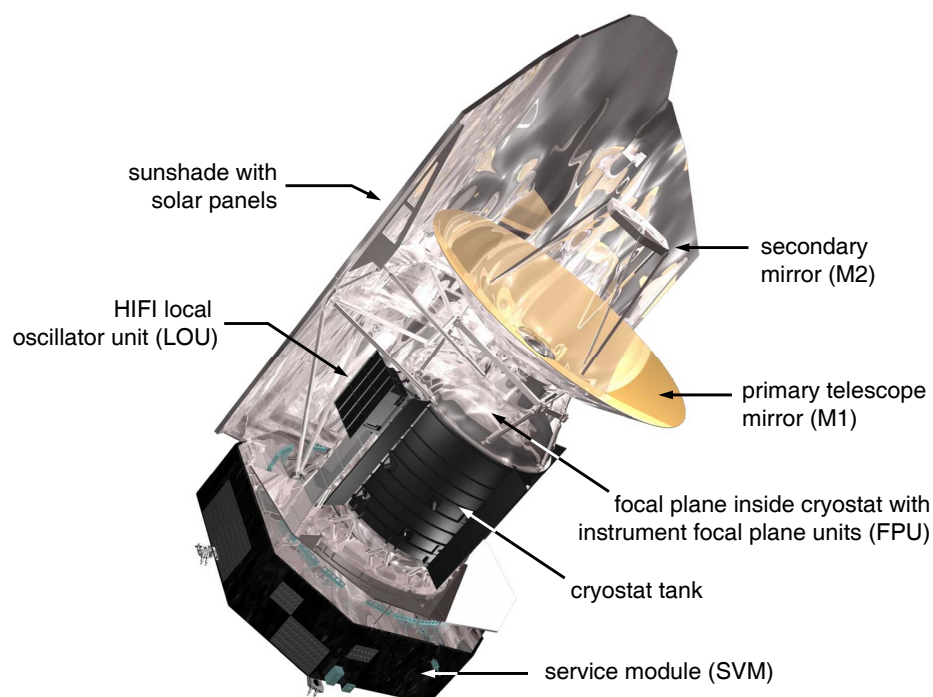


Fig. 1.1: *Artist's Impression of the Herschel Spacecraft: With its primary mirror of 3.5 m diameter, Herschel is going to host the largest mirror in space. Date: 16 Feb 2004, copyright: 2004 ESA.*

classical Cassegrain design with 3.5 m diameter primary mirror (aluminium-coated silicon-carbide). The focal plane units of the instruments (FPU) are placed in the superfluid helium cryostat, which is mainly necessary to cool the low noise detectors and amplifiers in the FPU. This reservoir of helium limits the routine science operation time to a minimum of 3 years after an expected 1/2 year for the transfer to the L2 orbit and the science demonstration phase.

The Herschel spacecraft has been tested with structural and thermal tests in

Feb 2006. The deliveries of the instrument flight models to ESA are expected towards the end of 2006.

Herschel houses three astrophysical instruments (for details see [5, 6, 2]):

- PACS: Photodetector Array Camera and Spectrometer (57-210 μm , 5.3-1.4 THz). The instrument is developed by a consortium, led by the Principle Investigator (PI) A. Poglitsch, MPE, Garching, Germany. PACS is a short wavelength camera and spectrometer. It consists of four detector arrays with a relative photometric resolution of $R \sim 2$ and a spectroscopy resolution of 75-300 km/s.
- SPIRE: Spectral and Photometric Imaging REceiver (200-670 μm , 1500-450 GHz). The PI of SPIRE is M. Griffin, University of Wales, Cardiff, UK. SPIRE is a long wavelength camera and spectrometer with five detector arrays. It has a relative photometric resolution of $R \sim 2$ and a relative spectrometric resolution at 250 μm $R \sim 100-1000$.
- HIFI: Heterodyne Instrument for the Far Infrared (480-1280 GHz and 1410-1910 GHz, 625-157 μm). The PI of HIFI is Th. de Graauw, SRON, Groningen, The Netherlands. In comparison to the other instruments it is a very high resolution spectrometer with a single spatial pixel, per frequency band two detectors for two orthogonal polarizations (V, H) with resulting velocity resolutions of 0.3-300 km/s. The main aspects of HIFI are summarized in the next paragraph.

1.1.2 The HIFI instrument

HIFI offers high resolution spectroscopy over the frequency range of 480-1280 GHz and 1410-1910 GHz. Low noise detection is achieved with superconductive devices operating close to the theoretical quantum noise limit. The very high spectral resolution is provided by the heterodyne technique, where the signal (RF: radio frequency) is transformed to lower frequencies (≤ 8 GHz, IF: intermediate frequency) with no loss in absolute frequency resolution (for heterodyne principle see Subsec. 2.1.1). In reference [2] a requirement for the instrument is called its versatility: *"The instrument is designed to provide very high spectral resolution over the widest possible frequency range."*

For HIFI three major research areas have been defined: (1) the observations of water lines, which is nearly impossible with ground-based telescopes, (2) to study the molecular complexity of the universe and (3) the observation of red-shifted CII. Details are especially given in [2].

The heterodyne mixers, which are the sensitive detectors of HIFI, are located in the focal plane unit (FPU). The FPU is mounted on the optical bench

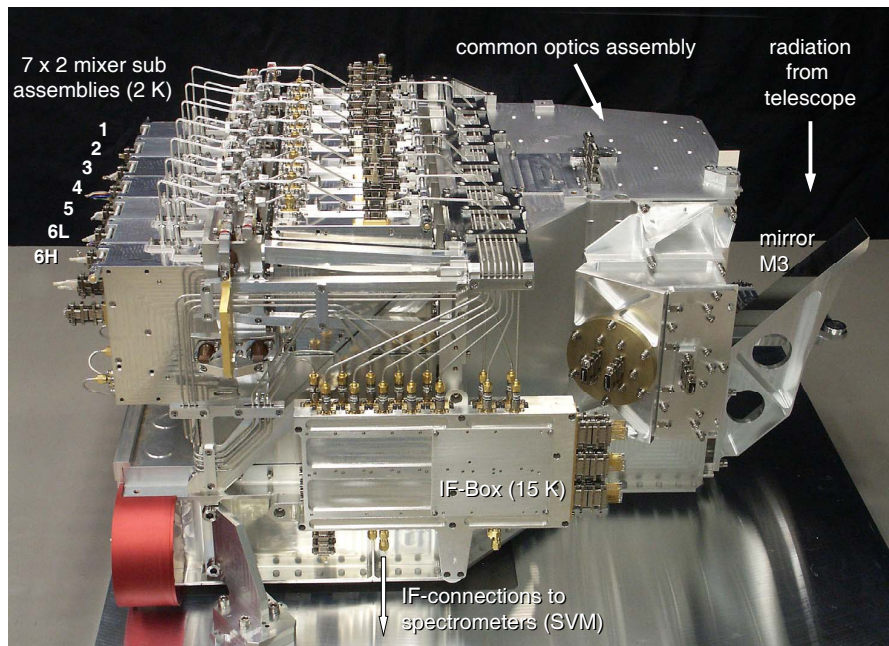


Fig. 1.2: Fully assembled flight model of the HIFI focal plane unit: for each frequency band one mixer for horizontal and one mixer for vertical polarization processes the signal. One mixer band will operate at a time selected by switching the respective IF-amplifiers to operation (source: SRON, NL, April 2006)

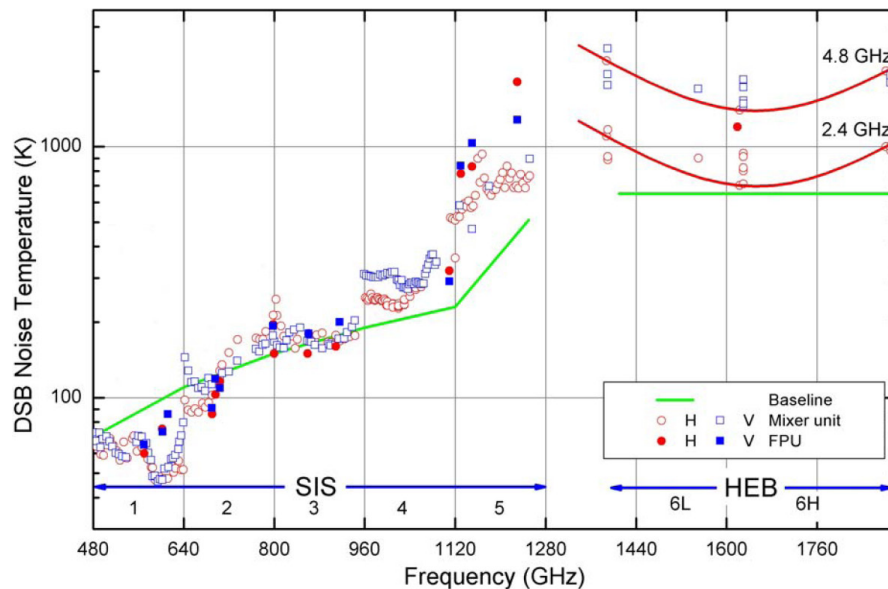


Fig. 1.3: Noise temperature data for HIFI frequency bands. The lower five bands are realized as SIS-mixers. Frequency bands 6L and 6H use HEB-devices as mixers. The green line shows the mixer performance baseline. For band 2 the data, acquired in the FPU (filled points) confirm the data, presented in this thesis (open points, compare Fig. 4.29). Source: G. de Lange, SRON, NL; see also [2].

inside the cryostat. The photograph in Fig. 1.2 shows the fully assembled HIFI FPU. Each mixer sub-assembly consists of a mixer on a special console to cool the mixer to 2.8 K, aligned with coupling optics and the first low-noise IF amplifier with isolators, both at 15 K. Per frequency band there are two mixer sub-assemblies combined, with the optics to couple to the local oscillator signal to the mixer assembly. The mixer assemblies for each band can be seen in Fig. 1.2 as seven outward identical boxes at the left hand side (1, . . . , 6H). In the IF-box in front of the FPU the IF-signals of the seven bands are combined with 3 dB-hybrid couplers. One frequency band operates at a time by switching the respective amplifiers to operation. The common optics assembly provides the splitting of the beam to the 14 mixers, the combination with the LO-signals and calibration sources.

The performance requirements of the different frequency bands for HIFI are given in Fig. 1.3 as the green line, which have been defined at the beginning of the project. It is defined for the predicted noise temperature of the mixers and the IF-chain². Added in the plot are the measured noise data for the flight-mixers before (open points) and after integration (filled points) into the FPU flight-model.

The lower five bands are realized with SIS-mixers (SIS: superconductor-isolator-superconductor junctions [7], details in Chap. 2). The upper two bands 6L and 6H are realized as HEB-mixers (HEB: hot electron bolometer, [8]). The detector technologies are discussed in [9, 10].

The data for band 2 show the performance results for two mixers developed, fabricated and characterized at KOSMA, Cologne. The design of the RF-matching circuits, the selection of the devices and the RF-characterization of these mixers has been done within this thesis.

1.2 Mixer development for the HIFI frequency band 2

The low noise and broadband performance requirements for the HIFI band 2 mixers are given by the baseline, as presented in Fig. 1.3.

The mixer development for the HIFI band 2 (RF: 636-802 GHz, IF: 4-8 GHz) is based on the previous successful development of low noise SIS-mixers at 660 and 800 GHz [11, 12]. The SIS-devices have been fabricated in the KOSMA microfabrication laboratories. A challenge for the mixer development in the HIFI frequency band 2 is the gap-frequency of Nb at 700 GHz. Nb previously has been used as material for Nb/Al₂O₃/Nb SIS-junctions and at the same time for the lossless matching circuits. These micro-strip matching circuits

²Here the noise temperature $T_{\text{noise}} = P_{\text{noise}}/(k_B \cdot B)$, where B is the output bandwidth, is a measure for the noise power of the instrument. Details are found in Subsec. 2.1.3

are necessary for impedance matching and compensation of the SIS-junction's intrinsic capacitance. Nb micro-strips are lossless below its gap-frequency but show significant losses above, resulting in a significant increase in input noise.

In order to reduce the micro-strip losses NbTiN-films with a gap-frequency above 900 GHz have been developed [13] and the fabrication scheme has been adapted (for details in the choice of materials see Subsec. 3.4.3). Although significant performance improvements have been achieved with the lossless micro-strip material NbTiN, this modification of the fabrication scheme unfortunately was accompanied by a reduced DC-quality Q , which is defined as an increase in leakage current and thus increased intrinsic noise.

For the reliable, exact definition of the junction areas (required relative accuracy $< 5\%$), which is essential for an effective power coupling of the resonant matching circuit, new technologies (e-beam lithography, EBL; chemical-mechanical polishing, CMP) have been applied [14]. For the coupling of the SIS-device to the waveguide of the horn antenna a new broadband waveguide probe has been optimized with an electro-magnetic 3-dimensional field solver [15, 16]. The relative bandwidth of a SIS-device itself is given by its $\omega R_N C$ -product [17], proportional to its current density j_c . To increase j_c the SIS-junctions have to be fabricated with a thinner barrier. This gives a higher probability of barrier-defects resulting in a larger leakage current and mixer noise.

The main contributions of this thesis to the development of the HIFI band 2 mixers are

- the design of the RF-matching circuits including j_c and the junction area of SIS-devices, resulting in three lithography masks for the device fabrication,
- the analysis and selection of the fabricated and characterized devices via DC-measurements for the more time consuming RF-performance measurements,
- the RF-characterization of the mixers, including the extraction of the mixer performance from the measured performance in a test-receiver and
- the feedback based on the characterization results and data interpretation for the fabrication during the process development.

1.3 Organization of this thesis

Chap. 2 presents a summary of the theory for the use of SIS-devices as mixing elements in heterodyne receivers are revisited. In addition to the general

concept of a heterodyne receiver the main characteristics of a SIS-tunneling junction and the underlying tunneling effects with and without RF-radiation are presented. The most important results of the quantum theory of mixing (J. R. Tucker [18]) regarding the RF-performance of SIS-mixers are summarized, which are applied for the modeling of SIS-mixers later.

In Chap. 3 the design concepts applied for the HIFI band 2 devices are presented. A simple physical model of SIS-junctions is used to calculate the power coupling of the incoming radiation to the SIS-junction. It contains the modeling of striplines for superconductive and normal-conductive materials, which has been applied in a numerical optimization of the matching circuit parameters. These optimizations resulted in the designs of devices for three lithography masks. The selection of device designs for the masks is based on a tolerance analysis. For the tolerance calculations a set of slightly distributed fabrication parameters is selected in order to cover the most probable actual fabricated parameters.

Chap. 4 presents the DC- and RF-characterization results of the fabricated wafers and SIS-devices. Essential for the effective selection of a few promising devices for RF-characterizations out of several hundred devices is the interpretation of the DC-measurement data based on the design model. These effective selection criteria have been important to identify the optimum mixer devices within the limited time and man power resources. The data interpretation can not be documented for all devices within the frame work of this thesis but is illustrated for three selected wafers. This includes the interpretation and analysis of one wafer (PS8), which has showed a superior RF-performance and has yielded the devices for the HIFI flight-mixers (compare Fig. 1.3). The interpretation of this wafer illustrates the tight fabrication tolerances, which are required to meet the ambitious HIFI baseline.

Then, in Chap. 5 Tucker's quantum mixer theory is applied in a three-frequency approximation to model the RF-performance of a mixer numerically more completely than with the simple model. On the one hand these model calculations are used to evaluate the impact of the fabrication parameter variations on the RF-performance of the device designs. On the other hand the quantum mixer theory is applied to model the noise performance of the characterized HIFI flight-mixers. The effect of increased shot-noise due to multiple Andreev-reflection is included and thermal effects are discussed.

Finally, in Chap. 6 a summary and outlook of this thesis is given.

Chapter 2

The SIS tunnel-junction as mixing element in a heterodyne receiver

The most sensitive devices for the application in a heterodyne mixer in the frequency region above 300 GHz and below 1.2 THz are SIS tunneling devices. In this chapter the characteristics of a SIS-junction, the underlying tunneling mechanisms and the use of a SIS-junction in a heterodyne receiver are summarized.

First, in Sec. 2.1 the general principle of a heterodyne receiver is presented. It makes use of a mixing device with a strong nonlinearity in its current-voltage characteristics. The strong nonlinearity in the case of a SIS-junction occurs due to the tunneling of quasi-particles. The tunneling mechanisms of quasi-particles and Cooper-pairs in a SIS-junction with and without RF-radiation are given in Sec. 2.2. The DC-parameters, which are used to specify the properties and RF-behavior during the design and analysis process of the SIS-mixers (Chap. 3, 4, 5), are summarized in Sec. 2.3. In Sec. 2.4 the major results of Tucker's quantum mixer theory [18] are summarized, which are applied in this thesis for the performance analysis of the designed SIS-devices.

Sec. 2.2 and 2.4 are the background for the design calculations in Chap. 3. Sec. 2.4 contains the framework for the theoretical analysis of the optimum mixer performance in Chap. 5.

2.1 The heterodyne receiver

In this section the heterodyne principle independent of the use of a SIS-junction as mixing device and some practical aspects of heterodyne receivers are resumed.

The heterodyne principle and the classical mixer theory are described in Subsec. 2.1.1 and Subsec. 2.1.2. In Subsec. 2.1.3 the noise of a receiver system

in general is discussed, as is used in the detailed characterization of the SIS-mixers in Chap. 4.

2.1.1 The heterodyne principle

The heterodyne principle is illustrated in Fig. 2.1. Two input signals with slightly different frequencies which are simultaneously coupled to a device with a nonlinearity in its current-voltage characteristics induce an output signal in their difference frequency. This effect is utilized in a heterodyne mixer, where the weak astronomical signal in the radio frequency (RF, from the telescope, HIFI band 2: 636-802 GHz) is superposed with a much stronger signal of a well known frequency from the local oscillator (LO). The resulting signal in the difference frequency (“intermediate frequency”, IF; HIFI Band 2: 4-8 GHz) is amplified and processed to be analyzed with a spectrometer (acousto-optical spectrometer “AOS” or digital correlator etc.).

The RF-signal is coupled with an antenna (horn, lens, strip-line) to the mixing device. The LO-radiation can be coupled to the mixer via a dielectric beam-splitter as beam-combiner or for an optimized coupling efficiency via a diplexer. When the mixer is operated at cryogenic temperatures low noise HEMT (high electron mobility transistor) amplifiers can be used to amplify the IF-signal right after the mixer. Additional amplifiers at room temperature are added to produce a signal in the signal input level and in the dynamic range of the spectrometer back-end.

Utilizing this method with a moderate to low relative resolution in the IF-frequency a large relative resolution for the detected RF-signal is achieved. For HIFI an AOS with an IF-bandwidth of 4–8 GHz and a spectral resolution of 1 MHz is used, that is developed, built and space-qualified at KOSMA [19]. This implies that for example in the HIFI frequency band 2 a line in the RF of 700 GHz is detected with this resolution of 1 MHz.

2.1.2 Classical mixer theory

The effect of mixing at a device with a strong nonlinearity in its current-voltage characteristics $I(V)$ is illustrated by the analysis of the resulting changes in current. The DC-bias voltage and current are V_0 and $I(V_0)$. The LO- and the RF-radiation are assumed to be a sinusoidal change in voltage,

$$\Delta V = V_{LO} \cdot \cos(\omega t) + V_{sig} \cdot \cos((\omega + \Delta\omega) \cdot t)$$

After expanding $I(V_0 + \Delta V)$ in a Taylor-series, assuming that the signal is much smaller than the LO-radiation ($V_{sig} \ll V_{LO}$), neglecting terms proportional to V_{sig}^2 and higher powers of V_{sig} and V_{LO} the current becomes (Eq. 2.2):

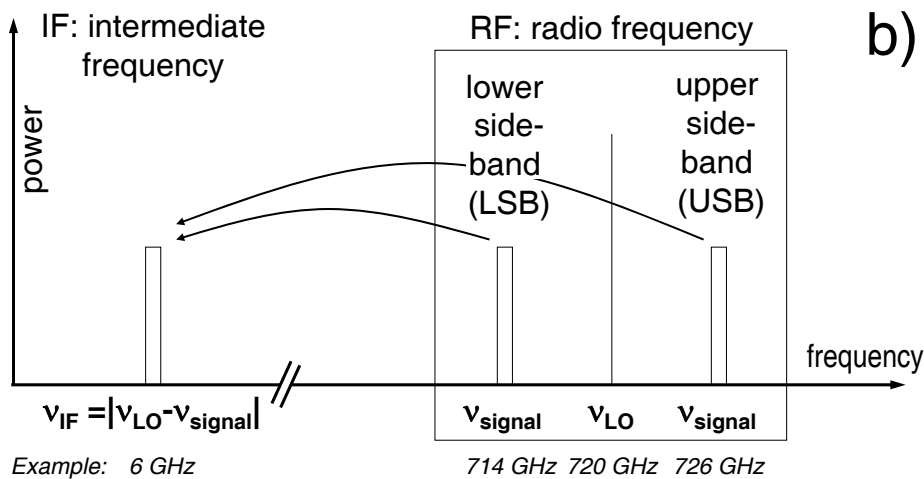
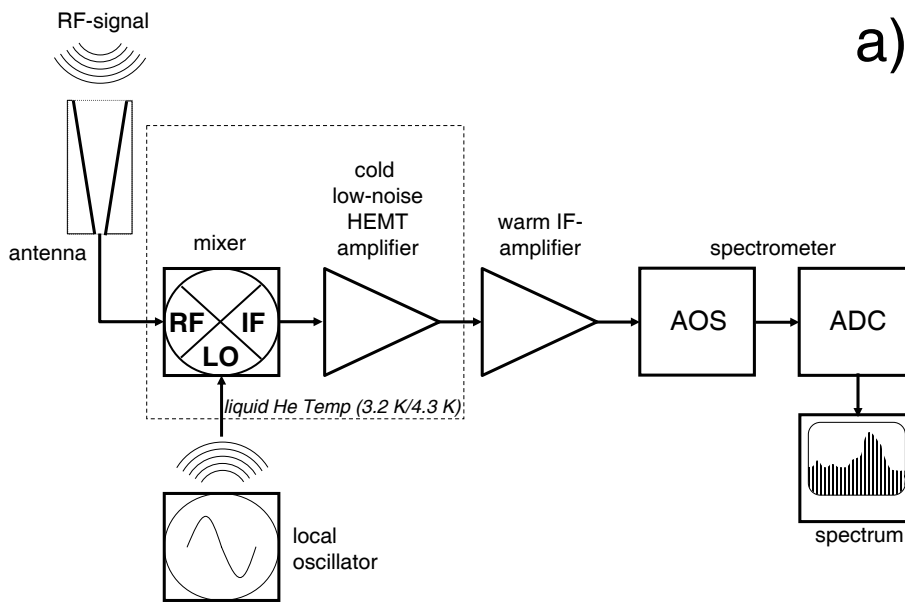


Fig. 2.1: Schematic of a heterodyne receiver and the down-conversion of the signal. **a)** The RF-signal is superposed with a fixed, exactly known signal of the local oscillator (LO) with a slightly different frequency. The mixer generates a signal in the difference frequency of RF- and LO-signal (intermediate frequency, IF). The IF-signal is amplified and processed in the spectrometer. **b)** Radiation at the frequencies of the lower and the upper sideband $\nu_{signal} = \nu_{LSB}$, ν_{USB} is converted to the same IF-frequency $\nu_{IF} = |\nu_{LO} - \nu_{signal}|$.

$$\begin{aligned}
 I = & \underbrace{I(V_0)}_{\text{DC-current}} + \frac{dI}{dV} \cdot \left[\underbrace{V_{LO} \cdot \cos(\omega \cdot t)}_{\omega_{LO}} + \underbrace{V_{sig} \cdot \cos((\omega + \Delta\omega) \cdot t)}_{\omega_{signal}} \right] \quad (2.1) \\
 & + \frac{1}{2} \frac{d^2 I}{dV^2} \left[\underbrace{\frac{1}{2} V_{LO}^2 + \frac{1}{2} V_{LO}^2 \cos(2\omega t)}_{\text{direct detection}} + V_{LO} V_{sig} \left\{ \cos((2\omega + \Delta\omega) t) + \underbrace{\cos(\Delta\omega t)}_{\omega_{IF}} \right\} \right]
 \end{aligned}$$

The terms in the first row of the equation are the DC-current and the contributions at the frequencies of signal and LO. The first term of the second row is a change in DC-current (the direct-detection effect). The last term is the current at the IF-frequency $\omega_{\text{IF}} = \Delta\omega$, which is processed and analyzed in the IF-chain of the receiver.

When the energy range of the nonlinearity $e \cdot \Delta V$ is of the same order as the energy of the LO-photons $h \cdot \nu_{\text{LO}}$, quantum effects have to be included. The major results of the quantum mixer theory [18], which are used for the analysis of the designed and fabricated mixers, are given in Sec. 2.4.

The classical analysis shows, that a signal in the so called “image frequency” $\nu_{\text{LSB}} = \nu_{\text{signal}} - 2 \cdot \nu_{\text{IF}}$ (see Fig. 2.1 (b), $-\Delta\nu$ instead of $\Delta\nu$ in Eq. 2.2) is transformed to the same frequency in the IF as from the signal frequency. During a measurement it is necessary to identify, whether the mixed signal – *a molecular line or any specific spectral shape* – is originating from the upper or the lower side-band. This is done by changing the LO-frequency and controlling whether the mixed signal changes the same or opposite direction in frequency. A technological approach to solve this problem is to operate the mixer as a single side-band mixer (SSB) by terminating one sideband with a load or absorber [20, 21, 16].

2.1.3 Receiver and mixer noise

The noise temperature of a receiver is defined as the temperature of a black body load at the input of the receiver that results in the same noise power at the output of the receiver as generated by the components of the receiver. The same way the noise temperature for each component of the receiver, including the mixer is defined.

In the following paragraphs four essential topics regarding the receiver and mixer noise are briefly summarized:

- the noise contributions of the components in a receiver,
- the impact of the receiver noise temperature on the receiver sensitivity and the necessary integration time,
- the general measurement concept for the noise characterization and
- the phenomenon of quantum noise.

Noise in an amplifier chain: A receiver can be regarded as a series of amplifiers or attenuators. The total receiver noise for a series of amplifiers/attenuators with power gains (G_1, G_2, G_3, \dots) and equivalent noise temperatures (T_1, T_2, T_3, \dots) is given by ([22])

$$T_{Rec} = T_1 + \frac{T_2}{G_1} + \frac{T_3}{G_1 G_2} + \frac{T_4}{G_1 G_2 G_3} + \dots, \quad (2.2)$$

where the equivalent noise T_{Rec} is determined at the input of element 1. Eq. 2.2 shows that it is important to optimize the first stages in noise and gain of an amplifier chain.

Eq. 2.2 is used to extract the noise contribution of the mixer from the characterization of the test-receiver (Subsec. 4.2.3). The same concept is necessary to estimate the noise contribution of the mixer to the HIFI instrument.

System noise and integration time: The system noise temperature T_{sys} is defined by the receiver noise and the coupling efficiency due to losses in the telescope optics. Usually also the atmospheric absorption is included in the system noise, but for the Herschel satellite observatory it can be neglected. T_{sys} is related to the minimum detectable signal temperature ΔT_{min} by the radiometer equation [23]

$$\Delta T_{min} = \frac{T_{sys}}{\sqrt{\Delta\nu \cdot \tau}}, \quad (2.3)$$

where $\Delta\nu$ is the fluctuation band-width and τ the integration time of the measurement. Thus the integration time τ to achieve the same sensitivity decreases quadratically with the reduction of the system noise.

Eq. 2.3 shows, that the optimum reduction of the system noise is essential for the effective use of the observing time. This is especially critical in the case of the Herschel-satellite, where the total operation time because of the limited reservoir of liquid helium is limited. The system noise in case of HIFI with nearly negligible atmospheric noise (in L2-orbit) is essentially limited by the mixer noise and input losses.

Hot-cold characterization of a receiver: The noise of a receiver is determined in a hot-cold-measurement with black-body input signals at two different ambient temperatures, the so-called Y-factor method. The receiver noise is extracted from the two corresponding IF output powers according to

$$\begin{aligned} P_{hot,out} &= k_B \cdot B \cdot G_{Rec} \cdot (T_{Rec} + T_{hot}) \\ P_{cold,out} &= k_B \cdot B \cdot G_{Rec} \cdot (T_{Rec} + T_{cold}). \end{aligned} \quad (2.4)$$

Here $T_{\text{hot/cold}}$ are radiation temperatures of blackbody load two different ambient temperatures, k_B is Boltzmann's constant and B the output bandwidth, defined by the IF band-pass. From Eq. 2.4 the receiver noise is evaluated as

$$T_{\text{Rec}} = \frac{T_{\text{hot}} - Y \cdot T_{\text{cold}}}{Y - 1}, \quad (2.5)$$

where $Y = P_{\text{hot,out}}/P_{\text{cold,out}}$. Eq. 2.5 can be used as long as the mixer is not saturated by the calibration load power [24, 25]. This method has been applied for the characterization of the mixers inside a test-receiver. The experimental test-setup is described in Subsec. 4.2.3.

A note regarding the quantum limit: In general an amplifier, which conserves the phase of the amplified signal, adds a noise quantum $h\nu/k_B$, calculated at the input to the signal, in order to be consistent with Heisenberg's uncertainty principle [26]. A mixer is in this respect the same as an amplifier, as it also conserves the phase, although the amplification is usually less than 1. For frequencies of the HIFI band 2 (636-802 GHz) this implies a quantum noise of 30.5-38.5 K. With an optimum measured mixer noise of 60 K at 660 GHz, the effect of quantum noise has to be considered in the analysis.

The equation for the radiation noise ($P_{\text{noise}} = k_B \cdot B \cdot T_{\text{noise}}$) of the black-body load, which includes the quantum noise and at the same time is consistent with the quantum mixer theory ([27]) is the Callen and Welton equation [28]:

$$T_{C\&W}(\nu, T) = T \cdot \left(\frac{\frac{h\nu}{k_B T}}{e^{\frac{h\nu}{k_B T}} - 1} \right) + \frac{h\nu}{2k_B}. \quad (2.6)$$

Therefore throughout this thesis Eq. 2.6 is used for the noise temperature of components, which are modeled as black bodies.

In different mixer configurations it is shown that the noise contributions attributed to the vacuum zero point fluctuations of the frequency sidebands (open or terminated) and the shot-noise of the mixer itself add up to one noise quantum consistent with the uncertainty principle [29]. In our case of a double-sideband mixer (DSB) the zero-point fluctuation noise contributes $h\nu/2k_B$ per sideband to the measured receiver noise, while the minimum mixer shot-noise according to the quantum mixer theory is zero.

2.2 The SIS tunnel-junction

The SIS tunnel junction is used as mixing element since it shows a very strong nonlinearity in its current voltage characteristics. The basic concept is illustrated in Fig. 2.2. Two superconductive electrodes are divided by a thin

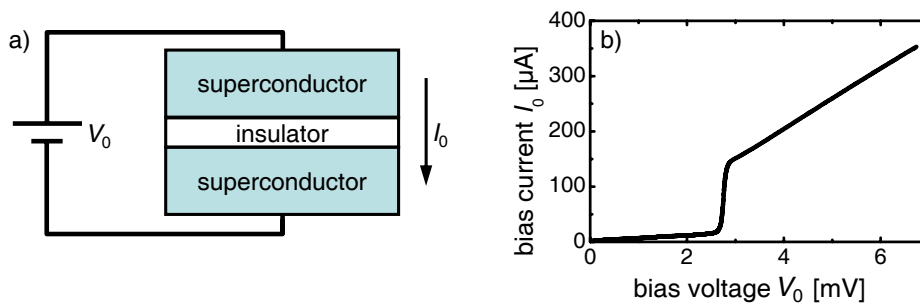


Fig. 2.2: Basic concept of a SIS-junction. **a)** Two superconductive electrodes (≈ 100 nm thickness) are divided by a thin insulating barrier (≈ 2 -5 nm thickness). **b)** The strong nonlinearity in the current-voltage characteristics $I_0(V_0)$ of a SIS-junction is attributed to the tunneling of quasi-particles.

insulating barrier. The effect, which is responsible for the strong nonlinearity in the current-voltage characteristics $I_{DC}(V)$ is the tunneling of quasi-particles.

Principles of superconductivity and superconductive devices are e.g. given in [30, 31]. Here, some characteristics of the SIS-junction are summarized, which are necessary to illustrate the design considerations for the actual SIS-devices. The presented basic effects are also the basis for the analysis and discussion of the noise performance of a fabricated SIS-device.

In a superconductive tunnel junction in general the tunneling of Cooper-pairs and of quasi-particles is observed. The tunneling is influenced by RF-radiation. The tunneling effects and their impact on the measured DC I-V-curve are briefly discussed first for the unpumped SIS-junction without RF-radiation (Subsec. 2.2.1), then for the pumped SIS-junction (Subsec. 2.2.2). Finally the additional effect of Andreev reflection and multiple Andreev reflection for current transport in a SIS-junction is mentioned in Subsec. 2.2.3.

2.2.1 DC-characteristics of an unpumped SIS-junction

An overview of the DC-characteristics of an unpumped SIS-junction is given in Fig. 2.3. The DC I-V-curve of a measured SIS-junction is given with applied magnetic field (dashed line) and without magnetic field (solid line). Without applied magnetic field the effects of tunneling of Cooper-pairs (Josephson effects) and quasi-particles are seen.

During the mixing process of a SIS-junction the Josephson-effects are obstructive, because they cause additional noise inside the junction [32]. Thus the Josephson effects are suppressed by applying a weak magnetic field.

2.2.1.1 Josephson effects (Cooper-pair tunneling)

Two effects related to the tunneling of cooper-pairs through a weak link of two superconductors are called “Josephson-effects” because B. D. Josephson has

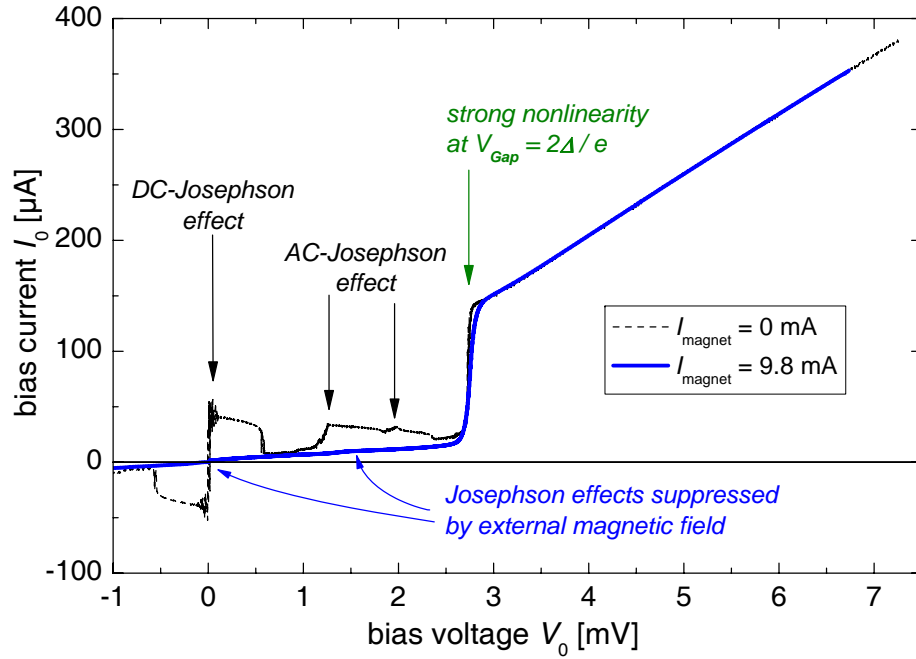


Fig. 2.3: Unpumped I-V-curve with magnetic field (dashed line) and without applied magnetic field (solid line). The Josephson effects are suppressed by the magnetic field, while the strong nonlinearity at 2.75 mV due to the quasi-particle tunneling remains also with applied magnetic field.

predicted these mechanisms in 1962 [33], before they have been confirmed experimentally.

The DC-Josephson effect is the tunneling of cooper-pairs through the barrier at zero bias-voltage (compare Fig. 2.3). Josephson has shown that this actual supercurrent as depending on the critical current I_c , which is the maximum supercurrent a junction can support, and the phase difference of the Cooper-pair wave functions on both sides of the insulating barrier.

The dependence of the critical current as a function of applied magnetic field is given as [31]

$$I_c(\Phi) = I_c(0) \cdot \left| \frac{\sin(\pi\Phi/\Phi_0)}{\pi\Phi/\Phi_0} \right|, \quad (2.7)$$

where $I_c(0)$ is the critical current without magnetic field, Φ is the total magnetic flux through the junction and $\Phi_0 = \pi\hbar/e$ is the flux quantum. The magnetic flux Φ through the junction depends on the junction area and its specific shape.

The AC-Josephson effect (which actually occurs, while no external AC-voltage is applied) describes the mechanism that in a tunnel junction a DC

voltage causes an alternating current of Cooper-pairs through the barrier of amplitude I_c and frequency

$$\nu_{Josephson} = \frac{2e \cdot V_{bias}}{h} \approx 483.6 \text{ GHz/mV}. \quad (2.8)$$

The AC-Josephson effect is used for the selection of the SIS-devices, since only for the resonance frequencies of the RF-circuit of the junction the increased current is seen at V_{bias} (details in Subsec. D.3.1).

2.2.1.2 Quasi-particle tunneling

In the environment of a metal or superconductor the behavior of the electrons is described with the terminology of “quasi-particles” (quasi-electrons and quasi-holes), which may have different effective masses and effective charge. In the superconductor two quasi-particles form a Cooper-pair, which carries the lossless super-current.

The semiconductor band model of a SIS-junction and the resulting theoretical DC I-V-curves for $T = 0$ and $T > 0$ are shown in Fig. 2.4. The band model illustrates that for the separation of a Cooper-pair into its original quasi-particles it is necessary to provide the energy $\Delta_1 + \Delta_2$. The resulting voltage, which is necessary to break a Cooper-pair at $T = 0$ is the gap-voltage

$$V_{Gap} = \frac{\Delta_1 + \Delta_2}{e}. \quad (2.9)$$

Quasi-particle tunneling below the gap-voltage V_{Gap} : For $T = 0$ no tunneling of quasi-particles is possible below the gap-voltage. For non-zero temperatures some Cooper-pairs are split by thermal excitation, which allows the tunneling of the resulting quasi-particles.

For the case of identical superconductors ($\Delta_1 = \Delta_2 = \Delta$), for low temperatures ($T_{amb} \ll T_c$) and voltages below the gap-voltage ($eV < 2\Delta$) the quasi-particle tunneling current is approximated as ([31], p. 90)

$$I_{ss} = \frac{2G_n}{e} \cdot e^{-\frac{\Delta}{k_B T}} \cdot \sqrt{\frac{2\Delta}{eV + 2\Delta}} \cdot (eV + \Delta) \cdot \sinh\left(\frac{eV}{2k_B T}\right) \cdot K_0\left(\frac{eV}{2k_B T}\right), \quad (2.10)$$

where G_n is the normal conductance and K_0 is the zeroth-order modified Bessel function. If the current below the gap-voltage is significantly larger than this thermally excited tunnel current, it indicates the existence of other parasitic currents (compare Subsec. 2.2.3, multiple Andreev reflection).

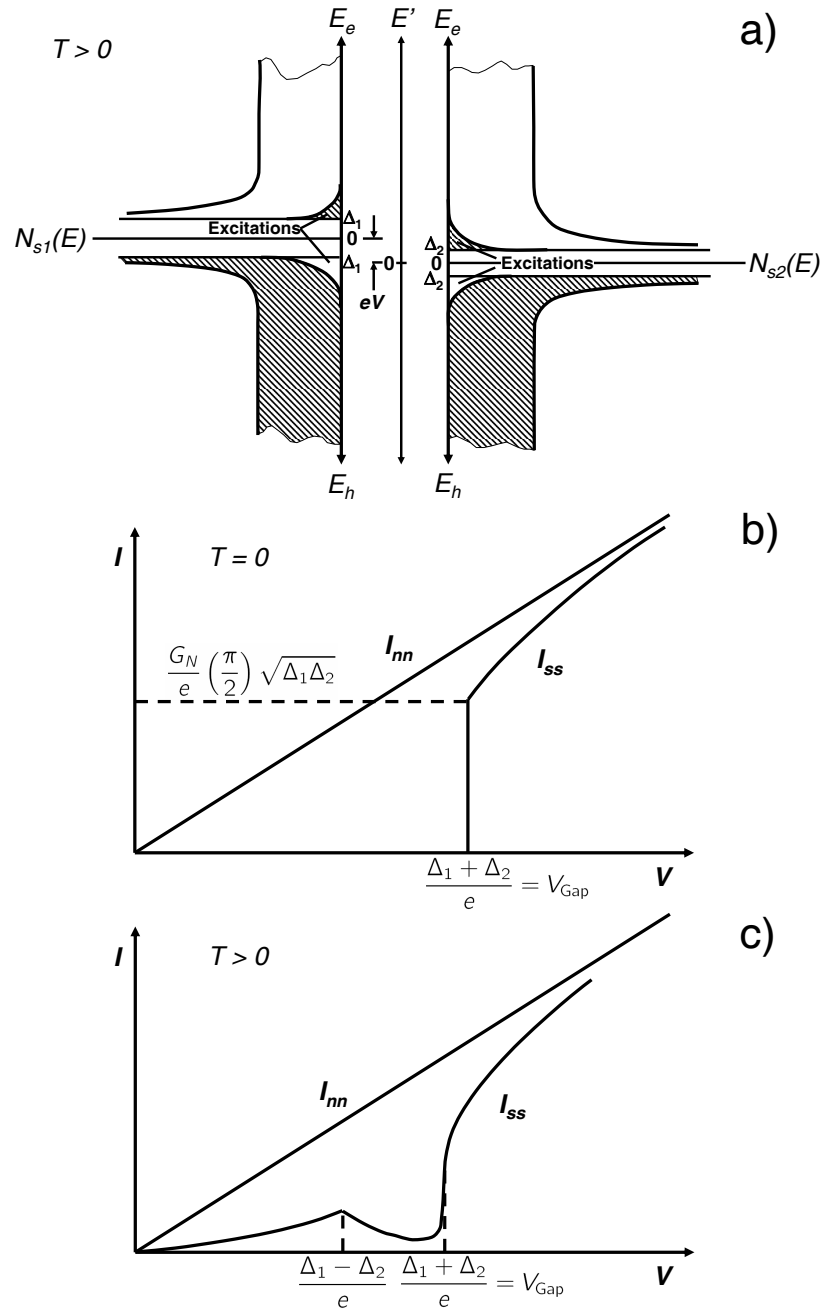


Fig. 2.4: Semiconductor-model of a SIS-junction for the tunneling of quasi-particles and resulting DC I-V-curves. **a)** Band model for two superconductors (Δ_1 , Δ_2) connected via an insulating barrier. Tunneling of quasi-particles occurs through thermal excitations below the gap-energy $\Delta_1 + \Delta_2$. Applied bias-voltages above $V_{\text{Gap}} = (\Delta_1 + \Delta_2)/e$ supply the necessary energy to split Cooper-pairs and allow a large number of quasi-particles to tunnel through the barrier. **b)** Theoretical I-V-curve for a SIS-junction at $T = 0$. Quasi-particle tunneling is possible only for voltages above V_{Gap} . **c)** Theoretical I-V-curve for a SIS-junction at $T > 0$. Thermally excited quasi-particle tunneling occurs also below V_{Gap} .

Quasi-particle tunneling above the gap-voltage V_{Gap} : From the band model in Fig. 2.4 (a) it is obvious, that for applied bias-voltages just at and above V_{Gap} the energy is large enough to split a number of Cooper-pairs and create quasi-particles, which tunnel through the barrier. Because of the large density of states just below and just above the gap energy the increase in current at the gap-voltage due to the quasi-particle tunneling is very steep. It becomes more smeared for increasing temperature, because the density of state just below the gap-energy decreases due to the thermal excited states above the gap (see Fig. 2.4 (a)).

2.2.2 DC-characteristics of a pumped SIS-junction

The SIS-junction is operated as mixer with an applied LO-radiation. This implies that in addition to thermal excitations and the energy from the applied bias-voltage a large number of photons with energy $E = h\nu$ are available. This has a significant influence of the tunneling effects, both of the Cooper-pairs and of the quasi-particles.

Photon assisted tunneling of quasi-particles The effect of photon assisted tunneling of quasi-particles is illustrated in Fig. 2.5. When a large number of photons with the energy $h \cdot \nu_{\text{LO}}$ is available, where ν_{LO} is the frequency of the local oscillator, a quasi-particle overcomes the gap-energy to tunnel through the barrier partly by absorbing the photons and partly by the applied DC-voltage. Thus steps with the voltage width $V = n \cdot h\nu_{\text{LO}}/e$ are seen in the pumped DC I-V-curve¹. The DC bias-voltages at which the photon assisted tunneling steps occur are given by:

$$\Delta_1 + \Delta_2 = e \cdot V_{\text{bias}} + n \cdot h\nu \quad (n = 1, 2, \dots)$$

For n is an integer there are also photon assisted tunneling steps above the gap. The effect of photon-assisted tunneling is used for SIS-junctions as direct detectors (see direct detection measurement with FTS in Subsec. 4.2.2). During the mixing process the device is in the pumped state.

Cooper-pair tunneling: Shapiro steps. When a SIS-junction is irradiated with LO-radiation of the frequency ν_{LO} , steps in bias-current are seen at voltages

$$V_{\text{Shapiro}} = n \cdot \frac{h\nu}{2e} \quad (n = 1, 2, \dots), \quad (2.11)$$

the Shapiro-steps in the DC I-V-curve [34]. The increased current is attributed to tunneling of Cooper-pairs. It can be obstructive for the mixing

¹For the HIFI band 2 the LO-frequency 636-802 GHz is of the same order as the gap-frequency. Thus only the first photon step with one involved photon is seen.

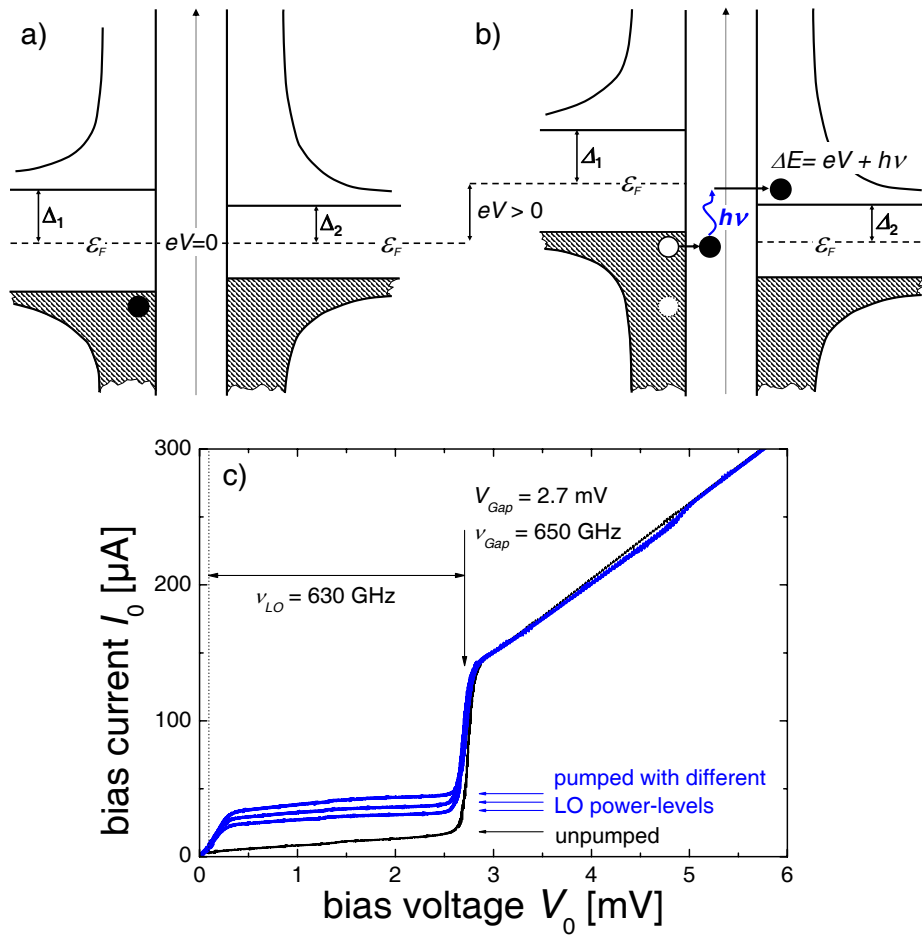


Fig. 2.5: Photon assisted tunneling: Semiconductor band model for a SIS-junction at temperature $T = 0$ and a measured DC I-V-curve. **a)** For the tunneling through the barrier the quasi-particle has to overcome the energy $\Delta E = \Delta_1 + \Delta_2 = e \cdot V_{\text{Gap}}$. **b)** If photons with $h\nu_{\text{LO}}$ are available the tunneling quasi-particle gains the energy gap partly by absorbing the photons and partly by the applied DC-voltage. **c)** Measured DC I-V-curve with applied LO-radiation (frequency ν_{LO}) the tunneling is possible for lower voltages ($V \geq e \cdot V_{\text{Gap}} - h\nu_{\text{LO}}$). The tunneling current depends on the total available number of photons (= LO-power level).

process, when it occurs in the bias-region. Therefore the tunneling of Cooper-pairs is suppressed with the applied magnetic field.

Upper frequency mixing limit: From the band model, given in Fig. 2.5 (b) it is also understandable, that the photon assisted tunneling only results in a pump step in the DC IV-curve for LO-frequencies ν_{LO} below twice the gap-frequency $\nu_{\text{Gap}} = e \cdot V_{\text{Gap}}/h$. For larger frequencies, the photon assisted tunneling is not preferred for one current direction (which for lower frequencies is defined by the direction of the bias-potential). Accordingly for LO-frequencies $\nu_{\text{LO}} \geq 2 \cdot \nu_{\text{Gap}}$ photon assisted tunneling occurs in both directions over the tunnel junction resulting in a zero net current.

The effect of zero net tunneling current because of quasi-particle tunneling in both current directions is already seen for LO-frequencies larger than the gap-frequency. But for LO-frequencies close to $2\nu_{\text{Gap}}$ the bias-region of effective tunneling current totally disappears.

For the presently used junction materials their gap-voltages and theoretical mixing limits are given in Table 2.1. For the HIFI frequency band 2 (636-

Junction material	V_{Gap} [mV]	ν_{max} [GHz]
Nb/Al-Al₂O₃/Nb	2.9	1400
Nb/Al-AlN/NbTiN	3.5	1700
NbTiN/MgO/NbTiN	5.2	2500
NbN/AlN/NbN	5.4	2600

Tab. 2.1: Gap-voltages and theoretical mixing limits for some relevant junction electrode materials. The different barrier materials are necessary due to fabrication requirements. The data for the gap-voltages are taken from [35, 36, 37, 38, 39, 13].

802 GHz) the mature technology of Nb/Al-Al₂O₃/Nb-junctions with a long experience in the KOSMA-laboratories is fully sufficient.

2.2.3 Andreev reflection

The phenomenon: The effect of Andreev reflection occurs at the interface of a superconductor and a normal-conductor [30] or at the interface of two different superconductors. In a single Andreev reflection an electron is reflected as a hole (or vice versa), while the charge $2e$ is transferred over the barrier by the tunneling of a Cooper-pair. This effect is relevant for the HIFI band 2 mixers under two aspects:

1. Andreev reflection is responsible for heat trapping and increased noise in Nb-junctions with all-NbTiN striplines [40]. This prevents NbTiN from being used as ground-plane and top-wiring for the matching circuits (compare Subsec. 3.4.2).
2. Multiple Andreev reflection (MAR) at the barrier has been identified as a source of increased sub-gap current and increased shot-noise [41, 42]. The so-called sub-gap structure, which is an indication for the occurrence of MAR, is seen in the measured DC I-V-curves of the fabricated junctions. It occurs in pinhole defects of the barrier, which for Al₂O₃-barriers are viewed as normal-conductive channels.

The effect of heat trapping in Nb-junctions with all-NbTiN striplines has already been analyzed and discussed in [13]. The increased noise because of MAR is relevant for the noise analysis of the fabricated SIS-mixers. The

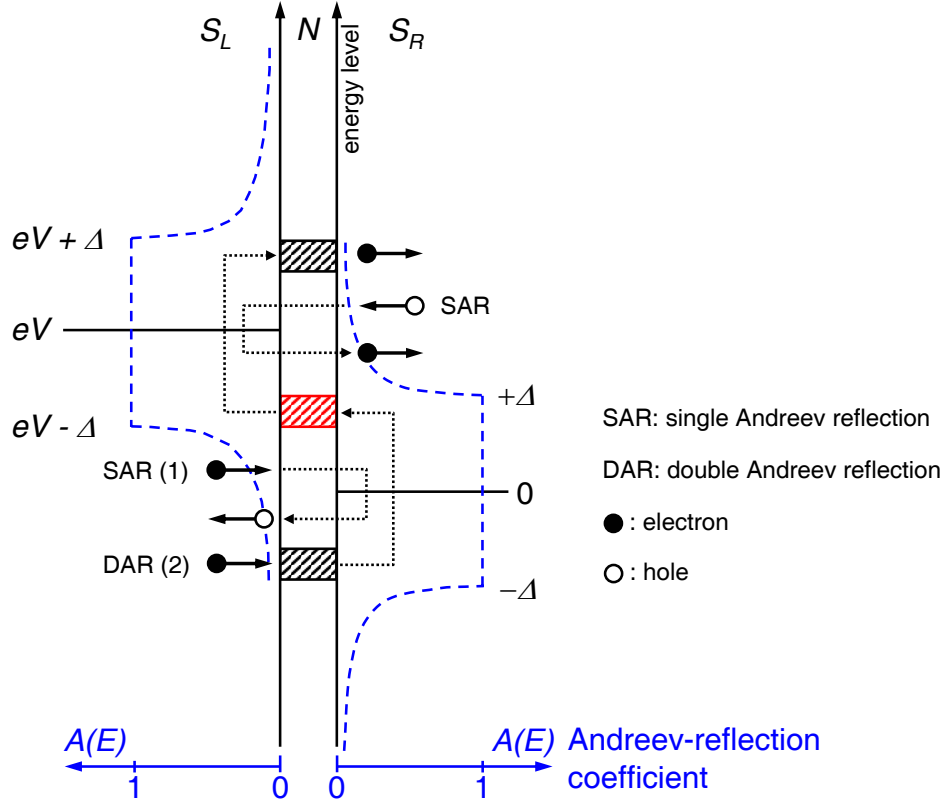


Fig. 2.6: Semiconductor picture for multiple Andreev reflection (MAR) with $eV \approx V_{\text{Gap}}/2$. Instead of the density of states the Andreev reflection coefficient $A(E)$ is plotted, which is 1 inside the energy gap. Multiple Andreev reflection (MAR) occurs when the Andreev-reflection coefficient $A(E)$ on both sides of the barrier is close to 1 (red hatched area). In a single Andreev reflection a quasi-electron is reflected as a quasi-hole (or vice versa), while the charge $2e$ is transferred over the barrier by the tunneling of a Cooper-pair. Illustration modified from [41].

effect of MAR is illustrated in Fig. 2.6. In the pinhole defects the barrier is viewed to be normal-conductive. The Andreev reflection coefficient is given as [41]

$$A(E) = \begin{cases} 1 & |E| < \Delta, \\ \frac{|E| - \sqrt{E^2 - \Delta^2}}{|E| + \sqrt{E^2 + \Delta^2}} & \text{else.} \end{cases} \quad (2.12)$$

A single Andreev reflection occurs e.g. for an electron from the left electrode, when it reaches the N:S_R-interface inside the energy-gap (SAR (1) in Fig. 2.6). Because of the energy conservation the electron reflects symmetrically around the pair chemical potential μ_R as a hole.

When the resulting reflected hole of an Andreev reflection has an energy level, which is not allowed in S_L (DAR (2) in Fig. 2.6, red hatched area), it is again reflected by Andreev reflection as an electron to S_R. This trajectory is possible for quasi-particles with energy levels marked by the black hatched areas. The quasi-particle totally has gained $2eV$ in energy.

For lower voltages with a larger overlap of the total reflection energy regions of S_L and S_R multiple Andreev reflections with larger numbers of reflections are possible.

Effective charge of an Andreev-cluster: MAR has been used to explain an increased sub-gap current of a SIS-device and the subharmonic structures in the measured $dI_{DC}(V)/dV$ of the device [41, 43]. In order to quantify this effect in the calculation of the resulting shot-noise a bias-voltage dependent effective charge $q(V)$ of the resulting “Andreev clusters” is defined. The effective charge specifies, how much charge carriers are effectively involved for the transport of the charge unity e . In [42] an upper limit for $q(V)$ of

$$q_{\text{MAR,max}}(V_{\text{bias}}) = \left(1 + \frac{V_{\text{Gap}}}{V_{\text{bias}}}\right) \cdot e. \quad (2.13)$$

is given.

This analysis is explicitly included in the noise analysis of the characterized flight mixers for HIFI band 2 in order to estimate the influence of MAR on the measured noise (Subsec. 2.4.4 and Sec. 5.2.3).

2.3 Summary of characteristic SIS-junction DC-parameters

In this section the main characteristics of a SIS-device are summarized. These parameters are used for the design of the matching circuits and throughout this thesis.

Gap-voltage V_{Gap} , critical temperature T_c : The gap-voltage is given by the sum of the gap-energies of both junction electrodes divided by the electron charge e (Eq. 2.9). Since the HIFI junctions are fabricated from two Nb-electrodes the gap-voltage is

$$V_{\text{Gap}}(0) = 2 \cdot \Delta_{\text{Nb}}/e.$$

The gap-parameter Δ is related to the critical temperature via the BCS-relation [44, 31]

$$2\Delta(0) = 3.52 \cdot k_B T_c. \quad (2.14)$$

With a measured critical temperature for Nb of $T_c = 9.2$ K, the gap-voltage at 0 K is expected to be 2.79 mV.

Normal resistance R_N : The normal resistance R_N is the resistance of the SIS-device in the normal conductive state (compare Fig. 2.4). For a given junction area A_J and gap-voltage V_{Gap} the normal resistance depends on the current density j_c :

$$R_N = \frac{\pi}{4} \cdot \frac{V_{\text{Gap}}}{j_c \cdot A_J}. \quad (2.15)$$

Critical current density j_c : The critical current is a parameter in BCS-theory, which characterizes the Cooper-pair tunneling. It is also used to characterize the physical properties of the insulating barrier, when the tunneling of quasiparticles is considered. The critical current density with respect to junction-area for temperatures well below the critical temperature is given by [45, 46]

$$j_c(T) = \frac{\pi}{4} \cdot \frac{V_{\text{Gap}}(T)}{R_N \cdot A_J}. \quad (2.16)$$

Within this these the parameter j_c is mainly used to characterize the ratio of gap-voltage and $R_N A_J$ -product of a device or a wafer².

Experimentally, the current density is determined by the thickness and the quality of the Al_2O_3 insulating barrier of the junction. The barrier in the HIFI band 2 devices is fabricated from an Al-layer of 8 nm thickness which is oxidized under the oxygen-pressure p_{Ox} for a time t_{Ox} . The value

$$E = p_{\text{Ox}} \cdot t_{\text{Ox}}$$

is called the *exposure* E in units of [Pa·s]. The dependence of the current density j_c on the exposure has been examined by S. Glenz and a nearly linear decrease of current density with increasing exposure was observed [13].

For purposes of optimum broadband coupling a high current density is desired (see Subsec. 3.6.2). In general high current density junctions, which have a thinner oxide barrier, have a higher chance on barrier defects and hence show also a higher sub-gap current, which in turn leads to a higher mixer noise. This effect is analyzed and discussed in Chap. 5.

Specific capacitance: Due to the geometry of the SIS-junction shown in Fig. 2.7 it is obvious, that the device also acts as a capacitor. Between two superconductive electrodes (S) there is a small insulating barrier (I) of some nanometers thickness, while the junction area is in the order of $1 \mu\text{m}^2$.

²In reference [31] it is remarked, that for superconductive materials like Nb and Pb, which exhibit a strong electron-phonon-electron coupling, the junction critical current density is reduced by a factor 0.75. In literature of applied SIS-mixers this factor of 0.75 is usually not included. Thus in this thesis the value of Eq. 2.16 is used realizing that the real critical current density in terms of Josephson tunneling is lower.

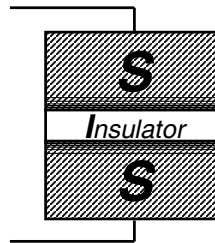


Fig. 2.7: Due to the superconductive electrodes with an area of $\approx 1 \mu\text{m}^2$ divided by a small insulating barrier of thickness of $\approx 2 - 3 \text{ nm}$ the junction has an intrinsic capacitance, which has a strong effect on its RF-performance.

The intrinsic capacitance depends on the dielectric properties of the barrier material and on the barrier thickness, which also influence its current density. For Nb/Al-Al₂O₃/Nb-junctions with a current density in the range of 8-13 kA/cm² a typical value of 85 fF/ μm^2 is assumed for the HIFI mixer junctions (compare the same value given in [47, 48]; a value of 90 fF/ μm^2 is given in [49]). The actual capacitance of a fabricated SIS-junction can hardly be measured, but conclusions from the RF-performance of the whole SIS-device can be drawn to evaluate the capacitance.

DC-quality Q : The tunneling current below the gap due to quasiparticle tunneling is given by Eq. 2.10. In this equation the tunneling current is inverse proportional to the normal resistance R_N . Thus the tunneling current for an ideal SIS-junction below and above the gap-voltage should be in a fixed ratio. But this ratio deviates from the theoretical value, if other mechanisms cause additional currents below the gap. For practical purposes the DC-quality is defined as

$$Q = \frac{R_{\text{sub-gap}}}{R_N}, \quad (2.17)$$

where $R_{\text{sub-gap}}$ for Nb-junctions usually is determined at 2 mV (see Fig. 2.8). The higher this quality factor Q , the lower is the sub-gap current. The difference between the measured and the theoretical value of the sub-gap current is an indication for the presence of other charge transfer mechanisms, which cause additional noise during the mixing process (e.g. multiple Andreev reflection in Subsec. 2.2.3).

2.4 Quantum mixer performance analysis

Quantum effects in the mixing process play a role, when the photon energy of the incoming signal $h\nu$ reaches the energy scale of the DC-nonlinearity $e \cdot \Delta V$ of the mixing device. In [50] the gap-sharpness ΔV_{Gap} is defined as the voltage width, which corresponds to the region of the I-V-curve with 10-90%

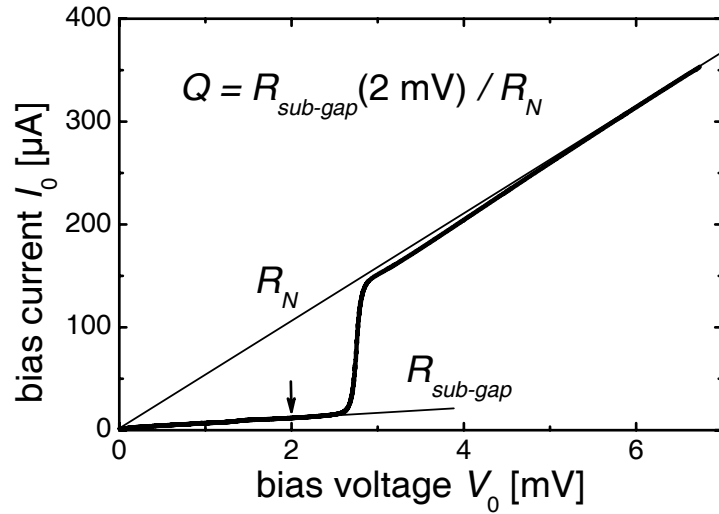


Fig. 2.8: Measured I-V-curve: The DC-quality Q is defined as the ratio of sub-gap resistance at 2 mV and normal state resistance R_N .

of the critical current $I_{\text{crit}} = V_{\text{Gap}}/R_N$. Another definition is the ratio of the second and third derivative of the DC I-V-curve $I(V)$. For the HIFI band 2 mixers, the pump voltage $h\nu/e$ (2.6-3.3 mV) is of the same order as the gap-voltage (2.6-2.8 mV), which is significantly larger than the width of the DC-nonlinearity $\Delta V \approx 0.1$ mV. This means, that the quantum mixer theory surely has to be applied for the relevant parameter region.

J. R. Tucker has developed a quantum-theory for SIS-mixers and published the results mainly in two contributions [27, 18]. Tucker's theory is applied to analyze the mixer performance in Chap. 5. The major results of Tucker's theory, which are used for this analysis, are summarized in this section. Details regarding the applicable equations for the DSB-mode of the mixer and the formalism to include lossy striplines are taken from [48] and [51].

The order of subsections follow the order, in which the given calculation is performed. First the pumped I-V-curve is calculated from a measured DC I-V-curve, including the embedding impedance and the LO power-level in the large signal analysis (Subsec. 2.4.1). The signal, which is detected by the mixer is modeled as a small signal perturbation (with linear response in voltages). The state of the mixer during the mixing process is characterized by the small signal admittance matrix, which allows the calculation of the voltage response to a set of current generators that model the RF-signal (Subsec. 2.4.2). This includes the analysis of the mixer gain G_{Mix} of the simulated device. The third step is the analysis of the noise properties with the noise correlation matrix (Subsec. 2.4.3) The shot noise in all involved side-bands is analyzed and the resulting output noise in the IF-frequency is evaluated, which characterizes the mixer noise T_{Mix} .

In the last subsection the analysis of the enhanced noise due to the MAR, as given in [42] (Subsec. 2.4.4) is described.

2.4.1 Large signal analysis (pumped I-V-curve)

The effect of photon assisted tunneling and the resulting pumped I-V-curve were described by Tien and Gordon [52] in 1963.

Tucker [18] extended the description of the photon assisted tunneling by including the SIS-junction's embedding network. This embedding network is necessary for the design of low noise SIS mixers and optimum power coupling from antenna to the junction. The results of Tucker which have been applied for the mixer simulation are briefly resumed.

Pumped I-V-curve without network environment: With $\psi_0(x, y, z, t) = f(x, y, z) \cdot \exp\left(-\frac{i}{\hbar} \cdot E \cdot t\right)$ being the solution of the Schrödinger-equation with the unperturbed Hamiltonian H_0 , the solution for the Hamiltonian,

$$H = H_0 + e \cdot V_{LO} \cdot \cos \omega_{LO} t \quad (2.18)$$

is required, where $V_{LO} \cdot \cos \omega_{LO} t$ is the perturbation due to the LO-radiation. The approach of a general time-dependent Fourier series as multiplier of ψ_0 because of the LO-radiation

$$\psi(x, y, z, t) = \psi_0(x, y, z, t) \cdot \sum_{n=-\infty}^{\infty} B_n \cdot e^{-i \cdot n \cdot \omega_{LO} \cdot t} \quad (2.19)$$

results in the equation for the coefficients

$$B_{n+1} + B_{n-1} = \alpha \cdot 2n \cdot B_n, \quad \text{with } \alpha = \frac{e \cdot V_{LO}}{h \cdot \nu_{LO}}. \quad (2.20)$$

This equation for the Fourier-coefficients is solved by $J_n(\alpha)$, the Bessel function of the first kind. The resulting pumped I-V-curve is calculated from the Tien-Gordon-relation [52]

$$I_0 = \sum_{n=-\infty}^{\infty} J_n^2(\alpha) \cdot I_{DC}(V_0 + n \cdot h \cdot \nu_{LO}/e). \quad (2.21)$$

The explicit derivation is given in [52] and [18].

Pumped I-V-curve with network environment: In order to couple signal and LO-radiation of a RF-frequency to the SIS-junction an optimized network environment is necessary. This is mainly necessary to compensate the junction's intrinsic capacitance C_J and to optimize the impedance matching to the antenna. The matching network is illustrated in Fig. 2.9 and is specified by the embedding impedance Y_{emb} , which includes C_J . For a given DC voltage V_0 and sinusoidal LO signal of amplitude V_{LO} , with the general time-dependent approach for the wave function [18]

$$\psi(x, y, z, t) = f(x, y, z) \cdot \exp\left(-\frac{i}{\hbar} e \cdot \left\{V_0 \cdot t + \int_0^t V_{LO} \cdot \cos(\omega_{LO} t') dt'\right\}\right) \quad (2.22)$$

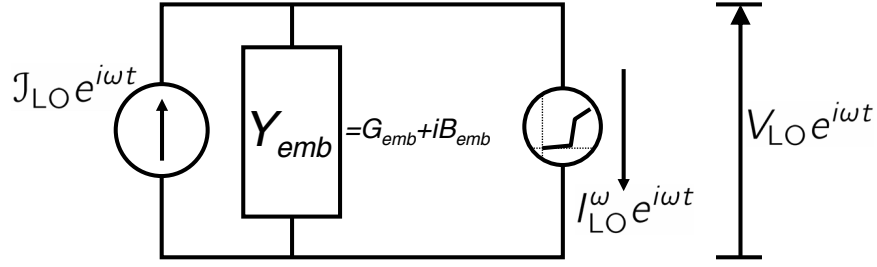


Fig. 2.9: Equivalent RF-circuit for the large signal analysis. The RF-current of the current generator (=LO) is split to a component through the linear embedding network and a component through the nonlinear SIS-device.

the components of the current $I_{LO}^\omega = I'_{LO} + iI''_{LO}$ are

$$I'_{LO} = \sum_{n=-\infty}^{\infty} J_n(\alpha) \{J_{n-1}(\alpha) + J_{n+1}(\alpha)\} I_{DC}(V_0 + n \cdot \hbar\omega/e) \quad (2.23)$$

$$I''_{LO} = \sum_{n=-\infty}^{\infty} J_n(\alpha) \{J_{n-1}(\alpha) - J_{n+1}(\alpha)\} I_{KK}(V_0 + n \cdot \hbar\omega/e). \quad (2.24)$$

Here, I_{KK} is the Kramers-Kronig-transform of the unpumped I-V-curve I_{DC} . Referring to Fig. 2.9 the current of the LO in terms of a current generator as a function of V_{LO} is then

$$\mathcal{J}_{LO}(V_{LO}) = \underbrace{I_{LO}^\omega(\alpha)}_{\text{nonlinear}} + \underbrace{Y_{emb} \cdot V_{LO}}_{\text{linear}}.$$

For a given \mathcal{J}_{LO} the value for V_{LO} is found by iteration. Then the DC-current is calculated from the Tien-Gordon relation (Eq. 2.21).

2.4.2 Small signal admittance matrix (mixer gain)

When the status of the pumped mixer is calculated from the large signal analysis, the RF-signal is modeled as a small signal. It is assumed, that the small signal induces a linear response in the other related frequencies

$$\omega_m = m \cdot \omega_{LO} + \omega_0, \quad m = 0, \pm 1, \pm 2, \dots \quad (2.25)$$

Here $m = 0$ denotes the IF-frequency, $m = 1$ is the signal- and $m = -1$ the image-frequency. A diagram of the network representation for the mixer is depicted in Fig. 2.10.

The signal voltage and current are written in the form

$$v_{sig}(t) = \text{Re} \left(\sum_{m=-\infty}^{\infty} v_m e^{i\omega_m t} \right) \quad (2.26)$$

$$i_{sig}(t) = \text{Re} \left(\sum_{m=-\infty}^{\infty} i_m e^{i\omega_m t} \right), \quad (2.27)$$

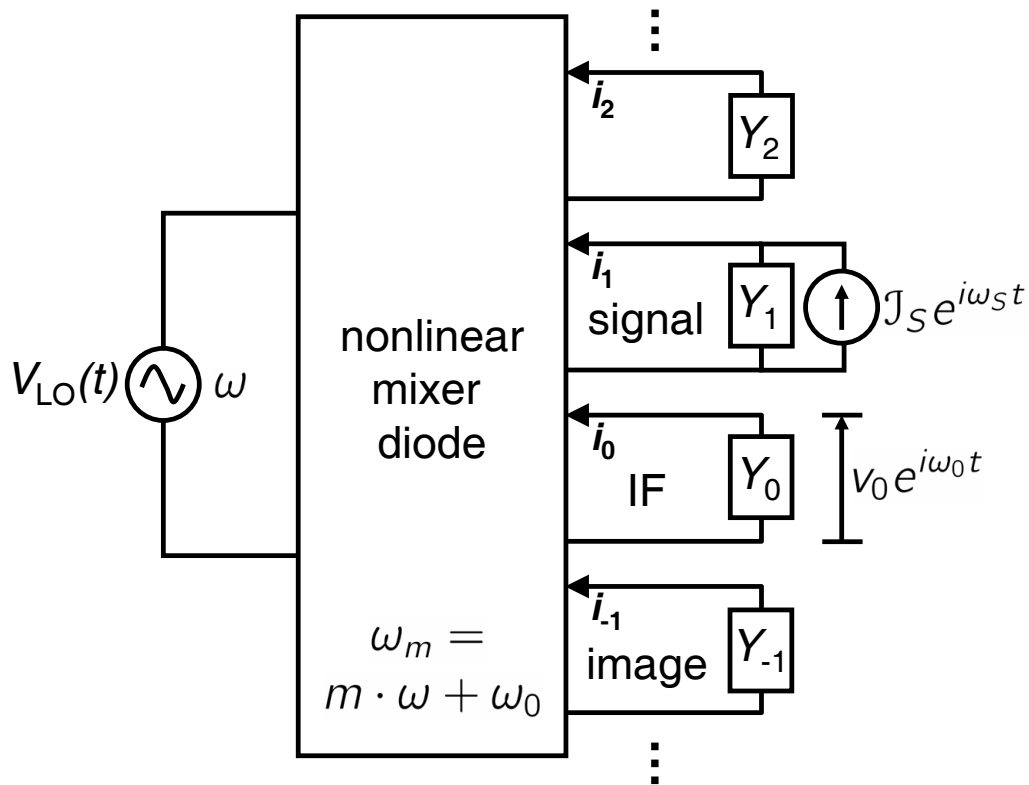


Fig. 2.10: Network representation of a SIS-mixer at frequencies $\omega_m = m\omega + \omega_0$ with termination admittances Y_m . The signal is represented as a current generator \mathcal{J}_S at the signal frequency $\omega_s = \omega_1$. The admittance $Y_0 = Y_L$ is the load-admittance at the IF-frequency.

where v_m are the voltages and i_m are the currents at the respective frequencies ω_m . The values for v_m and i_m depend on the actual state of the SIS junction, the applied LO- and bias-voltage. The admittance matrix $Y_{mm'}$ now is defined assuming a linear response caused by the signal with

$$i_m = \sum_{m'} Y_{mm'} v_{m'}, \quad (\text{admittance matrix definition}) \quad (2.28)$$

where $m, m' = -N, -N+1, \dots, 0, \dots, N$; the summation is extended over a number of $2N+1$ harmonic frequencies. The RF-signal is modeled as small deviations in voltage and current of the large signal result. The explicit results for $Y_{mm'} = G_{mm'} + iB_{mm'}$ are given in Eq. (4.72) and (4.73) in [18].

With the knowledge of the termination admittances Y_m the system can be analyzed for any set of current generators \mathcal{J}_m at the input and at the frequencies ω_m . The current generators are defined as

$$\begin{aligned} \mathcal{J}_m &= i_m + Y_m v_m \\ &= \sum_{m'} (Y_{mm'} + Y_m \delta_{mm'}) v_{m'}. \end{aligned} \quad (2.29)$$

For the HIFI Band 2 mixers a double side band mixer operation is assumed. In this case the signal ($m = 1$) and the image ($m = -1$) are mixed to the IF-frequency with approximately equal conversion efficiency. Then the current generators are $\mathcal{J}_1, \mathcal{J}_{-1} \neq 0$ and $\mathcal{J}_m = 0$ for $m \neq 1, -1$. The system is solved by inverting the matrix $Y_{mm'} + Y_m \delta_{mm'}$. So defining the *conversion matrix* according to Tucker with

$$Z_{mm'} = (Y_{mm'} + Y_m \delta_{mm'})^{-1} \quad (\text{conversion matrix definition}) \quad (2.30)$$

one obtains the signal voltages produced by an arbitrary set of current generators from

$$v_m = \sum_{m'} Z_{mm'} \mathcal{J}_{m'}$$

Calculated mixer gain: One important result, which is derived from the conversion matrix is the conversion efficiency of the mixer or “mixer gain”. It defines the ratio of converted power from the signal frequency ω_1 and the image frequency ω_{-1} to the IF-frequency ω_0 :

$$\begin{aligned} G_{Mix, Tucker} &= \frac{P_{out}(\omega_0)}{P_{in}(\omega_1) + P_{in}(\omega_{-1})} & (2.31) \\ &= 4 \cdot G_L \cdot \frac{|Z_{01}|^2 + |Z_{0-1}|^2}{1/G_{USB} + 1/G_{LSB}} \\ &= 2 \cdot G_L \cdot G_{USB} \cdot (|Z_{01}|^2 + |Z_{0-1}|^2) \quad \text{for } G_{USB} = G_{LSB} \end{aligned}$$

where G_L is the real part of the load admittance $Y_L = Y_0$, and $G_{USB/LSB}$ are the corresponding values of the signal admittances $Y_{USB/LSB} = Y_{1/-1}$.

For the simulation of a real mixer, the ohmic micro-strip losses G_{Strip} are included:

$$G_{Mix, eff} = G_{Mix, Tucker} \cdot G_{Strip} \quad (2.32)$$

Details regarding the calculation of the embedding impedance and the micro-strip losses are given in Sec. 3.5.

2.4.3 Current correlation matrix (mixer noise)

Within the quantum mixer theory the noise of the mixer is evaluated from the shot-noise caused by the DC-current $I(V)$ and the LO-current through the barrier. To obtain a result for the output noise at the IF-frequency ω_0 the noise at the side-bands m is modeled as current generators $\delta I_m(t)$. The *current correlation matrix* $H_{mm'}$ specifies the correlation of the noise currents between different side-band frequencies $(\omega_m, \omega_{m'})$.

The time-averaged mean-square noise current due to the LO-radiation and the DC-bias is given as

$$\langle [\delta I_0]^2 \rangle = B \cdot \sum_{mm'} \lambda_{0m} \cdot \lambda_{0m'}^* \cdot H_{mm'},$$

where $\lambda_{0m} = Z_{0m}/Z_{00}$ is calculated from the conversion matrix, B the IF-frequency bandwidth and $H_{mm'}$ the current correlation matrix³. A general expression of the current correlation matrix is given as [18]

$$H_{mm'} = e \sum_{n,n'=-\infty}^{\infty} J_n(eV_{LO}/\hbar\omega) \cdot J_{n'}(eV_{LO}/\hbar\omega) \delta_{m-m',n'-n} \quad (2.33)$$

$$\times \left\{ \coth \left[\beta(eV_0 + n'\hbar\omega + \hbar\omega_{m'})/2 \right] \cdot I_{DC}(V_0 + n'\hbar\omega/e + \hbar\omega_{m'}/2) \right. \\ \left. + \coth \left[\beta(eV_0 + n\hbar\omega - \hbar\omega_{m'})/2 \right] \cdot I_{DC}(V_0 + n'\hbar\omega/e - \hbar\omega_{m'}/2) \right\},$$

where $\beta = 1/k_B T$. The explicit results for $H_{mm'}$ with $m, m' = -1, 0, 1$ are given in Eq. (4.79) of reference [18].

Calculated mixer noise: From the noise correlation matrix and the conversion matrix the mixer noise temperature is calculated, which is defined via the minimum detectable power $P = k_B T_{Mix} B$:

$$T_{Mix, Tucker} = \frac{1}{k_B} \cdot \frac{1/G_{USB} + 1/G_{LSB}}{8 \cdot (|Z_{01}|^2 + |Z_{0-1}|^2)} \cdot \sum_{m,m'} Z_{0m} Z_{0m'}^* \cdot H_{mm'}. \quad (\text{mixer noise}) \quad (2.34)$$

In the case of devices with lossy micro-strips (attenuation $G_{Strip} \leq 1$) as matching circuit the actual input noise temperature of the mixer is increased by $1/G_{Strip}$:

$$T_{Mix, eff} = \frac{T_{Mix, Tucker}}{G_{Strip}}. \quad (2.35)$$

This value is applied for the simulation of the mixer performance in Chap. 5.

2.4.4 MAR-enhanced shot-noise

The effect of MAR (compare Subsec. 2.2.3) results in additional noise of the SIS-device. The method to include the noise contribution of the MAR-current to the calculated mixer noise is taken from P. Dieleman and T. M. Klapwijk [42].

³The current correlation matrix also is referred to as “noise matrix”.

Experimental indication for the occurrence of MAR: The occurrence of so-called subharmonic sub-gap structures, minima or maxima in the differential resistance dV/dI at voltages V_{Gap}/n with $n = 1, 2, 3 \dots$ is an indication for the occurrence of multiple Andreev reflection (MAR) [41]. These subharmonic sub-gap structures are clearly seen for the measured HIFI band 2 mixers (see Fig. 5.14).

Specification of effective charge $q(V)$ for a measured SIS-device: The theoretical tunneling current $I_{\text{tun}}(V)$ of quasi-particles is given in Eq. 2.10. The current, carried by MAR, $I_{\text{MAR}}(V)$ below the gap-voltage is calculated from the measured I-V-curve $I_{\text{DC}}(V)$ according to

$$I_{\text{MAR}}(V) = I_{\text{DC}}(V) - I_{\text{tun}}(V). \quad (2.36)$$

The actual voltage-dependent value for $q(V)$ is specified from the comparison of the calculated shot-noise (see App. A.1) with the measured IF-output power. If MAR is present, the measured IF-output power below the gap is larger than the calculated shot-noise.

In order to quantify the effect the standard shot noise spectral density

$$S_I(V) = 2 \cdot e \cdot I_{\text{DC}}(V) \quad (2.37)$$

in Eq. A.1 has to be replaced by

$$S_{I,\text{MAR}}(V) = 2 \cdot e \cdot I_{\text{tun}}(V) + 2 \cdot q(V) \cdot I_{\text{MAR}}(V). \quad (2.38)$$

The specification of the actual effective charge $q(V)$ is illustrated exemplary for two mixers in Fig. 2.11. The actual effective charge of the Andreev-clusters is defined as

$$q_{\text{MAR,var}}(V_{\text{bias}}) = (q_1 + q_2 \cdot V_{\text{Gap}}/V_{\text{bias}}) \cdot e, \quad (2.39)$$

with q_1 and q_2 as variable parameters.

In Fig. 2.11 (a) and (c) the measured IF-output power is plotted as black points. With $q_1 = 1$ and $q_2 = 0$, $q_{\text{MAR,var}}(V_{\text{bias}})$ reduces to the charge unity e , given as blue line in Fig. 2.11 (b) and (d). The correspondent calculated shot-noise power for the two measured I-V-curves is also given as the blue lines in Fig. 2.11 (a) and (c). It is below the measured output power. With $q_1 = q_2 = 1$, $q_{\text{MAR,var}}(V_{\text{bias}})$ results in the maximum value, given in Eq. 2.13. The voltage dependent effective charge is given in Fig. 2.11 (b) and (d) as red line, the resulting calculated shot-noise is also plotted as red lines in Fig. 2.11 (a) and (c). With this $q_{\text{MAR,max}}$ the calculated shot-noise power is larger than the measured output power.

Based on the measured IF-output power q_1 and q_2 are adapted to result in a calculated shot-noise, which is compliant with the measured IF-output power. The data are plotted as green lines in Fig. 2.11. Thus a function for the actual effective charge $q(V)$ for a measured SIS-mixer is obtained.

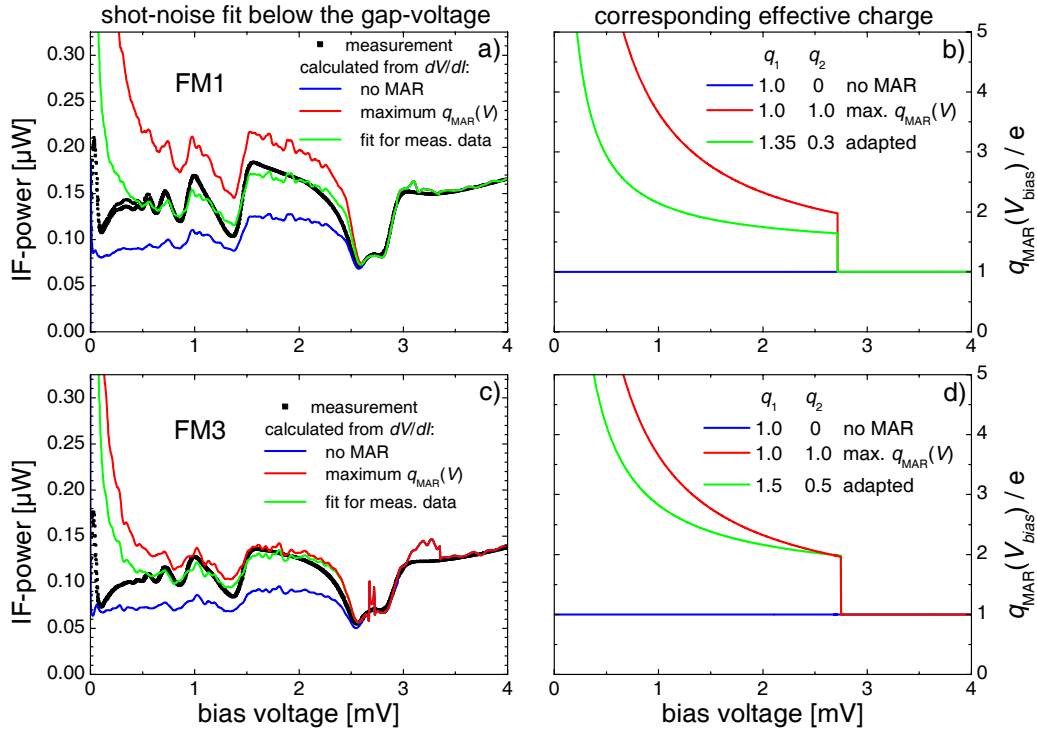


Fig. 2.11: Left column: Measured IF-power of unpumped mixer (black) for FM1 (top), FM3 (bottom) and calculated IF-power for three models for the effective charge $q(V)$ of Andreev clusters; blue line: no MAR present; red line: maximum effective charge $q(V)$; green line: fit for actual measured shot-noise. Right column: voltage dependent effective charge $q(V)$ of Andreev clusters for the three models below the gap-voltage. The relation with $q_1 = q_2 = 1$ refers to the analytical solution for the maximum value, given in [53].

Modified noise correlation matrix: With the obtained $q(V)$ for a measured SIS-mixer the noise calculation based on the Tucker formalism (Subsec. 2.4.3) is modified as specified in [42]. E.g. the matrix element H_{00} is replaced by

$$\begin{aligned}
 H_{00} = & 2 \sum_{n=-\infty}^{\infty} J_n^2(\alpha) \cdot q \cdot I_{MAR} \cdot \coth\left(\frac{q \cdot V}{k_B \cdot T}\right) \\
 & + 2 \sum_{n=-\infty}^{\infty} J_n^2(\alpha) \cdot e \cdot I_{tun} \cdot \coth\left(\frac{e \cdot V}{k_B \cdot T}\right). \quad (2.40)
 \end{aligned}$$

The other matrix elements are adapted equivalently. This method has been applied in Subsec. 5.2.3 for the analysis of the measured flight-mixers.

The numerical calculation of the noise performance for a simulated mixer over a specific frequency band is described in App. A.3.

Chapter 3

Design of broad-band matching circuits for SIS-devices in a waveguide environment

In a broad-band heterodyne receiver the RF-radiation (signal and LO) has to be coupled to the mixing element with minimum power losses. For the HIFI band 2 mixers, which are realized as waveguide mixers, this requires an effective broad-band power coupling of the radiation from the waveguide to the SIS-junction over the required frequency range. This is achieved with two major components

1. the waveguide probe, which transforms the radiation from the waveguide mode to micro-strip modes and
2. the resonant micro-strip matching circuit, which couples the radiation from the feed-point of the waveguide probe to the SIS-junction by means of impedance transformation and compensation of the junction's intrinsic capacitance.

The design and optimization of the waveguide probes has been done by T. Tils and is described in his thesis [16]. The design and analysis of the SIS-junctions and the corresponding micro-strip matching circuits is part of this thesis. The explicit design model for the physical description of an SIS-device, the numerical optimization of the matching circuits and selection of device designs for the lithography masks is documented in this chapter.

The optimization of the power coupling is based on the assumption that the intrinsic noise of a SIS-mixer does not show a strong frequency-dependence¹.

¹The validity and the limitation of this assumption is analyzed in Chap. 5 based on Tucker's shot-noise calculation in the three-frequency approximation. The calculated power coupling turns out to be the relevant criterion for the position of the band pass. For some parameters, especially lower DC-qualities Q discrepancies arise, when the relative power coupling for two frequencies is compared with the relative calculated noise at these frequencies.

In the first section an overview of the HIFI band 2 mixer is given, to illustrate the waveguide mixer concept. The other sections are focussed on the calculation of the power coupling of the RF-radiation from the waveguide to the SIS-junction. In Sec. 3.2 the utilized model for the impedance of the SIS-junction in a network environment is described. Then, in Sec. 3.3 the essential characteristics of the waveguide and the waveguide probe are summarized. The concept of superconductive micro-strips and their material-specific properties as transmission lines and impedance transformer are presented in Sec. 3.4. The formalism, which has been applied for the calculation of the band-pass, the frequency dependent power coupling to the SIS-junction, is described in Sec. 3.5. Finally in Sec. 3.6 the optimization of the device designs and the selection of the designs, which have been placed on the lithography masks for the SIS-device fabrication, are presented.

3.1 HIFI band 2 mixer overview

The waveguide mixer: The HIFI band 2 mixers are realized as waveguide mixers. For the discussion of the alternative quasi-optical techniques see e.g. [9, 10, 54].

The whole mixer fits into an envelope of $32 \times 32 \times 45 \text{ mm}^3$. The mass is just below 80 g. A sketch of the major components is given in figure 3.1. The mixing SIS-device is in the substrate channel across the waveguide of the the copper fixed tuned waveguide mixer-block. Some details of the block are found in [55].

The mixer block and its waveguide is connected and positioned to the corrugated feed horn and its bracket via dowel pins and screws. The horns are fabricated by Radiometer Physics [56] for a center frequency of 720 GHz (for characterization see [57], [58], [16]).

The mixer block is connected to the bias-T with an SMA connector and semi rigid cable. In the bias-T the DC connections are protected against electro-static discharge (ESD) and shielded against electro-magnetic interference (EMI). The bias-T consists of two compartments: one compartment (on top of the mixer) for the DC-connection to the semi rigid cable with the EMI-protection and a second compartment besides the mixer block with a circuit for protection against ESD from the DC-connector to the sensitive mixer device.

To suppress the Josephson effects in the SIS-junction a superconductive magnet is used. The maximum allowed current here is 10 mA, which leads to a magnet of 10,000 turns of $70 \mu\text{m}$ thick NbTi copper cladded wire. The pole pieces guide the field generated by the magnet towards the junction are out of pure iron ($\geq 99.9 \%$).

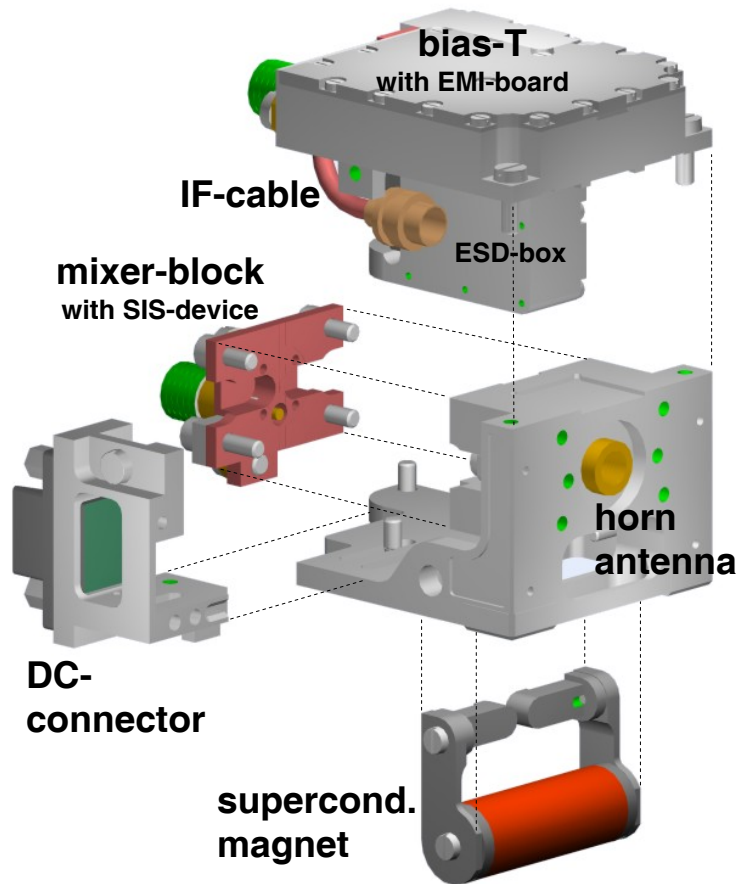


Fig. 3.1: The components of the mixer are mixer block with heater and SIS-device, horn antenna with bracket, bias-T with electro-static discharge (ESD)- and electromagnetic interference (EMI)-protection, DC-connector and super-conducting magnet.

The RF-signal is coupled with the corrugated horn to the waveguide. The coupling of the radiation from the waveguide to the mixing SIS-device has to be optimized over the given frequency band (602-802 GHz).

The device layout: The SIS-junctions are fabricated in the clean-room facilities of KOSMA in thin-film technology. The fabrication of the devices was not part of this thesis; it is described in [14] and [13].

A scheme of a SIS-junction is given in Fig. 3.2. Two superconductive Nb-electrodes (100 nm thickness) are divided by a thin Al_2O_3 -barrier ($\approx 8-10$ nm thickness). It is connected to the waveguide probe with NbTiN/ SiO_2 /Nb or NbTiN/ SiO_2 /Al micro-strips, which is discussed below (Sec. 3.4).

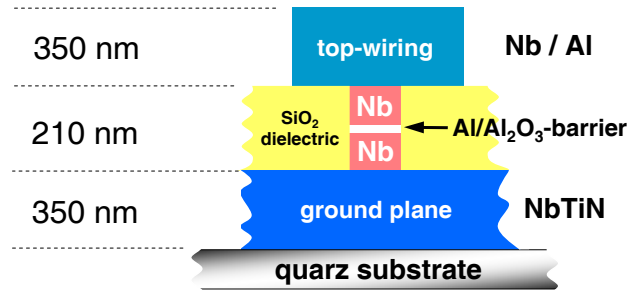


Fig. 3.2: For the HIFI band 2 devices Nb-junctions with Al/Al₂O₃-barriers are used. The junctions are embedded in NbTiN/SiO₂/Nb or NbTiN/SiO₂/Al micro-strips which function as DC-connections and RF-matching circuits.

3.2 RF-impedance of the SIS-junction

The RF-impedance of a SIS-junction according to a simplified model is specified by its normal resistance R_N and its capacitance C_J . For a complete description of the RF-performance of a SIS-junction, Tucker's theory has to be applied (compare Sec. 2.4). The validity and the limitations of this simplified model are illustrated for some the actual junction designs in Chap. 5.

In the simplified junction model the SIS-junction is viewed as a parallel connection of a resistance of the size R_N and the junction's intrinsic capacitance C_J (see Fig. 3.3). Typical values for junction impedances in the frequency

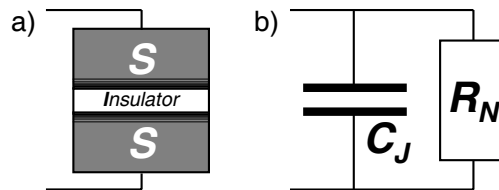


Fig. 3.3: Equivalent circuit of the SIS-junction in the simplified model. a) The superconductive electrodes (S) with an area of the order $1 \mu\text{m}^2$ are divided by an insulating barrier (I), which has a thickness of some nanometers. b) Illustration of the simplified junction model: a parallel connection of the normal conducting resistance R_N and a capacitor with capacitance C_J .

range of 600-900 GHz with junction areas of $0.5\text{-}1.0 \mu\text{m}^2$, current densities of $8\text{-}15 \text{ kA/cm}^2$, a gap-voltage of 2.75 mV and a specific junction capacitance of $85 \text{ fF}/\mu\text{m}^2$ are

$$Z_J = \{(0.7 \pm 0.6) - i \cdot (4.2 \pm 2.1)\} \Omega.$$

This capacitive impedance has to be matched to the impedance of the waveguide probe.

Bandwidth and current density j_c : A parallel resonant circuit in general is characterized by the Q -value

$$Q_{\text{res}} = \omega \cdot R \cdot C, \quad (3.1)$$

which is inversely proportional to its bandwidth. A single SIS-junction can be viewed as a parallel resonant circuit with $Q_{\text{res}} = \omega R_N C_J$. Since the R_N is inverse proportional to the junction area A_J and the capacitance C_J is proportional to A_J , variation of A_J does not change the bandwidth (compare Subsec. 2.3). But the bandwidth is increased, if the current density j_c is increased, which implies to first order no change in C_J and a decrease in R_N for the same A_J according to Eq. 2.16. Thus a high value for j_c is crucial for a broadband coupling of the RF-radiation to the SIS-junction.

3.3 Waveguide and waveguide probe

The main properties of the waveguide and the waveguide probe are given here briefly. Their frequency dependent impedance is the target value for the impedance matching of the micro-strip circuit on the source side.

3.3.1 The waveguide

The waveguide dimensions have been fixed in a very early stage of the project and are viewed as a given constraint.

The geometry and the impedances of the waveguide in the HIFI band 2 mixer-blocks are given in Fig. 3.4. The geometry (Fig. 3.4, left) is $325 \times 81 \mu\text{m}$, which results in a cutoff frequency of $\nu_c = 461 \text{ GHz}$. The field wave impedance of this waveguide is calculated from Eq. [59]

$$Z_{WG}(\nu) = 2 \cdot \frac{b}{a} \cdot \frac{\eta}{\sqrt{1 - (\nu_c/\nu)^2}},$$

where $\eta = \sqrt{\mu_0/\epsilon_0} \approx 377 \Omega$ is the free space impedance. A “half-height” waveguide ($a/b = 4$) has a 50% lower impedance than a “full-height” waveguide ($a/b = 2$).

In Fig. 3.5 the waveguide impedances of the HIFI band 2 waveguide and typical junction impedances are plotted. The junction impedances for the different values for the current densities of 8 kA/cm^2 and 15 kA/cm^2 are not clearly separated in this scale with normalization of the Smith-chart to 50Ω .

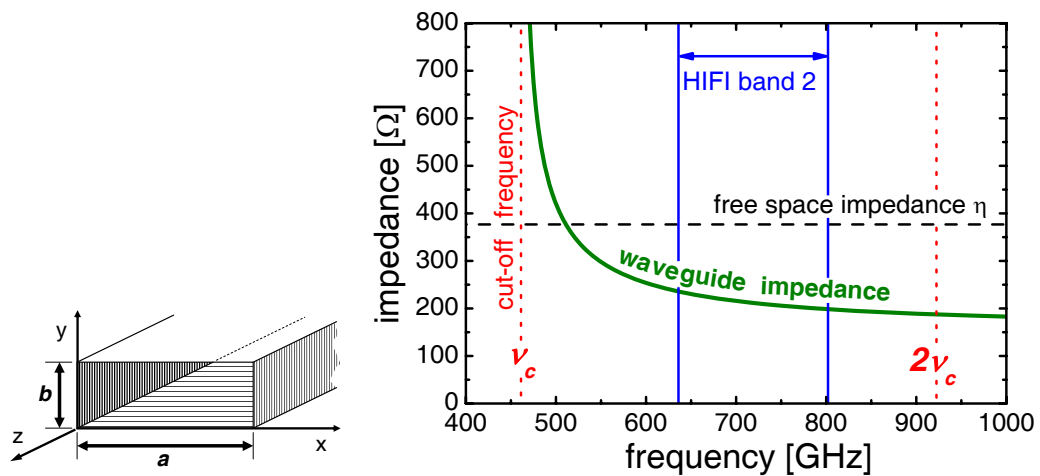


Fig. 3.4: Left: Rectangular waveguide with width a and height b . Right: Waveguide impedance for $a = 325 \mu\text{m}$ and $b = 81 \mu\text{m}$ (green). Also given are the HIFI band 2 frequency edges (blue), the cutoff frequency ν_c and $2 \cdot \nu_c$ (red) and the free space impedance of $\eta = \sqrt{\mu_0/\epsilon_0} \approx 377 \Omega$.

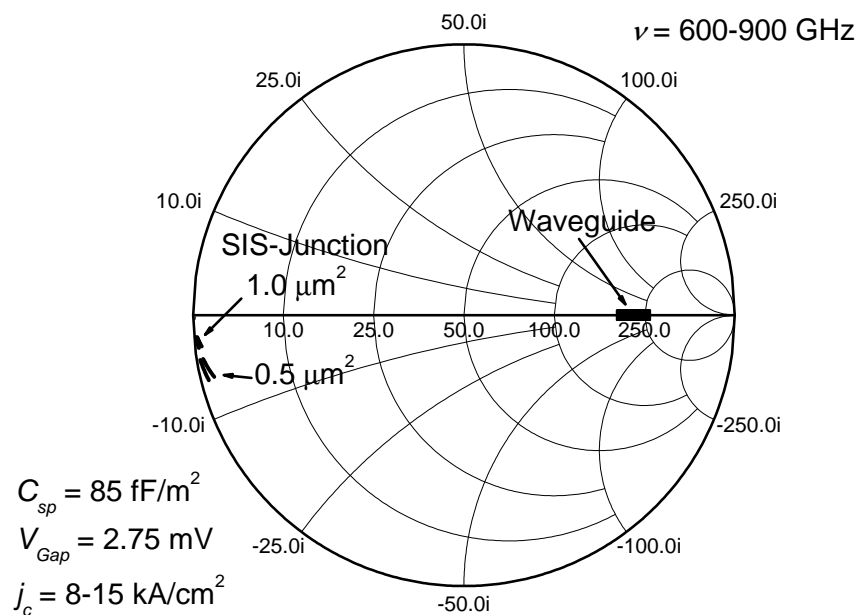


Fig. 3.5: Typical junction impedances for junction areas of $1.0 \mu\text{m}^2$ and $0.5 \mu\text{m}^2$, gap-voltage of 2.75 mV and a specific capacitance per area of 85 fF/cm^2 in comparison with the waveguide impedance for frequencies of $600\text{-}900 \text{ GHz}$. The upper junction impedances (smaller imaginary part) refer to the junction area of $1.0 \mu\text{m}^2$, the lower to $0.5 \mu\text{m}^2$. The junction impedances are calculated for current densities of 8 kA/cm^2 and 15 kA/cm^2 , the values barely can be identified as separate lines.

3.3.2 Micro-strip waveguide probe

The waveguide-probe collects the RF-radiation in the waveguide and transforms the electromagnetic radiation from a waveguide mode to a micro-strip mode, thereby transforming the waveguide impedance from approximately 250Ω to approximately 30Ω (dependent on frequency). For an optimized broadband power coupling the waveguide probes have been designed and optimized with an electro-magnetic 3-dimensional field solver by T. Tils [15, 16]. A sketch of the micro-strip probe inside the mixer block is given in Fig. 3.6. In the figure a symmetric probe with symmetric tapers, which collects the

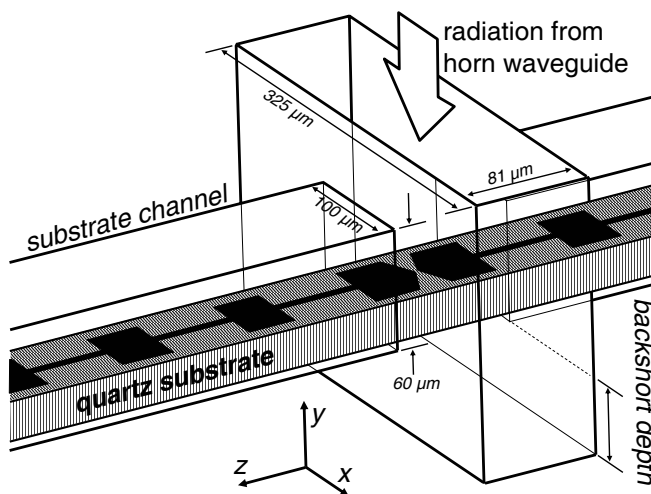


Fig. 3.6: The waveguide probe in the substrate channel. The 1×4 -waveguide is connected to the corrugated horn. Waveguide and substrate channel are realized in Cu, which is gold-plated for reasons of space-qualification. The waveguide probe is realized from metals and/or superconductor materials in micro-strip technique. It also works as a bandpass filter to prevent the escape of radiation through the substrate channel and contains DC-bias lines and connections for the IF-outcoupling.

RF-power, is shown. A low-pass filter is integrated with the waveguide probe. It blocks the RF-radiation to propagate through the substrate channel but allows the IF-product to be coupled to the IF-electronics.

The optimized waveguide probe impedances are shown in Fig. 3.8 for two different types of probes. Note that the impedance of the probes is already much lower than the original waveguide impedance shown in Fig. 3.5.

The impedances of the two different waveguide probes for the HIFI frequency band 2 are given in Fig. 3.8 from [16]. The impedances of the waveguide and the SIS-junction are the same as in Fig. 3.5. Added are the impedances of the waveguide probes. Also the frequencies of the junction-impedance are plotted. Higher frequencies imply lower imaginary part of junction impedances.

For a resonant matching the junctions' impedances have to be transformed to the complex conjugate of the waveguide probe impedances. The frequency

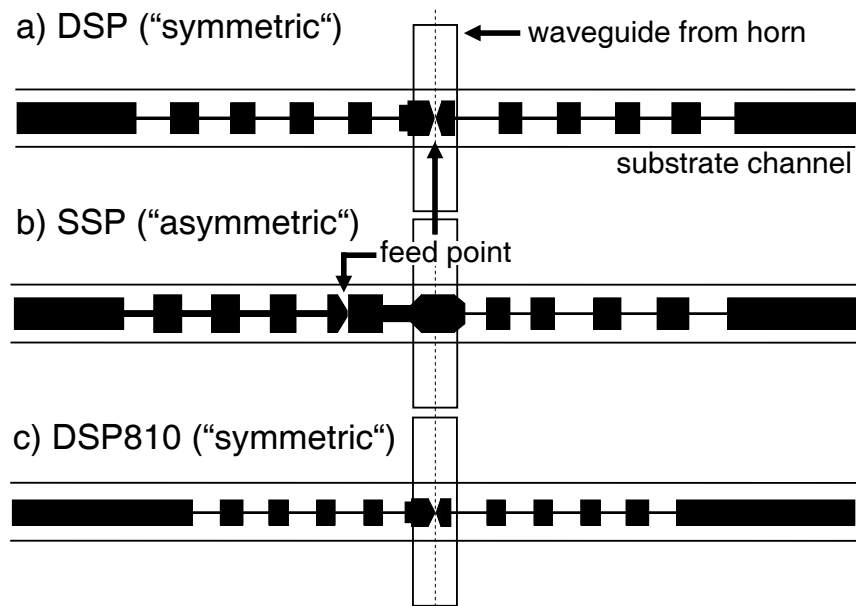


Fig. 3.7: Schematical layout of waveguide probes: a) DSP: symmetric probe on masks NbTiN3, CCN8 and NbTiN4; b) SSP: asymmetric probe on masks "NbTiN3" and "NbTiN4"; c) DSP810: symmetric probe on masks "NbTiN3" and "NbTiN4", scaled from probe "DSP" to the frequencies 790-880 GHz for SMART on KOSMA.

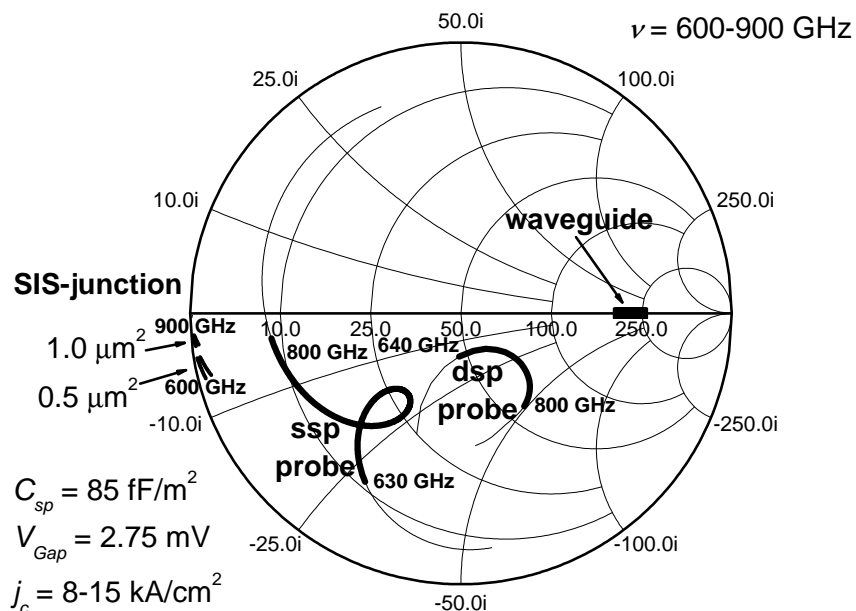


Fig. 3.8: Impedances of the reduced height waveguide, the two relevant waveguide probes ("DSP" and "SSP") and SIS-junctions for frequencies of 600-900 GHz. The SSP-probe shows a much lower output impedance than the DSP-probe. For details of the impedance calculation see [16].

dependent slope of the impedances for the probe SSP is preferable for the coupling to the SIS-junctions.

3.4 Micro-strip impedances for the relevant materials

The impedances for the micro-strips in the matching circuit are modeled as normal conductive or superconductive transmission lines from their surface impedances [60]. This allows the calculation of the micro-strip impedances from the surface impedance and the geometry of the transmission line.

3.4.1 Propagation of electromagnetic waves in micro-strips

The formalism, which has been used to calculate the propagation of the radiation dependent on frequency ν is taken from [22]. Here, some of its most important properties for the matching circuits are summarized.

Transmission line model: A transmission line is characterized by its characteristic impedance, which is the ratio of voltage and current of a travelling wave. The parameters that specify the wave propagation in a transmission line over a length dx are sketched in Fig. 3.9 [22]. Over the line length dx

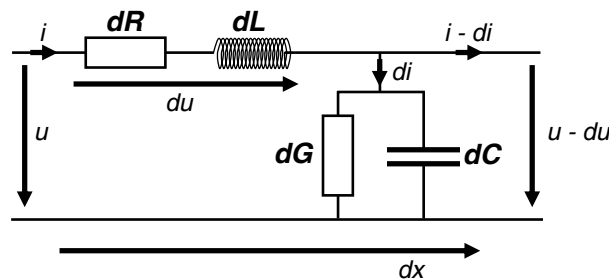


Fig. 3.9: The propagation of a wave with angular frequency ω through a transmission line is influenced by its series impedance $Z = i\omega \cdot L' + R'$ and its parallel admittance $Y = i\omega \cdot C' + G'$ per unit length.

the voltage u is reduced by du due to the specific resistance $R' = dR/dx$ and the specific inductance $L' = dL/dx$, while the current i is reduced by di because of the specific conductance $G' = dG/dx$ and the specific capacitance $C' = dC/dx$ of the line.

For a micro-strip, which consists of two thin conducting films divided by a thin insulating material (compare Fig. 3.10), the specific capacitance C' is the geometrical capacitance per unit length; the specific inductance L' occurs

because of self-inductance (and kinetic inductance for superconductors) the specific resistance R' is due to ohmic losses in the metallization per length and the specific conductance G' can be nonzero because of small currents through the non-ideal insulation. The characteristic impedance per unit length is

$$Z_C = \sqrt{\frac{\bar{Z}}{\bar{Y}}} = \sqrt{\frac{i\omega L' + R'}{i\omega C' + G'}}. \quad (3.2)$$

The propagation constant γ and phase velocity v_{phase} is calculated from Z and Y with

$$\gamma = \sqrt{\bar{Z} \cdot \bar{Y}}, \quad v_{phase} = \frac{\omega}{\text{Im}(\gamma)}. \quad (3.3)$$

If a transmission line with characteristic impedance Z_C is terminated with a load impedance of Z_L , the reflected wave is calculated from the reflection coefficient

$$\Gamma = \frac{Z_L - Z_C}{Z_L + Z_C},$$

which gives the ratio of voltage and current of a propagating wave in the stationary state. The reflected power is then the square of the reflected amplitude. It is obvious that a transmission line is optimum terminated with a load impedance of $Z_L = Z_C$ with no reflection. The same effect of power reflection appears where two transmission lines with different characteristic impedances are connected. Optimum power coupling is achieved with equal characteristic impedances.

A transmission line as impedance transformer: A transmission line with a characteristic impedance Z_C can also work as an impedance transformer. If a transmission line is terminated with a load impedance Z_L , the impedance at any other point in front of this load, which describes the ratio of voltage and current of the propagating wave in the stationary state is different in the transmission line and depends on the location of examination. The transformed impedance at a distance l from the termination load is given by the equation

$$Z_l = Z_C \cdot \frac{Z_L + Z_C \cdot \tanh(\gamma \cdot l)}{Z_C + Z_L \cdot \tanh(\gamma \cdot l)}. \quad (3.4)$$

From Eq. 3.4 it can be shown, that with a transmission line of a quarter wavelength $l = \lambda/4$ a real load impedance Z_L is transformed to any other desired real impedance Z_l with

$$Z_{(l=\lambda/4)} = \frac{Z_C^2}{Z_L},$$

by adjusting the characteristic impedance Z_C of the transmission line.

Micro-strip impedances from surface impedances: Strip-lines, transmission lines made of thin film metal lines, and dielectrics can be realized in several compositions, as micro-strips, slot-lines, coplanar waveguides, coplanar strips etc. [61]. For the HIFI band 2 mixer devices a *micro-strip layout* (Fig. 3.10) with two different materials is used.

The method to realize a strip-line with the possibility of two different materials for the two conductive elements is *the micro-strip layout*, which is used for the HIFI band 2 mixer devices. With this technique the waveguide probes are realized as one layer with larger dimensions. This layer serves as ground-plane for the matching circuit, which is defined with a second narrower layer on top of a dielectric with dielectric constant ϵ . The layout of a micro-

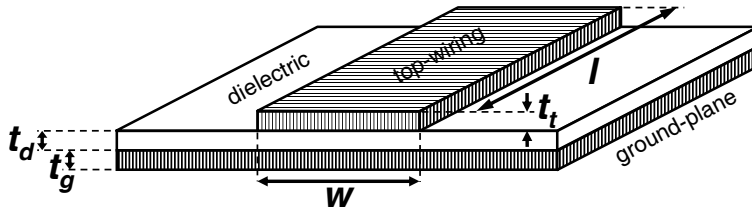


Fig. 3.10: Microstrip geometry: The groundplane with a thickness t_g is assumed to be of infinite width in comparison with the width of the top-wiring w which has a thickness t_t and a length l . The two conductors are divided by a dielectric of thickness t_d .

strip is given in Fig. 3.10. The series impedance Z and the admittance Y of the micro-strip are calculated from the surface impedance [60]:

$$Z = i \cdot \omega \cdot \mu_0 \cdot \frac{t_d}{W_{eff}} + \left(\frac{Z_{surf}(t_t)}{W_{eff,t}} + \frac{Z_{surf}(t_g)}{W_{eff,g}} \right) \quad (3.5)$$

$$Y = i \cdot \omega \cdot \epsilon_0 \cdot \epsilon_{eff} \cdot \frac{W_{eff}}{t_d}. \quad (3.6)$$

μ_0 is the permeability, ϵ_0 the permittivity of free space. Here Z_{surf} are the surface-impedances of the related materials depending on the layer thicknesses t_t or t_g .

The effect of fringing fields at the edges of the micro-strips is included with effective values of the micro-strip width w and dielectric constant ϵ . $W_{eff,g}$ and $W_{eff,t}$ are the effective widths of the ground-plane and the top-wiring and are combined to define the effective width of the micro-strip

$$W_{eff} = \frac{W_{eff,t} + W_{eff,g}}{2}.$$

The value ϵ_{eff} is the effective dielectric constant of the stripline

$$\epsilon_{eff} = \frac{\epsilon_{eff,t} + \epsilon_{eff,g}}{2},$$

where $\epsilon_{eff,t/g}$ respectively depend on the top-wiring and ground-plane material and geometry. The equations for the effective values, which are used in the design and analysis calculations are given in Appendix B.1.

Step inductance: At the transition from one stripline with a width w_1 to a stripline of the same materials and thicknesses with the width w_2 , which occurs at several types of matching circuits, causes a step inductance in series with the stripline impedances. This inductance is given as [62]

$$Z_{step} = \frac{i \cdot \omega \cdot t_t \cdot \mu_0}{\pi} \cdot \ln \left(\sin \left\{ \frac{\text{Re}(Z_{0,1}) \cdot \text{Re}(v_{ph,2})}{\text{Re}(Z_{0,2}) \cdot \text{Re}(v_{ph,1})} \cdot \frac{\pi}{2} \right\}^{-1} \right). \quad (3.7)$$

Here the correct order of micro-strips is given by $w_1 > w_2$. $Z_{0,1}$ and $Z_{0,2}$ are the characteristic impedances, $v_{ph,1}$ and $v_{ph,2}$ the phase-velocities of the two micro-strips defined according to Eq. 3.2, 3.3, 3.5 and 3.6.

3.4.2 Surface impedances for the relevant materials

Depending on the conduction mechanism (normal conductive or superconductive) and on the frequency range the formalism to specify the surface impedance has to be identified.

In a normal conductor the characteristic dimension for the electron is the mean free path l , while in the superconductor the distance of the interaction is the coherence length ξ , which is given by the intrinsic coherence length of the Cooper-pairs ξ_0 and the mean free path of the unpaired electrons l

$$\frac{1}{\xi} = \frac{1}{\xi_0} + \frac{1}{l}. \quad (\text{coherence length})$$

In general, high frequency fields have a limited penetration in the metallic conductor. For normal conductors the skin-effect which describes the effect of the declining electromagnetic field inside a conductor due to eddy-currents is characterized by the classical skin depth

$$\delta_c = \sqrt{\frac{2}{\omega \cdot \mu_0 \cdot \sigma}}, \quad (\text{classical skin depth})$$

where σ is the conductivity in the differential form of Ohm's law $\vec{j} = \sigma \cdot \vec{E}$. Here \vec{j} is the current density and \vec{E} the electrical field.

Kautz [60] has defined a value $\alpha = \frac{3}{2} \cdot l^2 / \delta_c^2$, to characterize the different regions of operation. For a superconductor the corresponding dimension is given by London's penetration depth λ_L , which also describes the exponential decay of the magnetic field in a superconductor [30, 63].

Three regions are usually distinguished:

- $l, \xi \ll \delta_c, \lambda_L$: normal skin effect ($\alpha \ll 1$),
- $l, \xi \approx \delta_c, \lambda_L$: anomalous skin effect and
- $l, \xi \gg \delta_c, \lambda_L$: extreme anomalous skin effect ($\alpha \gg 1$).

Thus it is necessary to examine these parameters for the employed materials incorporating the relevant frequency and ambient temperature region.

Choice of materials: A normal conductive material in general has higher stripline losses than a superconductive material as long as the RF-frequency is below the superconductor's gap-frequency. Nb has been available as micro-strip material. NbTiN has been developed for the HIFI mixer fabrication. A normal conductive material as an alternative also is fabricated and tested as wiring-layer for possible HIFI band 2 devices.

There are several possible normal-conductive materials to be used as thin film material as Al, Cu and Au. Due to practical reasons of feasible fabrication and after estimation of the possible improvements in surface-impedance with copper or gold [48] the choice for the material is aluminium.

3.4.2.1 Surface impedance of the normal-conductor Al

In order to identify the applicable regime for the surface impedance calculation the classical skin depth δ_c and the electron's free mean path l have to be estimated.

With a measured DC-normal-resistivity of Al at room-temperature of $\sigma|_{300\text{ K}} = 3.8 \cdot 10^7 \text{ } \Omega^{-1}\text{m}^{-1}$ and a residual resistance ratio of

$$RRR = \frac{\sigma|_{4.2\text{ K}}}{\sigma|_{300\text{ K}}} = 10$$

the classical skin depth is around 30 nm.

The electron free mean path l is calculated from the Drude electron conductivity

$$\sigma = \frac{n \cdot e^2}{m \cdot v_f} \cdot l.$$

With a mass density of $\rho_{Al} = 2.7 \cdot 10^3 \text{ kg/m}^3$, the atomic mass number $A_{Al}=27$, the atomic mass unit u one obtains an electron number density of

$$n = \frac{\rho_{Al}}{A_{Al} \cdot u} \approx 18.1 \cdot 10^{28} \text{ m}^{-3}.$$

With a Fermi-velocity of $v_f = 2.02 \cdot 10^6 \text{ m/s}$ [64] the resulting free mean path is $l = 150 \text{ nm}$.

This is about a factor 5 times the classical skin depth. In this region the condition ($l \gg \delta_c$) for the extreme anomalous skin effect is not fully given. Thus the surface impedances for Al have been calculated in the full anomalous limit. This calculation is mathematically the most complex of the three limits, since an integro-differential equation has to be solved numerically². The

²For this calculation software developed at KOSMA by D. Hottgenroth has been available [48].

major results of the explicit solution, given by Kautz [60] are summarized in App. B.2.

Further discussion of the validity of the different limits in the frequency-region around 800 GHz is found in [48], especially in the appendix.

3.4.2.2 Surface impedance of the superconductors Nb and NbTiN

The superconductive materials used for the matching circuits for the HIFI band 2 mixer devices are Nb and NbTiN. Nb previously has been used for SIS-devices below and above its gap-frequency [65, 12], while NbTiN as material for matching circuits has been developed for the HIFI band 2 mixer fabrication [66, 13].

For Nb and NbTiN the surface impedance has been calculated according to Mattis and Bardeen [67]. Although for the given frequency range the extreme anomalous limit condition is not fully satisfied the difference from the exact solution in the bulk limit is smaller than 10% [51].

Surface impedance according to Mattis and Bardeen: For the extreme anomalous limit and the dirty limit the conductivity $\sigma = \sigma_1 + i \cdot \sigma_2$ depends on the normal state conductivity σ_n according to Mattis and Bardeen [67]

$$\frac{\sigma_1}{\sigma_n} = \frac{2}{\hbar\omega} \int_{\Delta}^{\infty} \{f(E) - f(E + \hbar\omega)\} \cdot g(E) dE + \frac{1}{\hbar\omega} \int_{\Delta - \hbar\omega}^{-\Delta} \{1 - 2f(E + \hbar\omega)\} \cdot g(E) dE, \quad (3.8)$$

$$\frac{\sigma_2}{\sigma_n} = \frac{1}{\hbar\omega} \int_{-\tilde{\Delta}}^{\Delta} \frac{\{1 - 2f(E + \hbar\omega)\} (E^2 + \Delta^2 + \hbar\omega E)}{\sqrt{\Delta^2 - E^2} \sqrt{(E + \hbar\omega)^2 - \Delta^2}} dE, \quad (3.9)$$

where $-\tilde{\Delta} = \max(-\Delta, \Delta - \hbar\omega)$ and $f(E)$ is the Fermi function

$$f(E) = \frac{1}{1 + e^{E/k_B T}}$$

and

$$g(E) = \frac{E^2 + \Delta^2 + \hbar\omega E}{\sqrt{E^2 - \Delta^2} \sqrt{(E + \hbar\omega)^2 - \Delta^2}}.$$

According to [31] the first integral in σ_1 is the contribution to the conductivity caused by thermally excited quasiparticles, while the second integral represents the contribution of the photon-excited quasiparticles, which occur from the breaking of cooper-pairs for $\hbar\omega > 2\Delta$. The imaginary part of the conductivity σ_2 represents the contribution of cooper-pairs to the conductivity, also called “kinetic inductance” of the surface.

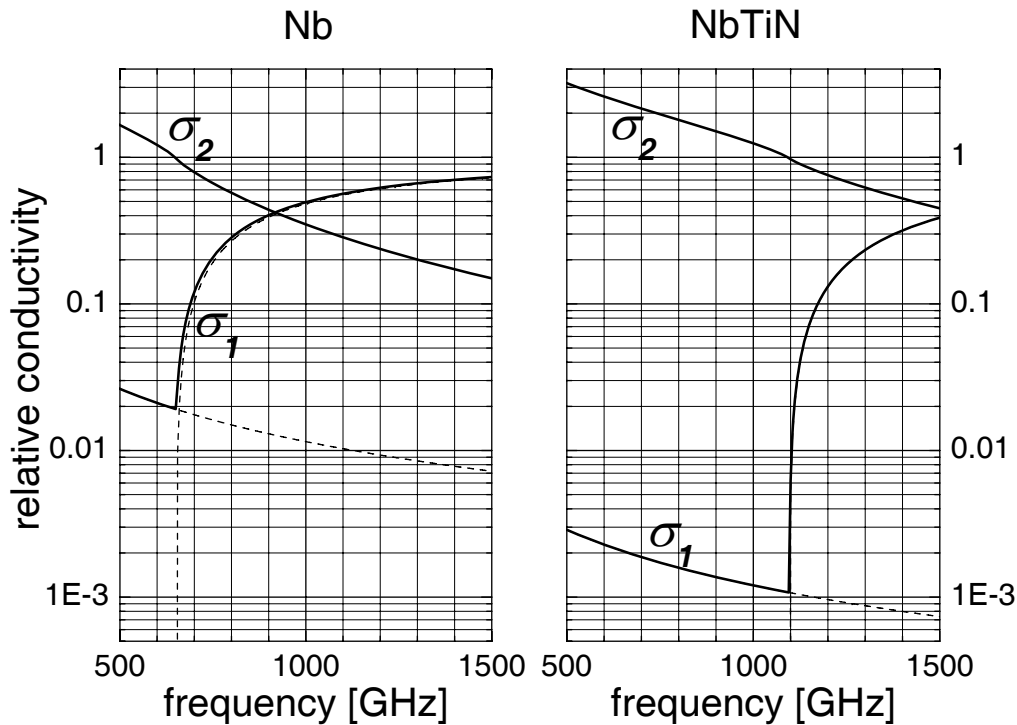


Fig. 3.11: Mattis-Bardeen conductivity $\sigma = \sigma_1 + i \cdot \sigma_2$ normalized by σ_n for Nb (left) and NbTiN (right), calculated from Eq. 3.8 and 3.9 with $T_c = 9.2$ K (15 K), $\rho = \sigma_n^{-1} = 5.9 \mu\Omega\text{cm}$ ($100 \mu\Omega\text{cm}$), $V_{\text{Gap}} = 2.75$ mV (4.55 mV) at 4.2 K. The values in brackets correspond to NbTiN. Above the gap-frequency the conductivity carried by the cooper-pairs σ_2 decreases and is not compensated by the rising conductivity σ_1 carried by the increasing number of quasiparticles.

The resulting values for Nb and NbTiN are shown in Fig. 3.11. The specific parameters are given in the caption of the figure. On the y-axis the normalized conductivities are given in a logarithmic scale. The feature that stands out, is the rise in σ_1 due to the breaking of cooper-pairs above the gap-frequency. In spite of this strong rise in σ_1 the resulting conductivity significantly decreases just above the gap-frequency due to the breaking of the cooper-pairs. This is explicitly demonstrated for some material combinations below.

3.4.3 Comparison of micro-strip materials

In Fig. 3.12 the power transmission of micro-strips with a length $\lambda/4$ are plotted for different material combinations. On the left side of the figure the transmission of micro-strips with the same material as ground-plane and top-wiring is plotted, while on the right side transmissions for combinations of micro-strip materials are given. The HIFI frequency band 2 is marked with dashed lines. The material parameters are given in Table 3.1. The thicknesses

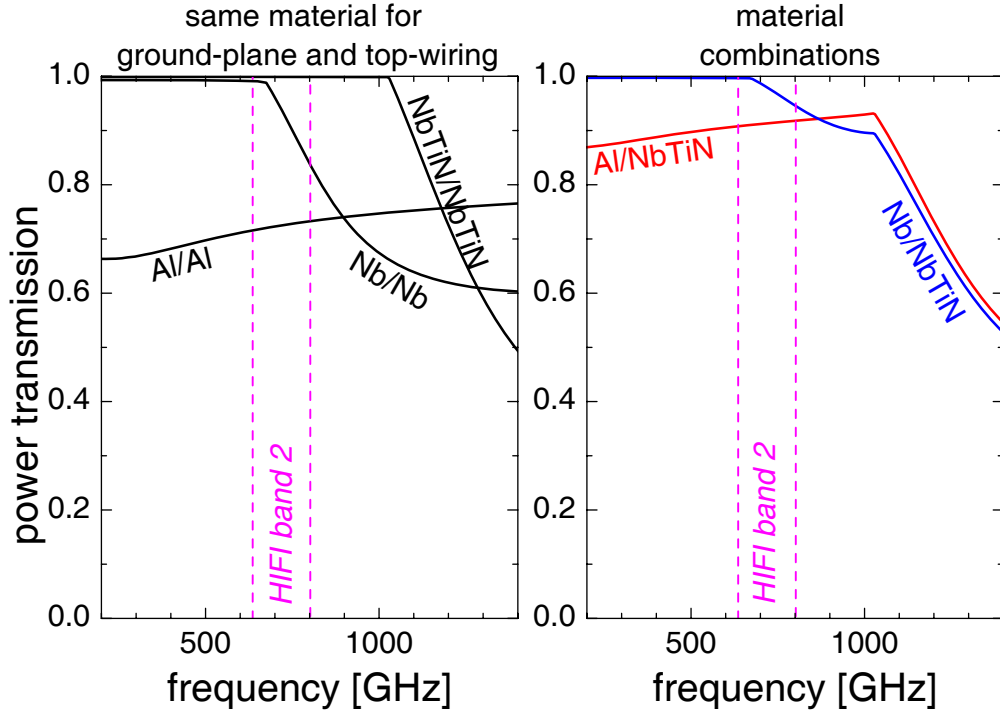


Fig. 3.12: Power transmission of micro-strips with a length $\lambda/4$ for different materials, calculated from surface impedances, for the same material as ground-plane and wiring (left) and for combinations of two materials (right). The length of the micro-strips is set to $\lambda/4$ for each frequency ν according to $\lambda = v_{\text{phase}}/\nu$.

	$\rho_n(4.2 \text{ K})[\mu\Omega\text{cm}]$	$T_c[\text{K}]$	$V_{\text{Gap}}[\text{mV}]$
Al	0.35	–	–
Nb	5.9	9.2	2.75
NbTiN	80	15.0	4.27

Tab. 3.1: Material parameters for calculated micro-strip transmissions in Fig. 3.12.

of the ground-plane and the top-wiring are $t_g = t_t = 350 \text{ nm}$, the thickness of the dielectric SiO_2 is $t_d = 220 \text{ nm}$ and its dielectric constant is $\epsilon = 3.8$.

An all-NbTiN micro-strip can not be used because of an insufficient cooling of the Nb-electrodes (compare [13]). Then the combination of Nb and NbTiN shows the optimum power coupling in the given frequency range. SIS-junctions with Al as top-wiring and NbTiN ground-plane also have been designed and analyzed, because they show a more homogeneous power coupling over the frequency band, because the surface impedance of Al is a weaker function of frequency.

3.5 Band-pass calculation for the matching circuit designs

In this section the actual calculation of the band-pass for two selected types of matching circuits are described. The bandpass is the frequency dependent power coupling of a specific SIS-device with SIS-junction, matching circuit and waveguide probe. It is calculated with the help of the ABCD-matrix formalism. The formalism of ABCD-matrices is summarized in Subsec. 3.5.1. It is most suitable for a series of transmission lines. Then, in Subsec. 3.5.2, the calculation for the actual realized two types of matching circuits for the HIFI band 2 devices is given.

3.5.1 Band-pass calculation with ABCD-matrix formalism

General formalism: For the use of a series of transmission lines ABCD-matrices are most suitable since a cascade of transmission lines is represented by the product of the respective ABCD-matrices [68].



Fig. 3.13: Definition of currents I and voltages U at a 4-port using the ABCD-matrix convention.

A transmission line or a lumped element in the matrix-formalism is viewed as a 4-port. The parameters of the 4-port are defined in Fig. 3.13. Then the transformation of the current and voltage by the 4-port is given by

$$\begin{pmatrix} U_1 \\ I_1 \end{pmatrix} = \begin{pmatrix} A & B \\ C & D \end{pmatrix} \cdot \begin{pmatrix} U_2 \\ -I_2 \end{pmatrix}. \quad (3.10)$$

Fundamental ABCD-matrices: The 4-port representation of fundamental network elements, a series impedance Z and a parallel admittance Y are given in Fig. 3.14. The matrix representations for the two fundamental 4-ports are:

$$M_Z = \begin{pmatrix} 1 & Z \\ 0 & 1 \end{pmatrix}, \quad M_Y = \begin{pmatrix} 1 & 0 \\ Y & 1 \end{pmatrix}.$$

The ABCD-matrix for a lossy transmission line according to Eq. 3.4 is

$$M_{\text{transm.-line}} = \begin{pmatrix} \cosh(\gamma \cdot l) & Z_C \cdot \sinh(\gamma \cdot l) \\ \frac{1}{Z_C} \cdot \sinh(\gamma \cdot l) & \cosh(\gamma \cdot l) \end{pmatrix}, \quad (3.11)$$

where l is its length, Z_C is the characteristic impedance and γ the propagation constant.

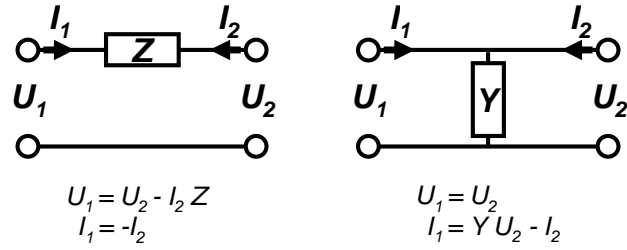


Fig. 3.14: 4-port representation of a series impedance Z (left) and a parallel admittance Y (right).

Power coupling to a SIS-junction: The matrix representations for the waveguide probe with impedance Z_{WG} and the SIS-junction's intrinsic capacitance C_J are

$$M_{WG} = \begin{pmatrix} 1 & Z_{WG} \\ 0 & 1 \end{pmatrix}, \quad M_{C_J} = \begin{pmatrix} 1 & 0 \\ iwC_J & 1 \end{pmatrix}.$$

For the actual calculation of the band-pass the RF-radiation is modeled as a current generator at the output port of the waveguide probe with I_{gen} and V_{gen} . Current and voltage at the device have been normalized according to $I_1 = 1$ and $V_1 = -R_N$. One obtains the general relation

$$\begin{pmatrix} V_1 \\ I_1 \end{pmatrix} = \begin{pmatrix} -R_N \\ 1 \end{pmatrix} = \underbrace{M_C \cdot M_{\text{micro-strip}} \cdot M_{WG}}_{M_{emb}^{-1}} \cdot \begin{pmatrix} V_{gen} \\ -I_{gen} \end{pmatrix}, \quad (3.12)$$

where $M_{\text{micro-strip}}$ is the ABCD-matrix of the micro-strip elements between waveguide probe and SIS-junction. The form of this relation does not depend on the actual design of the applied matching circuit. After inverting the product of the three ABCD-matrices, one obtains the "embedding matrix" M_{emb} , which characterizes the embedding impedance of the junction, the current and voltage of the generator ($V_{gen}, -I_{gen}$) are known. With the correspondent ABCD-matrices current and voltage at each point of the matching circuit are specified.

The band-pass of a SIS-device is calculated as the frequency-dependent ratio of power at the generator P_{gen} divided by the consumed power at the junction P_{SIS}

$$p_{rel}(\nu) = \frac{P_{SIS}}{P_{gen}(\nu)}. \quad (3.13)$$

3.5.2 Band-pass calculation for two types of matching circuits

The HIFI band 2 devices have been realized with two types of matching circuits:

- the three-step transformer and
- the double junction device.

There exist also other types of matching circuit geometries as shorted and radial stub, end-loaded stub, open stub etc. Several types of matching circuits are presented and discussed in [48, 54, 10]. Also there is a variety of distributed junctions or combinations of multiple junctions with matching circuits [69, 70, 71].

The first approach of a single junction design has been made with the three-step transformer because of the previously achieved noise results at 660 GHz (120 K measured receiver noise temperature, [51]). The modeling of matching circuit and the waveguide probe has been optimized to achieve a larger bandwidth. An alternative matching circuit for a single junction device is the open stub circuit. But the large area of the radial stub builds a capacitance, which is obstructive for the IF-performance.

In order to extend the bandwidth as a first step towards multi-junction devices double junction devices have been designed, fabricated and tested. The performance of these devices, which is nearly competitive to the three-step transformer devices, and other aspects regarding the bias-stability and LO-power requirements are discussed below. Since in the context of a space project the reliability of the applied technology had to be proven in a very early stage of the project (demonstration model, DM, in May 2002) no additional matching circuit types have been fabricated. Rather the fabrication parameters have been analyzed and optimized for an improved performance.

3.5.2.1 Band-pass calculation for a three-step transformer

The three-step transformer: The three-step transformer matching circuit connects the SIS-junction with micro-strips of three different widths resulting in three different characteristic impedances to the waveguide probe feed point. In Fig. 3.15 a photograph of a fabricated device and the equivalent circuit are shown. The photograph on the left side shows the top-view of a device with a three-step transformer during the fabrication process after the definition of the top-wiring. The first small micro-strip (1) is used as a series inductive tuner to compensate the junction's capacitance and to transform the junction impedance to a real value. This is exactly achieved only for a single frequency. Two $\lambda/4$ -micro-strips with a low (2) and a higher (3) characteristic impedance follow, to transform the nearly real impedance to the complex conjugate of the waveguide probe impedance for optimum power coupling.

With the equivalent circuit, given in Fig. 3.15 (right) the transformation matrix, which represents the sequence of micro-strips for the band-pass calculation is

$$M_{\text{stripline}} = M_{Z1} \cdot M_{\text{step12}} \cdot M_{Z2} \cdot M_{\text{step23}} \cdot M_{Z3}.$$

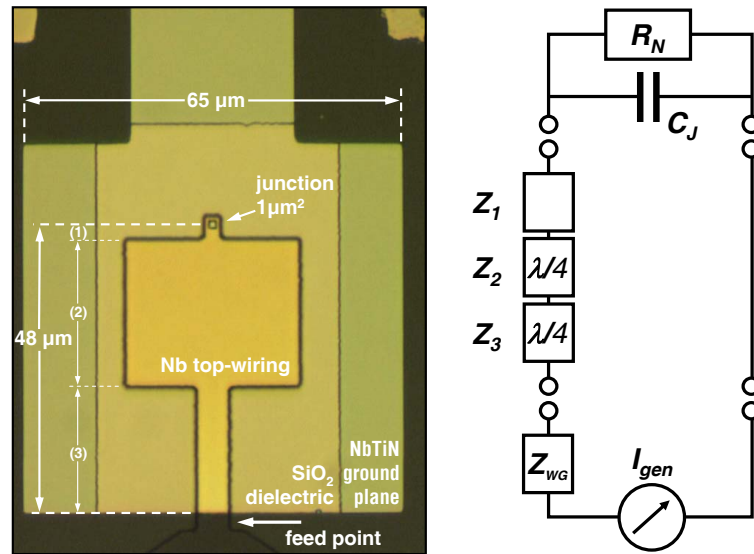


Fig. 3.15: Left: Photograph of junction device with three-step transformer. A Nb/Al-Al₂O₃/Nb-junction is connected with a Nb/SiO₂/NbTiN-stripline of three different widths to the feed-point of the waveguide probe. Right: Equivalent circuit of a three step transformer. Micro-strip 1 compensates the junction's intrinsic capacitance C_J ; micro-strips 2 and 3 transform the resulting impedance to required larger values.

M_{Z1} , M_{Z2} and M_{Z3} are the ABCD-matrices of the three micro-strips as given in Eq. 3.11. M_{step12} and M_{step23} are the ABCD-matrices of the step inductances as given in Eq. 3.7.

Realization of the matching circuit for HIFI band 2 mixers: An example for the design calculation for a device is given in Fig. 3.16. The plot (a) shows the relevant impedances of a the waveguide probe (SSP, black lines and points), the SIS-junction (blue line) and the SIS-impedances transformed by the three micro-strips (red line). The plot (b) shows the respective power coupling without ohmic micro-strip losses (dashed line) and with ohmic losses (bold blue line). The junction area of the SIS-device is designed to be $(0.9 \mu\text{m})^2$, a current density of 15 kA/cm^2 and a gap voltage of 2.77 mV are assumed; for the wiring typical values for Nb ($\rho_n = 5.9 \mu\Omega\text{cm}$, $T_c = 9.2 \text{ K}$) and NbTiN ($\rho_n = 100 \mu\Omega\text{cm}$, $T_c = 14.7 \text{ K}$) are assumed.

The concept of the three step-transformer (micro-strip 1: inductive tuning, micro-strips 2/3: $\lambda/4$ -transformers) is exactly only at the center of the band. The task to design a broadband matching-circuit requires an optimization of the power-coupling from waveguide probe to SIS-junction. over the whole frequency range.

The matching circuit design of Fig. 3.16 (b) has been optimized for largest total integral in the frequency band 640-800 GHz. It is obvious that the relative power coupling below 670 GHz is much larger, than above this gap-

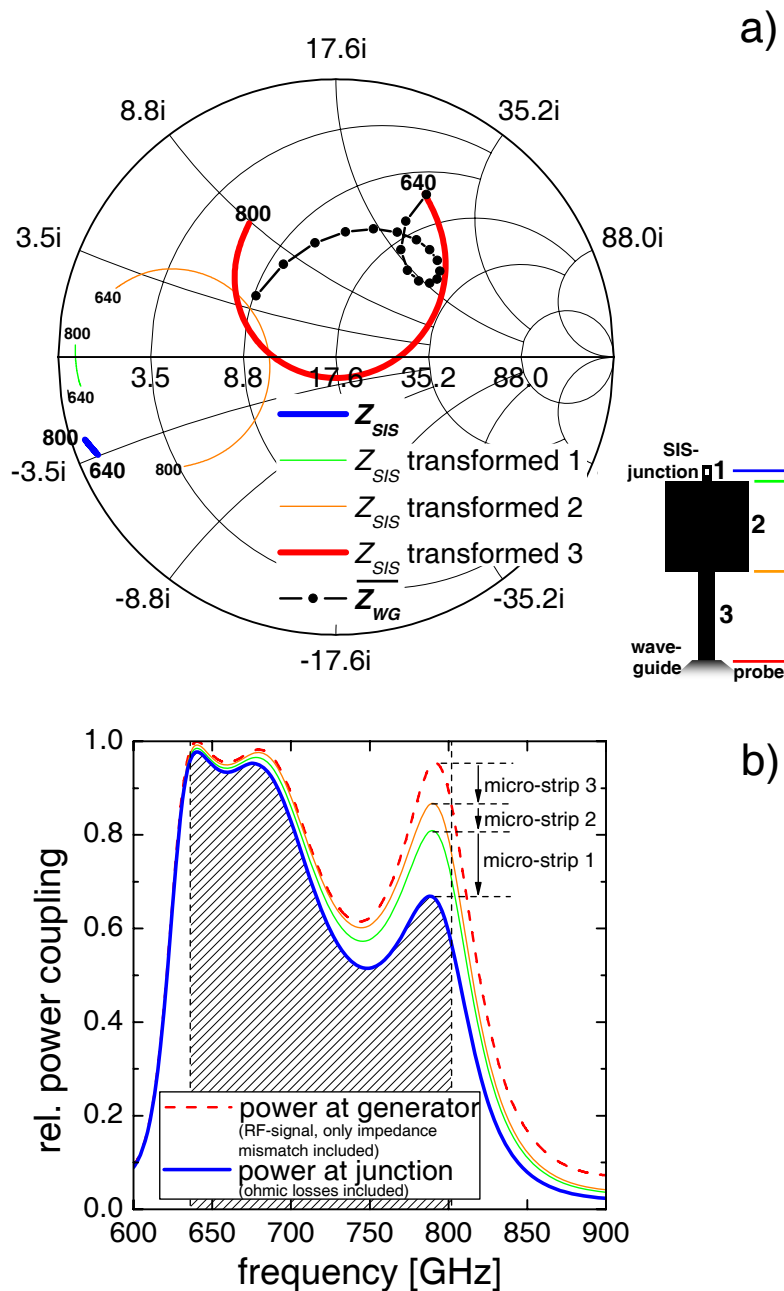


Fig. 3.16: Impedance matching and calculated power coupling for three step transformer. **a)** Impedances of the junction Z_{SIS} (blue line), transformed by the three-step transformer (red line) with with intermediate stages and the waveguide probe impedance complex conjugated (black line and points). The smith chart is normalized to the junction's normal resistance R_N . The numbers without units (640/800) denote the frequencies in GHz. The small sketch of the three-step transformer shows the numbering of the three micro-strips. **b)** The resulting power coupling from waveguide probe to SIS-junction with intermediate stages. The increased micro-strip losses above 670 GHz are visible as the increasing difference of the power at the generator (RF-signal, dashed line) and the power at the SIS-junction (bold solid line).

frequency of niobium. The ohmic micro-strip losses are seen from the difference between the dashed and the thicker solid line. The three maxima in the calculated bandpass (640 GHz, 675 GHz and 788 GHz) occur at the frequencies, where the transformed junction impedance and the complex conjugated impedance of the waveguide probe are the closest in the Smith-chart.

3.5.2.2 Band-pass calculation for a double-junction device

Concept of the double junction device: The double-junction design allows a more broadband power coupling, because the two SIS-junctions can have their optimum coupling in different parts of the frequency band. A photograph of a fabricated double-junction device and the equivalent circuit is given in Fig. 3.17. The concept of the double junction design is based on two identical

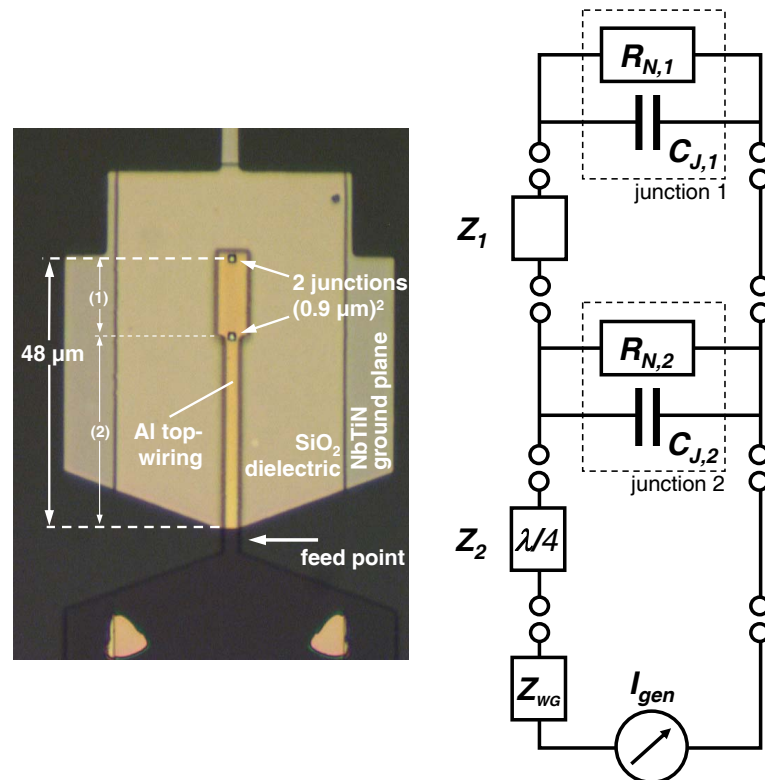


Fig. 3.17: Left: Photograph of a double junction device. The two Nb/Al- Al_2O_3 /Nb-junctions are connected with a Nb/SiO₂/NbTiN-stripline to the feed-point of the waveguide probe. Right: Equivalent circuit of a double junction device.

SIS-junctions in parallel. The matching circuit is designed to connect junction 1 with an inductive matching micro-strip to junction 2, which compensates the capacitance of both junctions resulting in an almost real impedance of the order of $R_N/2$, where R_N is the normal resistance of one junction. The two combined junctions are connected to the waveguide probe with a $\lambda/4$ -transformer, that matches $R_N/2$ to the probe impedance.

The power coupling is calculated from the same formalism, as given in Sub-sec. 3.5.1. The equation for the calculation of the current generator at the waveguide probe is

$$\begin{pmatrix} V_{junc1} \\ I_{junc1} \end{pmatrix} = M_{C1} \cdot M_{Z1} \cdot M_{R2} \cdot M_{C2} \cdot M_{step12} \cdot M_{Z2} \cdot M_{ZWG} \cdot \begin{pmatrix} V_{gen} \\ -I_{gen} \end{pmatrix}.$$

Here, V_{junc1} and I_{junc1} are the voltage and current at junction 1, $M_{C1/2}$ represent the junctions' capacitance, $M_{R1/2}$ their normal resistance, $M_{Z1/2}$ represent the characteristic impedances of the micro-strips, M_{step12} the step between the micro-strips and M_{ZWG} the impedance of the waveguide-probe.

Realization of the matching circuit design for HIFI band 2 mixers: The impedances and the calculated power coupling of an actual design with normal-conductive Al as top-wiring is given in Fig. 3.18. The impedances of the SIS-junction (blue line) and the waveguide probe (black lines and points) in plot (a) are the same as for the three-step transformer (Fig. 3.16). For a resonant matching the complex conjugated impedance of the waveguide probe for every frequency has to be as close as possible to the impedance of the whole matching circuit including the SIS-junctions (red line). To illustrate the coupling to the SIS-junctions individually the complex conjugate of the embedding impedances for junction 1 ($\overline{Z_{emb,1}}$, dark green) and junction 2 ($\overline{Z_{emb,2}}$, light green) are plotted. The embedding impedance at junction 1 shows an optimum impedance match around 640 GHz, for junction 2 it is optimum at 800 GHz.

The same effect is seen in the calculated power coupling in Fig. 3.18 (b). The power coupling for junction 1 is optimum in the lower part of the frequency band. For junction 2 it is optimum around 800 GHz. The total relative power coupling is just above 60% over the frequency band. This implies micro-strip losses of 30-40%. These strong losses are the cost for a homogenous band-pass with Al as top-wiring material.

3.5.2.3 Comparison of double junction design with three-step transformer including fabrication aspects

Advantages of the double junction design with respect to the single junction design

- Because the two junctions show optimum coupling in different parts of the frequency band, the two junction design yields a broad-band coupling.
- The relative positioning of the top-wiring with respect to the junction position is not as critical as for the three-step transformer. The relative position of the two junctions is defined in the same fabrication step and defines the length and impedance of the first micro-strip.

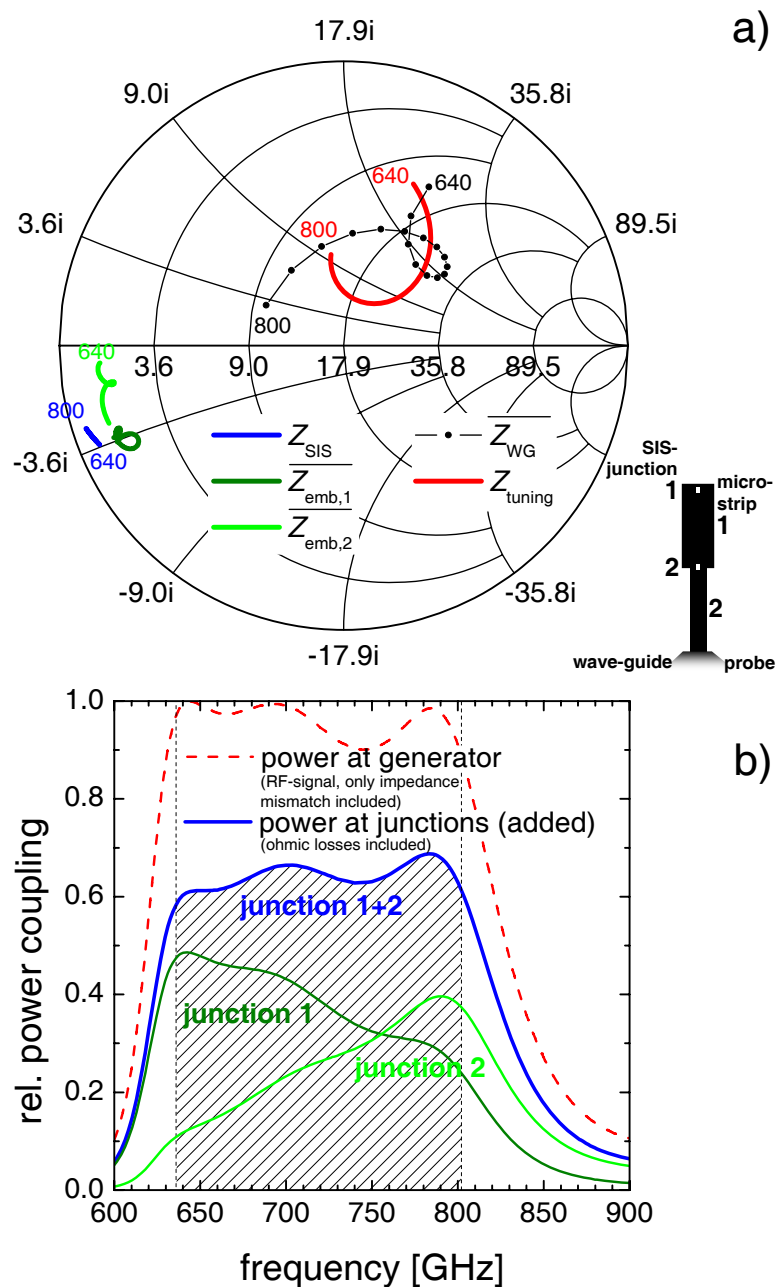


Fig. 3.18: Impedance matching and power coupling for double-junction design. **a)** Plotted are the impedance of the SIS-junctions Z_{SIS} (blue line) and the complex conjugate of the waveguide impedance $\overline{Z_{WG}}$, embedding impedances (complex conjugate) of the two junctions $\overline{Z_{emb,1}}$ (dark green) and $\overline{Z_{emb,2}}$ (light green), the impedances of the whole matching circuit including the SIS-junction Z_{tuning} is plotted in red. The number without units refer to the respective frequencies in GHz. **b)** Relative power coupling to the double junction device. The dashed red line shows the coupled power without micro-strip losses. The blue line shows the total coupled power to the junctions with micro-strip losses as the sum of coupled power to junction 1 (dark green) and junction 2 (light green).

At the same time the double-junction design has some disadvantages.

Disadvantages of the double junction design with respect to the single junction design

- The larger total area of two junctions results in a higher LO-power consumption. This is a problem, if LO-power is limited.
- The Josephson effects in two SIS-junctions of different area due to fabrication inaccuracies are not simultaneously suppressed for a specific applied magnetic field intensity. This results in additional noise due to Josephson effects for a given magnet current.
- The most serious problem of the double-junction devices is the effect of superconductive quantum-interference of the two SIS-junctions with superconductive ground-plane and top-wiring, which is utilized in SQUIDs, but parasitic for SIS-junctions as mixers. This interference causes additional noise currents and a high instability during operation in the device.

Because of the third disadvantage (superconductive quantum-interference) double junction devices have only been designed and fabricated with Al as top-wiring. This results in larger micro-strip losses in comparison to Nb top-wiring devices (compare Fig. 3.12).

3.6 Lithography mask design for HIFI band 2 mixer devices

With the given formalism to calculate the band-pass of a specific SIS-device the choice of actual matching circuit designs and geometry has been done to define devices for the lithography masks. In order to find quickly the optimum matching circuit geometry for a given set of fabrication parameters a numerical optimization of the calculated band-pass has been developed and applied. In Subsec. 3.6.1 the optimization and its results are presented. In Subsec. 3.6.2 a tolerance analysis of the calculated band-pass for the most critical fabrication parameters is given. A comparable tolerance analysis has been applied for the device designs to identify designs for the mask with acceptable variations in power coupling for small changes in fabrication parameters. Devices for different sets of the most probable fabrication parameters have been optimized and placed on the mask in order to obtain a reasonable number of suitable devices for the actual fabrication parameters.

The criteria and data, which have been the basis for the actual mask design are presented in Subsec. 3.6.3. These criteria (choice of materials, types of

matching circuits and waveguide probes) have been adapted for each mask based on the best knowledge of the actual fabrication parameters and previous RF-performance measurements of devices.

3.6.1 Numerical optimization of matching circuit geometry

For a systematical approach in the choice of the matching circuit geometry a numerical optimization has been applied. The data for the characteristic parameters (characteristic impedance Z_C , propagation constant γ and phase velocity v_{phase}) of the micro-strips for possible strip-widths with a given layer composition have been generated with previously existing Mathcad-files. These data as function of frequency and strip-width have been stored in look-up tables. The power-coupling of a chosen type of matching circuit as composition of micro-strips (three-step transformer or double junction device) and a specified SIS-junction (defined by gap-voltage V_{Gap} , normal resistance R_N , current density j_c) has been optimized with a new optimization tool, written in Java.

Different types of matching circuits with possibly different optimization criteria (see below) are represented by a class, which evaluates a measure for the validity of the power-coupling (impedance match or integrated power coupling) over the frequency band as a function of n micro-strip geometry parameters. The optimizer class handles the results and sequentially requests the evaluation of new combinations of the n micro-strip geometry parameters for the given type of matching circuit.

In this section, first the numerical concept of the optimizer is presented, then the applied optimization criteria and a classification of the optimization results.

3.6.1.1 The optimizer

For the optimization problem a sequential approach to evaluate the nearest neighbors of a starting set of geometry parameters has been chosen. For a three-step transformer, the optimization is a 6-dimensional problem, since the lengths and the widths of three micro-strips ($w_1, l_1, w_2, l_2, w_3, l_3$) are varied in the optimization process. For the three-step transformer this can be reduced to a 5-dimensional problem, if the first width w_1 is kept fix. This is justified, because the first micro-strip is used to compensate for the junction's intrinsic capacitance, where the optimum micro-strip can be specified by the ratio w_1/l_1 for a narrow range of $3 \mu\text{m} \leq w_1 \leq 5 \mu\text{m}$.

For the double-junction device it is a 4-dimensional problem since two widths and two lengths of striplines (w_1, l_1, w_2, l_2) are involved. Thus there are x_i parameters with $i = 1, \dots, n$, where n is the dimension of the problem.

Only a specified set of parameters for lengths and widths is defined. Listed parameters for micro-strip width and length are $x = 3.0, \dots, 50 \mu\text{m}$ with $\Delta x = 0.1 \mu\text{m}$ for $x \leq 10 \mu\text{m}$, and $\Delta x = 1 \mu\text{m}$ else. Thus for each parameter set x_i a maximum number of $3^n - 1$ nearest neighbors are defined³.

The optimizer starts at a given set of parameters $x_{i,0}$ and evaluates a characteristic value, which specifies the validity of the corresponding matching circuit, e.g. a measure for the impedance matching or the integrated power coupling over the whole frequency band. Then the characteristic values of the nearest neighbors $x_{i,1}$ of this start parameter set are evaluated. The neighbor parameter set with the optimum characteristic parameter, when better than for the start parameter set, is chosen as new start parameter set. If the previous parameter set is still the optimum the step width is sequentially increased and the farther vicinity of the local optimum is inspected.

This algorithm turned out to be suitable to find optimum sets of parameters within a few minutes⁴, with the possibility to continuously check, after the result is available, whether a better set might be available for rather different values for the micro-strip widths and lengths far off.

3.6.1.2 Optimization criteria

Two different optimization criteria were tested in the design of the HIFI band 2 devices. The first optimizes the impedance match of the junction impedance transformed by the matching circuit with the impedance of the waveguide probe. The second, which was mainly used, evaluates the calculated power conversion of the RF-power from the waveguide-probe which is coupled to the junction(s). The criterion, which has finally been applied is the weighted integral of the calculated power conversion over the RF-frequency.

Optimum impedance matching: For each data-set x_i the transformed junction impedance at the waveguide probe is calculated and its complex conjugate $\overline{Z_{tuning}}(\nu_j)$ compared with the impedance of the waveguide probe $Z_{WG}(\nu_j)$ with $\nu_j = (640, 650, \dots, 800)$ GHz. This resolution is sufficient, since the impedances of the SIS-junctions and of the waveguide probes do not significantly deviate from a linear interpolation over this intervals (compare impedance data in Fig. 3.21, 3.22). Optimum coupling is assumed if the two impedances are as close as possible for each frequency ν_j . The difference of the two sets of impedances is quantified by the value

$$\chi^2 = \frac{1}{J} \cdot \sum_{j=1}^J |\overline{Z_{tuning}}(\nu_j) - Z_{WG}(\nu_j)|^2$$

³If a parameter is already the minimum or maximum value or the total length of the matching circuit already reaches the maximum length, the number of allowed nearest neighbors is smaller than $3^n - 1$

⁴A computer with a 1 GHz-CPU has been used for the optimization.

and is minimum for optimum coupling.

The problem of this criterion is, that micro-strip losses are not included. This is acceptable for designs with Al as top-wiring, which shows homogeneous micro-strip losses over the frequency band, but not in general with Nb as top-wiring. Therefore the total integral of relative coupled power over the frequency band has been analyzed.

Maximum integral of relative power coupling: To analyze the total power coupling from waveguide probe to the junction or junctions it is integrated over discrete frequencies in the HIFI band 2

$$P_{\text{int}} = \sum_{j=1}^J p_{\text{rel}}(\nu_j) \quad \text{with } \nu_j = (640, 650 \dots 800) \text{ GHz.}$$

Here, p_{rel} is the relative power coupling at a given frequency ν_j as defined in Eq. 3.13 on page 52. The value P_{int} should be maximum for an optimum power coupling. One resulting band pass for a matching circuit with niobium as top-wiring, optimized with this criterion is shown in Fig. 3.19. It is obvious, that the conversion is not homogenous over frequency band. The reason is the higher stripline losses in the upper frequency band in the niobium. In order to gain higher coupling in this frequency region, the loss in conversion in the lower frequency band is much larger. Thus the matching circuit with the maximum total integral P_{int} has a relative power coupling of more than 90% in the lower frequency region and around 60% for higher frequencies.

For the double-junction devices with a normal-conductive top-wiring the problem of micro-strip optimization is solved at this point, because the total maximum integral yields a homogeneous band-pass. For a given set of material and junction parameters, the optimum geometry has been evaluated within a few minutes. But for three-step transformers with Nb top-wiring the results of the optimization are not sufficient at this point.

Maximum integral of weighted power conversion: The desired form of band-passes for three-step transformers with Nb as micro-strip material has been achieved by introducing weight-factors q_ν for different frequencies and q_p for different relative power coupling p_{rel} (compare Fig. 3.19). These weight factors have been defined straight forward: the relative power coupling p_{rel} for all frequencies above the critical frequency ν_{crit} is weighted with factor $q_\nu \geq 1$. This increases the resulting power coupling in the upper part of frequency band, where micro-strip losses are present. The fraction of the relative calculated coupling p_{rel} for a specific frequency above a critical relative conversion p_{crit} is scaled with the weight factor $q_p \leq 1$.

For example, the resulting band pass changes from the shape given in Fig. 3.19 if a weight factor $q_\nu = 5$ for frequencies higher than $\nu_{\text{crit}} = 720$ GHz

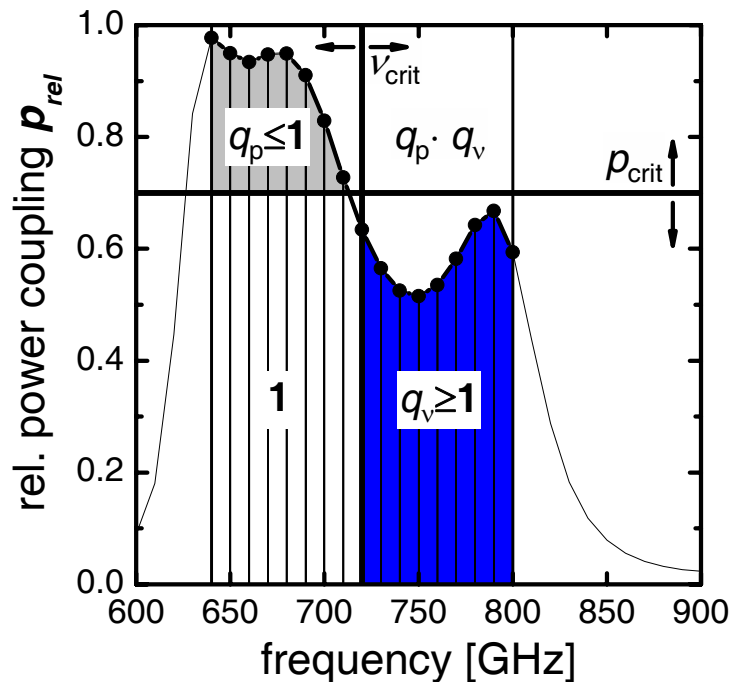


Fig. 3.19: Definition of weight factors q_p and q_v for optimized band-pass. To achieve a flat conversion for frequencies above a “critical” frequency ν_{crit} has been weighted with a weight factor $q_v \geq 1$. A second weight factor $q_p \leq 1$ has been applied for conversions higher than p_{crit} , to reduce the weight above this value.

is applied. The resulting optimum matching circuit has much larger power conversions in the upper part of the band, with decreasing conversion in the lower part of the band. If a weight factor $q_p = 0.01$ is applied for relative conversions higher than $p_{crit} = 60\%$, the high conversions in the lower band do not contribute much to the total integral, but the value for the integral is increased by raising the relative conversion at around 760 GHz even at the cost of strong losses in conversion at frequencies where has been larger than 90%. Thus it has been possible not only to obtain band-passes with a maximum total integral, but also with a more homogeneous distribution for different sets of material parameters.

3.6.1.3 Optimization results

For the double junction design (with Al-wiring, σ_n homogenous over the frequency band) the optimization results are of the shape, already given in Fig. 3.18 (b). An almost homogenous power coupling is achieved over the frequency band.

For three-step transformers (with Nb as top-wiring) the resulting matching circuits and their band passes, which are evaluated with the weighted optimization applying different weighting factors q_v and q_p during the design for the HIFI band 2 mixers are classified to three general types. The three types

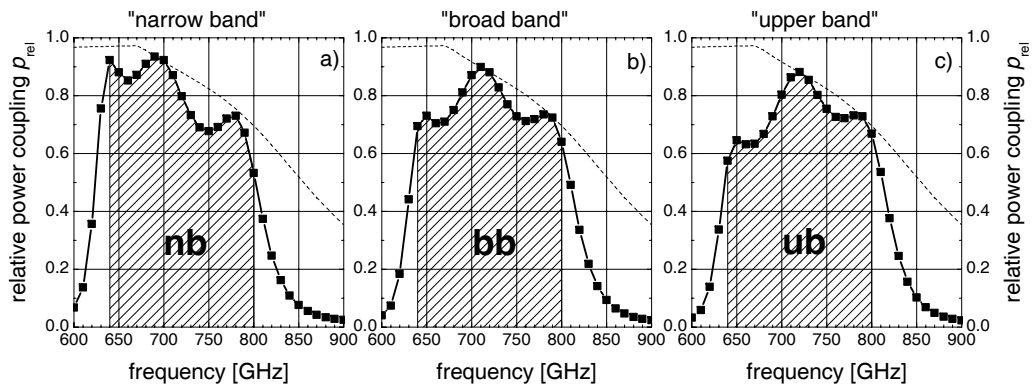


Fig. 3.20: Three types of matching circuits of the three-step transformer design with niobium top-wiring. The dashed line shows the theoretical maximum coupling assuming perfect impedance matching, with only micro-strip losses included. **a)** Matching circuit with maximum integral, $q_v = q_p = 1$ ("narrow band"). **b)** Matching circuit with same relative coupling in lower and upper band ("broad band"). **c)** Matching circuit with 10% higher coupling in upper than in lower band ("upper band").

are given in Fig. 3.20. In all three plots the theoretically maximum coupling is shown as the dashed line, where only micro-strip losses are included and impedance matching is assumed to be perfect.

Fig. 3.20 (a) shows the calculated coupling without any weight factors after maximizing the total integral ($q_v = q_p = 1$). This type of matching circuit is called "narrow band" matching circuit (nb). Fig. 3.20 (b) shows a band pass which is optimized for equal relative conversion in the lower and in the upper frequency band and is called "broad band" (bb). The total conversion integral is smaller than for the nb-design. The gain of conversion in the upper frequency band is obtained at the high cost of losing much more conversion in the lower frequency band. In Fig. 3.20 (c) the third type of matching circuit "upper band" (ub) is shown; it has been added to compensate a possible underestimation of the micro-strip losses in Nb.

With this optimization available still the selection of the most probable fabrication parameters, including their tolerances has to be done.

3.6.2 Tolerance analysis of fabrication parameters

The tolerance analysis has been used for the selection of devices to be placed on the lithography masks. In detail each device, which has been placed on the lithography mask has been analyzed with a tolerance analysis in order to estimate its performance for deviations in fabrication parameters. Devices, which show tolerable variations in calculated band-pass for the most probable variations in fabrication parameters, have been placed on the mask. Here the analysis is illustrated for a typical example.

The tolerance analysis also is the first step in the analysis of deviations in measured band-passes from the design calculation (compare Chap. 4).

The calculations are presented for a three-step transformer (broad-band type, see Fig. 3.20) with NbTiN/SiO₂/Nb micro-strips and current density $j_c = 15 \text{ kA/cm}^2$. Typical parameters for Nb- and NbTiN-quality parameters are assumed (Nb: $T_c = 9.2 \text{ K}$, $\rho_n = 5.88 \mu\Omega\text{cm}$, NbTiN: $T_c = 15 \text{ K}$, $\rho_n = 80 \mu\Omega\text{cm}$). The design junction area is $0.64 \mu\text{m}^2$.

Tolerance analysis of current density: The RF-impedance of the SIS-junction depends on the current density j_c according to

$$\begin{aligned} \frac{1}{Z_J} &= \frac{1}{R_N} + i\omega C_J \\ &= \tilde{k} \cdot j_c + i\omega C_J, \quad (\text{with } \tilde{k} = \frac{4}{\pi} \cdot \frac{A_J}{V_{Gap}}). \end{aligned}$$

It is assumed, that the junction's intrinsic capacitance C_J to the first order is independent of j_c .

The variation in transformed junction impedance and relative power coupling with variation in j_c are plotted in Fig. 3.21 for a three-step transformer with NbTiN/SiO₂/Nb micro-strips.

The impedances of the matching circuit including the SIS-junction in the Smith-chart in Fig. 3.21 (a) can roughly be described as concentric circles. The lower the current density is the larger the "radius" of such an impedance circle. The variation over the frequency (broad band) is the smallest for the highest current density.

The center and the shape of the band-pass (Fig. 3.21 (b)) does not significantly change with the current density. But the relative power conversion is strongly increased with higher current density, and for higher current density the band shape becomes more homogeneous. Thus from this result junctions with higher current densities are preferable.

For comparison the corresponding values for a current density of $j_c = 30 \text{ kA/cm}^2$, which can be achieved with AlN-barriers are plotted as stars in the Smith-chart and the relative conversion plot. The variation of the matching circuit impedance over the band is very small and the relative conversion is very homogeneous over the band. In effect now such high-current density devices the waveguide probe is the band limiting factor.

Tolerance analysis of junction area: The impedance of the SIS-junction is inverse proportional to the junction area (compare Eq. 2.16):

$$\frac{1}{Z_J} = \left(\frac{1}{R_N} + i\omega C_J \right) \sim A_J.$$

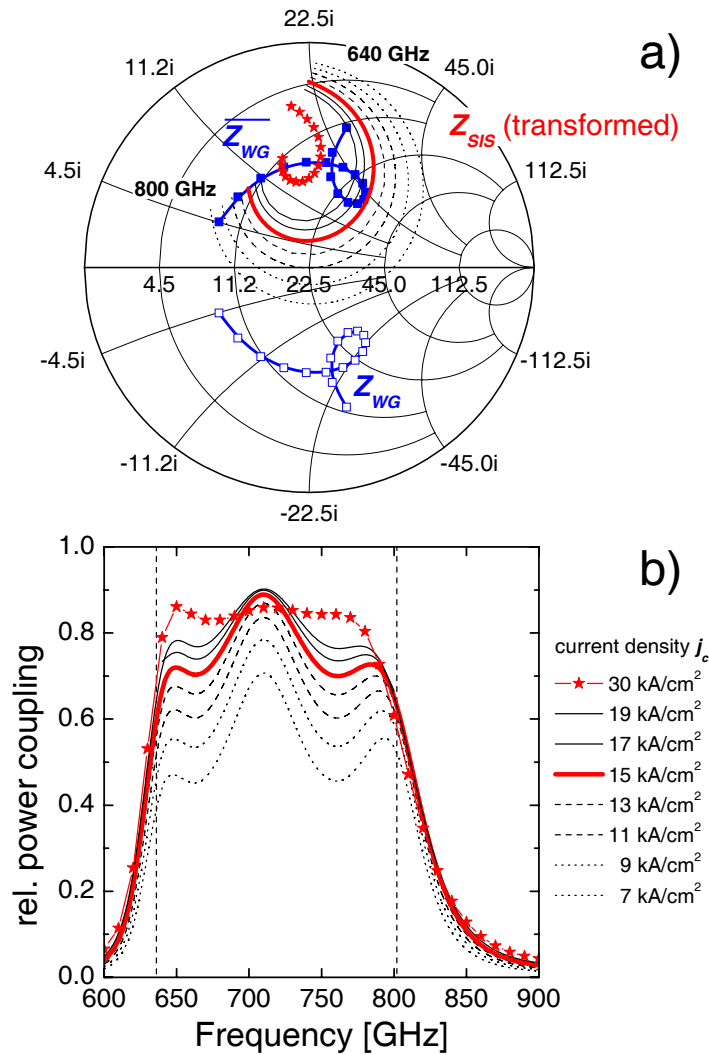


Fig. 3.21: Tolerance analysis of the current density j_c and its effect on transformed junction impedance (a) and relative power coupling (b). The broad solid line shows the data for a three-step transformer design with NbTiN/SiO₂/Nb micro-strips and a design value for $j_c = 15 \text{ kA/cm}^2$. **a)** Transformed junction impedance (red line) with variation in j_c and the complex conjugate of the waveguide probe impedance Z_{WG} (blue). **b)** The calculated band-pass of a broad-band (bb) matching circuit (red line) with variation in j_c . For comparison a current density of 30 kA/cm^2 , which can be achieved with AlN-barriers, is also added as filled stars.

The effects of variations in junction area for the example device design on the transformed SIS-impedance and the calculated power coupling is given in Fig. 3.22

A shift in junction area results in a systematical shift of the band-pass in frequency. Smaller junction areas imply larger frequencies and vice versa. The tolerance analysis depends on the original type of matching circuit. A bb-type of matching circuit (Fig. 3.20 (b)) allows shifts in junction width $l_J = \sqrt{A_J}$ in both directions of $\Delta l_J = 0.05 \text{ } \mu\text{m}$ with quite tolerable shifts

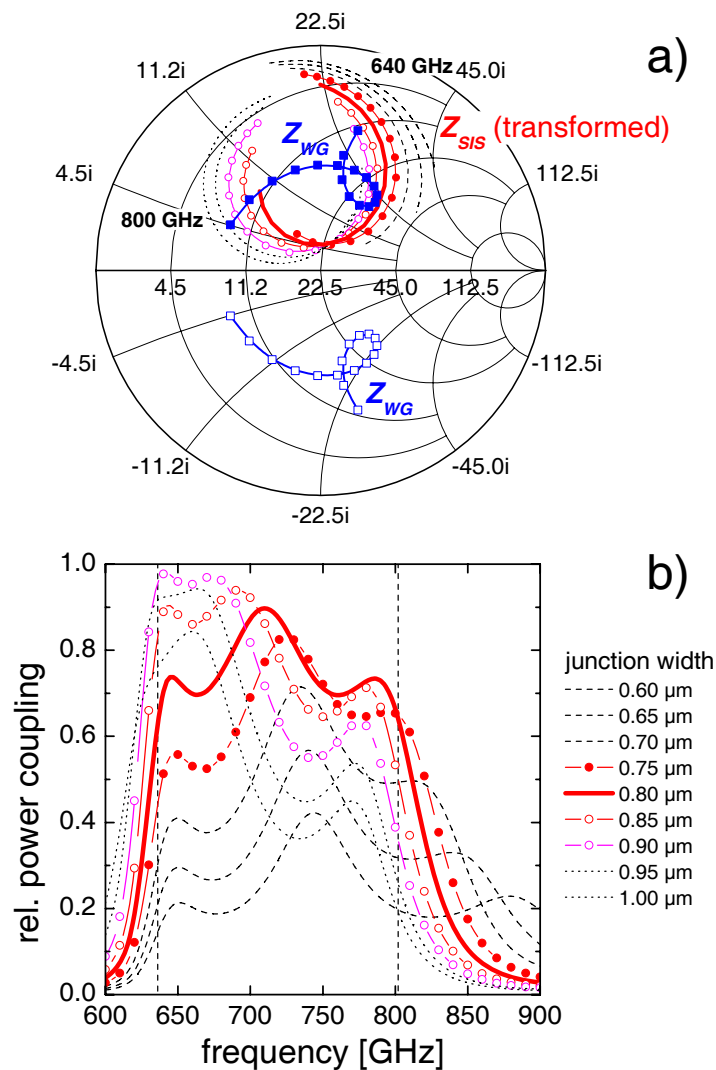


Fig. 3.22: Tolerance analysis of the junction area A_J and its effect on transformed junction impedance (a) and relative power coupling (b). **a)** A shift in junction area implies a rotation and shift of the transformed SIS-impedance in the Smith-chart. **b)** A shift to a larger junction area results in a shift of the band-pass to lower frequencies (compare with nb-type, Fig. 3.20 (a)). For a shift to a smaller junction area the band-pass shifts to higher frequencies (compare with ub-type, Fig. 3.20 (c)).

in the band-pass. Similar analysis calculations show, that nb-type matching circuits are sensitive for shifts to larger areas and quite insensitive for shifts to smaller areas (results in band-pass similar to bb-type). For the ub-type matching circuit the opposite is true. It transforms to a bb-type for larger areas and is strongly deformed for smaller areas.

From this analysis the accuracy of the junction width has to be below $\Delta l_J = 0.05 \mu\text{m}$. This is confirmed from RF-measurements (compare Fig. 4.28).

Tolerance analysis of NbTiN-quality: The results from the tolerance analysis of the matching circuit design with respect to changes in the DC-quality of NbTiN in the ground-plane are given in Fig. 3.23. The parameters ρ_n and

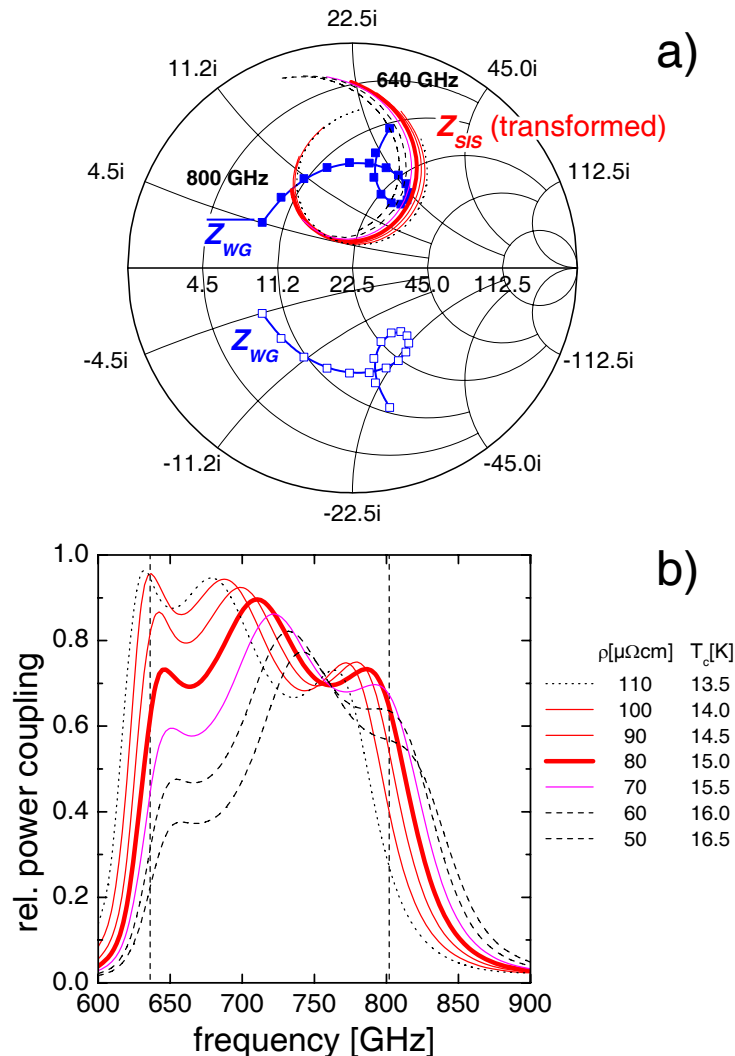


Fig. 3.23: Tolerance analysis of the DC-quality of NbTiN for the ground-plane in terms of critical temperature T_c and normal resistivity ρ_n and its effect on transformed junction impedance (a) and relative power coupling (b). The NbTiN-parameters (ρ_n , T_c) are changed simultaneously from (110 $\mu\Omega\text{cm}$, 13.5 K) to (50 $\mu\Omega\text{cm}$, 16.5 K). Influence of changes in quality of NbTiN (normal resistivity ρ_n and crit. Temperature T_c) as ground-plane material on the impedance and power coupling for a three-step transformer with NbTiN/SiO₂/Nb micro-strip matching circuit. The broad solid line shows the data for the design parameter of $\rho_n = 80 \mu\Omega\text{cm}$ and $T_c = 15.0$ K.

T_c are changed simultaneously, because from experience a low resistivity is correlated to a high critical temperature.

In Fig. 3.23 (a) the transformed impedances of the SIS-junction show a significant shift in frequency. This is seen as a shift of the calculated band-pass in Fig. 3.23 (b). It is a quite similar deformation of the band-pass observed for

variations in junction area (Fig. 3.22 (b)). The design bb-type matching circuit is deformed to a ub-type (see Fig. 3.20) matching circuit for an improved NbTiN-quality ($70 \mu\Omega\text{cm}$, 15.5 K). It is transformed to a nb-type matching circuit for a lower NbTiN-quality ($100 \mu\Omega\text{cm}$, 14.0 K). This illustrates the result of a comparable tolerance analysis for nb-type and ub-type matching circuits. A device design with a nb-type band-pass is quite insensitive to a higher NbTiN-quality and sensitive to a lower NbTiN-quality. For a ub-type design the opposite is true.

In average the shift in frequency is 5 GHz/ $10 \mu\Omega\text{cm}$ at the low-frequency band edge and 7.5 GHz/ $10 \mu\Omega\text{cm}$ at the upper band-edge for this tolerance analysis.

Effects of variations in A_J and NbTiN-quality on the calculated coupling can compensate or amplify each other: The current density does not have much effect on the shape of the band-pass and the frequency-dependency of the relative power conversion, but merely on its power level (Fig. 3.21). But variations in junction area and quality of NbTiN significantly change the shape and position of the band-pass in a similar manner (compare Fig. 3.22 and 3.23). This implies that to first order the two effects can not be distinguished from the calculated or measured band-pass and can possibly add up in a strong deformation of the band-pass.

This is illustrated for the same example as in the previous tolerance analysis calculations in Fig. 3.24. The design band pass is plotted as the red line. In Fig. 3.24 (a) a possible shift in junction width I_J in both directions is compensated by variations in NbTiN-quality. In Fig. 3.24 (b) the same parameters are used, but in the opposite combination. This results in significant shifts and deformations of the calculated band-pass.

In order to include both effects in the mask design, the device designs are calculated for a set of NbTiN-qualities. Then, a reasonable probability is achieved, that a fraction of devices on the mask are optimized for the actually fabricated device parameters.

3.6.3 Three lithography masks: “NbTiN3”, “NbTiN4”, “CCN8”

For the HIFI band 2 mixer device fabrication three sets of lithography masks have been designed, fabricated and analyzed. Two of the masks are used for fabrication at KOSMA (NbTiN3, NbTiN4) and one (mask CCN8) for fabrication at DIMES, NL [72].

First, the general overview of a mask layout is given. Then, mask specific details with regard to the selection of layer parameters and the device designs

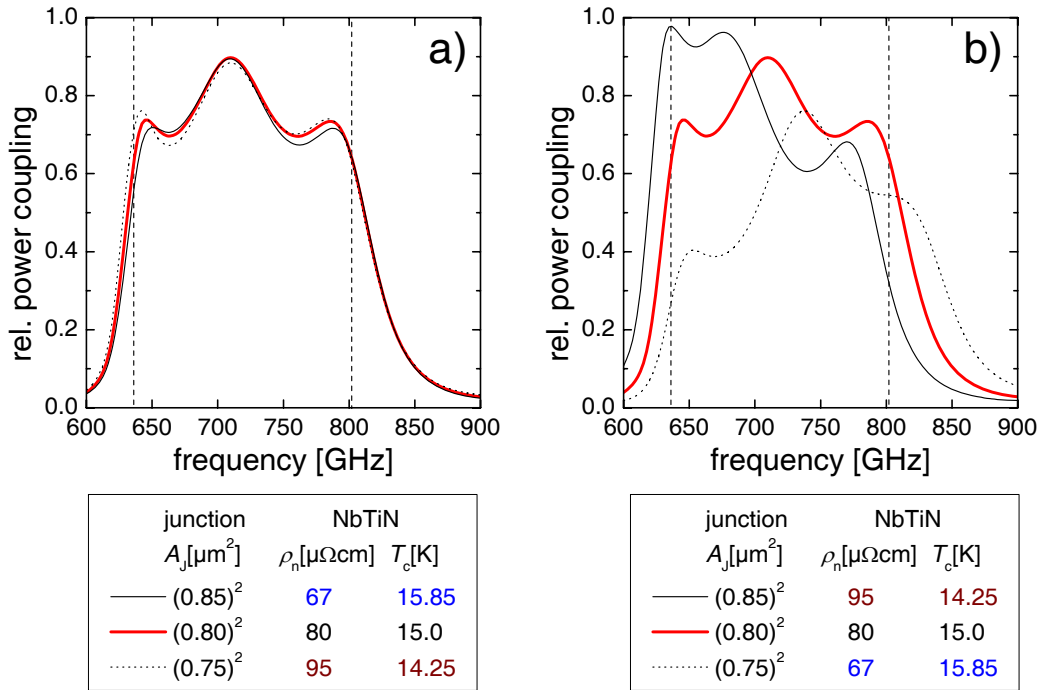


Fig. 3.24: Calculated band-pass for simultaneous variation in junction width I_J and NbTiN-quality. **a)** Variations in junction width of $\Delta I_J = 0.05 \mu\text{m}$ are compensated by variations in NbTiN-quality ($\Delta\rho_n=13/15 \mu\Omega\text{cm}$, $\Delta T_c = 0.85/0.75 \text{ K}$). **b)** The same variations in I_J , T_c and ρ_n of NbTiN in the opposite direction add up to strong deformations in the band-pass.

are given. The mask layout CCN8 (only normal-conductive Al as top-wiring) has been realized within a HIFI-related co-operation, while the mask designs NbTiN3 and NbTiN4 contain the major design approaches for the HIFI band 2 SIS-device design.

The systematical layout of the masks “NbTiN3” and “NbTiN4” for the KOSMA micro-structure laboratory is given in Fig. 3.25. The SIS-devices are placed in four columns “B” to “E”, which are surrounded by mass lines to shield the devices from possible electro-static discharge (ESD) during the fabrication process and the further processing (dicing, lapping). Test-structures are placed in column “A” for van der Pauw- and line measurements of the fabricated films. Furthermore adjustment crosses are necessary for the relative positioning of the different layers. In the small magnified inset in the figure the filter structures of the waveguide probe and the matching circuits of the devices can be seen.

The layout of the mask “CCN8”, a cooperation with SRON (NL) is similar, where the devices for two columns were designed by KOSMA.

Mask design CCN8: The mask CCN8 has been used within a collaboration with the DIMES fabrication laboratories (Delft Institute of Microelectronics

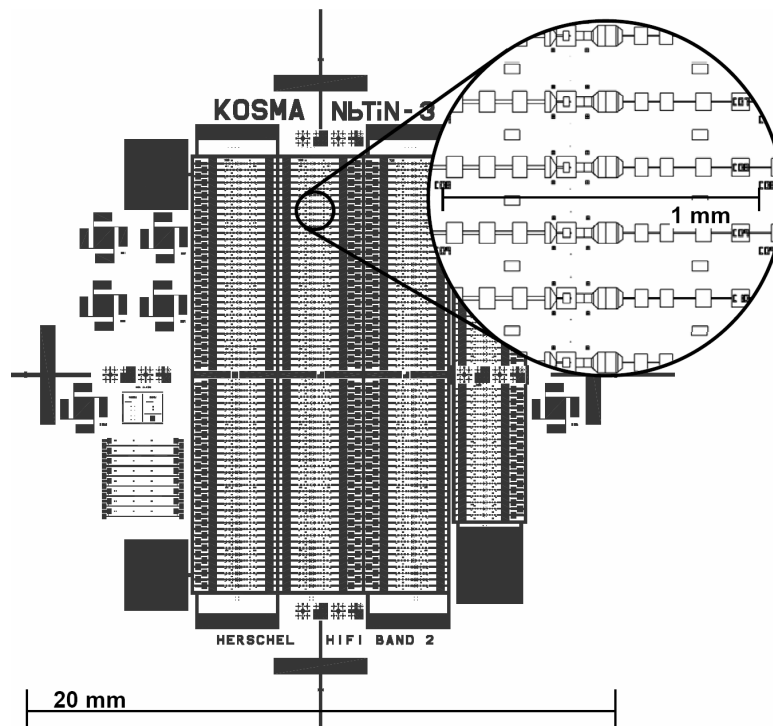


Fig. 3.25: General layout of the masks “NbTiN3” and “NbTiN4”; the SIS-devices are placed in four columns (“B” to “E”). In column “A” test-structures for van der Pauw- and line-measurements and also mark crosses for the relative adjustment are placed on the mask.

and Submicrontechnology, NL) and SRON (Netherlands Institute for Space Research, NL) under an ESA-contract⁵. Because devices for HIFI bands 2 and 3 (800-960 GHz) have been placed on the same mask, only Al as top-wiring material has been chosen, which is superior to Nb above 860 GHz. The main characteristics are given in Table 3.2.

Mask designs NbTiN3 and NbTiN4: These two mask sets have been part in a series of mask iteration for the use of NbTiN as ground-plane. The mixers for HIFI band 2 have been selected from wafers, which have been fabricated with mask set NbTiN3, while NbTiN4 is the most recent design approach with the improvements in design parameters and selection criteria based on the previous RF-measurements (see Chap. 4). A tabular overview of the most important mask parameters is given in Table 3.6.3.

There are some major improvements which refer to the choice of parameters for the NbTiN-quality, since the quality with respect to ρ_n has been improved but the measured spread in T_c has been larger than for mask design NbTiN3. Based on the RF-measurement results the asymmetric waveguide probe SSP (see Subsec. 3.3.2) with a lower impedance and optimum power coupling is

⁵ESTEC Contract No. 11653/95

CCN8	
frequency band:	636-802 GHz
SIS-junction:	
A_J [μm^2]	$(0.92)^2$
V_{Gap} [mV]	2.80
j_c [kA/cm ²]	8-12
matching circuit:	double junction devices
NbTiN parameters:	
ρ_n [$\mu\Omega\text{cm}$]	110
T_c [K]	14.3
waveguide probe:	only DSP
each device design	6×
different designs	40

Tab. 3.2: Characteristic data for the KOSMA part of mask design CCN8. The double-junction design concept is found in Subsec. 3.5.2.2; the waveguide probe DSP is presented in Subsec. 3.3.2

widely applied on the mask. And a preferred use of Nb as top-wiring layer justified from the RF-measurement results.

The design gap-voltage is marginally corrected to lower values. Lower target values for the junction areas are chosen, because of the more reliable use of the junction definition process electron-beam lithography (EBL). The number of equally designed devices is increased from 4 to 9, because for the HIFI instrument two possibly equal devices are required for the two polarizations. On mask set NbTiN4 the 9 equal devices are distributed over the wafer in three groups of three devices in order to compensate a possible inhomogeneity in fabrication parameters over the wafer.

Based on the presented calculations and selection of device designs the lithography masks⁶ have been produced by an external supplier [73]. Then the wafers with SIS-devices have been fabricated in the KOSMA clean room facility. A description of the fabrication techniques and optimization is given in [14, 13]. The characterization and selection of the fabricated devices is described in the next chapter.

⁶Within this thesis an automated software tool has been developed, to generate the lithography masks in Autocad based on the device design data (type of waveguide probe, junction size, matching circuit geometry and materials). This especially has been used for a flexible variation of the e-beam exposure parameters for the junction definition. These parameters have been specifically adapted for different wafers to compensate a systematical shift in junction area.

NbTiN3			NbTiN4				
frequency band							
636-802 GHz:	192×		636-802 GHz	230×			
790-880 GHz:	40×						
test-devices:	8×		test-devices:	10×			
SIS-junction							
A_J [μm^2]:	$(0.8)^2, (0.9)^2, (1.0)^2$		A_J [μm^2]:	$(0.7)^2, (0.8)^2, (0.9)^2$			
V_{Gap} [mV]:	2.77		V_{Gap} [mV]:	2.75			
j_c [kA/cm ²]:	15		j_c [kA/cm ²]:	15			
type of matching circuit							
3-step trafo:	180×		3-step trafo:	230×			
nb: 44×, bb: 136×			nb: 72×, bb: 113×, ub: 45×				
double junction:	52×						
end-loaded stub:	8×		end-loaded stub:	10×			
NbTiN parameters							
	ρ_n [$\mu\Omega\text{cm}$]				ρ_n [$\mu\Omega\text{cm}$]		
T_c [K]	80	100	120	T_c [K]	70	80	90
14.5			100×	14.5		18×	27×
14.7		72×		15.0	33×	34×	27×
14.9	68×			15.5	32×	42×	
				16.0	18×		
top-wiring							
Al:	140×						
Nb:	100×			Nb:	240×		
waveguide probes							
DSP:	80×			DSP:	26×		
SSP:	118×			SSP:	214×		
810DSP:	42×						
each device design:	4×			each device design:	9×		
different designs:	58			different designs:	27		

Tab. 3.3: Overview of characteristic data for mask designs NbTiN3 and NbTiN4. If a number is followed by the “times”-symbol (×) it refers to the number of devices; A_J : junction area; V_{Gap} : gap-voltage; j_c : current density. Types of matching circuits are found in Subsec. 3.5.2 and 3.6.1.3, waveguide probes are given in Subsec. 3.3.2. The major improvements in NbTiN4 are the adapted quality parameters for the NbTiN-layer; the preferred use of the waveguide probe SSP and the top-wiring material Nb are justified from previous RF-measurement results.

Chapter 4

Device and mixer characterization for the selection of flight-mixers

The driving force during the design process has been to design SIS-devices, which can be used in low noise heterodyne mixers in the HIFI frequency band 2 (636-802 GHz). Two SIS-devices for low noise and broad-band mixers are required, which comply with the HIFI performance base-line and are integrated in the HIFI flight receiver¹. In this chapter the characterization and selection process is described, which has been necessary to identify the devices and mixers compliant with the ambitious HIFI performance requirements.

In the first section (Sec. 4.1) the performance requirements for the HIFI band 2 mixers are given in detail. Then, in Sec. 4.2 the methods, which have been applied to characterize the devices of a wafer or an assembled mixer, are described. In Sec. 4.3 the measurement results for the most relevant wafers are presented and in Sec. 4.4 the interpretation methods are illustrated, which have been applied during the selection process. In the data interpretation the measurement results are related to the design model in order to obtain a reliable estimate for fabrication specific parameters (j_c , ΔA_J , ...) and thus for the performance of a whole wafer after a limited number of measurements. Examples for the data interpretation of three characterized wafers (two rejected, one accepted wafer with flight-models) are given.

4.1 The HIFI band 2 performance baseline

Contribution of the mixer to the HIFI receiver noise: The contribution of the mixer to the HIFI receiver temperature can be specified according to

¹For the purpose of reliability in the space project three flight mixers and two flight spare mixers have been qualified and delivered. The HIFI flight model is already assembled (see Fig. 1.2).

(compare Eq. 2.2)

$$\begin{aligned} T_{\text{Rec}} &= T_{\text{pre}} + \frac{\mathbf{T}_{\text{Mix}}}{G_{\text{pre}}} + \frac{T_{\text{post}}}{G_{\text{pre}} \cdot \mathbf{G}_{\text{Mix}}} \\ &= T_{\text{pre}} + \frac{1}{G_{\text{pre}}} \left(\mathbf{T}_{\text{Mix}} + \frac{T_{\text{post}}}{\mathbf{G}_{\text{Mix}}} \right). \end{aligned} \quad (4.1)$$

Here “pre” denotes the contributions of the components in the signal processing sequence in front of the mixer, and “post” denotes the contributions which are fed with the mixer’s IF-output signal. The performance in front of the mixer is mainly determined by the telescope and optics components. The noise contribution in the sequence behind the mixer is mainly determined by the first IF-amplifier ($T_{\text{post}} \approx T_{\text{IF}}$).

Since the goal for the IF-contribution is 10 K, the baseline for the HIFI mixers is defined for the noise contribution, given as

$$T_{\text{Mix,IF}} \equiv T_{\text{Mix}} + \frac{10 \text{ K}}{G_{\text{Mix}}}. \quad (4.2)$$

The actual baseline for $T_{\text{Mix,IF}}$ in the HIFI band 2 is 110 K at 636 GHz and 150 K at 802 GHz (Fig. 4.1). The mixers in this chapter are characterized by this value for $T_{\text{Mix,IF}}$ if nothing different is explicitly mentioned.

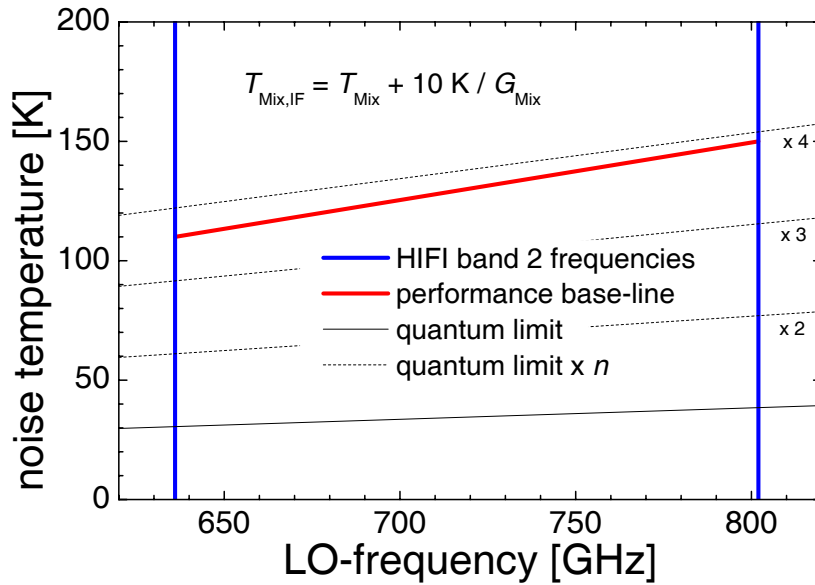


Fig. 4.1: The red line shows the required mixer performance for the HIFI frequency band 2 in terms of $T_{\text{Mix,IF}}$ (Eq. 4.2). Added are multiples of the quantum noise limit for comparison.

Priority list of frequencies for HIFI band 2: Since a specific mixer shows its specific shape in the noise band-pass, an absolute criterion has to be applied

in order to quantify the validity of a mixer for HIFI band 2. A first simple criterion is the noise average over n measured frequencies

$$T_{\text{avg}} = \frac{1}{N} \sum_n T_{(\text{Mix,IF}),n}.$$

In order to include the requirements of the HIFI Science Programm to the receiver performance a weighted average of a mixer over the required frequencies has been evaluated. The expected mixer performance at a specific frequency ν_i has been calculated by linear interpolation of the measured frequencies, resulting in a value $T_{\text{Mix,IF}}(\nu_i)$. Then the weighted noise temperature, which has to be minimized, has been defined as

$$T_{\text{weight}} = \frac{\sum_i T_{\text{Mix,IF}}(\nu_i) \cdot w_i}{\sum_i w_i}. \quad (4.3)$$

The weight factors w_i for a specific frequency ν_i is $w_i = \sum_j w_{i,j}$, where j is the index of a specific science research field. The applied weight factors for the required frequencies grouped by their research field based on an internal technical paper for HIFI [74] are given in Table 4.1. The mixers with minimum value for T_{weight} have to be identified for integration in the HIFI receiver.

		gala- xies	solar system bodies	inter- stellar medium	star for- mation	stellar evolu- tion	total weight
species	ν_i [GHz]	$w_{i,1}$	$w_{i,2}$	$w_{i,3}$	$w_{i,4}$	$w_{i,5}$	$\sum_j w_{i,j}$
H ₂ O- <i>para</i>	654.8	–	–	–	–	2	2
H ₂ O- <i>ortho</i>	651.1	–	–	–	–	2	2
SiH	658.0	–	–	–	3	–	3
DF	660.0	–	–	1	–	–	1
¹³ CO	661.0	–	–	–	–	3	3
CO	691.4	–	–	–	–	3	3
O ₂	715.4	–	–	–	3	–	3
H ₂ S- <i>ortho</i>	736.0	–	1	1	1	–	3
H ₂ ¹⁸ O- <i>ortho</i>	745.3	5	–	–	3	–	8
H ₂ O- <i>para</i>	750.5	5	–	–	–	2	7
H ₂ O- <i>ortho</i>	750.6	5	–	–	–	2	7
H ₂ O- <i>para</i>	752.0	5	2	3	3	2	15
¹³ CO	766.9	5	–	–	–	2	7
O ₂	773.8	–	–	–	3	–	3

Tab. 4.1: Weight factors for the most requested frequencies to observe with HIFI band 2 based on internal technical paper [74]. The weight factors are grouped based on the main five scientific research fields.

4.2 Experimental device and mixer characterization methods

In this section three experimental methods are documented, which are used for the characterization of the fabricated SIS-devices and -mixers. The three methods and the resulting characteristic parameters are in detail:

- **DC-measurement:** I-V-curve, from which the gap-voltage V_{Gap} , normal resistance R_N , DC-quality Q , Josephson resonance frequencies ν_{res} are extracted
- **FTS-measurement:** direct detection band-pass $p(\nu)$ (photon coupling efficiency as a function of frequency)
- **Heterodyne measurement:** mixer performance $T_{\text{Mix}}(\nu)$, $G_{\text{Mix}}(\nu)$ (for definition see Subsec. 2.1.3).

In the DC-measurements (Subsec. 4.2.1) the I-V-curves of several SIS-devices are recorded in a single run. This allows the characterization of a wafer in a few days. This measurement is routinely done for all fabricated devices.

The two other characterization methods characterize the RF-performance of a SIS-device. For these measurements a SIS-device is mounted in a waveguide mixer block. The FTS-measurement (Subsec. 4.2.2) yields the direct detection band-pass of the mixer. From the heterodyne measurements (Subsec. 4.2.3) the noise and conversion gain performance of the mixers is extracted. These latter two measurements are only done for devices which have passed the criteria for an acceptable DC I-V-curve.

4.2.1 DC-measurement method

In the DC-measurements 27 devices of a wafer are characterized simultaneously in one dip in liquid helium with a four-point measurement of their DC-current and -voltage. These measurements yield the first check of the contacts and then a more detailed characterization. Examples of measured DC IV-curves are shown in Fig. 4.2 (a).

From the I-V-data, the following characteristic parameters are evaluated (compare Sec. 2.3):

- The gap-voltage V_{Gap} ,
- The normal resistance R_N ,

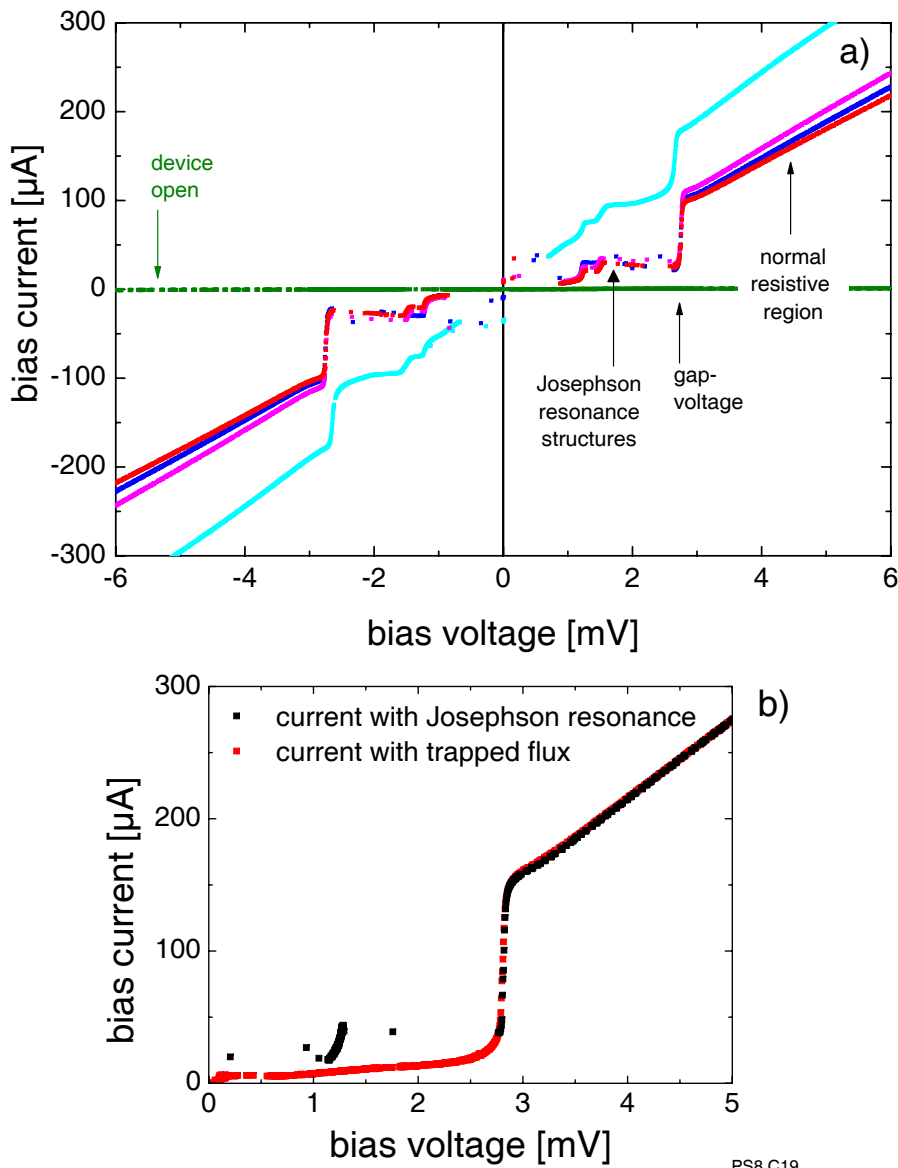


Fig. 4.2: **a)** *I-V-curves from dipstick-measurement: data for normal resistance R_N , gap-voltage V_{Gap} , DC-quality Q and Josephson resonance frequencies ν_{res} are extracted. Defects (normal resistive device, open or short circuit) are identified. The green points denote the data of a open circuit device. **b)** Two different DC-measurements of the same SIS-device. The black points show the data with Josephson resonance and thus increased measured sub-gap current. The red points show the data with magnetic flux in the barrier, which suppresses the Josephson effects.*

- The Josephson resonance frequencies ν_{res} : The bias-voltages of the maxima in current are related to the resonance frequencies according to $\nu_{res} = 2e \cdot V_{bias}/h$ (Eq. 2.8). The resulting accuracy of ν_{res} is ± 40 GHz. The Josephson resonance frequencies by experience mark the lower edge of the band-pass. This is illustrated and justified in Subsec. 4.4.1.2.

- The DC-quality Q (see Eq. 2.17 for definition): Q cannot always be determined very accurately from the dipstick DC measurements, because the sub-gap current is increased due to the Josephson resonances (see Fig. 4.2 (b)).

The final value for Q only can be determined in the heterodyne set-up where a magnetic field is applied to suppress the Josephson effects.

Thanks to trapped flux in some devices a fair estimate for Q can nevertheless be obtained from the dipstick measurements.

4.2.2 FTS-measurement method

A commercial Fourier transform spectrometer (FTS) [75] is used for the measurements of the mixer direct detection response². The setup for the direct detection characterization of the mixers is given in Fig. 4.3.

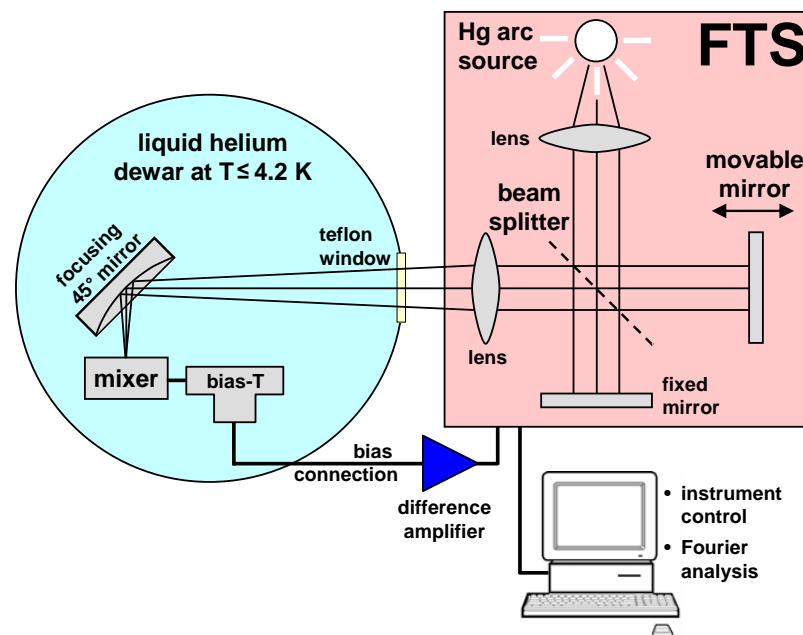


Fig. 4.3: Measurement setup for the FTS-measurement. The radiation of a broadband Hg arc-source is split and brought to interference with a Michelson interferometer via a fixed and a movable mirror. For the mixer characterization the response to the radiation in bias current or voltage is amplified by a difference amplifier. The resulting interferogram is transformed to a frequency-dependent spectrum with Fourier analysis.

The FTS-instrument uses a broadband Hg arc-lamp (with a quartz bulb) as radiation source. With a Michelson interferometer two interfering beams are produced. The response of the SIS-mixer signal is recorded as a function of

²The power transmission of the optical components for the heterodyne setup are also specified with FTS-measurements (see Subsec. 4.2.3)

the optical retardation of one of the beams. The resulting interferogram is afterwards Fourier-transformed to a power spectrum.

The resulting data from this characterization method is the photon coupling efficiency as a function of radiation frequency ν . The spectra have been corrected for the internal beam-splitter of the FTS, because its transmission varies significantly in the range of 500-1200 GHz, although it shows no minima in this region. The beam-splitter characteristic is given in Fig. 4.4. From

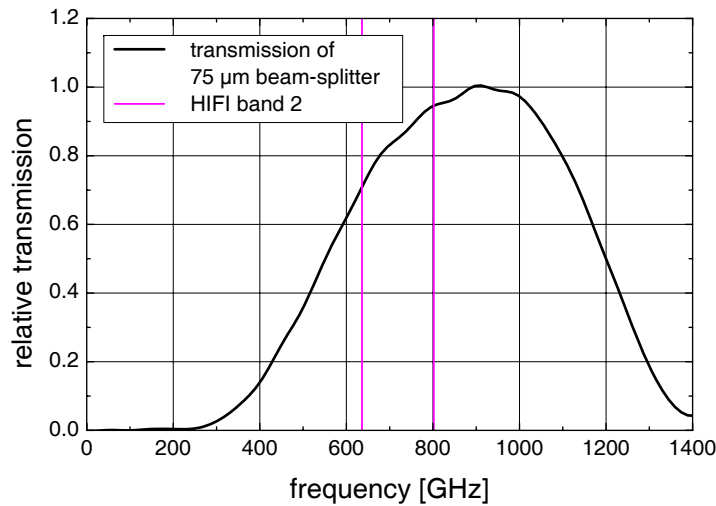


Fig. 4.4: *Relative transmission of internal beam-splitter (thickness 75 μm) of FTS. Correction of FTS-data for beam-splitter characteristics is necessary in HIFI frequency band 2.*

measurement to measurement the coupling of the radiation to the mixer and the signal amplification and filtering have been optimized independently to obtain an optimum signal-to-noise ratio. This implicates that the absolute measured power values for different mixers can not be compared and only relative information about the band-pass of the individual mixer is obtained.

4.2.3 Heterodyne measurement method

The principle of a hot-cold measurement, which is used to characterize the noise and gain of a receiver, is already given in Subsec. 2.1.3. For the performance-characterization a mixer is integrated in a test-receiver setup. Then, the mixer performance is extracted from the measured receiver performance.

First, the measurement setup is presented. Then, the characterization of the noise contribution related to the optics components and the IF-chain is presented. This is necessary to extract the mixer performance data from the measured receiver performance.

4.2.3.1 The heterodyne measurement setup

The schematic of the measurement setup for the heterodyne measurements is given in Fig. 4.5. The mixer and the cold IF-components are mounted on

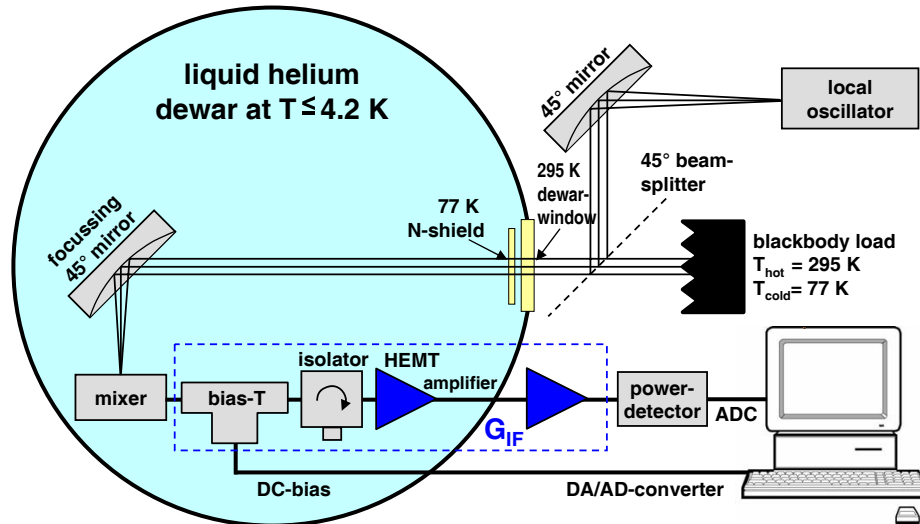


Fig. 4.5: Measurement setup for heterodyne measurements. The mixer is operated inside a liquid-helium dewar at temperatures down to 2.8 K. Local oscillator and black-body radiation are coupled by a dielectric beam-splitter through a Teflon-window into the vacuum dewar. The IF-signal is amplified by a cold low-noise HEMT amplifier and a warm additional amplifier and filter chain.

the cold plate of a liquid helium dewar. The signal (black-body) radiation is combined with the LO-radiation by a dielectric beam-combiner³ to be fed to the mixer. The bias-T provides the DC-connections to the mixer and couples out the IF-signal. The HIFI bias-T for Band 2 is designed by M. Justen and details of the HIFI bias-T design and the characterization are found in [76]. The whole IF-chain consists of the bias-T, an isolator (4-8 GHz, -15 dB isolation, 0.2 dB attenuation, [77]), cold and warm IF-amplifiers and finally a power detector, calibrated with a power-meter.

Within this thesis the data acquiring software for the hot-cold measurements has been adapted for the HIFI tests and the bias-calibration has been done.

With this setup the contributions to the measured receiver performance can be divided into three major parts:

1. optics components: beam-splitter, dewar-window at room temperature and infrared shield at 77 K, and focussing elliptical mirror at 4.2 K,
2. the mixer (corrugated horn, mixer-block and device),

³This beam-combiner is referred to as “beam-splitter”, although it functions as a beam-combiner in this case.

3. the IF-chain, beginning with the bias-T and the following sequence of components.

The measured performance parameters are composed of the performance characteristics of these three major component groups according to

$$T_{\text{Rec}} = T_{\text{Opt}} + \frac{\mathbf{T}_{\text{Mix}}}{G_{\text{Opt}}} + \frac{T_{\text{IF-chain}}}{G_{\text{Opt}} \cdot \mathbf{G}_{\text{Mix}}}. \quad (4.4)$$

$$G_{\text{Rec}} = G_{\text{Opt}} \cdot \mathbf{G}_{\text{Mix}} \cdot G_{\text{IF-chain}}. \quad (4.5)$$

The optics contribution T_{Opt} is an effective radiation temperature, which contains the radiation temperatures and transmission coefficients of the respective components.

The characterization of the optics components, the specification of the IF-contribution and the numerical correction of the receiver performance to obtain the mixer performance has been done within this thesis for all presented mixers and frequencies.

4.2.3.2 Effective radiation temperature of the optics components

Three attenuating optical components contribute to the effective noise temperature. The three components are: the beam-splitter (BS), the dewar-window (Win) and the N-shield (N-Sh), which is necessary to prevent heating of the mixer device due to diffuse room temperature radiation. The mirror on the cold plate directly in front of the horn is assumed to be perfect, in reflectivity and in beam matching. The ambient temperature of the beam-splitter and the dewar-window is room temperature (293 K); for the N-shield it is 77 K.

The effective optics contribution to the receiver noise is calculated from

$$T_{\text{Opt}} = \frac{T_{\text{BS}} \cdot A_{\text{BS}}}{G_{\text{BS}}} + \frac{T_{\text{Win}} \cdot A_{\text{Win}}}{G_{\text{BS}} \cdot G_{\text{Win}}} + \frac{T_{\text{N-Sh}} \cdot A_{\text{N-Sh}}}{G_{\text{BS}} \cdot G_{\text{Win}} \cdot G_{\text{N-Sh}}}. \quad (4.6)$$

Here, the radiation temperatures (T_{BS} , T_{Win} , $T_{\text{N-Sh}}$) of the components have been calculated according to the Callen and Welton equation (Eq. 2.6) from their ambient temperature and the operating frequency. G denotes the transmission coefficients and $A = 1 - G$. It can be shown with a straight-forward calculation of the resulting radiation temperature of the black-body load and the three optics components directly in front of the mixer, that the definition in Eq. 4.6 is consistent with the Callen-Welton equation (see Appendix C.1).

The frequency dependent power transmission G of each component has been measured with the FTS using a broadband room temperature DTGS-detector [75]. Details of the measurements and further analysis of the transmission coefficients for the three optics components are given in Appendix C.

Two different setups (“test-dewar” and “FM-dewar”) have been used, which both have the same concept as given in Fig. 4.5, but contain different hardware for the three optics components. In Fig. 4.6 the applied values for the transmission of the optics-components (top) are given together with the resulting effective noise temperatures for the optics T_{optics} (bottom) evaluated according to Eq. 4.6.

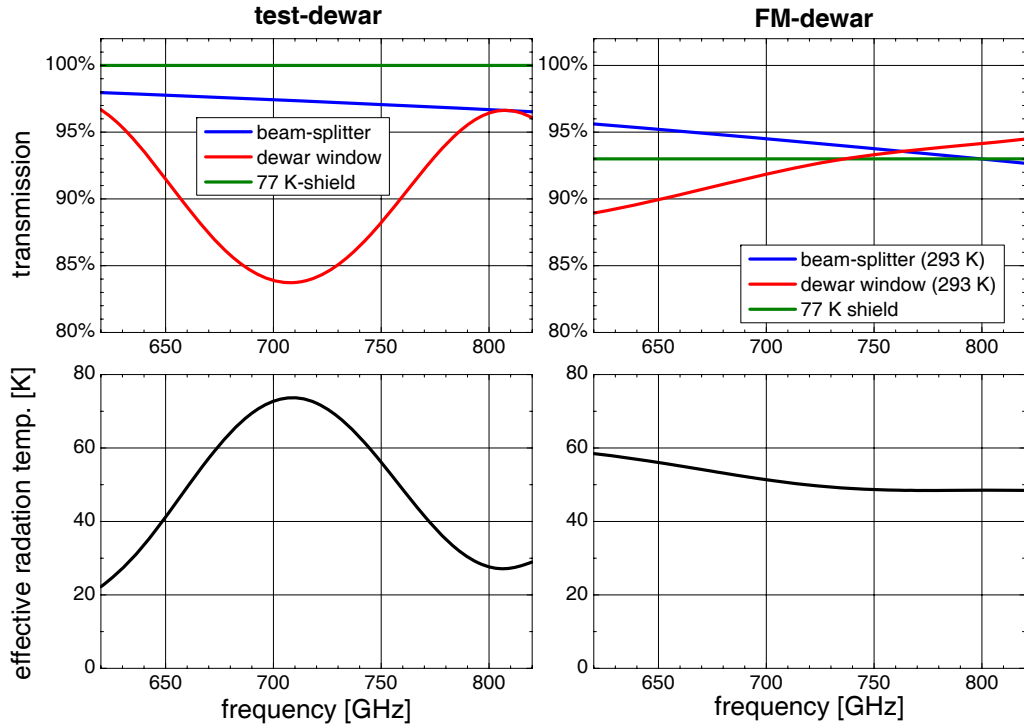


Fig. 4.6: Summary of the applied transmission of the optics components (top) for the test-dewar setup (left) and the FM-dewar setup (right). The resulting effective noise temperatures are given in the two bottom plots.

4.2.3.3 Specification of the IF contribution from the shot-noise fit

The contribution of the IF-chain ($T_{\text{IF-chain}}$ in Eq. 4.4, $G_{\text{IF-chain}}$ in Eq. 4.5) has been specified with the shot-noise fit. The general concept of this method is found in [78]. The calculation of the shot-noise based on the measured I-V-curve and the knowledge of the IF-circuit for an unpumped SIS-mixer is given in App. A.1.

Optimum parameters during the flight-mixer characterization have been $G_{\text{IF-chain}} = 80 - 82$ dB and $T_{\text{IF-chain}} = 5 - 7$ K. A lower performance of the IF-chain results in a larger inaccuracy of the corrected mixer noise performance T_{Mix} and G_{Mix} .

Accuracy of the shot-noise fit: The shot-noise fit itself has an accuracy of $\Delta T_{\text{IF}} = 2 \pm \text{K}$ because of the typical spread in calculated IF-power. For the FM-tests a systematical offset $+2 \text{ K}$ of the shot-noise fit data (7 K) in comparison to a hot-cold characterization of the IF-chain (including the bias-T) with a heated load instead of the mixer (5 K) has been observed. For the FM-tests the IF-noise temperature T_{HEMT} of 5 K has been used. With this value for T_{HEMT} the resulting values from the shot-noise fit for G_{IF} comply with the value from the hot-cold characterization of the IF-chain within $\pm 0.5 \text{ dB}$. During the characterization for the selection of the mixers as flight-mixers, the values for T_{HEMT} of the shot-noise fit have been used.

4.3 RF-performance results for fabricated wafers

The HIFI band 2 mixer devices have been developed in a sequence of wafers, fabricated in the KOSMA-clean room facilities. After the technology development (NbTiN as ground-plane material [13], electron beam lithography, EBL, for junction definition [14]) the designed lithography mask has been realized in thin-film technology. Based on the measurement results and the data interpretation the fabrication process has been optimized from wafer to wafer in order to reach the performance baseline. The optimization of the fabrication process is documented in [14, 13].

The sequence of this development can not be treated in detail within this thesis. But the measurement results of the 9 most relevant and successful wafers are presented and summarized in this section. Then, in the following section the data analysis methods and the applications for three exemplary wafers are presented.

First, in Subsec. 4.3.1 a consistent data set is defined, which is used to characterize the wafers. In Subsec. 4.3.2 a summarizing overview of the wafer-specific data is given. Here the relations of the fabrication concepts and the characteristic data are discussed, and some first conclusions regarding the optimum noise performance are drawn. Then, as reference the actual characteristic data for the 9 wafers are presented in Subsec. 4.3.3.

A table of all RF-characterized wafers and devices, the applied fabrication concepts and an overview of the measured noise performance are given in Appendix D.

4.3.1 A consistent set of wafer characterization data

The data set for a wafer is presented in five plots (a) to (e) in two columns (Figure 4.7). The left column - with plots (a) to (c) - contains statistical data for the DC-parameters of a whole wafer, measured in the dipstick-setup. For

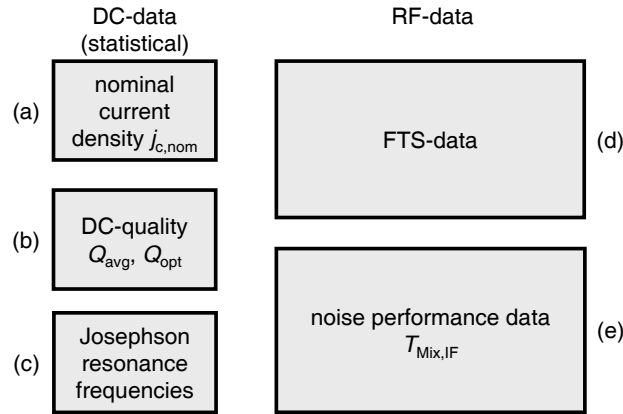


Fig. 4.7: Five consistent data plots are given for all presented wafers.

this analysis devices which show the typical characteristics of an SIS-device⁴ are included. The right column - with plots (d) and (e) - contains RF-data for the measured mixers of the respective wafer.

The description of the data in detail:

- (a) In plot (a) the distribution of the **nominal current density**

$$j_{c,nom} = \frac{\pi}{4} \cdot \frac{V_{Gap}}{R_N \cdot A_{J,nom}} \quad (4.7)$$

is given. The distribution of $j_{c,nom}$ can be used to estimate the **relative junction area accuracy** $\Delta A_{J,real}/A_{J,real}$. The measured normal resistance R_N is inversely proportional to the actual junction area

$$R_N \sim \frac{1}{A_{J,real}}.$$

By multiplying R_N with the nominal junction area $A_{J,nom}$ of that device the effect of different nominal junction areas is eliminated. To examine $j_{c,nom}$ instead of $R_N \cdot A_{J,nom}$ is justified as long as the variation in V_{Gap} is much smaller than in $R_N \cdot A_{J,nom}$. This is the case for the presented wafers.

- (b) In plot (b) the distribution of the **DC-quality** Q of the devices and the average value are given. For definition see Eq. 2.17. From the distribution the average value Q_{avg} is evaluated. The optimum value Q_{opt} is marked for the largest available Q , not including possible outliers, but giving the upper limit of the distribution.
- (c) In plot (c) the distribution of **Josephson resonance frequencies** is given. This is a hint, whether the frequency band of the fabricated

⁴Required characteristics of an SIS-device: A significant step in current at the gap-voltage around 2.7 mV and a DC-quality $Q \geq 2$.

junctions is generally shifted to lower or higher frequencies, or hits the desired frequency band. Some devices show 0 or 1 resonances, while for some devices a maximum of 3 frequencies is recorded. The interpretation of the Josephson resonance frequencies is discussed in Subsec. 4.4.1.2.

- (d) In plot (d) data from the **FTS-measurements** of the characterized mixers are given. The absolute values are scaled to comply with the relative size of the noise temperatures in (e).
- (e) In plot (e) the **noise performance of the mixers** specified by $T_{\text{Mix,IF}} = T_{\text{Mix}} + 10 \text{ K}/G_{\text{Mix}}$ is given, which specifies the expected noise contribution of the mixer in the HIFI instrument (see Subsec. 4.1).

4.3.2 Overview of wafer characterization results

Nearly all RF-measurements and the complete numerical correction for the evaluation of the mixer performance from the measured receiver noise have been made within the scope of this thesis⁵.

The actual measured DC- and RF-characterization data of the 9 selected wafers are presented in the next subsection 4.3.3 in Figures 4.11 to 4.19. The wafers “CCN8” (Fig. 4.15) have been fabricated within a cooperation with DIMES and SRON⁶. All other wafers have been fabricated at KOSMA.

Figures 4.8 and 4.9 summarize the characterization parameters derived from the wafer-specific data for the eight wafers, which are fabricated by KOSMA and thus are directly compared. Fig. 4.8 shows the relative junction area accuracy $\Delta A_J/A_J$ and the average and optimum DC-quality Q_{avg} , Q_{opt} . In Fig. 4.9 the number of measured Josephson resonance frequencies ν_{res} vs. frequency ν_{res} and the optimum measured mixer performance $T_{\text{Mix, IF}}$ vs. LO-frequency ν_{LO} are plotted. In Fig. 4.9 (b) the superior noise performance of the mixers from wafer PS8 is obvious. While mixers from other wafers show some competitive noise temperatures at some frequencies especially for lower frequencies, no broad band mixers have been identified from these wafers. Around 40% of all heterodyne measurements have been performed on mixers of PS8.

In order to identify the reasons for the differences in performance between the wafers, first the results are discussed under three aspects:

1. the applied fabrication schemes and variations,

⁵The RF-measurements have been done in co-operation with C.E. Honingh, M. Justen, T. Tils, B. Deckert, M. Schultz. The DC-measurements have been performed by S. Wulff, S. Glenz, P. Pütz.

⁶ DIMES: Delft Institute for Micro-Electronics and Submicrontechnology; SRON: Netherlands Institute for Space Research; ESTEC Contract No. 11653/95

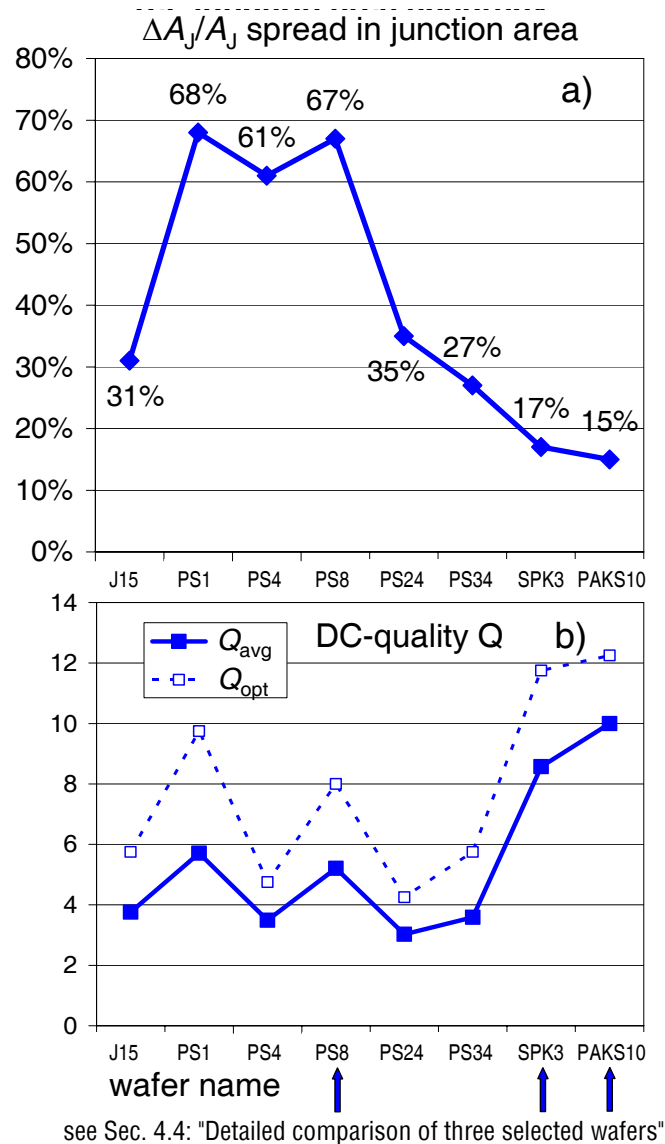


Fig. 4.8: Comparison of characteristic wafer DC-parameters (for definition see Subsec. 4.3.1): **a)** relative spread in junction area $\Delta A_J/A_J$, derived from the $j_{c,nom}$ -distribution, as shown in Fig. 4.11 to Fig. 4.19 (a); **b)** DC-quality Q (average and optimum) as specified in Fig. 4.11 to Fig. 4.19 (b). (The wafers PS8, SPK3 and PAKS10 are discussed in the following Section 4.4.)

2. the junction area accuracy and measured frequencies of optimum power coupling (specified by the Josephson resonance frequencies) and
3. the optimum noise performance in relation to DC-quality Q .

The significant differences of PS8 in comparison to the two other most promising wafers - SPK3 and PAKS10 - are explicitly analyzed in the next section ("Detailed comparison of three selected wafers").

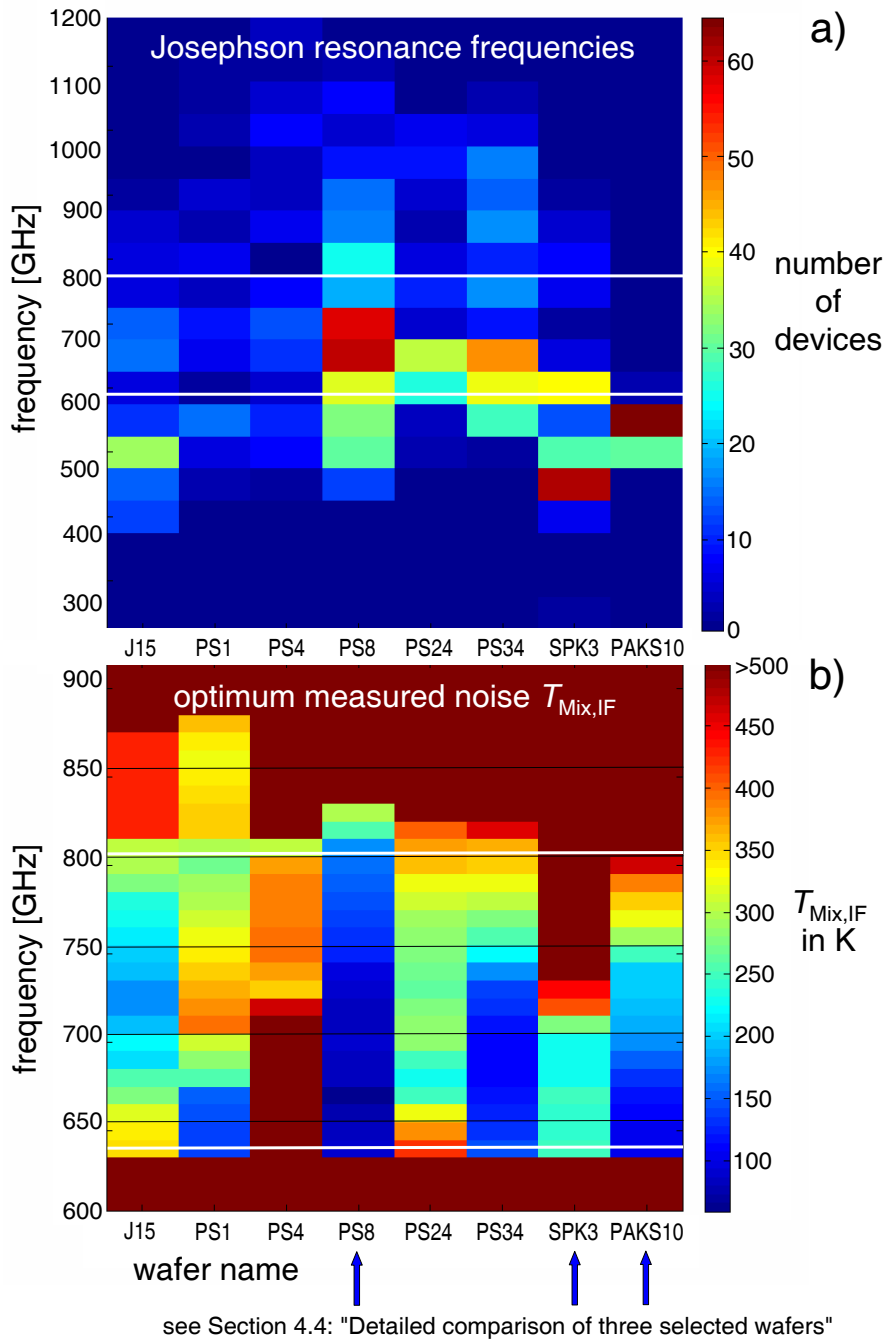


Fig. 4.9: Comparison of characteristic wafer DC-parameters: **a)** Number of measured Josephson resonance frequencies ν_{res} in intervals of $\Delta\nu = 50$ GHz as specified in Fig. 4.11 to Fig. 4.19 (c). One device can show 0, 1, 2 or 3 Josephson resonances. The HIFI mixer frequency band 2 is marked with white lines. **b)** Optimum measured $T_{Mix,IF} = T_{Mix} + 10 \text{ K}/G_{Mix}$ for mixers from a wafer sorted by frequencies in intervals $\Delta\nu_{LO} = 10$ GHz. Only values for $T_{Mix,IF} \leq 500$ K are included. Frequency intervals without measurement are marked with the color for 500 K. (The wafers PS8, SPK3 and PAKS10 are discussed in the following Section 4.4.)

1. The applied fabrication schemes and variations: Wafers with the same prefix have been fabricated according the same fabrication scheme. A detailed documentation of the KOSMA fabrication schemes is found in [14] and [13].

For wafers J15 and SPK3 the junction definition has been done with UV-lithography. For wafers, starting with “P” the junction areas have been defined with EBL. In spite of this advanced technology of the junctions the relative spread in junction area increased after the introduction of this technology (compare Fig. 4.8 (a)), starting with PS1. This attributed to the e-beam resist, which is much more sensitive to the etching⁷.

“PAKS” is a slight modification of the scheme “PS” with an additional anodic oxidation step after the junction is etched and insulated with dielectric SiO₂. This oxidation step is applied in order to improve the insulation of the junction and thus reduce parasitic currents. This has resulted in a significant reduction of the spread in relative junction area (Fig. 4.8 (a)) and an improvement in junction DC-quality Q (Fig. 4.8 (b)).

“SPK” implies basically the exchange of the materials for top-wiring and ground-plane of the micro-strip. This allows the use of the Nb-ground-plane as superconductive electrode and requires the etching of only one electrode, especially no etching of the barrier, which results in a decrease of DC-quality Q . The effect of a reduction in relative junction area and the improvement in junction DC-quality Q is also seen with this fabrication concept (Fig. 4.8 (a) and (b)). Since in this concept the NbTiN-layer is not fabricated as ground-plane under increased ambient temperature, its RF-quality is assumed to be reduced. This is analyzed in the data interpretation section (Subsec. 4.4.2.2).

The “CCN8”-wafers (-02 and -05) have been fabricated at DIMES, NL[72]. Devices for KOSMA for band 2 and devices for SRON for band 3 (800-960 GHz) have been placed on the same mask. All devices have been designed with Al as top-wiring material, since it is preferable in comparison to Nb above 860 GHz. These devices have been fabricated with a significant lower j_c around 5-7 kA/cm² and a significant larger DC-quality of 16 ± 4 , while the target value for the KOSMA-fabricated wafers has been 12-15 kA/cm². The CCN8-devices show a comparable noise performance as the optimum devices with Al-wiring on PS8 at the higher frequency end of the band above the gap-frequency of Nb. The comparable noise performance of devices with Al-wiring fabricated at KOSMA ($j_c = 13$ kA/cm², $Q = 6$) and fabricated at DIMES ($j_c = 6$ kA/cm², $Q = 18 - 25$) is discussed in [79] and also plays a role in the analysis of Chap. 5. The performance of CCN8-devices still has not been as good as for devices with Nb-wiring on PS8.

⁷In order to reduce these variations, a more anisotropic etching recipe has been used, which has resulted an additional reduction of the junction area due to under-etching [13]. For compensation the nominal junction width parameters have been increased to achieve the desired values.

2. The junction area accuracy and measured frequencies of optimum power coupling

(specified by the Josephson resonance frequencies): In Fig. 4.9 (a) the Josephson resonance frequencies for all KOSMA-fabricated wafers are presented. These resonances show the frequency regions of optimum power coupling to the junction. In the plot first it is seen, that for wafers PS1 and PS4 only few devices have been available because of a low device yield.

Then there are three wafers with maximum numbers of measured Josephson resonances below the lower frequency edge of the HIFI band 2 (636 GHz): J15, SPK3, PAKS10. The low Josephson resonance frequencies are a first indication, that for these three wafers the junction areas are fabricated larger than designed (compare tolerance analysis of junction area A_J in Subsec. 3.6.2).

The feature of a sharp maximum in Josephson resonance frequencies is especially seen for wafer PAKS10, which is the first and only wafer in this series fabricated from mask design NbTiN4. In comparison to the previous mask design NbTiN3, no devices designed for the frequency band of 790-880 GHz have been placed on this mask. This together with a low spread in junction area of 15% is assumed to be responsible for this sharp maximum.

The wafer PS8 with many mixers of low-noise performance shows a relative large spread in junction area (67%). In the plot of the Josephson resonance frequencies this can be related to the relatively wide spread in resonance frequencies below and above the frequency band edges. But the maximum and center of this distribution is inside the desired frequency band. This suggests that the average shift in junction area shows a distribution close to zero and thus the applied correction to compensate the under-etching has been correct.

3. The optimum noise performance of a single device in relation to its DC-quality Q :

So far, the characteristic parameters have been discussed on a wafer-specific scope. Here no clear systematic relation between the DC-quality Q and the noise temperature $T_{\text{Mix,IF}}$ is seen.

In Fig. 4.10 the optimum measured mixer performance for each mixer (at its respective optimum frequency) is plotted against its DC-quality measured in the heterodyne dewar with applied magnetic field. Because of non-optimum matching due to junction area or strip-line inaccuracies, higher strip-line losses or thermal coupling problems the receiver noise can be larger than optimum for a specific device. But for the optimum receiver noise for a given DC-quality Q the values, specified by the blue line are found from the measured data. From this experimental analysis it seems that for SIS-junctions with a Q already of 8–10 a further optimization of this parameter does not result in a significant improvement in the mixer noise performance. This correlation is analyzed in more detail in Chap. 5 based on Tucker's quantum mixer theory.

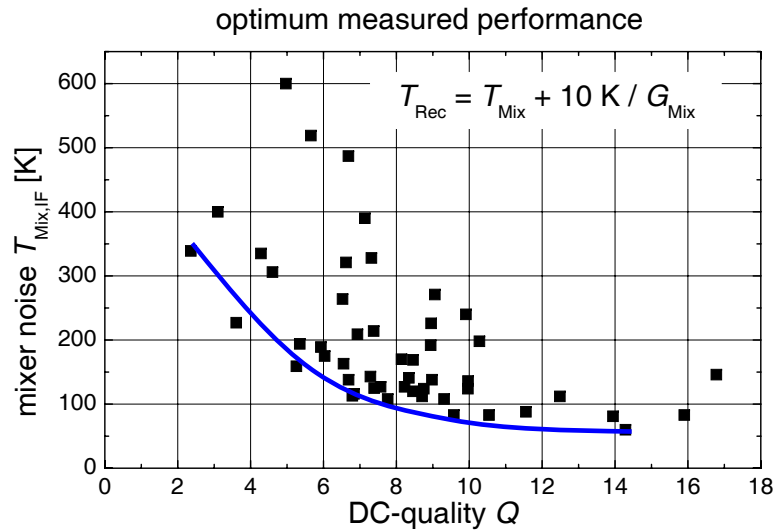


Fig. 4.10: Optimum measured receiver noise for mixers with SIS-devices fabricated at KOSMA. The HIFI receiver noise at the optimum frequency for each mixer is plotted against its DC-quality Q of the measured I-V-curve. The blue line is a guide to the eye for the optimum available performance.

Three wafers for the detailed data interpretation: Based on the DC-parameters in Fig. 4.8 spread in junction area $\Delta A_J/A_J$ and the DC-quality Q the most recent wafers SPK3 and PAKS10 show the optimum results. Unfortunately the absolute value of the area is in both wafers probably too large, which results in a good noise temperature only at the lower end of the HIFI Band 2. The mixers with optimum noise performance regarding the HIFI performance requirements have been from wafer PS8. Thus these three wafers are selected for the more detailed analysis in the next section.

SPK3 and PAKS10 are examples for wafers which had to be rejected as possible flight mixers in spite of some promising DC-characteristics and some competitive performance results around 650 GHz. But PS8 has been identified as the most successful wafer with the most low-noise and broad-band mixers.

Wafer PS34 in spite of its low noise performance is not included in this analysis because only additional devices with significant lower DC-quality Q have been available (compare Fig. 4.8 (b)).

4.3.3 Wafer characterization data

In this subsection the measured DC- and RF-characterization data of the 9 selected wafers according the consistent data-set, defined in Subsec. 4.3.1 are presented. Per wafer all measured RF data is presented. Because of the large number of RF-characterized mixers for wafer PS8 in Fig. 4.14 only the results of the flight-mixers are presented. An additional plot for the noise performance of all RF-characterized mixers of PS8 is given in Fig. 4.20.

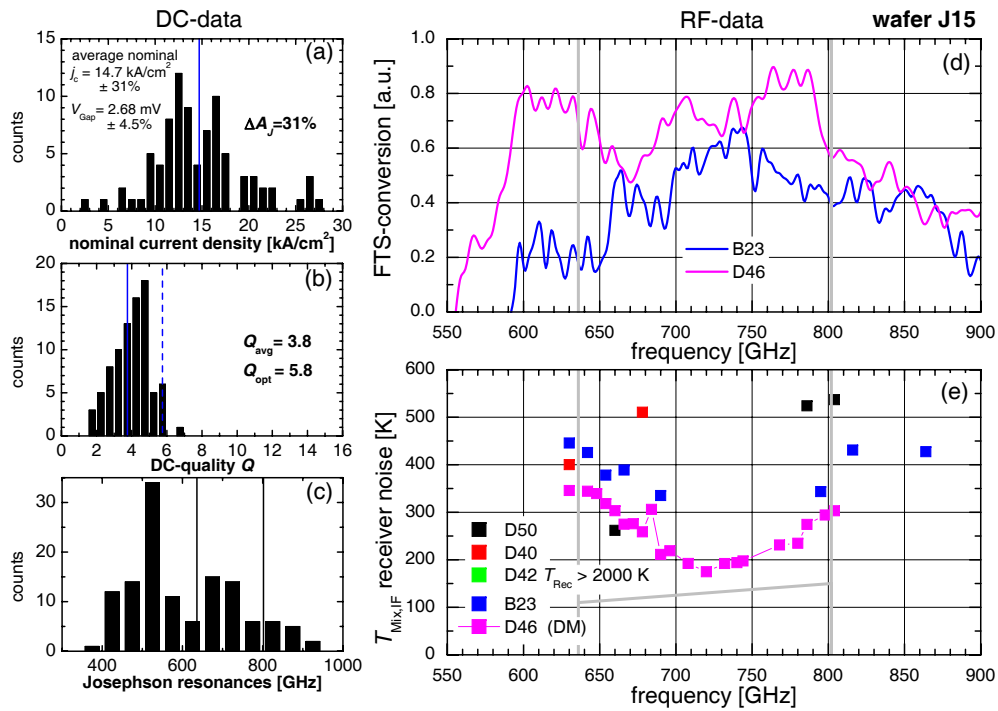


Fig. 4.11: Characteristic parameters for wafer J15 in plots (a) to (c). Two mixers from this wafer have been characterized with FTS-measurements, while five mixers are characterized in noise performance.

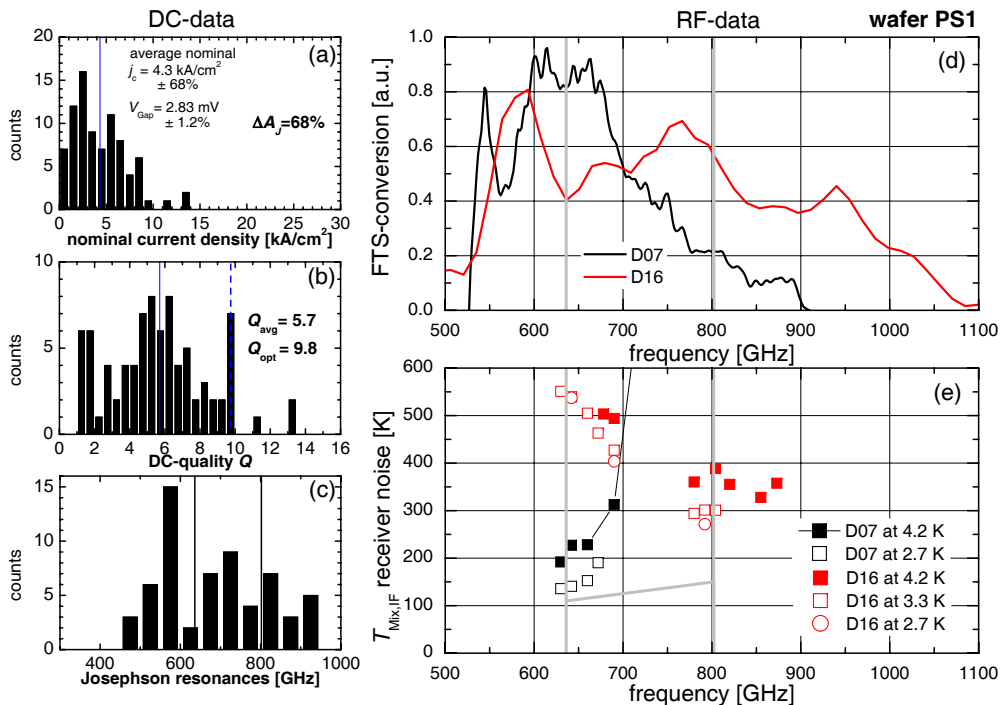


Fig. 4.12: Characteristic parameters for wafer PS1 in plots (a) to (c). Two mixers from this wafer have been characterized with FTS-measurements (d) and heterodyne measurements (e).

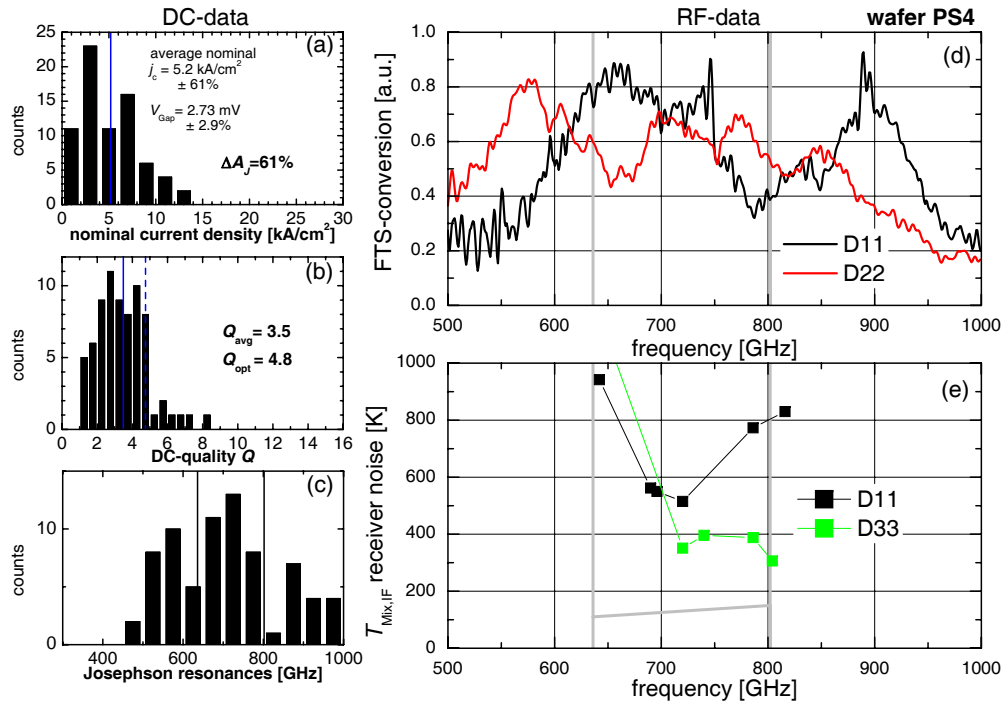


Fig. 4.13: Characteristic parameters for wafer PS4 in plots (a) to (c). Two mixers from this wafer have been characterized with FTS-measurements (d) and two mixers with heterodyne measurements (e).

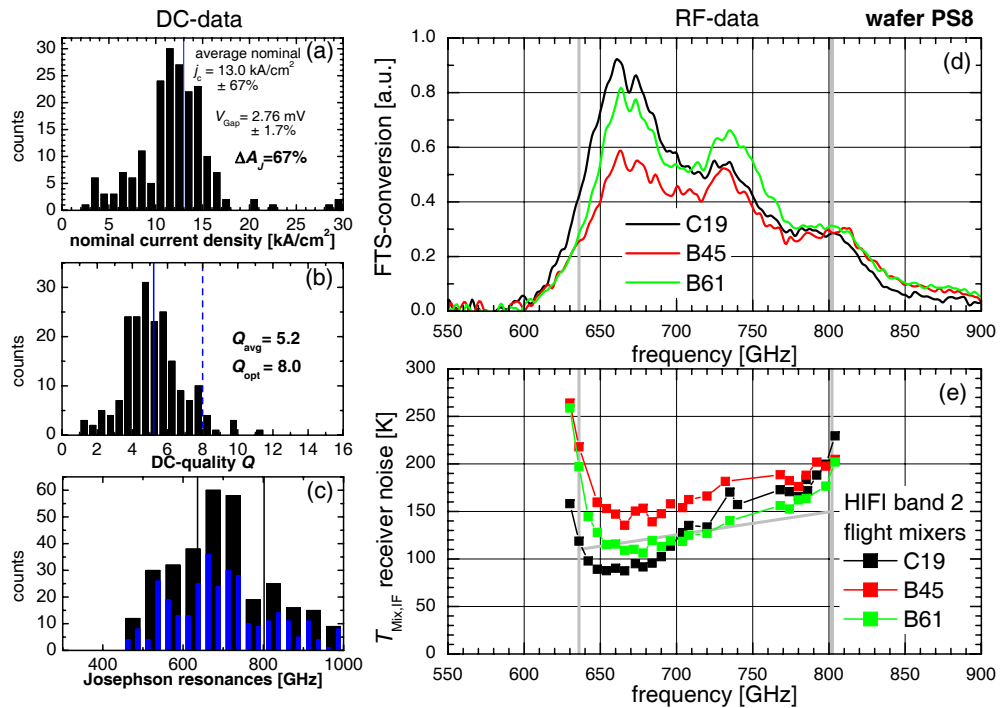


Fig. 4.14: Characteristic parameters for wafer PS8 in plots (a) to (c). RF-performance of the FM-mixers (d) and (e), acquired in the FM-dewar with the corresponding correction for the optics components (see Appendix C).

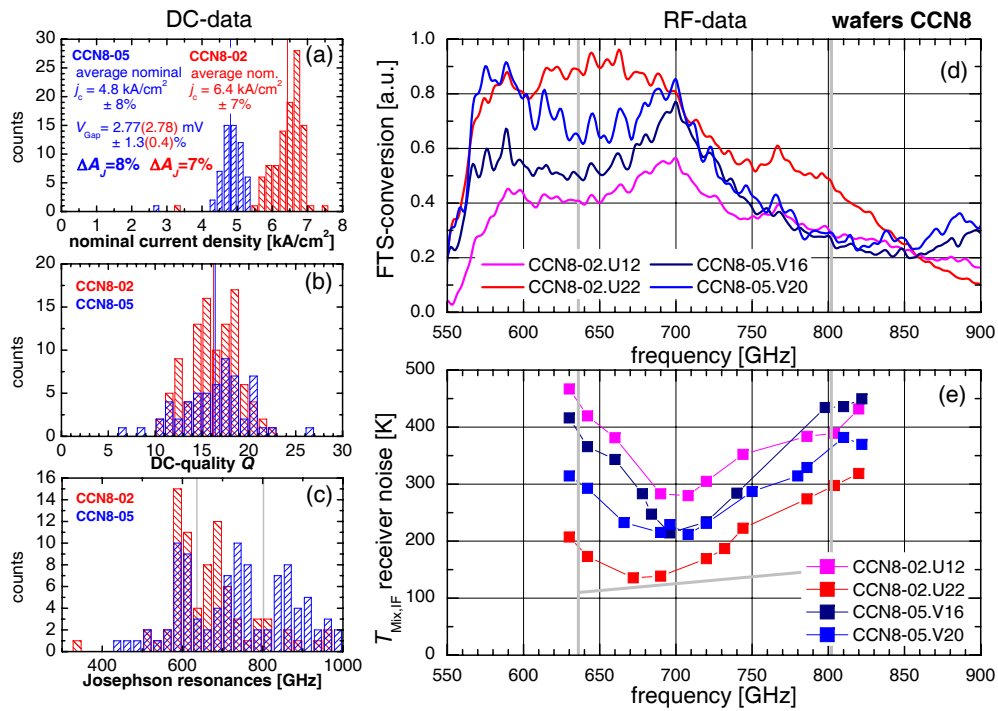


Fig. 4.15: Characteristic DC-parameters for wafers CCN8-02 and CCN8-05 in plots (a) to (c). RF-performance of four measured mixers (d) and (e), acquired in the test-dewar.

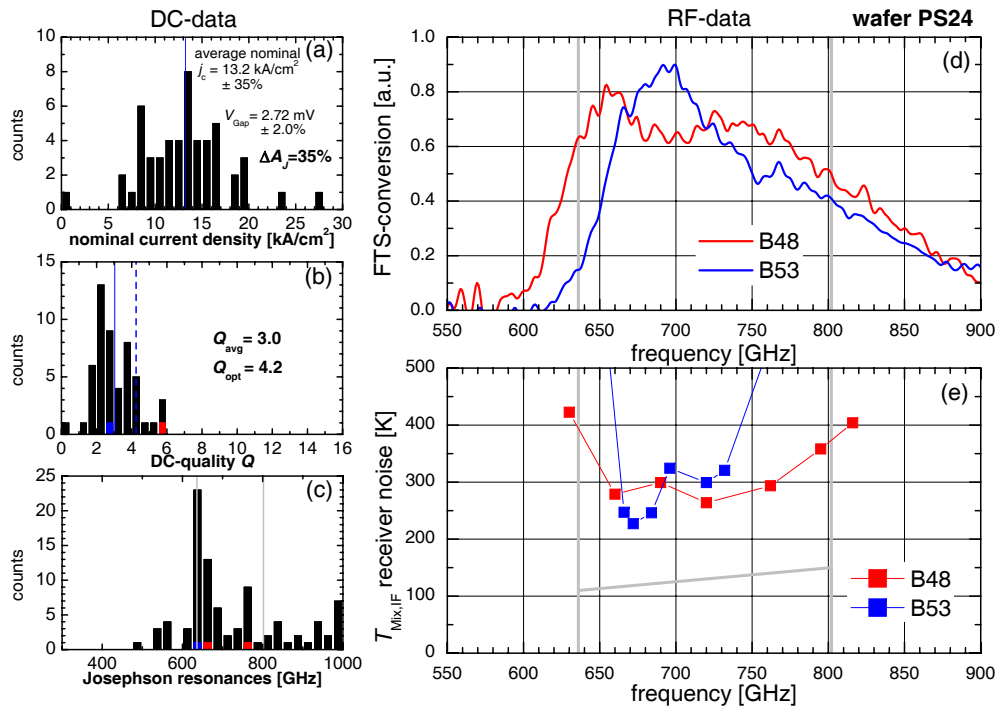


Fig. 4.16: Characteristic DC-parameters for wafer PS24 in plots (a) to (c). Two mixers from this wafer have been characterized with FTS-measurements (d) and heterodyne measurements (e).

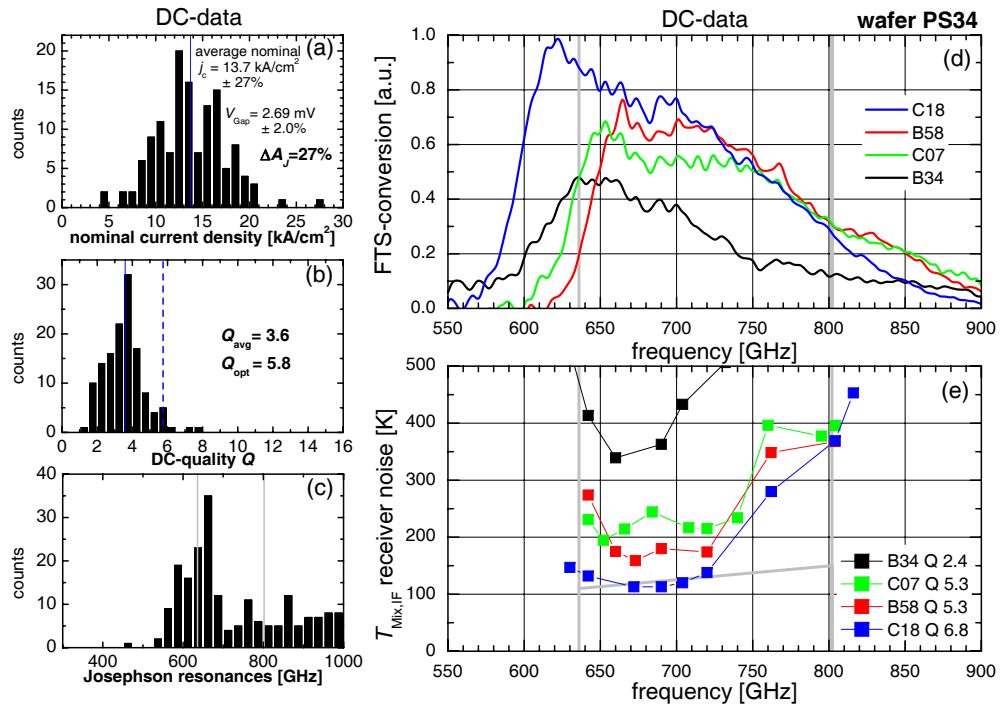


Fig. 4.17: Characteristic parameters for wafer PS34 in plots (a) to (c). Four mixers from this wafer have been characterized with FTS-measurements (d) and heterodyne measurements (e). The given values for Q in (e) are measured inside the heterodyne setup.

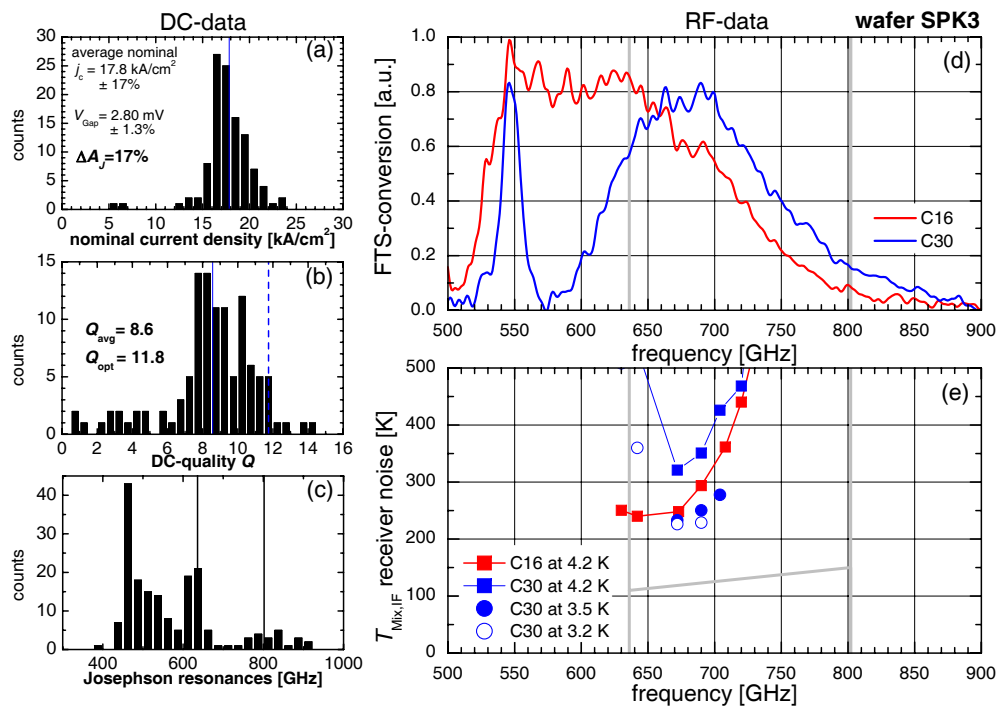


Fig. 4.18: Characteristic DC-parameters for wafer SPK3 in plots (a) to (c). Two mixers from this wafer have been characterized with FTS-measurements (d) and heterodyne measurements (e).

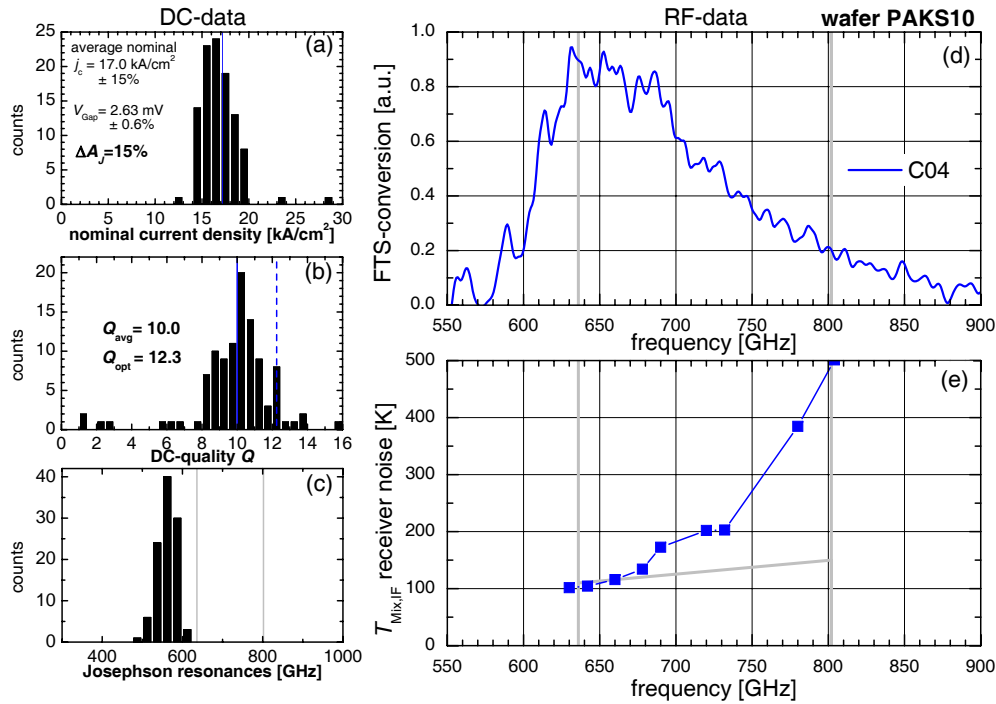


Fig. 4.19: Characteristic DC-parameters for wafer PAKS10 in plots (a) to (c). One mixer with the device of highest Q from the candidates showing a Josephson resonance frequency above or at 600 GHz has been characterized with a FTS-measurement (d) and a heterodyne measurement (e).

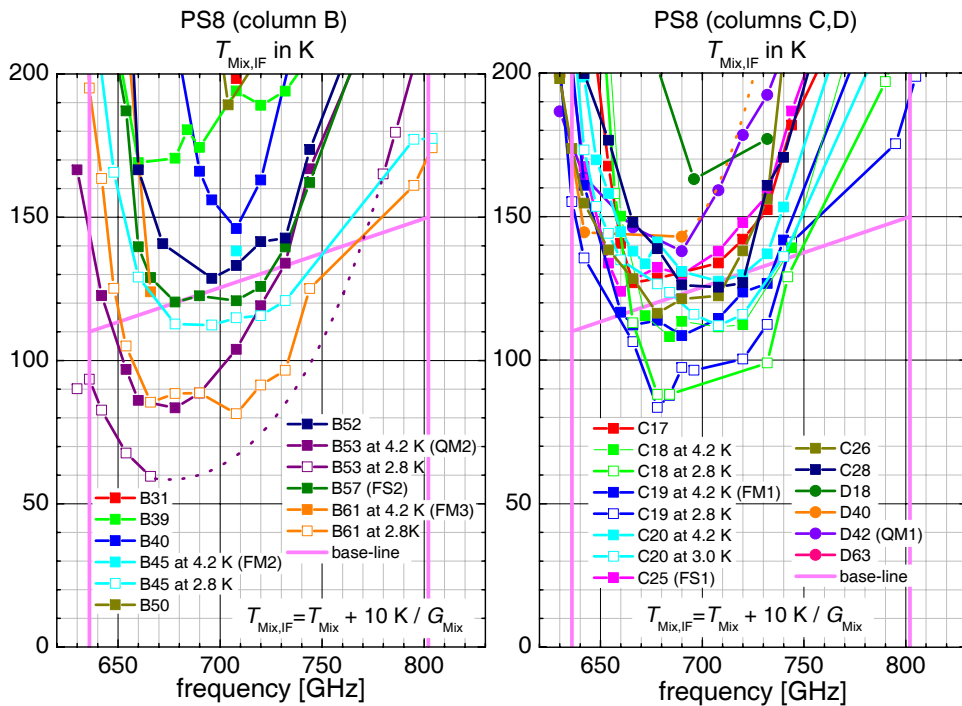


Fig. 4.20: Measured noise performance $T_{\text{Mix,IF}}$ for all characterized mixers of PS8. Nine devices (B45, B53, B57, B61, C18-C20, C26, C28) show a performance below the baseline; QM: qualification model, FM: flight model, FS: flight spare; data acquired in the test-dewar (see App. C).

4.4 Detailed comparison of three selected wafers

In this section a detailed data interpretation is presented for the wafers PAKS10, SPK3 and PS8. Here the same methods are applied, which are used during the selection of devices for RF-measurements.

The purpose of all methods is to choose, based on measurement data and analysis, the best devices of a wafer. Therefore a good estimate of the power coupling from the the DC-characteristics of the device must be made. Here the simplified model, which has been presented in Chap. 3, is also used. The analysis starts with an estimation, as accurate as possible, of the junction area A_J and j_c . The results of this analysis also have been used as input for the optimization of the parameters in the next fabrication run, especially for the compensation of the junction under-etching and the target value for j_c .

First, in Subsec. 4.4.1 three methods used for the data interpretation are presented. Then, in Subsec. 4.4.2 three wafers are explicitly analyzed. Here it is illustrated why, in spite of a relatively high DC-quality of wafers PAKS10 and SPK3, it could be excluded to find competitive mixer devices from these wafers after a few measurements. In the analysis of PS8 it is illustrated how tight tolerances are required for the fabrication of SIS-devices, which are compliant with the HIFI performance requirements.

4.4.1 Data interpretation methods

The RF-characterization of a SIS-mixer takes a few days despite the general preparation of the measurement setup and infrastructure. Therefore the decision for this measurement and the selection of the SIS-device is important. With the presented interpretation methods the expected performance in terms of power coupling is estimated for some promising devices. And again, after the RF-measurement the estimates are revisited.

The first two interpretation methods are based on the DC-measurements of a large number of devices of a wafer. First, based on the data for all devices of a wafer the most probable wafer current density j_c is evaluated with a linear fit (Subsec. 4.4.1.1). This allows an estimate of the calculated band-pass for specific devices. The second method (Subsec. 4.4.1.2) is the analysis if the Josephson resonance frequencies, which mark the region of optimum power coupling. And finally based on the FTS-measurement of a few single SIS-mixers a more accurate estimate of its current density is obtained (Subsec. 4.4.1.3). This allows a more reliable prediction for the optimum power coupling for other devices of the same wafer.

4.4.1.1 Estimation of j_c from a linear fit of the DC-measurement data

After the DC-measurements of a wafer the current density j_c

$$j_c = \frac{\pi}{4} \cdot \frac{V_{\text{Gap}}}{R_N \cdot A_J} \quad (4.8)$$

(compare Eq. 2.16) is the most uncertain parameter. Unfortunately an estimate of the area from a microscopic inspection of the device cannot be done with an accuracy better than 50% because the edges of the junction cannot be determined accurately through the wiring layer [13].

The analysis of j_c based on statistical approaches is based on the assumption that the current density is the same for all SIS-devices on a wafer. Two approaches are

1. to evaluate the mean value $\langle j_{c,\text{nom}} \rangle$ for all DC-characterized junctions
2. to apply a linear regression to $(x, y) = (A_{J,\text{nom}}, \frac{\pi}{4} \cdot \frac{V_{\text{Gap}}}{R_N})$, where j_c results is the slope and an average constant offset in area ΔA_J is obtained (compare [14]).

The first approach averages statistical variations, but does not include systematical offsets in junction area. The second approach results in a constant offset in junction area, which is not viewed to be optimum for different nominal junction areas on a wafer.

In order to model the under-etching as a linear effect in x- and y-direction a linear regression of the parameters $x_i = l_{J,i} = \sqrt{A_{J,i}}$ and $y_i = \sqrt{\pi \cdot V_{\text{Gap},i}/4 \cdot R_{N,i}}$ has been applied. Then $\sqrt{j_c}$ is the proportionality factor and an average offset in junction width Δl_J is obtained.

This analysis has been applied for several wafers, and the application to wafer PS8 is presented in Fig. 4.21⁸.

The accuracy of this method depends on the relative accuracy in junction area and the number of available devices. With this method j_c is determined with an error less than 30%. At the same time a rough estimate for a linear offset in junction width Δl_J has been found. For the example of PS8 there is no indication for a systematical offset in junction width.

The limitation of this analysis is that it is based on the extrapolation of data with a wide spread, thus causing large error bars. And it implicitly is based on the assumption that the function $G(l_J)$ with

$$l_{J,\text{real}} = G(l_{J,\text{nom}}),$$

⁸For the double junction devices the nominal junction width of one junction and the double of the measured normal resistance R_N has been taken. If the "real" junction area $2 \cdot l_J^2$ and the measured R_N is included the double junction devices obtain an unwanted large weight for the linear regression.

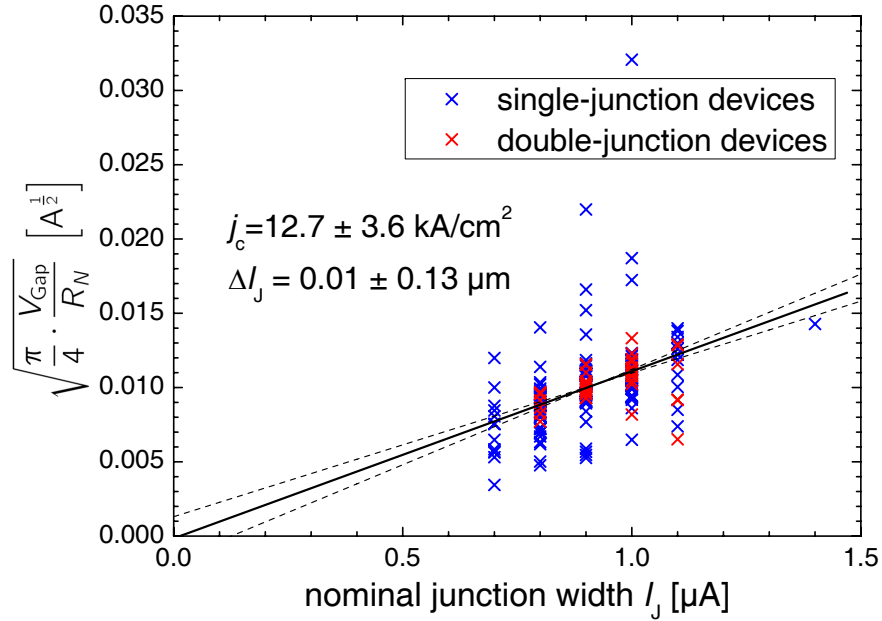


Fig. 4.21: Linear fit for the estimation of the current density j_c and a systematical offset in junction width l_J of wafer PS8 from the DC-measurements.

is not only linear but is assumed to fulfill the relation

$$\frac{\Delta G(l_J)}{\Delta l_J} = 1.$$

This need not necessarily be the case [80]. But since no other information of the real junction areas is known, this analysis has been applied to obtain an estimation for the current density of the wafer and a possible geometry offset.

4.4.1.2 Estimation of the band-pass from the DC-measured Josephson resonances

For the illustration of this method, the analysis of the Josephson resonance frequencies ν_{res} is performed for the three FM mixers and a mixer which shows optimum coupling for very low frequencies. In the plots in Fig. 4.22 DC I-V-curves measured in the dipstick setup (black data points) and in the heterodyne setup (red data points) are presented. The black vertical lines denote the Josephson frequencies from the first DC-measurement. Added are the later FTS-measurements which are not available during the device selection phase. They specify the actual band-pass of the devices in the mixer block.

In general it must be stressed, that the Josephson resonances in the DC-measurement setup and the heterodyne setup comply quite well⁹. The DC-measurements in the dipstick setup are performed in the current sweep mode,

⁹This need not naturally be the case, because the embedding impedances for the junction

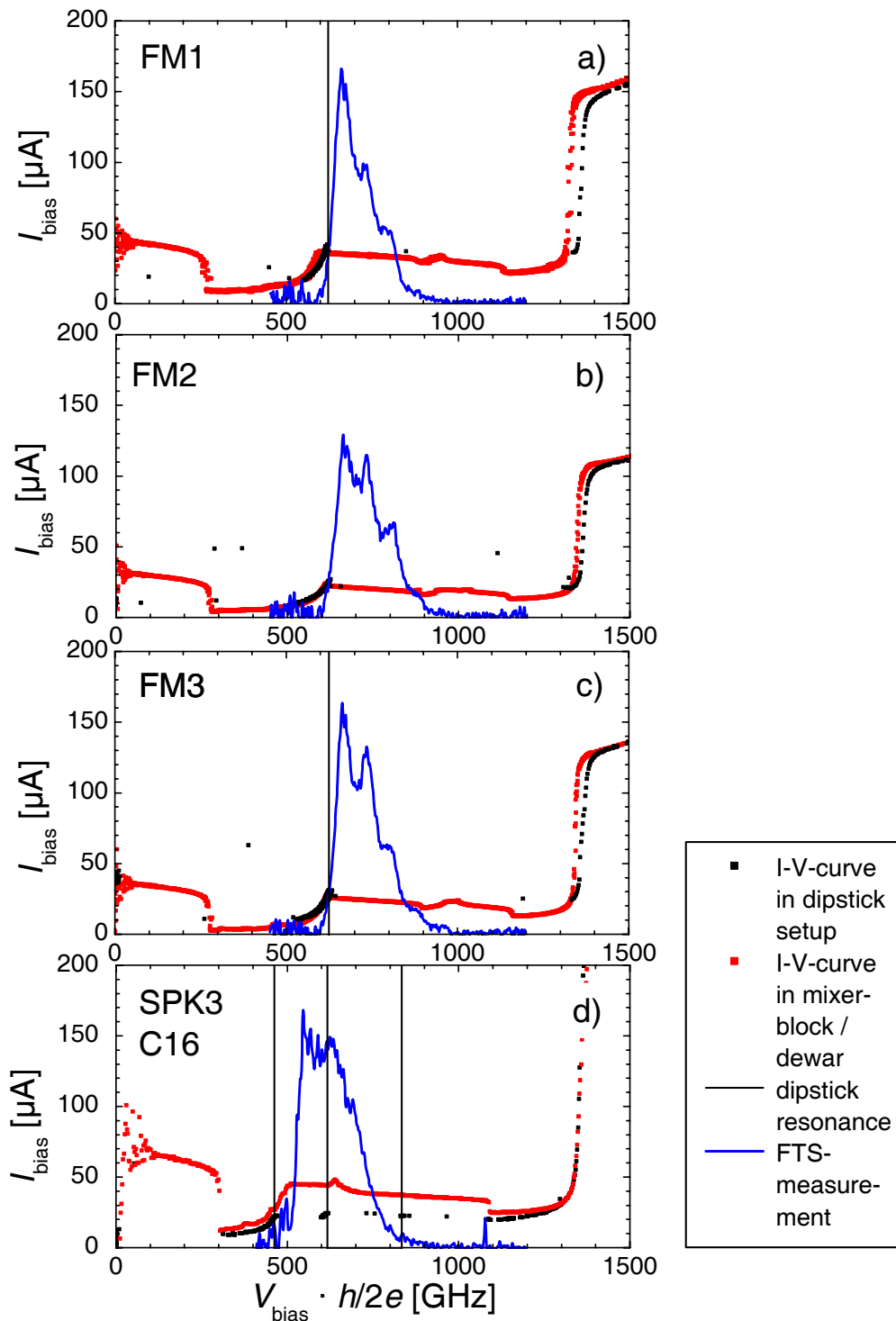


Fig. 4.22: Analysis of the Josephson resonance frequencies for four devices. The Josephson resonances measured in the dipstick-setup are verified in the heterodyne setup. Usually the Josephson resonances mark the lower edge of the frequency band. Resonance frequencies in the dipstick-setup close to the waveguide cut-off frequency are shifted to higher frequencies in the heterodyne setup (plot (d) for SPK3 C16).

design have been calculated utilizing the simulated waveguide impedances of the waveguide probe inside the mixer block. In the dipstick setup the device on the substrate is surrounded by an open (helium filled) half space.

because no voltage sweep control has been available. Thus the shape of the I-V-curve just above a resonance is not resolved. With the heterodyne setup operated in voltage sweep mode, the exact shape of the I-V-curve below the gap is specified. Resonances above 800 GHz may marginally be identified in the FTS-spectrum, because the absolute amplitude is largely reduced due to the RF-coupling losses. The comparison of the Josephson resonances for these three mixers with the FTS-response shows, that the resonance frequencies mark the lower edge of the mixer's direct detection band pass.

The fourth device SPK3 C16 (Fig. 4.22 (d)) showed a very low Josephson resonance in the dipstick-setup at 460 GHz. It is right at the cut-off frequency of the waveguide. Accordingly the lower edge of the frequency band, specified by the FTS-spectrum, and the measured Josephson-resonance in the mixer block are shifted to ≈ 500 GHz. The second resonance at 620 GHz, which has been identified in the dipstick setup, has been verified from the measurement in the mixer-block and is identified as a maximum in the FTS-response. The third weak resonance at 830 GHz was not observed in the I-V-curve in the mixer-block, but as a small maximum in the FTS-measurement.

Many devices do not show as clear maxima as the four discussed devices. But from the RF-characterized devices the strong relation between DC-resonances and RF-coupling is demonstrated.

This analysis also illustrates that the Josephson resonances yield an accuracy of 20-40 GHz for the identification of the lower frequency edge of the band-pass and possibly additional maxima in power coupling.

4.4.1.3 Estimation of critical current density j_c from FTS-measurement

Based on the analysis of the DC-parameters a few devices are mounted in a mixer block and characterized with a FTS-measurement. From this measurement the current density of the specific device (and by assumption of the whole wafer) can be deduced from a fit of the FTS-spectrum with the calculated coupling.

Assumption of perfect micro-strip geometry: The method is illustrated for the three characterized flight-mixers. In Fig. 4.23 the measured FTS-conversion for the three mixers is plotted as the black line and hatched area, together with the calculated coupling. Included in the calculations are the measured DC-parameters of the junction V_{Gap} and R_N and the measured quality of the NbTiN-groundplane ρ_n and T_c . The current density j_c and thus, by keeping R_N equal to the measured value, implicitly the junction area A_J is varied. Possible deviations in this parameters are discussed below. The underlying data for the three calculations are given in Table 4.2.

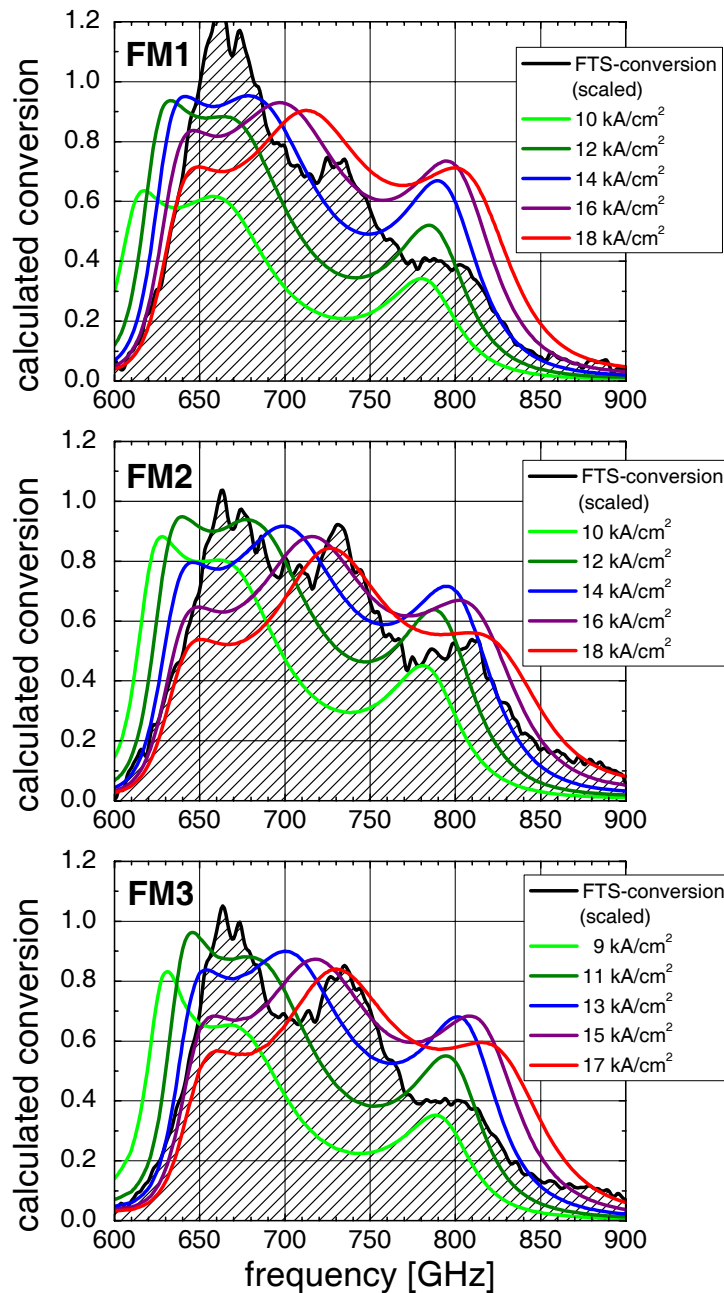


Fig. 4.23: Comparison of calculated power coupling for measured DC-parameters with the FTS-measurement. For the three FM-mixers this results in a current density of 13-14 kA/cm².

From the given calculated band-pass in Fig. 4.23 for the three mixers the current density j_c has been specified with an accuracy of ± 1 kA/cm². The results for the current density are 14 kA/cm² (FM1, FM2) and 13 kA/cm² (FM3).

Effect of micro-strip geometry offsets: One factor, which also determines the actual band-pass and thus the accuracy of the fitted j_c is the geometry of

	j_c [kA/cm ²]	R_N [Ω]	V_{Gap} [mV]	A_J [μm ²]	NbTiN	
					ρ_N [μΩcm]	T_C [K]
FM1 design	15	17.9	2.77	(0.9) ²	100	14.7
FM1 meas.	14*	18.9	2.715	(0.76) ² *	80	13.8
FM2 design	15	22.7	2.77	(0.8) ²	100	14.7
FM2 meas.	14*	26.3	2.71	(0.76) ² *	80	13.8
FM3 design	15	22.7	2.77	(0.8) ²	80	14.9
FM3 meas.	13*	20.7	2.715	(0.89) ² *	80	13.8

Tab. 4.2: Data for calculations in Fig. 4.23. For the design calculation the parameters j_c , V_{Gap} , A_J , R_N and the quality parameters of NbTiN are defined by the mask design (NbTiN3). For the calculation based on the measured data, ρ_N and T_C are the parameters for NbTiN measured for the whole wafer. The parameters for R_N and V_{Gap} are measured in the dewar. The values, marked with a star (*) are the results of the j_c -fit in Figure 4.23.

the matching circuit. To quantify this effect, in Fig. 4.24 the parameters Δl for the relative positioning accuracy and Δw for an offset in the micro-strip widths have been defined.

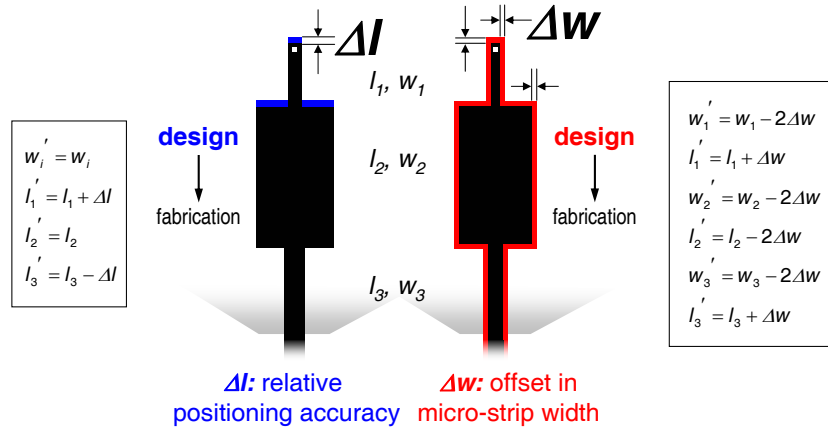


Fig. 4.24: Possible offsets in matching circuit geometry. Left: shift Δl of complete top-wiring layer with respect to the ground-plane and junction position. Right: changes in micro-strip width Δw due to under-etching or exposure parameters.

For the actual relative alignment Δl an accuracy of $\pm 0.5 \mu\text{m}$ is achieved, while the accuracy in micro-strip width Δw with UV-lithography is $\pm 0.3 \mu\text{m}$ [13]. In order to compensate an offset of $\Delta l = 0.5 \mu\text{m}$ the fitted current density j_c has to be corrected by $\Delta j_{c,l} = 1.5 \text{ kA/cm}^2$. The offset of $\Delta w = 0.3 \mu\text{m}$ results in a correction for the fitted j_c of $\Delta j_{c,w} = 2 \text{ kA/cm}^2$. Together with the accuracy of the j_c -fit for a perfect micro-strip geometry of $\Delta j_{c,0} = 1 \text{ kA/cm}^2$ this results in the **accuracy for the j_c -fit**

$$\Delta j_c = \sqrt{(\Delta j_{c,0})^2 + (\Delta j_{c,l})^2 + (\Delta j_{c,w})^2} = 2.7 \text{ kA/cm}^2. \quad (4.9)$$

This accuracy can not be improved by the inspection of device photographs,

because the edge of the microstrip itself has a width of $\approx 0.8 \mu\text{m}$.

4.4.2 Analysis results for three selected wafers

In this subsection, the analysis presented in the previous subsections is applied for three wafers: PAKS10, SPK3, PS8.

The detailed analysis of PAKS10 (Subsec. 4.4.2.1) has resulted in a rejection of this wafer even after the RF-measurement of only one device because of the systematical shift in junction area that was identified in the analysis. With the detailed analysis of SPK3 (Subsec. 4.4.2.2) it is illustrated how a major change in the fabrication concept (exchange of NbTiN ground-plane and Nb top-wiring) also has affected the measured noise performance. For the analysis of the most successful wafer PS8 four devices are examined, which have been designed with the identical matching circuit and have been fabricated with slightly different junction areas. The comparison of the resulting noise performance illustrates the tight tolerance requirements to the junction area when the ambitious HIFI performance requirements have to be achieved (Subsec. 4.4.2.3). It is illustrated that with the given fabrication tolerances the concept of variations in the device designs on the lithography mask sets together with the applied selection methods have been key components to obtain SIS-devices compliant with the performance requirements.

4.4.2.1 Example PAKS10: Rejection due to oversized junction area

If the DC-parameters of wafer PAKS10 are examined (Fig. 4.19 (a) and (b) on page 97, Fig. 4.8 on page 88) they positively show the optimum value for the spread in junction area ($\Delta A_J/A_J = 15\%$) and the optimum values for the DC-quality (average: 10, optimum: 12). But if the Josephson resonance frequencies are examined (Fig. 4.19 (c), Fig. 4.9, p. 89) they are below the desired frequency band. This from the first impression is attributed to a significant shift to larger areas. This impression is confirmed from the following detailed analysis.

The analysis of wafer PAKS10 is divided into two parts. First the analysis is presented, which has been done after the DC-measurements for the selection of the optimum device. In the second part the analysis of the RF-measurements are presented, which comply in general with the results of the DC-measurement analysis.

Estimation of the band-pass for DC-characterized devices of PAKS10:

In Fig. 4.25 (a) the linear fit for the DC-measurements of the wafer is shown. It yields a quite low result for the j_c around 10 kA/cm^2 and implies that the junction widths in average are $0.26 \mu\text{m}$ larger than designed.

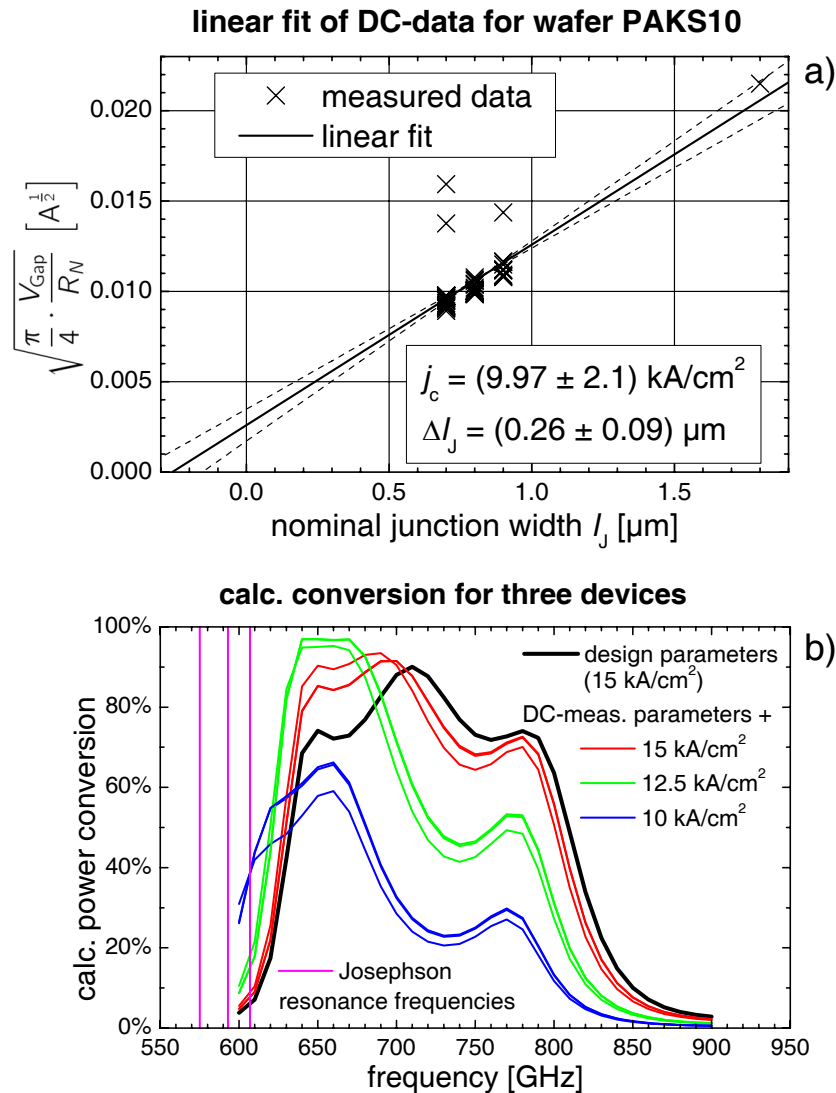


Fig. 4.25: Analysis of the DC-measurements for wafer PAKS10. **a)** the linear fit for the DC-measurement data yields estimations for j_c and Δl_j . **b)** Calculated conversion for three identical designed devices based on the measured DC-parameters with variation of current density j_c . The low Josephson resonance frequencies around 600 GHz are most consistent with the calculated band-pass for $j_c = 10 \text{ kA/cm}^2$. The underlying data are found in Tables 4.3 and 4.4.

After the DC-characterization of PAKS10 the device C04 has been a candidate for RF-measurements because of its relatively high value for the DC-quality Q of 9.5. It also shows a relatively high Josephson resonance frequency of 590 GHz, while most devices of the wafer show lower Josephson resonances.

In Fig. 4.25 (b) the calculated power coupling for the identical designed devices C04, C05, C06 is shown (according to the device model, presented in Chap. 3). The design parameters for these three devices are given in Table 4.3. The design band-pass is plotted as the black line and shows the shape

	device	$V_{\text{Gap}}[\text{mV}]$	$R_N[\Omega]$	NbTiN		$j_c[\text{kA}/\text{cm}^2]$	$l_J[\mu\text{m}^2]$
				$\rho_n[\mu\Omega\text{cm}]$	$T_c[\text{K}]$		
design	all 3	2.75	29.4	80	15.5	15	0.7
meas.	C04	2.63	25.1	70	15.0	$\leq 10^*$	$\geq 0.908^*$
	C05	2.64	24.3				$\geq 0.926^*$
	C06	2.61	24.9				$\geq 0.907^*$

Tab. 4.3: Design parameters for devices C04, C05, C06 from wafer PAKS10, together with the results of the DC-measurements. Values for j_c and l_J marked with * are obtained from the comparison of the calculated band-pass with the Josephson resonance frequencies in Fig. 4.25 (b).

of a broad-band design.

Then in the same calculation the design values for V_{Gap} and R_N have been replaced by the measured values, but the current density design value of $15 \text{ kA}/\text{cm}^2$ has not yet been changed. The resulting band-passes for the three devices are given in 4.25 (b) as red lines¹⁰. The corresponding parameters for the junction width l_J evaluated from

$$A_J = l_J^2 = \frac{\pi}{4} \cdot \frac{V_{\text{Gap}}}{R_N \cdot j_c} \quad (4.10)$$

are given in Table 4.4 and are just above the design value of $0.7 \mu\text{m}$.

device:	C04	C05	C06	$j_c[\text{kA}/\text{cm}^2]$
$V_{\text{Gap}}[\text{mV}]$	2.63	2.64	2.607	
$R_N[\Omega]$	25.1	24.2	24.9	
$l_J[\mu\text{m}]$	0.741	0.756	0.741	15.0
$l_J[\mu\text{m}]$	0.812	0.828	0.811	12.5
$l_J[\mu\text{m}]$	0.908	0.926	0.907	10.0

Tab. 4.4: Values for V_{Gap} and R_N from DC-measurements of devices C04, C05, C06 on wafer PAKS10. Resulting junction widths l_J according to Eq. 4.10 for these devices assuming the values for j_c given in column 5.

The same calculation has been evaluated for current densities of 12.5 and $10.0 \text{ kA}/\text{cm}^2$. The band-passes are also plotted in Fig. 4.25 (b) and the resulting values for l_J for the three devices are given in Table 4.4.

The calculation with the most probable value of $j_c = 10 \text{ kA}/\text{cm}^2$ implies that the optimum coupling for the three devices is just above 600 GHz and the power coupling strongly decreases for higher frequencies. This assumption for j_c also complies with the measured Josephson resonance frequencies, which are known to mark the lower edge of the frequency band (see Subsec. 4.4.1.2). The corresponding shifts in junction width, which are given in Table 4.4 (last row), imply that these three junctions have an actual junction width of $0.90 - 0.92 \mu\text{m}$ instead of the designed $0.7 \mu\text{m}$.

¹⁰Because of the only marginal difference in R_N and V_{Gap} for C04 and C06 the curves for these devices can not be distinguished. The same is true for $j_c = 12.5, 10 \text{ kA}/\text{cm}^2$.

The estimate of the band-pass for these devices, which results from the linear fit of the DC-data and the resulting j_c is quite consistent with the measured Josephson resonance frequencies. From this analysis it has been expected, that the noise performance of the device C04 shows optimum coupling below 650 GHz and a strong decrease in coupling efficiency with increasing frequency.

Current density and junction area analysis for PAKS10 from FTS-measurements: The RF-measurements of PAKS10 C04 (Fig. 4.19) show optimum coupling and low noise ($T_{\text{Mix,IF}} = 100 \text{ K}$) at the lower band edge and a decrease in power coupling with an increase in noise for increasing frequency ($T_{\text{Mix,IF}} = 500 \text{ K}$ at 800 GHz).

A fit of the calculated conversion for C04 to the measured FTS-conversion is shown in Fig. 4.26. The conversion for the design parameters shows again

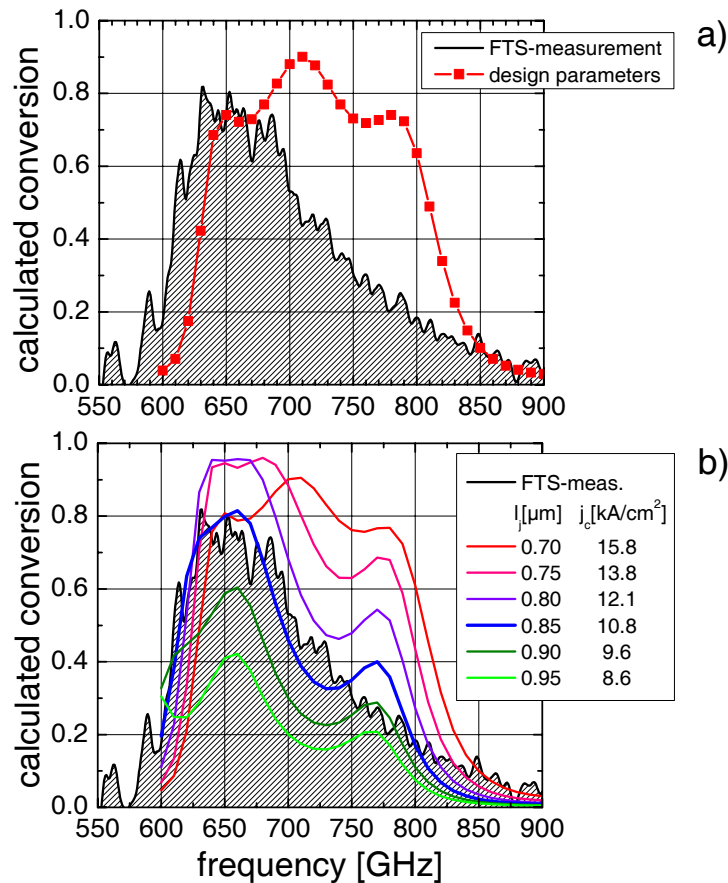


Fig. 4.26: Comparison of calculated Band-pass and FTS-measurement for mixer PAKS10 C04; top: Calculated conversion for design parameters (red) and measured FTS-spectrum; bottom: calculated conversion for measured V_{Gap} , R_N with variation of junction area A_J and current density j_c .

the broad-band type, while the measured FTS-conversion shows a maximum

conversion around 650 GHz (Fig. 4.26 (a)). To estimate the shift in junction width l_J in Fig. 4.26 (b) the calculated conversion for the measured DC-data V_{Gap} , R_N and for estimated quality data of NbTiN ($\rho_n=80 \mu\Omega\text{cm}$, $T_c=15 \text{ K}$) is given. The junction width is step by step is varied from the design value of $0.70 \mu\text{m}$ to $0.95 \mu\text{m}$. The corresponding values for j_c according to Eq. 4.10 are given in the legend of the figure. From this analysis the shift in junction width is $(1.5 \pm 0.5) \mu\text{m}$ and the value for j_c is estimated to $(11 \pm 1) \text{ kA/cm}^2$.

Conclusion: Together with the result for Δl_J from the fit to the DC-data of the whole wafer the result for the linear offset in junction width is $\Delta l_J = 0.2 \mu\text{m}$. This strongly suggests, that the fabrication concept PAKS in general because of its relatively large values in Q and high relative junction area accuracy is very promising. But for this specific fabricated wafer the significant offset in junction area has been evaluated to be the exclusion criterion for other devices of this wafer with respect to the HIFI performance requirements.

4.4.2.2 Example SPK3: Rejection due to reduced effective micro-strip quality

The fabrication concept SPK already has been sketched in Subsec. 4.3.3 and is documented in [13]. The ground-plane (NbTiN) and top-wiring layer (Nb) have been exchanged, to simultaneously use the Nb-layer as lower superconductive electrode. By this means the etching of the insulating barrier and the lower superconductive electrode is avoided resulting in larger values for the DC-quality Q of the junctions. But this also implies that the NbTiN is not sputtered on a heated substrate and is expected to show a lower quality.

The analysis of the DC-measurements of the wafer results in a fit for the current density of $13\text{-}14 \text{ kA/cm}^2$ and a linear offset in junction width Δl_J of $0.1 \mu\text{m}$ ($\pm 100\%$). This implies, that the junctions in average are expected to be marginally too large. The significant shift of the Josephson resonance frequencies to very low values (Fig. 4.18 (c) on page 96, Fig. 4.9 (a) on page 89) suggests, that an additional effect is responsible for the low resonance frequencies. It could be expected, that a decreased quality of the NbTiN-layer is responsible for this shift. But the DC-measured values ($\rho_n=90 \mu\Omega\text{cm}$, $T_c=15.3 \text{ K}$) of the NbTiN-quality do not dramatically deviate from the design parameters ($80 \mu\Omega\text{cm}$, 14.9 K).

The analysis of the FTS-measurement of device C30: Two devices of wafer SPK3 have been characterized with RF-measurements. In spite of their comparably good DC-quality measured in the DC-measurement setup (C16:

10.4, C30: 7.5), they show an optimum noise performance around twice the HIFI baseline (compare Fig. 4.18 on page 96). The optimum power coupling is in the lower part of the frequency band and even below.

In Fig. 4.27 the band-pass of device C30 is analyzed based on the FTS-measurement and power coupling calculations. In Fig. 4.27 (a) the data of the

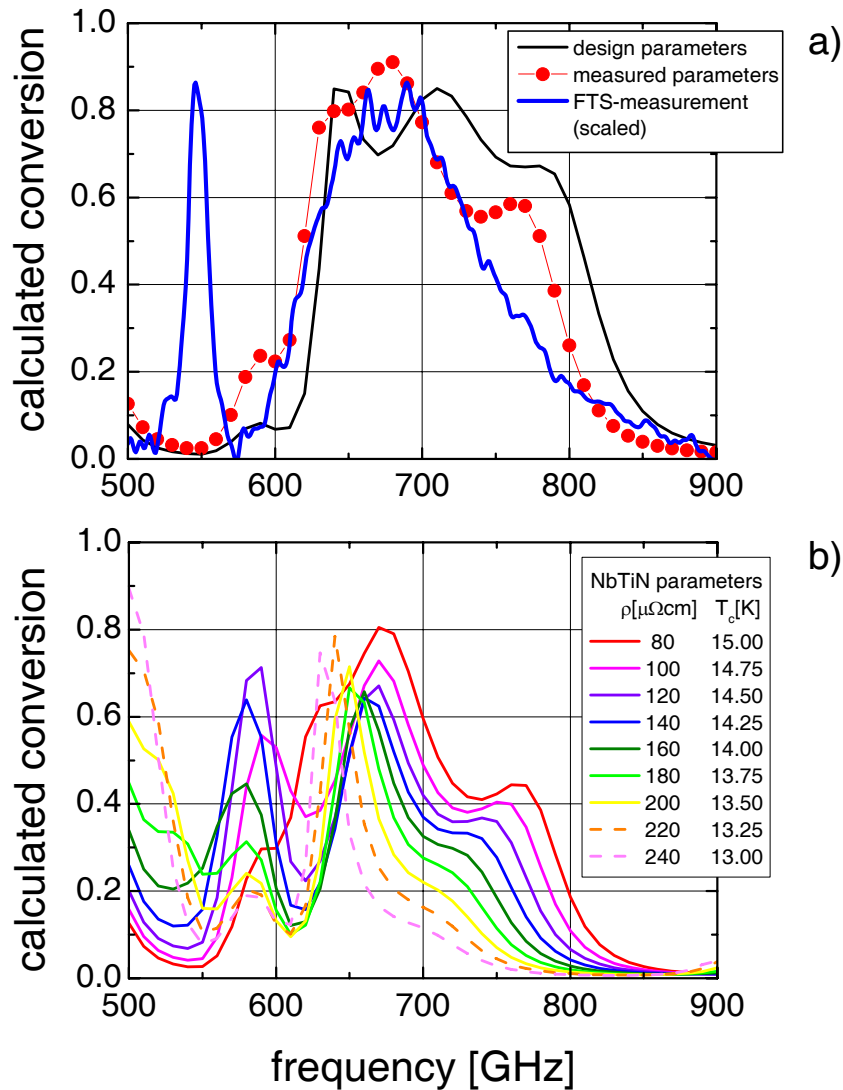


Fig. 4.27: Calculated conversion and FTS-measurement of SPK3 C30. Top: calculated conversion with design parameters (black line) and measured parameters for V_{Gap} , R_N , ρ_{NbTiN} , $T_{c,NbTiN}$ and an assumed j_c of 13 kA/cm^2 (red lines and points); FTS-response (blue line, scaled). Bottom: variation of top-wiring NbTiN parameters.

FTS-measurement are plotted as the blue line, while the designed band-pass of this device is plotted as black line. The same band-pass calculation has been performed with the measured DC-data of the device and the NbTiN-quality, resulting in the data, plotted as red lines and points. For this calculation a j_c of 13 kA/cm^2 has been assumed to possibly explain the shift to lower

	j_c [kA/cm ²]	R_N [Ω]	V_{Gap} [mV]	A_J [μm ²]	NbTiN	
					ρ_N [μΩcm]	T_C [K]
design	15	22.7	2.77	(0.80) ²	80	14.9
meas.	13*	16.5	2.69	(0.98) ²	90	15.3

Tab. 4.5: DC-parameters for SPK3 C30. The design parameters are defined in the mask design NbTiN3. The values for R_N and V_{Gap} are acquired in the heterodyne setup. The value for j_c of 13 kA/cm² is a rough guess from previous wafers.

frequencies. The underlying data are given in Table 4.5. Based on these data the calculated band pass roughly complies with the measured FTS-response above 600 GHz. But the significant maximum in power coupling at 550 GHz can not be explained, also not from additional variations in j_c .

Reduced effective layer quality: In order to analyze the origin of the measured resonance at 550 GHz the influence of the NbTiN-quality on the calculated power coupling is studied. Since the NbTiN is sputtered as top-wiring and not as ground-plane on the heated substrate, it is expected to show lower quality parameters. The measured DC-data for NbTiN are given in Table 4.5. No significant changes in the DC-parameters with respect to the design parameters are seen. Nevertheless these measured DC-parameters might not represent the RF-conductivity of the NbTiN-layer. The penetration depth of NbTiN (≈ 300 nm) is of the same order as the layer thickness (350 nm). But the field is most concentrated at the interface with the dielectric. This part probably does not show the same quality, as specified by the DC-quality measurements. It is unlikely that the DC-parameters are much influenced by the first tens of nm of the layer that may be of worse quality, if the following 250 nm are of better quality. This is just modeled by an effective NbTiN quality, which is assumed to be lower than the measured DC-parameters.

In Fig. 4.27 (b) the quality of NbTiN is modeled by effective parameters of normal resistivity ρ_n and critical temperature T_c . In general ρ_n and T_c are independent parameters, but from experience it is seen, that a high T_c corresponds to a low ρ_n . For the sake of simplicity a linear relation of these two parameters has been assumed and the parameters have been varied from (80 μΩcm, 15 K) to (240 μΩcm, 13 K). For resistivity values around 120 to 140 μΩcm a maximum in power coupling below 600 GHz is seen very similar to the measured FTS-response. There is still an absolute offset in frequency of the measured and calculated power coupling of ≈ 20 GHz. But the simulation with lower NbTiN-quality fits the measured behavior much better. Possible differences in calculated power coupling arise from the gradient in ρ_n in the NbTiN-layer. Also the reliability of the waveguide impedance data decreases as the considered frequency approaches the cut-off frequency of the waveguide.

If the parameters ρ_n and T_c are varied individually no significant change of the effect is seen. If only T_c is varied, only the relative size of the two resonances are changed.

Conclusion for SPK3: The major problem with the fabrication concept SPK is viewed to be the higher effective value for ρ_n of the NbTiN top-wiring. On the other side this fabrication concept has shown the best values for the junction DC-quality Q , relative junction accuracy $\Delta A_J/A_J$ and junction yield in comparison with the previous fabricated wafers. For future applications it could be worthy to utilize this fabrication concept with dedicated matching circuits based on the nominal $\rho_n = 140 \mu\Omega\text{cm}$ for NbTiN. Within the scope of the HIFI project this concept was not continued.

4.4.2.3 Example PS8: Acceptance of devices for flight mixers

Based on the presented interpretation methods the superior noise performance of the devices from wafer PS8 is related to their fabrication parameters. These fabrication parameters (j_c , Q , junction area, NbTiN-quality) are not in general superior to the other wafers. But for this wafer they are all in the desired range at the same time. The most relevant parameters are

- a large DC-quality Q , which is related to a low sub-gap current and thus a low intrinsic noise of a device, this has been a challenge especially at the beginning of the HIFI band 2 mixer fabrication,
- the NbTiN-quality has to be within the given range of the underlying mask design ($T_c = 14 \pm 1 \text{ K}$, $\rho_n = 70 \pm 10 \mu\Omega\text{cm}$), this usually has been achieved for most of the wafers.
- the junction area turned out to be the most critical parameter in order to exactly hit the desired frequency band. Its accuracy has to be below 5%. Variations in junction area immediately result in shifts of the band-pass and have been the exclusion criterion for many of the rejected wafers. Thus an illustration for the sensitivity of the frequency band with junction area is given below.

The devices of PS8 show a relatively large spread in junction area (67%, compare Fig. 4.14 on page 94). But from the analysis of the current density and the junction area offset (see Subsec. 4.4.1.1 and 4.4.1.3) it has been concluded that with this spread the junction areas are fabricated centered around the design values.

In order to illustrate the sensitivity of the noise performance of a mixer for variations in junction area, the noise performance of four mixers on wafer PS8 with the same designed matching-circuit is presented. Devices C17 - C20 are

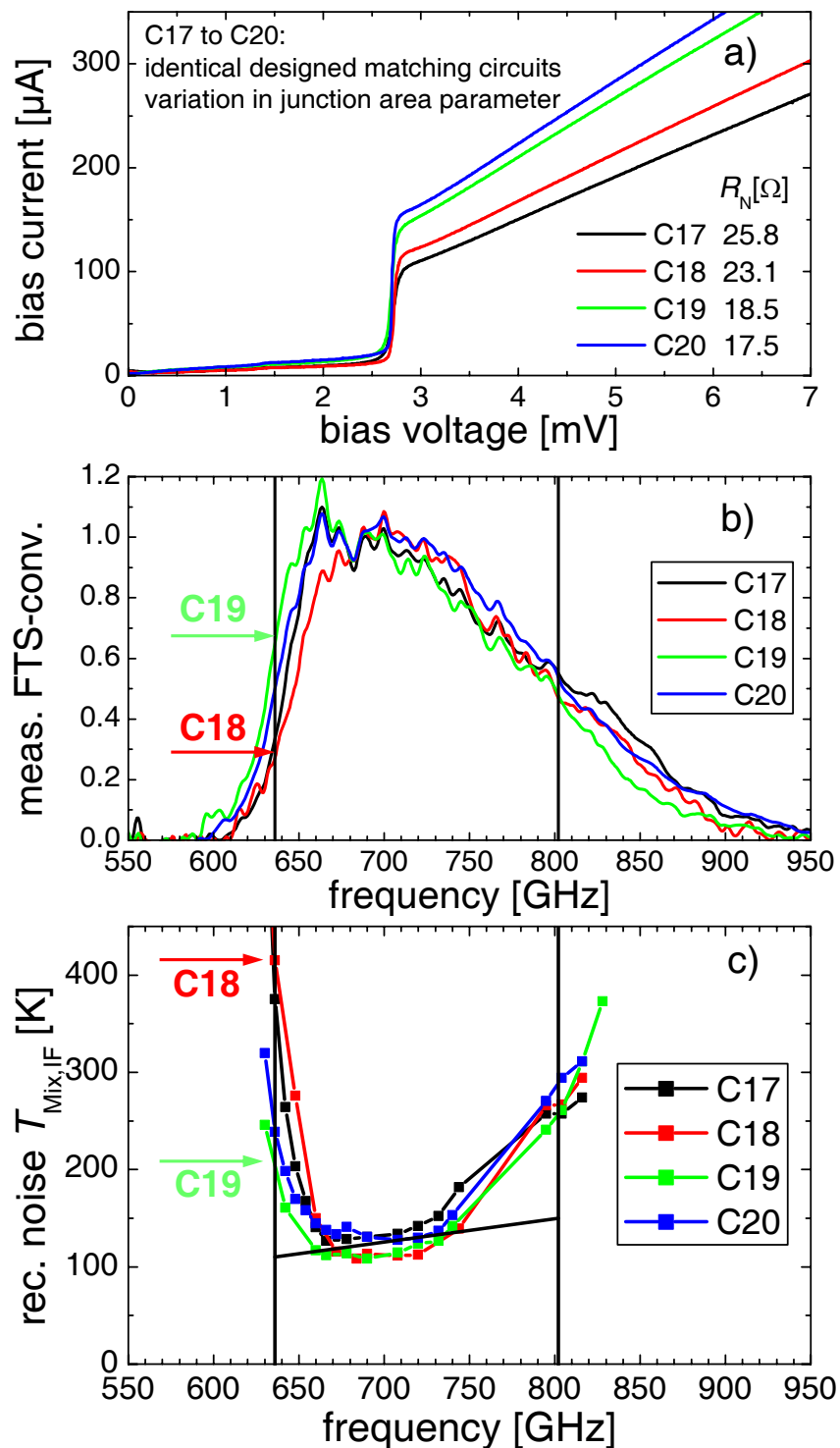


Fig. 4.28: Four devices of wafer PS8 with identical designed matching-circuits. Devices C18 and C19 have been fabricated with a $+0.4 \mu\text{m}$ -correction for under-etching, C17: $+0.3 \mu\text{m}$, C20: $+0.5 \mu\text{m}$. **a)** Measured I-V-curves: variations in R_N are expected to occur mainly due to variations in junction area. **b)** The measured band-pass shows relative small variations in frequency ($\Delta\nu = 10\text{-}20 \text{ GHz}$), resulting in significant variations at 630 GHz. **c)** The variations in noise temperature especially at 636 GHz are significant.

direct neighbors on the wafer. The DC I-V-curves measured in the dewar, the FTS-response and the noise performance of these four devices are presented in Fig. 4.28.

Devices C18 and C19 have been fabricated with a $+0.4 \mu\text{m}$ -correction for under-etching; C17: $+0.3 \mu\text{m}$, C20: $+0.5 \mu\text{m}$. For a constant wafer current density the normal resistances, given in Fig. 4.28 (a) are assumed to be inverse proportional to the junction area. The relative spread in absolute junction area is illustrated by the larger difference R_N between C18 and C19, than between C17 and C18, equally between C19 and C20.

The shifts in the measured band-pass around 10–20 GHz (Fig. 4.28 (b)), which is mainly attributed to changes in junction area around $0.05\text{--}0.1 \mu\text{m}$ seem to be marginal. But the resulting increase in mixer noise at the lower band-edge is severe (factor $2\times$). As a result only one of these very similar devices (C19) could be selected as flight-mixer.

Three short conclusions are drawn from this analysis:

1. The junction area parameter $A_J=l_J^2$ is not direct proportional to the real junction area (for assumed constant j_c). Devices C18 and C19 with same junction area parameter show significant difference in R_N (Fig. 4.28 (a)). The relative spread in junction area (67% for this wafer) is erratic even for nearest neighbor devices on the mask.
2. Assuming that the spread in junction width l_J for devices C17 to C20 is in the order of $0.1 - 0.2 \mu\text{m}$ with a doubling of the mixer noise at the lower band edge, a junction width accuracy of $\Delta l \leq 0.05 \mu\text{m}$ is required.
3. Since the frequencies of the lower band edge for the four devices do not follow the order of R_N (which is assumed to be a measure for A_J), other erratic inaccuracy effects of the same order in frequency (10–20 GHz) are responsible for shifts in the band-pass. These effects are a relative misalignment and inaccuracies of the matching micro-strips or local variations in micro-strip parameters, which can not be identified independently.

One important factor, why devices of wafer PS8 could successfully be used as mixers for HIFI band 2 is, in spite of the relatively large spread in junction area a large number of devices with areas centered around the desired values. This has allowed a selection of suitable devices after DC-characterization, data interpretation and RF-characterization¹¹.

The performance characterization and the applied correction for the noise contributions of the delivered flight-mixers as presented in Fig. 4.29 have been confirmed by the HIFI consortium during the tests of the mixer units [81, 2].

¹¹A more complete overview of the whole selection process is given in App. D.3.

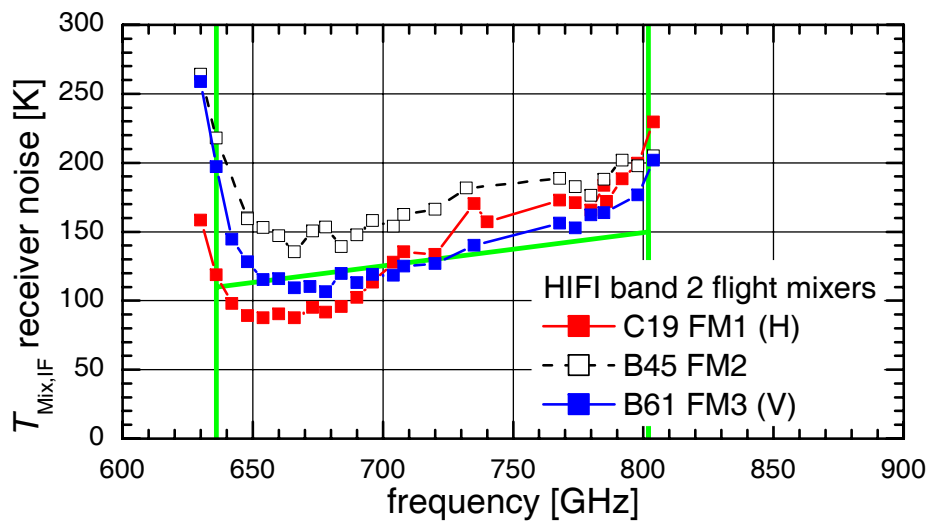


Fig. 4.29: Noise performance of three delivered flight mixers for HIFI band 2. The mixer with device C19 has been integrated to the HIFI-receiver for the horizontal polarization, B61 for vertical polarization (compare Fig. 1.3). The mixer with device B45 has been delivered as attrition mixer for testing purposes and as possible backup.

Chapter 5

Noise analysis of the device design and the fabricated mixers

In this chapter the noise calculation for a variety of mixer models in the three-port approximation of Tucker's theory [18] are presented. The software, which allows the calculation of the noise performance of a mixer model for a given frequency range has been completely developed in Matlab within this thesis.

In the first Section 5.1 the effect of variation in the most critical fabrication parameters on the mixer performance is evaluated. This is especially of use, if parameters can not be optimized independently, as it is the case for the current density j_c and the DC-quality Q . The resulting data allow an estimate of the decrease in noise temperature because of a larger j_c against the increase in noise temperature because of the simultaneous reduction of Q . This can be used for future design calculations and the definition of target fabrication parameters.

With the same formalism in Section 5.2 physical models for the flight-mixers are developed. Included are the shot-noise according to Tucker's theory and additional noise attributed to multiple Andreev reflection (MAR). Thermal effects are documented based on the measurements and their influence on the noise performance is discussed. With this analysis the reliability of the applied physical mixer models is examined and qualitatively justified by comparison with experiments.

5.1 Influence of SIS-device fabrication parameters on the calculated mixer noise

In this section the junction model, which has been used for the design of the SIS-devices in Chap. 3 is extended by the noise calculation of simulated mixers. The calculation is based on the three-frequency approximation of Tucker's

theory. For the estimate of the embedding impedance the junction model, presented in Chap. 3 is used. For the noise calculation measured I-V-curves are included, and for a given LO-frequency comparable to the measurement procedure the bias-voltage and the LO-power level are optimized with respect to the receiver noise $T_{\text{Mix,IF}}$. For more details of the calculation see App. A.3.

On the one hand, this allows an analysis of the optimum design parameters for the devices. On the other hand, with this method all performance-relevant fabrication parameters - especially also the DC-quality Q - are included in the analysis.

First, the effect of the parameters NbTiN-quality (ρ_n and T_c), gap-voltage V_{Gap} , current-density j_c and DC-quality Q on the calculated mixer noise for a specific mixer design is evaluated independently for each parameter (Subsec. 5.1.1). Then the parameters j_c and Q , which can not be optimized totally independent in the fabrication process, are varied simultaneously.

5.1.1 Independent variation of four selected fabrication parameters

The impact of the parameter variation on the calculated mixer noise for a specific mixer design is analyzed. The results for the power coupling in the simplified junction model (see Chap. 3.5) are compared with calculated noise temperatures of the more complete mixer model. Especially the dependence of the calculated noise performance on individual parameters is studied and compared.

5.1.1.1 Influence of NbTiN-quality on the mixer performance

Based on the power coupling calculation NbTiN/SiO₂/Nb is the optimum available material for micro-strips in the HIFI band 2 (compare Subsec. 3.4.3). Nb has been fabricated with a sufficiently reliable quality with small optimization potential left¹.

Considerable effort has been made to develop NbTiN as micro-strip material for the HIFI band 2 mixers [13]. With NbTiN a lossless micro-strip material up to frequencies around 1 THz is available. Even if the critical temperature is the lowest measured value for the presented wafers of 13.5 K, the corresponding gap-frequency is still above 900 GHz.

Unfortunately deviations of the design values variations in ρ_n and T_c for NbTiN have an impact on the surface impedance of the NbTiN-layer and thus on the

¹The conductivity of Nb can be improved, if it is sputtered epitaxially, as done by Karpov et al. [82]. But this technique cannot be used for top electrodes in the fabrication of HIFI band 2 devices.

calculated power coupling of a device (see Subsec. 3.4.2.2). This is illustrated in Fig. 5.1.

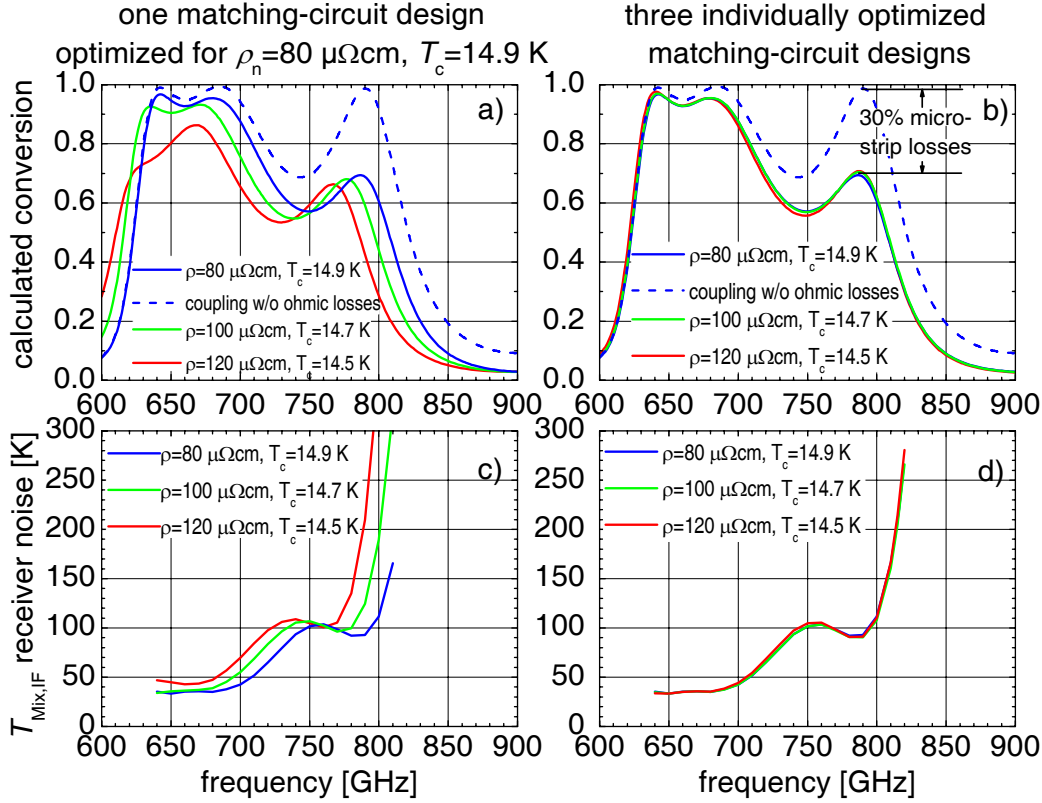


Fig. 5.1: Left: Effect of variations in NbTiN-quality for a specific matching-circuit design on the power coupling (plot (a)) and receiver noise (plot (c)). Right: Power coupling (plot (b)) and receiver noise (plot (d)) for three individually optimized matching circuits for the three different sets of NbTiN-quality (ρ_n, T_c).

Plots (a) and (c) in Fig. 5.1 show the power coupling and calculated noise performance for a single matching circuit design for three different sets of quality parameters for NbTiN. The matching circuit is a narrow band design from the mask NbTiN3 for a j_c of 15 kA/cm^2 with a junction area of $(0.8 \mu\text{m})^2$. This design has been optimized for NbTiN-parameters of $\rho_n = 80 \mu\Omega\text{cm}$ and $T_c = 14.9 \text{ K}$ (blue line). For the noise calculation a measured I-V-curve with a DC-quality of $Q = 10$ has been used. If this matching circuit is fabricated with lower DC-quality parameters for NbTiN-parameters, which are given in the legend of the figure, the band shifts to lower frequencies, the power coupling, the mixer noise and mixer gain suffer from this deviation (green and red line).

If the matching circuit is optimized individually for each NbTiN parameter set (Fig. 5.1 (b)), the resulting power conversion and receiver noise are nearly

indistinguishable. The corresponding calculated noise data are given in Fig. 5.1 (d).

This implies that for the Band 2 mixer development in the available parameter range not so much the optimization of the DC-quality of NbTiN (ρ_n and T_c) but rather its reproducibility is required.

5.1.1.2 Influence of the gap-voltage on the mixer performance

The fabrication parameter gap-voltage V_{Gap} is analyzed as a characteristic parameter for the material in the superconductive electrodes. Temperature or thermal coupling effects also have an impact on V_{Gap} , but are not included in this analysis (for thermal effects see discussion in Subsec. 5.2.2).

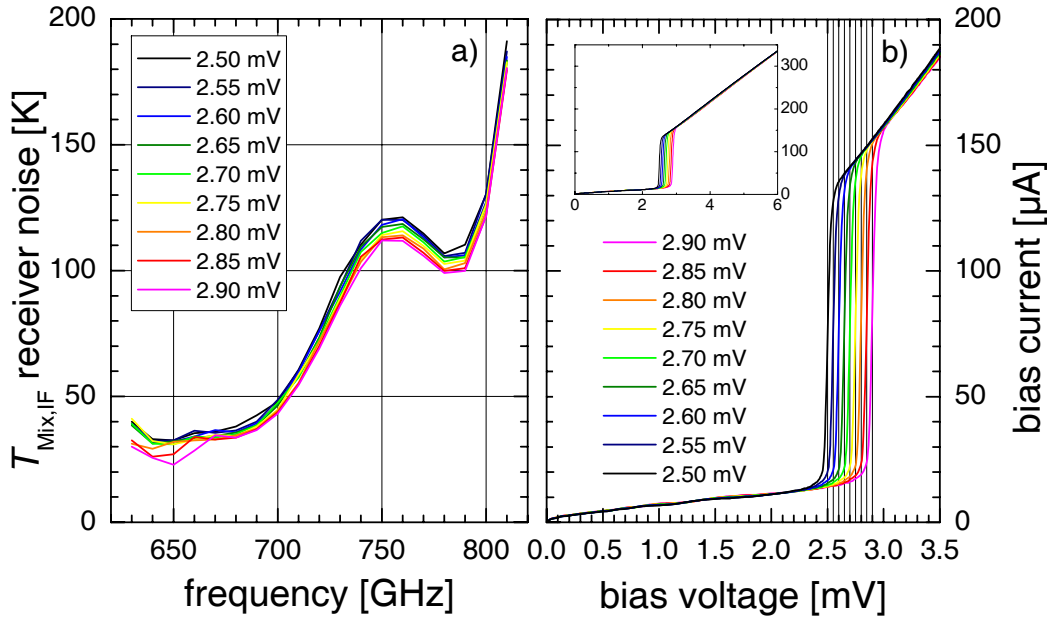


Fig. 5.2: **a)** Effect of variations in gap-voltage V_{Gap} on the calculated noise performance for the FM1-design ($A_J = 0.81 \mu\text{m}^2$) with a measured I-V-curve of $Q=10$. **b)** The experimental I-V-curve has been scaled to a j_c of 15 kA/cm^2 and to the respective V_{Gap} . The small inset shows the I-V-curves over a larger voltage range.

In Fig. 5.2 the results of the Tucker calculation for an optimum design with variation of V_{Gap} are given. A measured I-V-curve with a DC-quality of $Q = 10$ has been scaled to the design current density of $j_c = 15 \text{ kA/cm}^2$ and to the respective gap-voltages $V_{\text{Gap}} = 2.50, 2.55 \dots, 2.90 \text{ mV}$. The resulting maximum differences in noise temperature are around $\Delta T_{\text{Rec}} \approx 10 \text{ K}$. While the fluctuations in gap-voltage are experimentally found to be much smaller than 0.4 mV , the range of 10 K is around or below the accuracy for the determination of the noise performance of a measured mixer. This implies that

the influence of changes in V_{Gap} based on differences in the superconductive properties of the electrode material Nb is negligibly small.

5.1.1.3 Influence of the current density j_c on the mixer performance

The impedance calculation shows, that for a broadband matching circuit to a SIS-junction a high current density is necessary (compare Subsec. 3.2). To estimate the changes in mixer performance because of variations in j_c the HIFI receiver noise has been calculated for the same design as in Subsec. 5.1.1.2.

The results are given in Fig. 5.3. Here again an I-V-curve with a constant

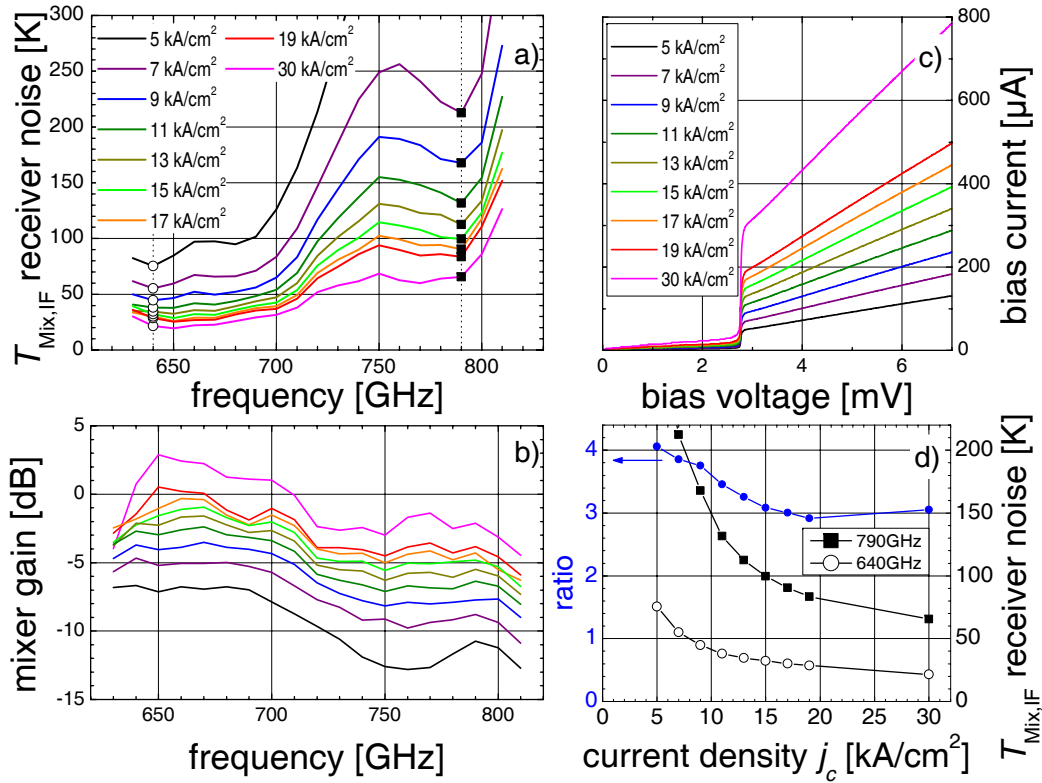


Fig. 5.3: Effect of variations in current density j_c on the calculated receiver performance for the narrow band FM1 design with a measured I-V-curve of $Q=10$. a) calculated receiver noise over the frequency band. b) calculated mixer gain over the frequency band. c) I-V-curve scaled to $V_{\text{Gap}}=2.77$ mV and different values for j_c . d) calculated receiver noise at 640/790 GHz as function of j_c and the resulting ratio between them (blue).

$Q = 10$ is used. In Fig. 5.3 (c) the I-V-curves, scaled to the gap-voltage of $V_{\text{Gap}}=2.77$ mV and to the required values for the normal resistance

$$R_N = \frac{\pi}{4} \cdot \frac{V_{\text{Gap}}}{j_c \cdot A_J}$$

with $A_J = 0.81 \mu\text{m}^2$ are shown. To include a possible fabrication progress for the future with Nb/AlN/Nb-junctions, a value for j_c of 30 kA/cm^2 is added. In Figure 5.3 (a) and (b) the results from Tucker's theory for the HIFI receiver noise and the mixer gain are given. The results for 640 GHz and 790 GHz are plotted as a function of j_c in Figure 5.3 (d).

From the resulting data it is seen, that the variations in receiver noise due to changes in j_c are much larger in the upper frequency band than in the lower frequency band. The main difference between these two frequency regions is the ohmic losses in the micro-strip matching circuit above the gap-frequency of Nb. Based on these results it is possible to partly compensate micro-strip losses with a larger j_c of the SIS-junction; at least for a single junction matching circuit as is used here. In the region below $12\text{-}13 \text{ kA/cm}^2$ the dependence of the HIFI receiver noise as function of j_c is much stronger than for larger values of j_c .

In Fig. 5.3 (d) also the ratio of the calculated mixer noise values at 790 GHz and 640 GHz is given as function of j_c . A low ratio illustrates the more broad-band power coupling as expected. The fact, that for $j_c = 30 \text{ kA/cm}^2$ the bandwidth slightly decreases again, is specific for the used waveguide-probe. In order to design broad-band SIS-junctions with large values for $j_c \approx 30 \text{ kA/cm}^2$ the waveguide-probe has to be adapted.

5.1.1.4 Influence of the DC-quality Q on the mixer performance

The DC-quality Q is viewed to be a parameter, which is an indicator for the magnitude of the intrinsic noise of a SIS-mixer (compare Subsec. 2.3). A large sub-gap current implies increased shot-noise of the mixer, and thus a higher mixer noise temperature for the same RF-coupling. This effect is analyzed in the relevant parameter range with a series of measured I-V-curves.

Noise temperature band-pass for three different designs: The mixer noise for the three typical types of matching circuits as presented in Chap. 3 is evaluated for three different I-V-curves (see Fig. 5.4). In the first row the respective band-passes are plotted. In the second row the calculated receiver noise is given for the I-V-curves with $Q=6.0$, 12.5 and 16.9 .

For the first column ("narrow band" design) the calculated noise performance qualitatively complies with the band-shape, which would be expected from the calculated conversion. The absolute values for the noise are correlated to the values for Q .

The "broad band" design in the second column displays equal power coupling in lower and the upper part of the frequency band but the calculated noise is larger for 790 GHz than for 650 GHz for all three DC-quality values. For for a lower DC-quality Q this discrepancy becomes larger.

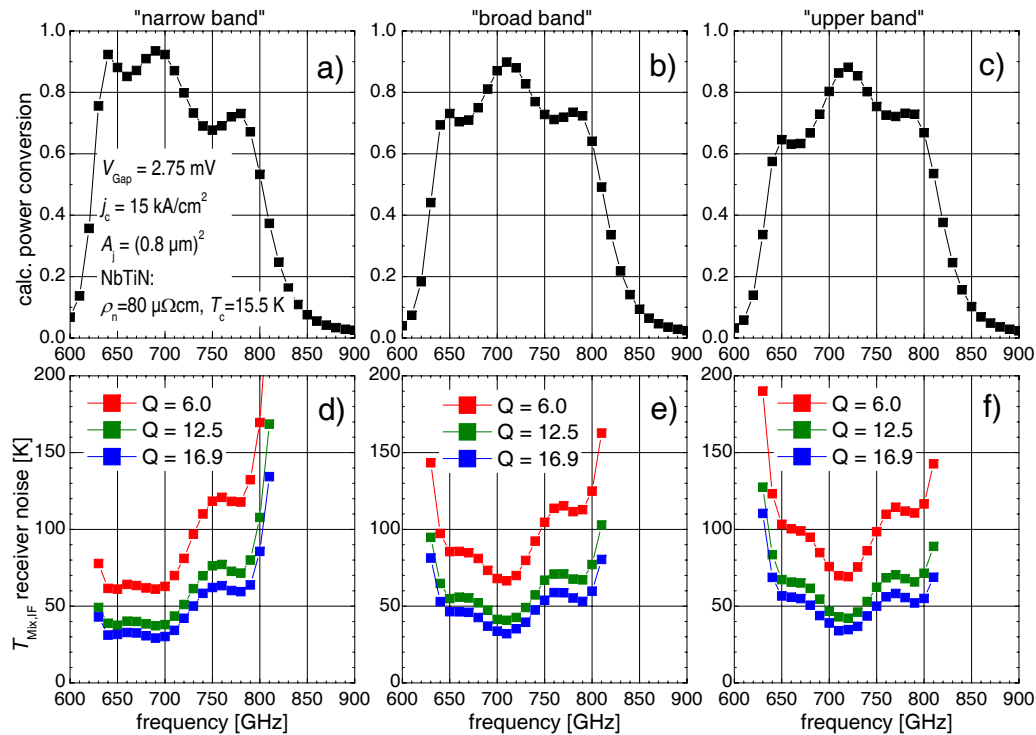


Fig. 5.4: Calculated HIFI receiver noise for three SIS-device designs from mask NbTiN4. Plots (a) to (c) show the calculated conversion, in plots (d) to (e) the calculated HIFI receiver noise is given. The explicit design parameters for all devices are given in plot (a). The three designs only differ in matching circuit geometry. A clear dependence of the calculated noise on the DC-quality Q of the underlying I-V-curve is seen in plots (d) to (e).

For the “upper band” design this effect is more severe. The calculated conversion is larger for 790 GHz than for 650 GHz, but the noise is equal at these frequencies for the I-V-curves with $Q = 12.5$ and $Q = 16.9$. For the I-V-curve with $Q = 6.0$ the relation is even inverse, that the larger power coupling at 790 GHz in comparison to 650 GHz, is related to the larger receiver noise.

This calculation illustrates, that differences in DC-quality Q not only shift the absolute level of the receiver noise, but also the relative shape. For SIS-devices with DC-qualities above 10, this effect is less important.

Noise temperature for one device design with more than 50 measured I-V-curves: In order to obtain a more systematic information about the Q -dependence of the calculated noise, noise temperatures for more than 50 measured I-V-curves are calculated. The I-V-curves have been scaled in current and voltage to comply with the FM1 design parameters of $j_c = 15$ kA/cm², $V_{\text{Gap}} = 2.75$ mV and a junction area of $A_j = 0.81$ μm². The optimum noise performance for the HIFI receiver noise at the lower frequency band (640-650 GHz) and at 790 GHz has been calculated incorporating the respective

embedding impedances of the FM1-design.

The results are given in Fig. 5.5. A clear dependence of the receiver noise with the DC-quality Q of the I-V-curve is seen. The data at the lower band and the upper band of this design can be viewed as the extreme cases for all HIFI band 2 mixer designs with respect to their power coupling. For the

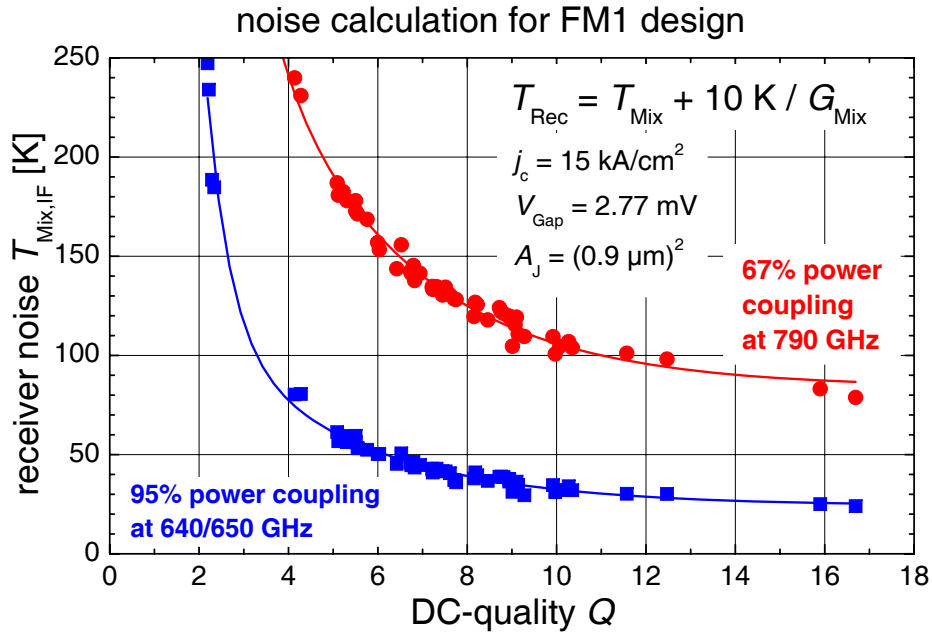


Fig. 5.5: Calculated receiver noise (Tucker) for measured I-V-curves as function of DC-quality Q . The data points show the results for two frequency regions of the FM1-design embedding impedance. The lines are obtained from a double exponential fit.

broad-band and upper-band designs the variations in power coupling over the frequency band are more moderate. But Thus the relation between Q and the performance is valid for all HIFI Band 2 designs for a given frequency and a given power coupling.

5.1.2 Simultaneous variation of j_c and Q and the effect on the calculated mixer performance

In the previous subsection it is shown that the NbTiN-quality and the gap-voltage V_{Gap} in the relevant range and for the materials used for the HIFI band 2 mixers do not limit the mixer performance. The most significant parameters for the noise temperature are the current density j_c of the SIS-device and DC-quality Q of the I-V-curve. In the fabrication process j_c and Q can not be optimized totally independently. There are some factors, which influence the DC-quality Q independent of j_c , e.g. the stress in the ground-plane. But from the fabrication step, the oxidization of the thin Al-layer, which defines

the barrier thickness, a larger j_c is related to a reduced DC-quality Q^2 . Thus in this j_c and Q are varied simultaneously in order to quantify and compare the effects.

Simultaneous, independent variation of j_c and Q : The calculation is done based on the specific device design of the FM1 on the mask design NbTiN3. The measured I-V-curves of the characterized mixers are the set of I-V-data with different DC-qualities Q . As in Subsec. 5.1.1.4 the I-V-curves are scaled to the design gap-voltage of 2.77 mV. In addition to that, the I-V-curves are scaled in current for the same set of j_c as already applied in Subsec. 5.1.1.3. The calculation is performed for two typically different frequency regions, 640/650 GHz with optimum power coupling of 95% and at 790 GHz with a power coupling of 67%.

The resulting data for the calculated HIFI receiver noise are given in Figure 5.6. Each curve in the figure shows the variation in calculated receiver noise for a given j_c with variation in the DC-quality Q . The receiver noise is much larger at the upper part of the band at 790 GHz because of the increased micro-strip losses in Nb above its gap-frequency.

Two general results can be drawn, assuming that the shot-noise, which is evaluated with this formalism is the major noise component of the mixers:

- (R1) There is a significant reduction in $T_{\text{Mix,IF}}$ when increasing the DC-quality until $Q \approx 8 - 10$. Above this region only minor improvement of the mixer performance is obtained by an increase of Q . The relative shape for the relation $T_{\text{Mix,IF}}(Q)$ is comparable for different values for j_c and different micro-strip coupling.
- (R2) The absolute reduction in receiver noise because of an increase in j_c is much larger for higher micro-strip losses. If by means of superconductive micro-strip materials a good coupling is achieved, the reduction in $T_{\text{Mix,IF}}$ caused by increased j_c is moderate (Figure 5.6 (a)). On the other hand for higher micro-strip losses – *as for Nb above its gap-frequency and expected also for Al in normal conductive state* – significant reduction in calculated receiver noise is achieved by an increase of j_c (Figure 5.6 (b)).

These two results support the design approach for the HIFI band 2 mixer optimization to achieve a relatively high current density around 15 kA/cm², even at the cost of moderate DC-qualities.

²A smaller exposure E implies a thinner oxidized insulating layer with a larger j_c and potentially larger leakage currents due to pinholes resulting in a lower DC-quality Q (compare Subsec. 2.3, [13]).

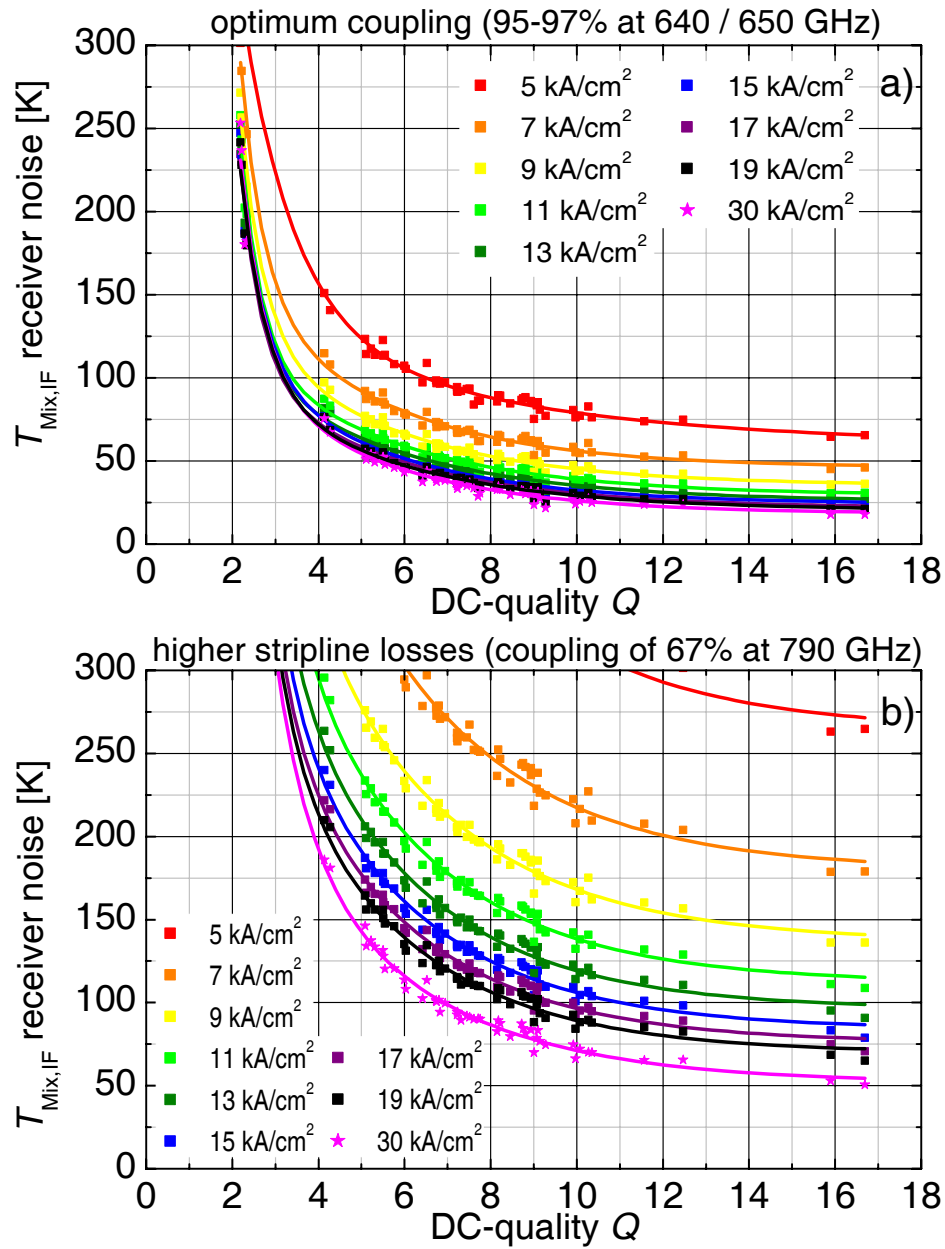


Fig. 5.6: Calculated receiver noise for the FM1-design with $A_J = 0.81 \mu\text{m}^2$, $V_{\text{Gap}} = 2.77 \text{ mV}$. The data are calculated for more than 50 measured I-V-curves (variation in DC-quality Q). The I-V-curves are scaled in current to several values of current density j_c . Embedding impedance and micro-strip losses at the lower band (plot (a)) and the upper band (plot (b)) are applied.

From the second result it is expected that the use of AlN-barriers, which promise a larger j_c , improves the mixer performance for larger micro-strip losses as for Nb above its gap-frequency or normal-conductive Al. But it is not expected to improve the mixer performance significantly for Nb below its gap-frequency.

Application of a j_c - Q -relation: The thinner barrier of high- j_c devices is expected to show larger leakage currents due to pin-hole defects. But for the fabricated and analyzed wafers for HIFI mixers this relation has not been observed. The estimated current density j_c of the characterized wafers as function of the optimum DC-quality Q are presented in Fig. 5.7, where a j_c - Q -relation is not seen. This suggests, that the DC-quality not only has been defined by the barrier oxidation process, but is strongly influenced by additional fabrication steps.

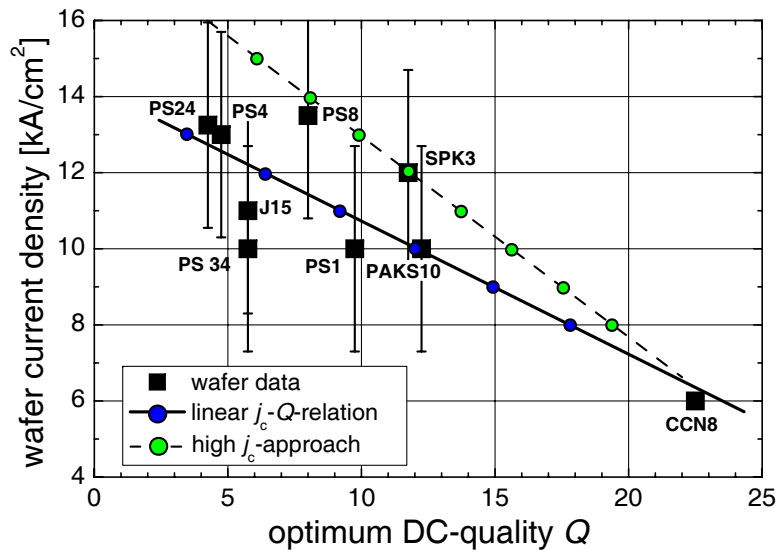


Fig. 5.7: Current density j_c and optimum DC-quality Q of the characterized wafers. Two linear j_c - Q -relations are added to illustrate their impact on the resulting optimum calculated mixer performance.

For illustration purposes an assumed linear relation of j_c and Q is used and applied to the calculated noise data. The linear relation is obtained from a line, which connects the average values for j_c and Q for the KOSMA-fabricated wafers with the j_c and Q of the CCN8-wafers. These wafers are obtained by a different fabrication process at DIMES³. An additional “high- j_c -approach” is added to include PS8 to the analysis.

The linear relations are applied to the calculated receiver noise data at the more critical frequency at 790 GHz, which already have been given in Fig. 5.6 (b). The result is presented in Fig. 5.8 with an optimum Q of 10-13 with respect to the resulting receiver noise $T_{\text{Mix,IF}}$. In this way, the presented data can be used to obtain the optimum target value for j_c with a given, fabrication-specific j_c - Q -relation. The j_c - Q -pairs of the two lines in Fig. 5.7 are added to the noise temperature results. The noise data yield a respective optimum region for j_c and Q . This illustrates, how for a given j_c - Q -relation

³The fabrication of SIS-devices at DIMES has significantly been improved since the fabrication of the CCN8-wafers [83]. Devices with a j_c of 13.5 kA/cm² (equivalent to PS8) have been measured with a DC-quality Q of 20.

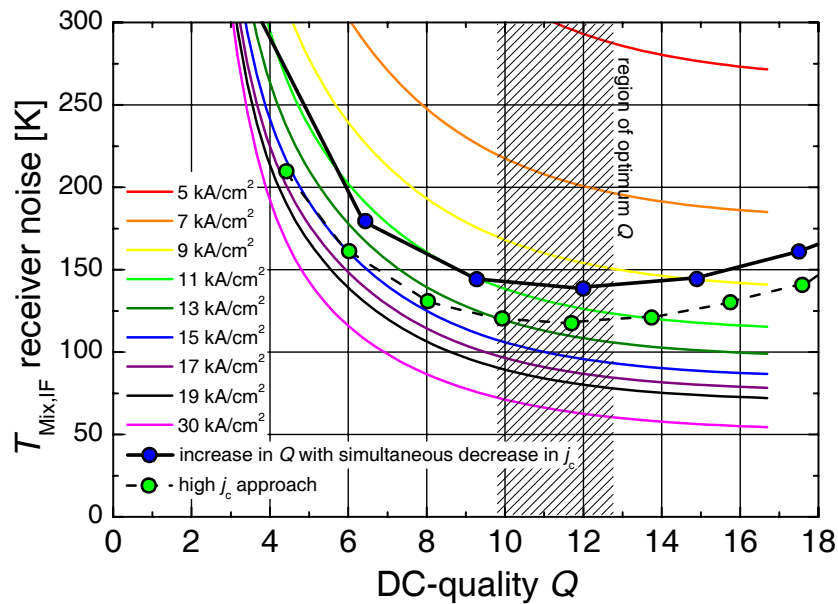


Fig. 5.8: Calculated receiver noise performance for variation in j_c and Q for the upper frequency band. Data points are added for two linear relations of j_c and Q , as specified in Fig. 5.7. This pays tribute to the fact that an increase of j_c usually goes along with a decrease in Q .

the optimum design parameters the optimum design parameters for SIS-mixer devices can be determined to achieve optimum noise performance.

Comparison with literature data: A similar analysis of a j_c - Q -relation for a different fabrication location (DIMES, NL) is found in [83]. B. D. Jackson et al. present SIS-mixers with the combinations $j_{c,1} = 6.5 \text{ kA/cm}^2$, $Q_1 = 60$ and $j_{c,2} = 13 \text{ kA/cm}^2$, $Q_1 = 20$, which show the same performance at 880 GHz. There, an additional j_c - Q -relation for a constant receiver noise at that frequency based on a receiver noise model is given (for details see [83]). The relation is sketched in Fig. 5.9 as the black line and points. The data for the two experimentally characterized receivers are marked with blue crosses.

Added are two j_c - Q -relations for constant calculated receiver noise $T_{\text{Mix,IF}}$ for HIFI band 2 design at 790 GHz derived from the data in Fig. 5.6. Both relations correspond qualitatively, but refer obviously to a different parameter space.

5.2 Noise analysis of the optimum measured mixer performance

In this section a physical model for the characterized mixers is presented and compared with the measurement data. It is illustrated, that the shot

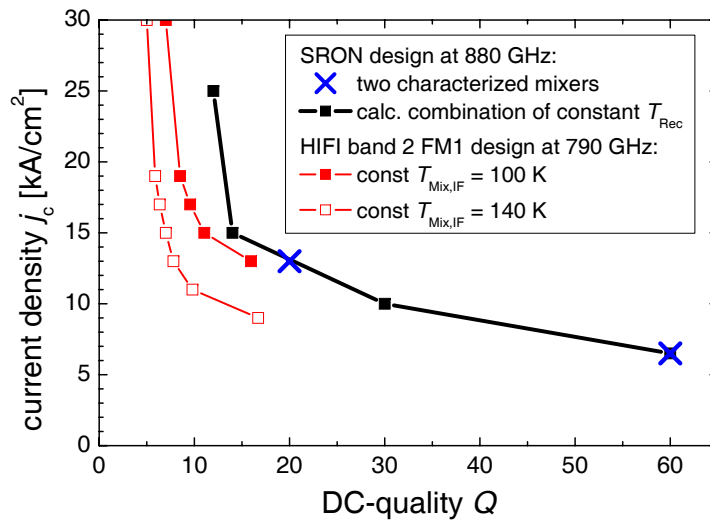


Fig. 5.9: Relations for j_c and Q for constant receiver noise: Black lines and points: relation of constant calculated receiver noise from ref. [83] at 880 GHz. Blue crosses: two characterized mixers with same noise performance from ref. [83]. Red lines and points: j_c - Q -relation for calculated constant $T_{\text{Mix,IF}}$ (100 K/140 K) for FM1 design from Fig. 5.6.

noise according to the three frequency approximation of Tucker's theory and increased noise due to MAR qualitatively represent the frequency-dependence of the measured noise temperatures. Here, a qualitative agreement of the measured and simulated data is achieved.

The calculation is performed for the optimum mixers, the flight-mixers FM1 and FM3. Only temperature effects are studied for the case of QM2 instead of FM3, since no sufficiently reliable temperature-dependent performance data are available for FM3⁴.

In the first subsection (Subsec. 5.2.1) the noise temperature for FM1 and FM3 is evaluated from the best estimate of the embedding impedances, as the shot-noise from the three-frequency approximation of Tucker's theory. The effect of variations in temperature is discussed in Subsec. 5.2.2. Finally, the increased noise because of multiple Andreev reflection (MAR) is included in the noise analysis (Subsec. 5.2.3).

5.2.1 Calculated shot-noise

The starting point for the noise analysis is the fit of the calculated conversion with the measured FTS-data. in order to estimate the frequency-dependent embedding impedance for the two SIS-devices. The FTS-data and the fits for FM1 and FM3 are given in the first row of Fig. 5.10. The

⁴The performance of FM3 at 2.8 K and 4.2 K has been measured in different heterodyne setups with different optics components. FM1 and QM2 have been characterized at 2.8 K and 4.2 K in the same test-facility.

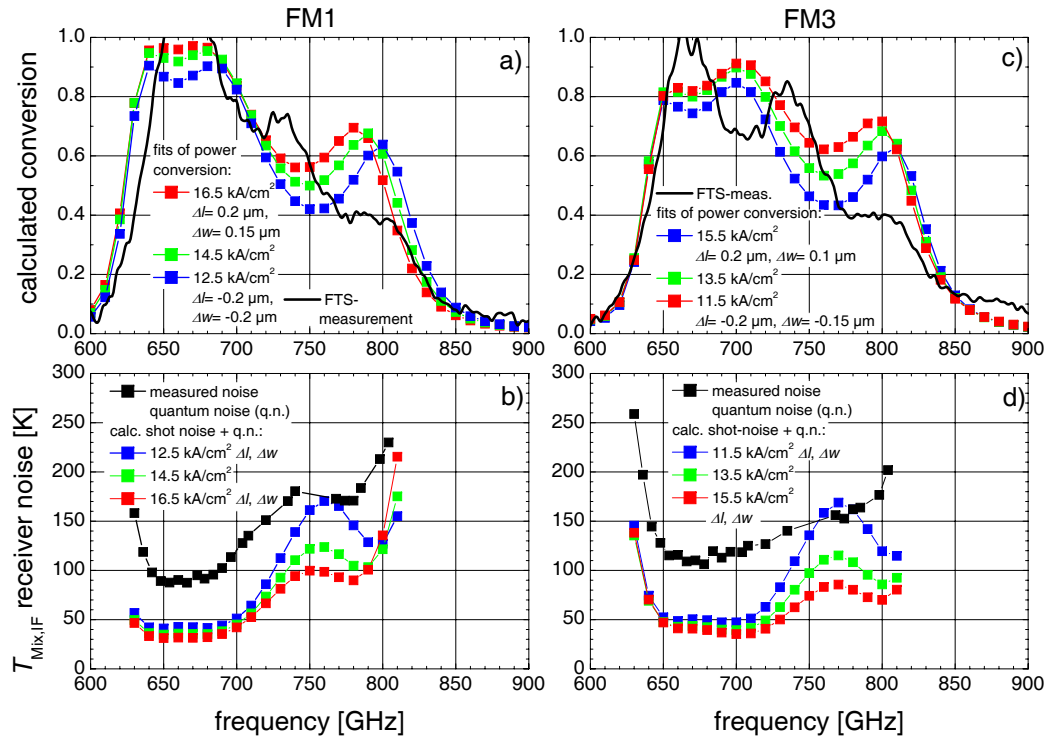


Fig. 5.10: Measured and calculated noise for FM1 and FM3. Top: Fit of calculated conversion (red, green, blue) with the FTS-measurement (black) with three values for j_c . Bottom: Measured noise (black) and calculated noise from Tucker's calculation plus quantum noise. Embedding impedances are defined from the three fits in plots (a) and (c). The actual measured I-V-curve is used.

resulting frequency-dependent power-conversion is plotted as green data in the first row of Fig. 5.10. Added are the power conversion spectra for current densities with a variation of $\Delta j_c = \pm 2 \text{ kA/cm}^2$ together with adapted values for offsets in micro-strip geometry, in order to remain compliant to the measured frequency band (the definition of Δw and Δl is given in Subsec. 4.4.1.3).

From these fits a frequency-dependent estimate for the embedding impedances of FM1 and FM3 is made. The embedding impedance values for the perfect matching circuit geometry ($\Delta w = \Delta l = 0$) are taken as long as no deviation is indicated. The DC I-V-curves measured at 2.8 K in the dewar with magnetic field and their Kramers-Kronig-transform are used in the shot-noise calculation.

The resulting noise temperatures from the shot-noise calculation are given in the second row of Fig. 5.10. Added to the shot-noise is the quantum-noise, since for a double-side mixer the minimum calculated shot-noise is zero, the zero-point fluctuation noise from the two side-bands yields the quantum-noise [29] that is measured. The calculated noise temperatures (green and

red data) except for the region between 750 GHz and 800 GHz qualitatively comply quite well with the measured data (black). Especially below 700 GHz the calculated noise qualitatively complies much better with the measured noise than expected from the fit with the FTS-measurement.

The calculated noise data are generally lower than the measured data. The deviations in noise temperature are around $\Delta T_{\text{Mix,IF}} = 40 - 70$ K. This is a significant difference, which has to be solved.

The significant qualitative discrepancy in the shape of the curves around 750 GHz appears just above the gap-frequency of Nb. In this frequency region the variations of the conductivity and thus of the micro-strip impedance in Nb with frequency, with temperature or with Nb-quality are very strong (compare Fig. 3.12). Especially variations in Nb-quality over the micro-strip width and height result in strong variations in micro-strip impedances just in this frequency region. Consequently the measured frequency dependence is more smeared out than in the calculation data.

5.2.2 Temperature and heating effects

Comparison of calculated and measured temperature dependency: The comparison of measured and calculated noise performance at 4.2 and 2.8 K is done for two mixers. The presented data are the corrected mixer performance $T_{\text{Mix,IF}} = T_{\text{Mix}} + 10 \text{ K}/G_{\text{Mix}}$, which are calculated from the actual measured receiver noise. The data of mixers FM1 and QM2 are analyzed here, since they have been characterized at 2.8 and 4.2 K in the same test-dewar setup. Thus possible differences in corrected mixer noise and gain because of differences in noise characterization of the involved optics components are excluded.

In Fig. 5.11 (a) and (b) the I-V-curves of both mixers for different ambient temperatures are plotted. The I-V-curves measured in the dipstick-setup with direct contact to liquid helium are added. The gap-frequencies in the dewar at 2.8 K are nearly the same as in the dipstick setup at 4.2 K. In Fig. 5.11 (c) and (d) the measured noise temperatures $T_{\text{Mix,IF}}$ are given for the same ambient temperatures of the cold plate. The values for QM2 exhibit a larger error, since the noise of the corrected IF-chain has been much larger.

In Fig. 5.11 (e) and (f) the calculated values for $T_{\text{Mix,IF}}$ are plotted. They are calculated from the three-frequency approximation of Tucker's theory for the nominal ambient temperatures of 2.8 K, 4.2 K and 4.8 K. The embedding impedances estimated in the previous subsection (for QM2 the same concept has been applied) and the measured I-V-curves for the respective cold plate temperatures are used to evaluate the shot-noise.

For FM1 the relative difference in calculated noise performance complies quite well with the difference in the measured data. If the deviations only occurred above the gap-frequency of Nb, it could have been an effect of the coupling

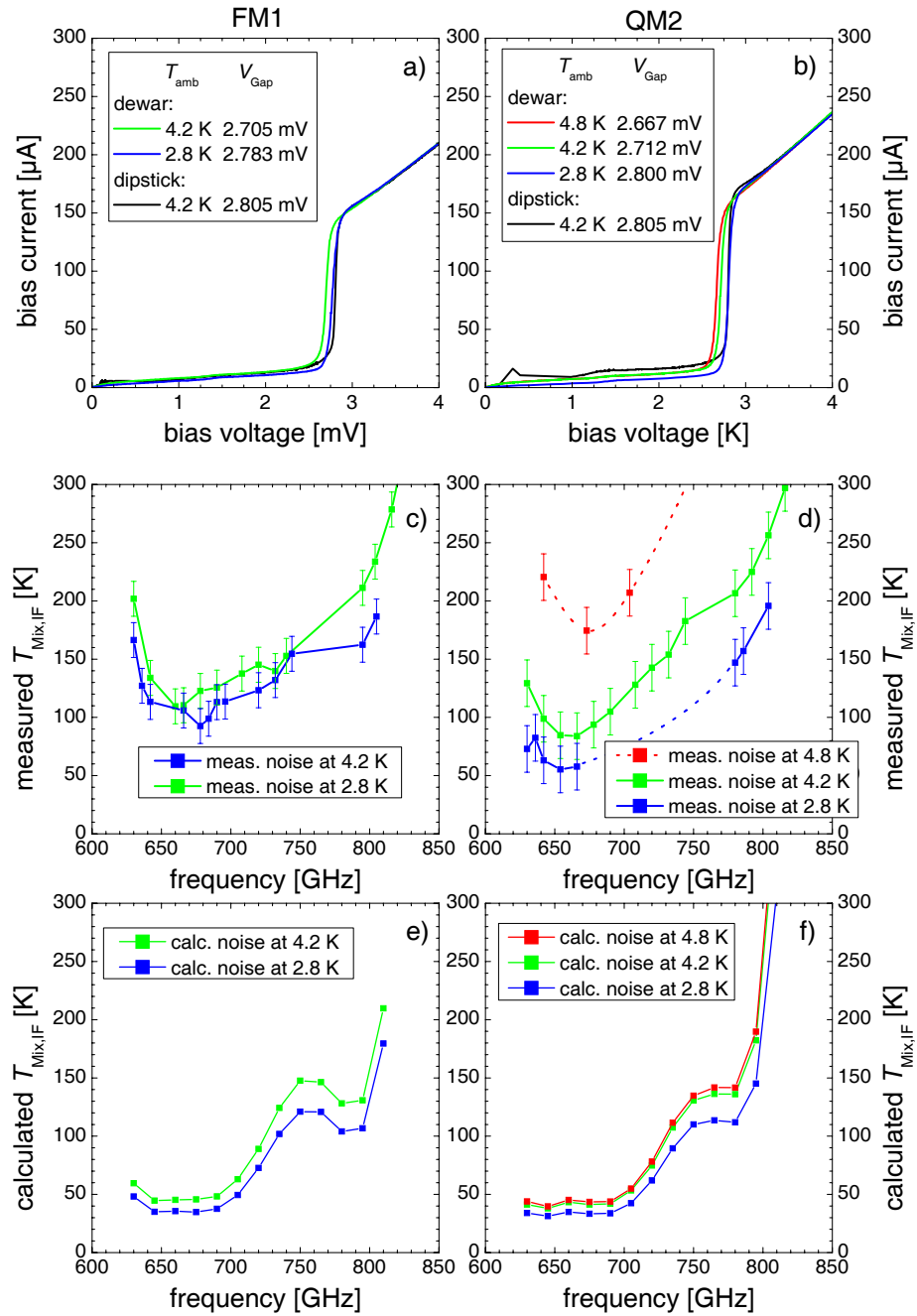


Fig. 5.11: Increase in noise temperature with rising ambient temperature T_{amb} can not always be explained from the calculated shot-noise: Measured and calculated noise temperatures for two mixers (left column: FM1; right column: QM2). Plots (a) and (b): DC I-V-curves in test-dewar for variation in T_{amb} and in dipstick-setup with direct contact to liquid helium at 4.2 K. Note, that I-V-curves in dipstick setup are measured without magnetic field with increased sub-gap current. Plots (c) and (d): measured receiver noise $T_{\text{Mix,IF}}$ for variation in T_{amb} . Plots (e) and (f): calculated receiver noise $T_{\text{Mix,IF}}$ for variation in T_{amb} .

in the matching circuit. But since the decrease in noise temperature is nearly constant over the frequency band, it is more likely attributed to the SIS-

junction. But for QM2 there is a significant difference in calculated and measured shift of the noise temperatures, especially for 4.8 K. This implies that other effects, which increase the noise, are present.

External thermal coupling: In order to estimate the real temperature at the SIS-device in the mixer-block inside the dewar, the measured gap-voltages for QM2 are plotted as a function of T_{amb} in Fig. 5.12 together with a general temperature dependency for the gap-voltage

$$V_{\text{Gap}}(T_{\text{amb}}) = 3.6 \cdot \frac{k_B \cdot T_C}{e} \cdot \sqrt{1 - \left(\frac{T_{\text{amb}}}{T_C}\right)^4}. \quad (5.1)$$

This comparison shows that an ambient temperature of $T_{\text{amb}} = 2.8$ K in the

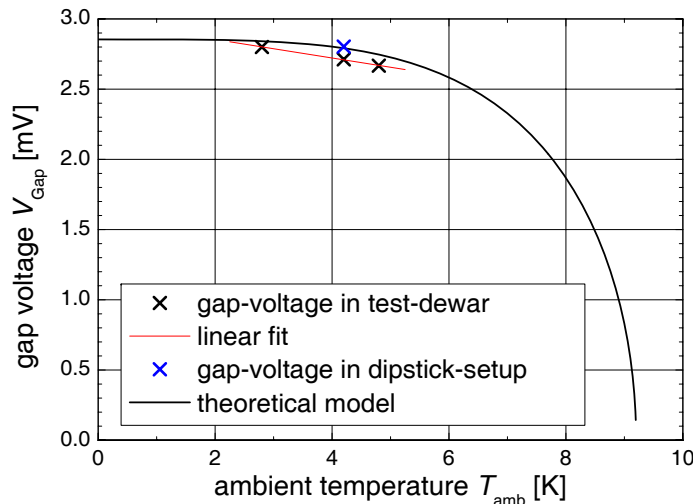


Fig. 5.12: Temperature dependency of the gap-voltage V_{Gap} for QM2. The black crosses mark the values for V_{Gap} measured in the test-dewar. The blue cross marks V_{Gap} measured in the dipstick-setup with direct contact to liquid helium. The black line shows the temperature dependency of V_{Gap} given in Eq. 5.1.

dewar is comparable to 4.2 K in the dipstick setup with direct contact to liquid helium. This illustrates that during the noise measurements at 4.2 and 4.8 K in fact the ambient temperature has been much larger. To quantify these effects, a thermal model of the junction is necessary, which is beyond the scope of this thesis, but can e.g. be found in [40].

Intrinsic heating effect: Intrinsic heating of the SIS-devices due to LO-radiation also increases the measured noise temperatures. This effect is not included in the shot-noise calculation, which is based on the unpumped DC I-V-curves. But in the pumped DC I-V-curves the effect of a lower gap-voltage for increasing LO-power is obvious (see Fig. 5.13). Plotted are the I-V-curves

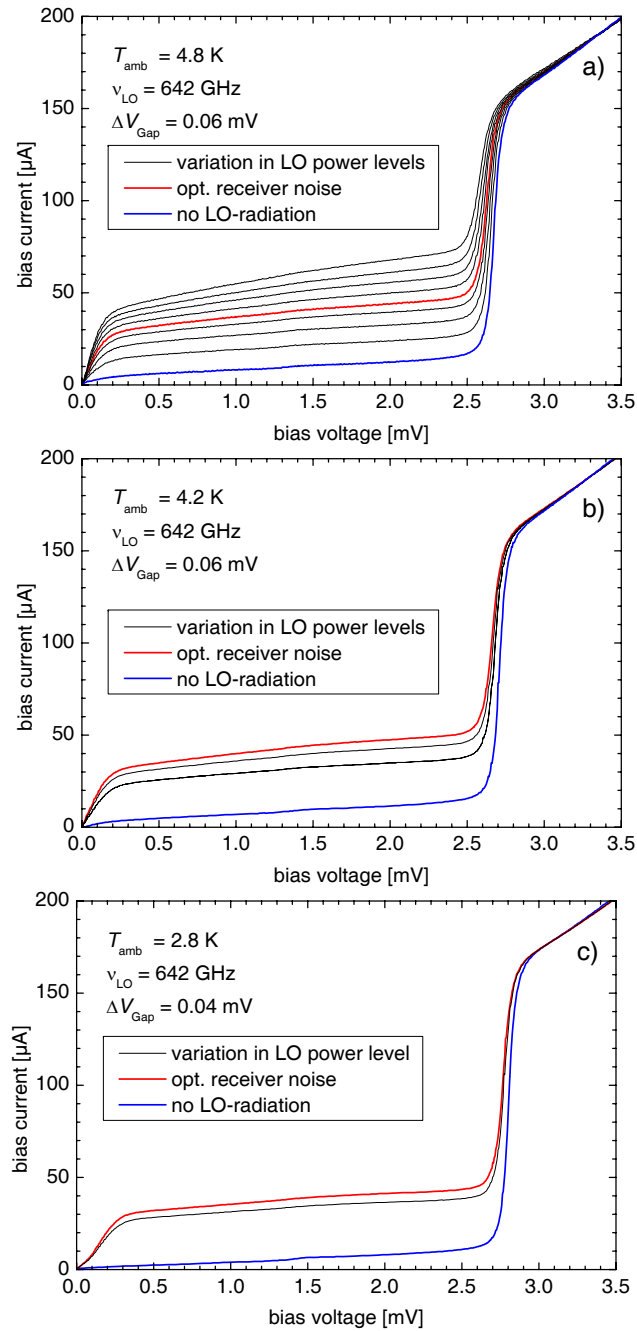


Fig. 5.13: Effect of variation on LO-power on DC I-V-curve of QM2 at 4.8, 4.2 and 2.8 K. Not only the increased current below the gap-voltage due to photon-assisted tunneling arises; but also the gap-voltage decreases with increasing LO-power. This indicates intrinsic heating of the SIS-junction [40]. The effect decreases at 2.8 K.

of the mixer QM2 at 4.8, 4.2 and 2.8 K. The blue line shows the unpumped I-V-curve. The red line shows the optimum pump-level with respect to the measured receiver noise. Added are variations in LO-power. The qualitative behavior is the same for other devices from the same wafer also at lower temperatures. But for lower temperatures, especially at 2.8 K the shift in

gap-voltage due to the LO-radiation is smaller.

Because of the insufficient cooling at the Nb/NbTiN-interface at the bottom electrode a temperature gradient over the two electrodes is present. Without the explicit thermal model it is only concluded that these heating effects significantly degrade the noise performance of the mixer. As shown for QM2 the heating effects have been significantly reduced at $T_{\text{amb}} = 2.8$ K, where the measured performance is compliant to the physical model.

5.2.3 Influence of multiple Andreev reflection (MAR) on the mixer performance

The formalism, which is necessary to include increased noise because of MAR is already presented in Chap. 2 (2.4.4). In Fig. 5.14 the differential resistance of FM1 and FM3 is plotted. The subharmonic gap-structure, which is an

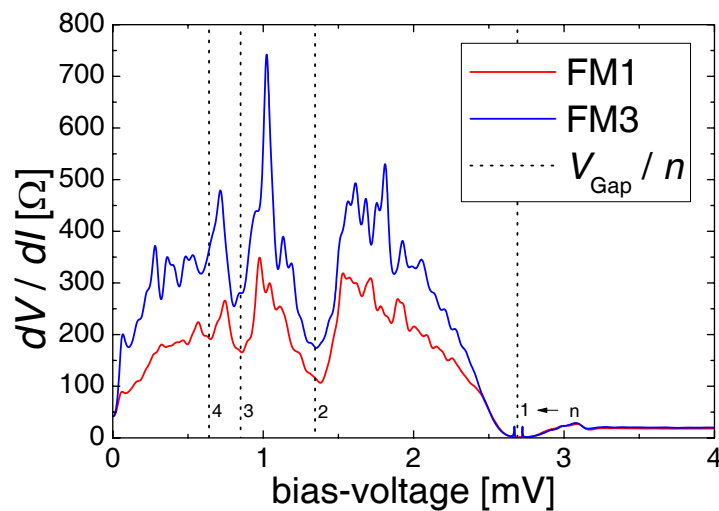


Fig. 5.14: Differential resistance $dV/dI(V)$ for two FM mixers. Subharmonic gap-structures are seen at voltages $2\Delta/ne$ as minima. This is a strong indication for the occurrence of multiple Andreev reflection (MAR) [41].

indication for the existence of MAR is seen [41]. Thus the noise calculation for FM1 and FM3 is repeated based on the presented physical model (Subsec. 5.2.1) with MAR included. The results are presented in Fig. 5.15. In the first row, again the FTS-measurements and the calculated conversion for the two mixers are plotted. In the second row the mixer noise T_{Mix} is plotted and in the third row the mixer gain G_{Mix} .

For both mixers, the relative shape of the calculated mixer noise complies quite well with the measured data. But for the absolute values there is a difference of a factor 2 for FM1 and even larger for FM3. There is also seen an offset in mixer gain of 2 dB can not be explained and is attributed to unconsidered losses in the horn, the waveguide, the quartz substrate and

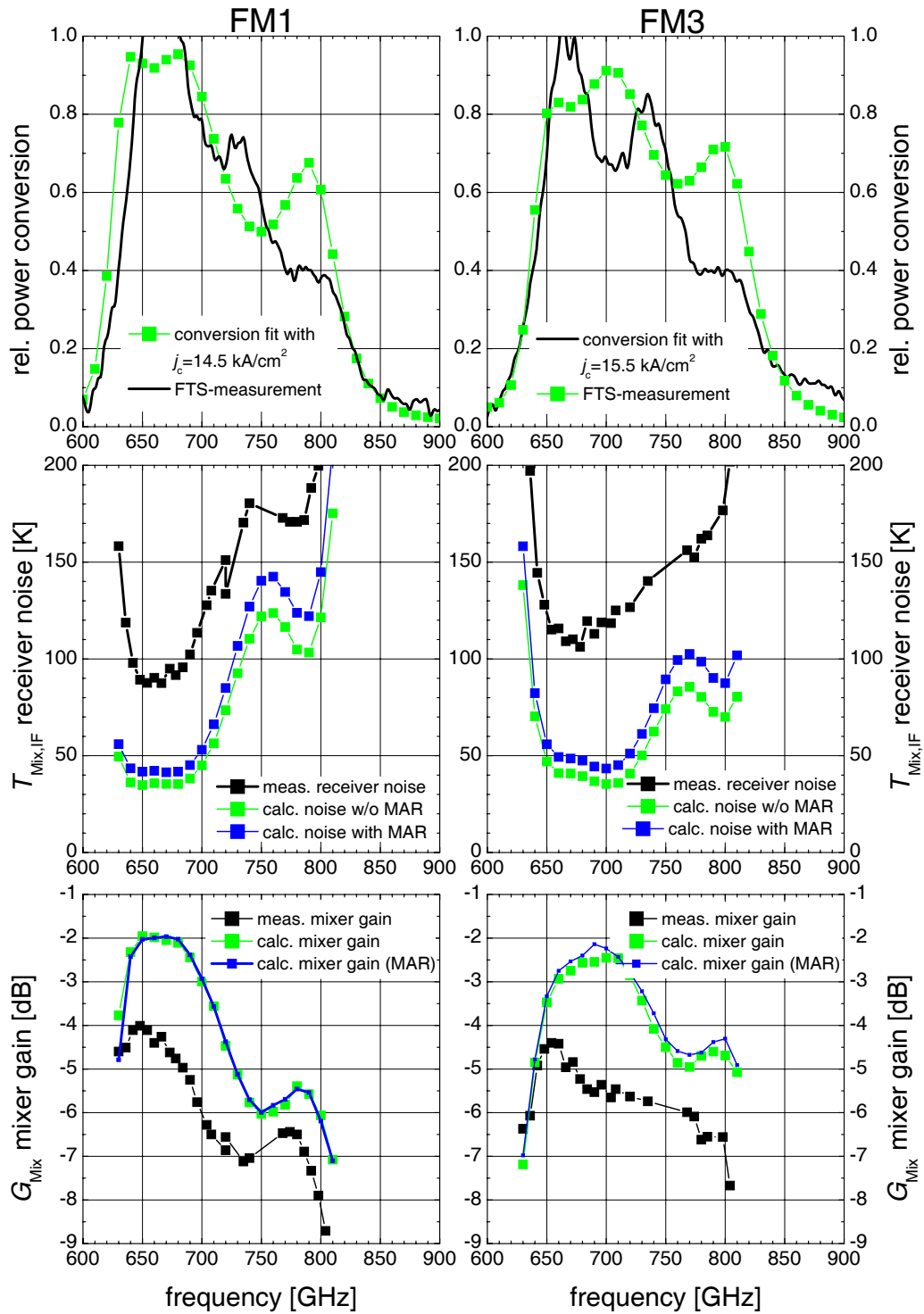


Fig. 5.15: Tucker noise calculations for mixers FM1 (left) and FM3 (right) with included effect of MAR. First row: Measured FTS-spectrum (black) and calculated conversion from j_c -fit (green). Second row: Measured mixer noise (black); calculated mixer noise without MAR (green) and with MAR included (blue). Third row: Measured mixer gain (black); calculated mixer gain (green, blue) is in principle not affected from MAR.

possible IF-mismatch losses. This suggests that the increased sub-gap current is not only carried by MAR, and the calculated shot-noise is not the only noise mechanism in the junction.

Nevertheless, the presented calculation based on Tucker's shot-noise calculation in the three-frequency approximation is viewed to be a suitable method to analyze the relative effect of different parameters (especially j_c and Q , Sec. 5.1) on the mixer performance for the identification of optimum design parameters.

A more complete approach to model the mixer is to include higher harmonics in the analysis ("harmonic balance", [84, 85]) to model saturation effects and additional noise from thermal fluctuations in the dissipative sideband terminations. Its application requires the knowledge of the waveguide-impedances at higher harmonics. The method is implemented in open available libraries ("Supermix"-libraries, [86, 87]). The results of this implementation have been verified [88]. For the exact description of the thermal effects, e.g. the temperature gradient inside the barrier due to the asymmetric cooling a dynamic thermal model of the device should be developed (compare [40]).

Chapter 6

Summary and Outlook

6.1 Summary

In this thesis the design of the HIFI band 2 mixer devices (Chap. 3) and the DC- and RF-characterization of the fabricated mixers (Chap. 4) has been presented. Three flight-mixers and two flight-spare mixers have been delivered to the HIFI consortium and the two best mixers have been integrated into the HIFI instrument. Their performance has been confirmed to be compliant with the HIFI performance baseline over 80% of the frequency band.

The design and its dependence on the fabrication parameters have been analyzed based on a three-frequency approximation of Tucker's quantum mixer theory (Chap. 5.1). The same formalism has been applied to simulate the characterized flight-mixers (Chap. 5.2).

Based on the simplified model, presented in Chap. 3 the microstrip geometry of the devices has been numerically optimized for maximum power coupling to the SIS-junction. The tolerance analysis has resulted in maximum allowed variations of $\Delta l_J = 0.05 \mu\text{m}$ for the junction width and $\Delta \rho_n = 10 \mu\Omega\text{cm}$ for the NbTiN-quality in order to fit the required frequency band. A sequence of three lithography masks with SIS-devices have been designed. On the first mask three-step transformers and double-junction devices with NbTiN/SiO₂/Nb- and NbTiN/SiO₂/Al-microstrips have been placed. A second mask has been designed for the comparison with another fabrication laboratory (DIMES, [72]) containing double-junction devices with NbTiN/SiO₂/Al-microstrips. Based on the performance results of the first two mask designs on the third mask only NbTiN/SiO₂/Nb-microstrips realizing a three-step transformer have been included.

The first selection of fabricated devices for RF-measurements has been done based on their Josephson resonance frequencies ν_{res} and DC-quality Q . The use of Josephson resonance frequencies for the identification of the optimum coupling frequencies has been justified experimentally (Subsec. 4.4.1.2). The

reduction in optimum noise performance with increasing DC-quality of a SIS-mixer is confirmed experimentally (see Fig. 4.10) and, based on the advanced quantum mixer model, also theoretically (see Fig. 5.5 and 5.6). Here, a strong effect is seen below $Q = 8 - 10$, a weaker effect for larger values of Q .

The most recent wafers SPK3 and PAKS10 have shown the optimum values for the relative spread in junction area ($\Delta A_J/A_J = 15 - 17\%$) and optimum DC-quality $Q_{\text{opt}} = 12$. But due to their shift of the band-pass to lower frequencies, they had to be rejected as flight-mixers. This decision has been confirmed based on a statistical analysis of the DC-measurement data¹ and based on j_c -fits of the simplified model to the measured FTS-data. PAKS10 showed a systematical offset in junction width $\Delta l_J = 0.3 \mu\text{m}$ ($A_J = l_J^2$, Subsec. 4.4.2.1). For SPK3 the same analysis resulted in a reduced effective NbTiN-quality, which has been attributed to the exchange of top-wiring and ground-plane material (Subsec. 4.4.2.2).

The wafer PS8 has shown the optimum noise performance with measured $T_{\text{MIX,IF}}$ for 9 SIS-mixers below the HIFI baseline at some frequencies (Fig. 4.20). The flight mixers and flight-spare mixers have been selected from this wafer. PS8 shows a large relative spread in junction area $\Delta A_J/A_J = 67\%$ and medium values for the DC-quality ($Q_{\text{opt}} = 8$) (Fig. 4.8). Its superior noise performance is attributed to its relatively large j_c of 13-14 kA/cm² and no significant average shift in absolute junction area, resulting in a good match of the frequency band (Subsec. 4.4.2.3). Based on the noise results the required junction area accuracy has to be better than 5% to meet the HIFI performance requirements. This follows from the comparison of the noise results for four direct neighbor devices with identically designed matching circuits.

From the theoretical performance analysis of the mixer designs based on a three frequency approximation of the quantum theory of mixing j_c and Q have been identified as the most critical fabrication parameters for the mixer performance optimization. The increase of j_c , at constant Q , results in a significant noise reduction especially for frequencies with microstrip losses of 30-40%.

The measured flight-mixer performance also has been modeled with the quantum theory of mixing based on the measured I-V-curves and actual parameters for j_c and Q . It is known that for devices with moderate Q like the FM-devices the effect of MAR increases the shot-noise. Thus MAR is included in the analysis by means of an effective charge $q(V)$ (compare Subsec. 2.4.4). The absolute calculated noise data deviate with a factor 2 from the measured data. But the calculated results show a good agreement with the measured noise data regarding the frequency-, bias-voltage and LO-power dependence. Thus the theory is expected to give reliable estimates for relative variations in noise performance.

¹Here, a reasonably large number of available devices is required for the applied extrapolation.

6.2 Outlook

With the presented results and analysis there are still several open issues and also new questions, which are to be resolved for an optimized design and realization of SIS-mixers in the future.

Material development: The noise calculations presented in this thesis predict a significant reduction in noise temperature with increased current density j_c especially for considerable microstrip losses (e.g. in Nb around 800 GHz, Fig. 5.6 (a)). At the moment AlN is developed as barrier-material for SIS-devices [89] with expected current densities around and above 30 kA/cm². With the same fabrication scheme applied for the HIFI band 2 mixers and AlN-barriers an improvement in noise performance of mixers for the KOSMA-telescope at 790-880 GHz is expected.

With AlN-barriers it is possible to fabricate Nb/Al-AlN/NbTiN-junctions, allowing to shift the upper mixing limit to higher frequencies (up to 1.5 THz, compare HIFI band 5 [82]). This technology also eliminates the cooling problem of Nb-junctions with all-NbTiN-microstrips (compare Subsec. 3.4.3) and lossless NbTiN could be used also as top-wiring material, which significantly improves the power coupling.

Matching circuit electro-magnetic design and analysis: Given the geometry of the matching circuits (Fig. 3.2), the accuracy of the simulation is very likely to be improved by using a 2D or even 3D approach for the simulation of its microwave properties. With modern 3D electromagnetic field solvers this is possible. These have already been used for the simulation of the waveguide probe and environment, but have been limited in their application to the integrated matching circuits because superconducting material properties have not been included in the standard implementation. But newer versions or new tools allow the definition of user defined material properties and dispersion relations (e.g. ADS [90]) or already include superconductive properties (e.g. time domain field simulator Mefisto [91]). With this method the SIS-junction, the matching circuit and the waveguide probe can be simulated and optimized within one model.

When using Nb as matching circuit material just around its gap-frequency, small local variations in device parameters (especially critical temperature T_c and ambient temperature T_{amb}) result in significant variations of the resulting microstrip impedances. In this frequency region the Mattis-Bardeen formalism to calculate the characteristic impedances shows an accuracy of better than 10%. This is still above the relative required accuracy for the junction areas of 5% and thus should be optimized. This requires the application of the more complex bulk solution of the surface impedances presented by R. Pöpel [92] with considerable numerical effort.

With the presented design approach, the applied characterization methods and selection criteria it has been possible to develop SIS-devices for the HIFI band 2 flight-mixers. The ambitious performance baseline regarding the noise and bandwidth of the mixers have been sufficiently met.

Appendix A

Details regarding the mixer noise calculation

A.1 Shot-noise calculation for an unpumped SIS-device

The shot-noise calculation for an unpumped SIS-device is used for two different purposes:

- for the determination of the effective charge $q(V)$ of Andreev-clusters responsible for enhanced sub-gap current and noise (see Subsec. 2.2.3 for theory and Subsec. 2.4.4 for noise calculation)

and

- for the determination of the IF-contribution (T_{IF} and G_{IF}) to the measured receiver noise T_{Rec} (see Subsec. 4.2.3.3).

In both cases the bias-voltage dependent shot-noise calculated from the unpumped DC I-V-curve is compared with the measured IF-output power. Here the actual calculation for the test-setup for the HIFI mixer characterization is given.

The shot noise output power of the unpumped SIS-device per Hz bandwidth is calculated from

$$p_{\text{shot}}(V)d\nu = \frac{1}{4} \cdot S_I(V) \cdot \frac{dI(V)}{dV} \cdot \coth\left(\frac{e \cdot V}{2k_B T_{\text{amb}}}\right) d\nu. \quad (\text{A.1})$$

Here, $I(V)$ is the measured I-V-curve of the device and $dI(V)/dV$ its derivative. $S_I(V) = 2 \cdot e \cdot I(V)$ is the shot noise spectral density and T_{amb} is the device ambient temperature.

Referring to the measurement setup (Fig. 4.5) the IF-chain starts at the mixer's SIS junction¹. The IF-output power can be simplified to

$$P_{\text{out}}(V) = B \cdot G_{\text{IF}} \cdot \{ p_{\text{shot}}(V) \cdot (1 - |\Gamma(V)|^2) + k_B \cdot T_{\text{ISO}} \cdot |\Gamma(V)|^2 + k_B \cdot T_{\text{HEMT}} \}. \quad (\text{A.2})$$

Here, B is the frequency band-width of the band-pass in the IF-chain, G_{IF} the input gain of the IF-chain, k_B Boltzmann's constant, T_{ISO} and T_{HEMT} the noise temperatures of the isolator and the HEMT-amplifier. The mismatch of the SIS-junction with current-voltage characteristics $I(V)$ to the IF-load admittance Y_L is given as

$$\Gamma(V) = \frac{Y_L - dI(V)/dV}{Y_L + dI(V)/dV}.$$

The fit of the calculated data $P_{\text{out}}(V)$ to the measured IF-output power as a function of bias-voltage allows the determination of G_{IF} , T_{ISO} and T_{HEMT} . The noise temperature of the IF-chain is then given as

$$T_{\text{IF}} = T_{\text{ISO}} \cdot |\Gamma(V)|^2 + T_{\text{HEMT}}.$$

A.2 Truncation of Bessel series in large signal analysis

In Equations 2.23, 2.24 and 2.21 series of Bessel functions with coefficients calculated from the I-V-curve and its Kramers-Kronig-transformed are calculated.

A.2.1 Factors containing the device characteristics

First the coefficients, containing the current-voltage coefficients and their convergence for large n are discussed.

- $I_{dc}(V_0 + n \cdot \hbar\omega/e)$: Due to the shape of an unpumped I-V-curve of an SIS-junction for large n this value converges to a linear function defined by the normal resistance (with $V_n = V_0 + n \cdot \hbar\omega/e$)

$$I(V_n) = V_n/R_N$$

- $I_{KK}(V_0 + n \cdot \hbar\omega/e)$: With respect to n this value for large n converges to zero.

¹In detail, the IF-chain includes the bond-wires for the outcoupling from the mixer-block, a first short semi-rigid cable, the bias-T, a second semi-rigid cable, the isolator, a third semi-rigid cable the first cold amplifier, the cable to the room-temperature IF-filters and -amplifiers.

A.2.2 Bessel function coefficients

(R1) The remaining factor in Eq. 2.23 is $J_{n-1}(\alpha) + J_{n+1}(\alpha)$. This factor is plotted for several α and n in figure A.1. For typical optimum pumped

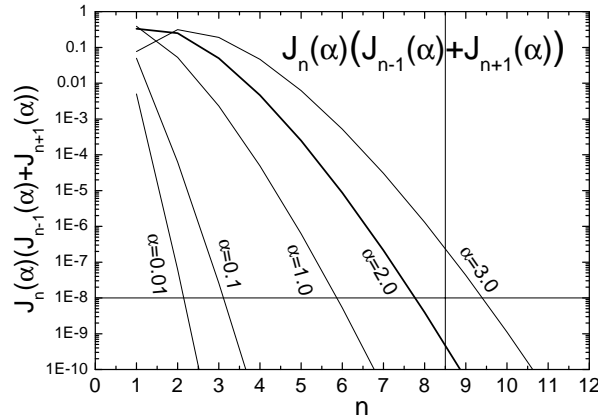


Fig. A.1: Bessel coefficients for several pump-levels α , depending on the order of the involved Bessel functions n in logarithmic scale. For pump-levels well below 2.0 summation over $n = 8$ orders yields a reasonable precision.

SIS-junctions of the size and current density in the range of the HIFI junctions, the pump-level α is well below 2.0. Thus if the 8th factor ($n = 8$) is included, its relative contribution to the total sum is 10^{-8} or less. That means, it is not necessary to include more coefficients with higher n .

Numerical considerations

- All calculations are done with normalized voltages and currents. The voltages are scaled with the gap-voltage V_{Gap} . The currents are scaled with the “gap-current” $I_{Gap} = V_{Gap}/R_N$.
- If not mentioned explicitly the summation in Eq. 2.23, 2.24 and 2.21 is generated for $n = -8, \dots, 8$. The Bessel function J_n converges stronger than exponentially to zero for increasing $|n|$, while the other factors are linear or less than linear in n^2 . Thus the truncation of the summands with $|n| > 8$ means no loss in accuracy while these summands themselves are in the order of accuracy for the first, major summands.
- The Kramers-Kronig-transform is calculated according to the equation

$$I_{KK}(V_0) = \frac{1}{\pi} P \int_{-\infty}^{+\infty} \frac{I_{dc}(V'_0) - V'_0}{V'_0 - V_0} dV'_0,$$

²The term $I_{dc}(V_0 + n \cdot \hbar\omega/e)$ converges to a linear function defined by the normal resistance of the device. The term $I_{KK}(V_0 + n \cdot \hbar\omega/e)$ converges to a constant.

where P is the Cauchy principal value, with the transformation given in the appendix in [93]. The integration limits are $\pm 6 \cdot V_{Gap}$. The actual limits are given by the maximum and minimum acquired bias-voltage of the I-V-curve, which is usually $(2.5 - 3.5) \cdot V_{Gap}$. Beyond these limits currents are calculated according to the normal resistance R_N . The integration steps are limited by the sample rate of the measurements, which is usually below 0.005 mV.

A.3 Calculation of the noise band-pass

Based on the previous subsections the noise performance for mixer designs and for models of the measured mixers has been calculated. The results are included in the analysis in Chap. 5.

Here, the necessary data and the optimization methods, which are applied for the calculation of the performance band-pass are briefly summarized. The **input data**, which are necessary to perform a calculation are in detail

- a measured DC I-V-curve $I_{DC}(V)$ and its Kramers-Kronig-transformed $I_{KK}(V)$,
- the frequency-dependent embedding impedance $Z_{emb}(\nu)$ and strip-line losses G_{Strip}
- the IF load-admittance $Y_{load} = 1/50 \Omega$,
- the LO-frequency ν_{LO} and
- the LO-pump level V_{LO} .

For the modeling of a measured SIS-mixer with analysis of the effect of MAR the measured IF-output power is also necessary.

The resulting **output data** are

- the pumped DC I-V-curve $I_{DC,pump}(V)$,
- the small signal admittance matrix $Y_{mm'}$ and the resulting value for mixer gain G_{Mix} (Eq. 2.32),
- the current correlation matrix $H_{mm'}$ and the resulting value for the mixer noise T_{Mix} (Eq. 2.35).

The general concept of the modeling of the embedding impedances and strip-line losses is given in the next chapter (Sec. 3.5).

The LO-frequencies ν_{LO} are defined by the considered frequency range. But the LO pump-level V_{LO} and the bias voltage V_{bias} had to be optimized numerically, to obtain a performance characterization of a mixer at a given frequency. Here, the optimization criterion has been the minimized noise performance for (compare Subsec. 4.1)

$$T_{Mix,IF} = T_{Mix} + \frac{10 \text{ K}}{G_{Mix}}. \quad (\text{A.3})$$

This optimization is close to the optimization, which is done during the experimental characterization and complies with the HIFI performance requirement definition for the mixers (compare Subsec. 4.1).

The optimization for $T_{Mix,IF}$ with respect to V_{LO} and V_{bias} has been done with nested intervals based on the experimental experience. The optimization with respect to V_{LO} is uncritical since for a given bias-voltage in the considered range only one minimum of $T_{Mix,IF}$ appears. With variation of V_{bias} below the gap-voltage often two minima of $T_{Mix,IF}$ appear in the measurements and in the calculations. In this case the larger bias-voltage has been chosen, since it is known that the optimum bias-voltage is around 2 mV.

Appendix B

Microstrip impedances

B.1 Effective microstrip width and dielectric constant

The geometry of the microstrip is given in Figure 3.10.

B.1.1 Normal conductive layer

The effective stripline width and effective dielectric constant for a stripline containing a normal conductive layer is calculated from [94]

$$W_{eff,n} = \frac{t_d \cdot \sqrt{\mu_0/\epsilon_0}}{Z_{Wheeler}(W_{eff,0}(\epsilon), \epsilon)},$$
$$\epsilon_{eff,n} = \left\{ \frac{Z_{Wheeler}[W_{eff,0}(\epsilon = 1), \epsilon = 1]}{Z_{Wheeler}[W_{eff,0}(\epsilon), \epsilon]} \right\}^2$$

where

$$Z_{Wheeler}(w, \epsilon) = 30 \cdot \sqrt{\frac{2}{\epsilon + 1}} \cdot \ln \left(1 + a \cdot \left\{ a \cdot b + \sqrt{a^2 \cdot b^2 + \frac{1 + \frac{1}{\epsilon}}{2} \cdot \pi^2} \right\} \right)$$

with $a = 4t_d/w$ and $b = \frac{14+8/\epsilon}{11}$ and

$$W_{eff,0}(\epsilon) = w + \frac{1 + \frac{1}{\epsilon}}{2} \cdot \frac{t_g/t}{\pi} \cdot \ln \left(\frac{4 \cdot e}{\left\{ \frac{t_g/t}{t_d} \right\}^2 + \left\{ \frac{\frac{1}{\pi}}{\frac{w}{t_g/t} + 1.1} \right\}^2} \right).$$

Here e is Euler's number $\exp(1)$; t_g/t is the thickness of the corresponding ground-plane or top-wiring layer. μ_0 is the permeability, ϵ_0 the permittivity of free space, t_d is the thickness of the dielectric layer, w the width of the stripline.

B.1.2 Superconductive layer

The effective stripline width for one involved layer due to fringing effects is evaluated from the following set of formula [95, 96]

$$\begin{aligned}
 w_{eff} &= k_{fringe} \cdot w \\
 k_{fringe} &= \frac{t_d}{w} \cdot \frac{2}{\pi} \cdot \ln \left(\frac{2 \cdot r_b}{r_a} \right) \\
 r_b &= \eta + \frac{p+1}{2} \cdot \ln(\Delta) \\
 \Delta &= \max(p, \eta) \\
 \eta &= \sqrt{p} \cdot \left(\frac{\pi w}{2t_d} + \frac{p+1}{2\sqrt{p}} \left\{ 1 + \ln \left[\frac{4}{p-1} \right] \right\} - 2 \tanh^{-1}(\sqrt{p}) \right) \\
 \ln(r_a) &= -1 - \frac{\pi \cdot w}{2t_d} - \frac{p+1}{\sqrt{p}} \tanh^{-1}(\sqrt{p}) - \ln \left(\frac{p-1}{4p} \right) \\
 p &= 2\beta^2 - 1 + 2\beta \cdot \sqrt{\beta^2 - 1} \\
 \beta &= 1 + \frac{t_{g/t}}{t_d},
 \end{aligned}$$

where t_d is the thickness of the dielectric layer, $t_{g/t}$ is the thickness of the related ground-plane or top-wiring, w is the stripline-width. All other values are defined in the set of formula above.

The effective dielectric constant for the dielectric with ε in a microstrip with geometrical width w where one involved layer is a superconductor of thickness $t_{g/t}$ is calculated from ([61], p. 105)

$$\varepsilon_{eff} = \frac{\varepsilon + 1}{2} + \frac{\varepsilon - 1}{2} \cdot \frac{1}{\sqrt{1 + 12 \cdot t_d/w}} - \frac{\varepsilon - 1}{4.6} \cdot \frac{t_{g/t}/t_d}{\sqrt{w/t_d}}.$$

B.2 Surface impedance for a normal conductive stripline in the limit of anomalous skin effect

The limit of the anomalous skin effect is given by $\delta_c \approx l$, the classical skin depth δ_c is in the same order of magnitude as the mean free path of the conducting electrons l . The geometrical orientation of the stripline is given in Figure B.1. The formula are used for the calculation of the stripline-impedances of the matching circuits. They were given by Kautz in [60], a misprint is removed in [97]. The surface impedance for a sinusoidal electric field $E_x(z, \omega) \cdot e^{i\omega t}$ and a current density $j_x(z, \omega) \cdot e^{i\omega t}$ is defined as

$$Z_{surf}(\omega) = \frac{E_x(0, \omega)}{\int_0^{t_d} j_x(z, \omega) dz}. \quad (B.1)$$

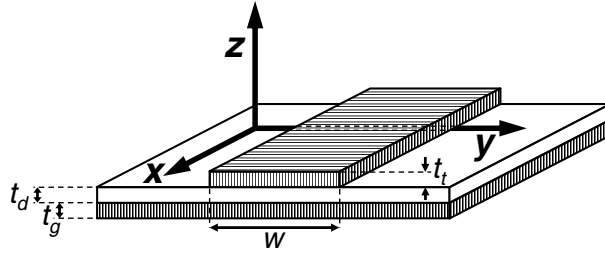


Fig. B.1: Microstrip geometry (same as in Figure 3.10): The propagation of the field is in direction of the x -axis, while the stripline thickness is the parameter in z -direction.

With the given geometry Maxwell's equations lead to the integro-differential equation

$$\frac{d^2 E_x}{dz^2} = i\alpha^{-3} \int_0^{t_t} E_x(z') \cdot K \left(\frac{z' - z}{l} \right) dz', \quad (\text{B.2})$$

$$\text{where } K(u) = \int_1^\infty \left(\frac{1}{r} - \frac{1}{r^2} \right) e^{-|u| \cdot r} dr$$

Formula B.2 can be transformed to

$$E_x(z) = E_x(t_t) + i\frac{\alpha}{l} \int_0^{t_t} E_x(z') \cdot G_1 \left(\frac{z' - t_t}{l}, \frac{z' - z}{l} \right) dz', \quad (\text{B.3})$$

where for the relevant range $u \leq 0$ and $v \geq u$ the function $G_1(u, v)$ is given by

$$\begin{aligned} G_1(u, v) &= \frac{1}{24} \{ (u^3 + u^2 - 10u - 6)e^u + (u^4 - 12u^2) \cdot E_1(|u|) \} \\ &+ \frac{1}{24} \{ (|v^3| - v^2 - 10|v| + 6)e^{-|v|} - (v^4 - 12v^2) \cdot E_1(|v|) \} \\ &+ \frac{1}{6} (v - u) \{ (u^2 + u - 4)e^u + (u^3 - 6u) \cdot E_1(|u|) \} \\ &+ \frac{2}{3} (|v| + v). \end{aligned}$$

The used function $E_1(u)$ is the solution of the integral

$$E_1(u) = \int_u^\infty \frac{\exp(-u')}{u'} du',$$

which can be approximated with a polynomial ([98] p. 231). Thus by dividing the interval $[0, t_t]$ into n equidistant values for x_i , and approximating the integral in formula B.3 by the sum of the integrand values at x_i multiplied by $\Delta x = t_t/n$, one obtains a linear system of equations for $\vec{E}_z = E_z(x_i)$ with $i = 0 \dots n - 1$, which can be solved by matrix inversion.

The electrical field at the top of the stripline $E_x(z = t_t)$ can be chosen to be any nonzero normalization factor, because the related current is calculated

from the electrical field thus scaled with the same factor. The resulting surface impedance does not depend on the absolute value of $E_x(z = t_t)$.

From the solution $E_x(z)$ the current can be calculated according

$$\int_0^{t_t} j_x(z) dz = \frac{3}{4} \sigma \int_0^{t_t} E_x(z) \cdot G_2 \left(\frac{z - t_t}{l}, \frac{z}{l} \right) dz,$$

$$\text{where } G_2(u, v) = \int_u^v dr \int_1^\infty \left(\frac{1}{s} - \frac{1}{s^3} e^{-|r|s} \right) ds.$$

Here in the relevant range $u \leq 0$ and $v \geq 0$ the solution of the integral $G_2(u, v)$ is

$$\begin{aligned} G_2(u, v) = & \frac{3}{4} + \frac{1}{6} \{ (u^2 + u - 4)e^u + (u^3 - 6u) \cdot E_1(|u|) \} \\ & + \frac{1}{6} \{ (v^2 - v - 4)e^{-v} - (v^3 - 6v) \cdot E_1(v) \}. \end{aligned}$$

Thus the contributions for the surface impedance in formula B.1 are evaluated.

Appendix C

Specification of the optics contribution to the measured receiver noise

The optics contribution to the measured receiver noise is included in the analysis as the effective optics noise temperature T_{Opt} , as given in Eq. 4.6. In this appendix the FTS-measurements of the transmission coefficients and the analysis are presented.

C.1 Consistent calculation of optics noise contribution

In order to validate the consistent use of Eq. 4.6 for the effective noise contribution for the optics component the radiation temperature of the load signal and the optics components just in front of the mixer is evaluated.

The radiation temperature according to Callen and Welton is already given in Eq. 2.6. It fulfills the following relation

$$T_{\text{C\&W}}(\nu, T) = T_{\text{Pl}}(\nu, T) + \frac{h\nu}{2k_B}, \quad (\text{C.1})$$

where $T_{\text{Pl}}(\nu, T)$ is the radiation temperature according to Planck. Indices “C&W” denote radiation temperatures according Callen and Welton, while indices “Pl” denote the use of the Planck radiation temperature.

The radiation temperature of the load signal and the optics components in front of the mixer with G_{comp} the linear power gain (< 1) of a component

and $A_{\text{comp}} = 1 - G_{\text{comp}}$ is then

$$\begin{aligned}
 T_{\text{rad}} &= T_{\text{load,C\&W}} \cdot G_{\text{BS}} \cdot G_{\text{Win}} \cdot G_{\text{N-Sh}} \\
 &\quad + T_{\text{BS,C\&W}} \cdot A_{\text{BS}} \cdot G_{\text{Win}} \cdot G_{\text{N-Sh}} \\
 &\quad + T_{\text{Win,C\&W}} \cdot A_{\text{Win}} \cdot G_{\text{N-Sh}} \\
 &\quad + T_{\text{N-Sh,C\&W}} \cdot A_{\text{N-Sh}} \tag{C.2}
 \end{aligned}$$

$$\begin{aligned}
 &= T_{\text{load,PI}} \cdot G_{\text{BS}} \cdot G_{\text{Win}} \cdot G_{\text{N-Sh}} \\
 &\quad + T_{\text{BS,PI}} \cdot A_{\text{BS}} \cdot G_{\text{Win}} \cdot G_{\text{N-Sh}} \\
 &\quad + T_{\text{Win,PI}} \cdot A_{\text{Win}} \cdot G_{\text{N-Sh}} \\
 &\quad + T_{\text{N-Sh,PI}} \cdot A_{\text{N-Sh}} \\
 &\quad + \frac{h\nu}{2k_B} \cdot (G_{\text{BS}} \cdot G_{\text{Win}} \cdot G_{\text{N-Sh}} + A_{\text{BS}} \cdot G_{\text{Win}} \cdot G_{\text{N-Sh}} \\
 &\quad + A_{\text{Win}} \cdot G_{\text{N-Sh}} + A_{\text{N-Sh}}) \tag{C.3}
 \end{aligned}$$

If the expression inside the brackets is equal to unity the consistency of the definition for the equivalent noise temperature of the optics components (Eq. 4.6) is shown.

$$\begin{aligned}
 &G_{\text{BS}} \cdot G_{\text{Win}} \cdot G_{\text{N-Sh}} \\
 &+ A_{\text{BS}} \cdot G_{\text{Win}} \cdot G_{\text{N-Sh}} \\
 &\quad + A_{\text{Win}} \cdot G_{\text{N-Sh}} \\
 &\quad + A_{\text{N-Sh}} = G_{\text{BS}} \cdot G_{\text{Win}} \cdot G_{\text{N-Sh}} \\
 &\quad + (1 - G_{\text{BS}}) \cdot G_{\text{Win}} \cdot G_{\text{N-Sh}} \\
 &\quad + (1 - G_{\text{Win}}) \cdot G_{\text{N-Sh}} \\
 &\quad + (1 - G_{\text{N-Sh}}) \\
 &= G_{\text{BS}} \cdot G_{\text{Win}} \cdot G_{\text{N-Sh}} \\
 &\quad + G_{\text{Win}} \cdot G_{\text{N-Sh}} - G_{\text{BS}} \cdot G_{\text{Win}} \cdot G_{\text{N-Sh}} \\
 &\quad + G_{\text{N-Sh}} - G_{\text{Win}} \cdot G_{\text{N-Sh}} \\
 &\quad + 1 - G_{\text{N-Sh}} \\
 &= 1 \tag{C.4}
 \end{aligned}$$

For the beam-splitter and the N-shield transmission the measured and extrapolated data have been applied. For the transmission of the dewar window further analysis has been necessary to obtain consistent results.

C.2 Transmission measurements of the Mylar beam-splitter

For the beam-splitter Mylar with a nominal thickness of 12 μm has been used. In the heterodyne setup it is irradiated under an angle of 45°. Thus the

polarization of the radiation has to be considered. For a first characterization it is measured under an angle of 0° . The results are shown in Fig. C.1 (left). The noise in the measured transmission at several frequencies (≈ 1450 GHz,

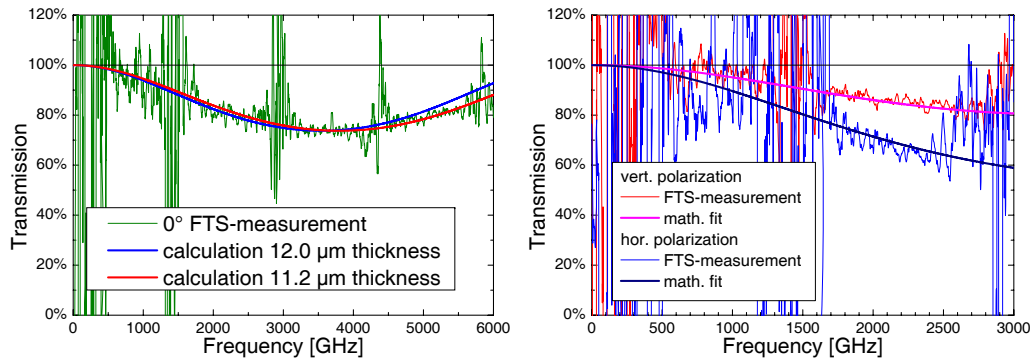


Fig. C.1: FTS-transmission of 12 μm mylar beam-splitter. Left: Transmission of beam-splitter under 0° . A calculation with a refraction index of $n=\sqrt{3.1} \approx 1.781$ yields a thickness of 11.2 μm (red line). Right: Transmission of beam-splitter under 45° with mathematical extrapolation to lower frequencies.

2900 GHz, 4350 GHz, 5800 GHz) refers to minima in the transmission of the internal beam-splitter of the FTS. The manual fit yields a thickness of 11.2 μm .

For the measurement of the polarization dependent transmission of the beam-splitter under 45° a polarization grid has been integrated in the FTS-setup (Fig. C.2, left). The resulting data are given in Fig. 4.5 (right). The ac-

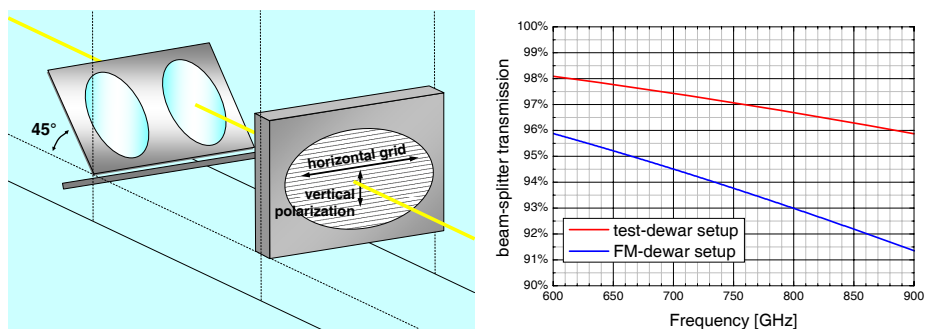


Fig. C.2: Left: Schematic setup of FTS-measurement under 45° with polarization filter. In the picture the vertical polarization direction is depicted. During a heterodyne measurement the beam splitter is rotated by 90° along the optical axis. Right: Beam-splitter transmissions for both heterodyne setups.

tual transmission data for the beam-splitter transmission at the HIFI band 2 frequency band edges are given in the following table:

polarization	transmission at	
	636 GHz	802 GHz
vertical	97.87 %	96.72 %
horizontal	95.42 %	92.98 %

The bold values for the horizontal polarization are applied for the calculation of the optics contribution in the FM-dewar setup, because the mixer unit has been in vertical polarization during the FM-tests. During the FTS-measurement the beam splitter has been rotated by 90° relative to its position in the heterodyne setup. The transmission data for the beam-splitter used with the test-dewar setup are given by the red line in Fig. C.2 (right).

C.3 Transmission coefficients of the Teflon dewar window

C.3.1 Transmission measurements of the Teflon dewar window

The dewar windows for both heterodyne setups have been made from Teflon with a nominal thickness of 0.5 mm. The transmission of the test-dewar window previously has been characterized and shows a minimum in the center of the HIFI frequency band 2. For the window of the FM-dewar the thickness of Teflon has been reduced to 0.44 mm, in order to obtain a maximum in transmission in the desired frequency band. The corresponding data are given in Fig. C.3.

For the calculated transmission the losses have been derived from the interferometric reflection at a plane parallel plate and dielectric losses in the material. A refraction index of 1.41 has been used for Teflon. The fit of the physical model to the measured data above 2000 GHz has been performed by variation of the thickness. For the raw material (Fig. C.3, top) a thickness of $0.52 \mu\text{m}$ has been found. This results in a transmission minimum in the relevant frequency range.

The transmission data for Teflon with a reduced thickness of $d = 0.44 \mu\text{m}$ are given in Fig. C.3 (bottom) with a fitted thickness of 0.436 mm.

C.3.2 Revision of dewar-window transmission data from measured mixer performance

After the application of the fitted FTS-data for the dewar-window transmission significant discrepancies in the resulting corrected mixer noise temperatures appeared. Thus the data had to be revisited.

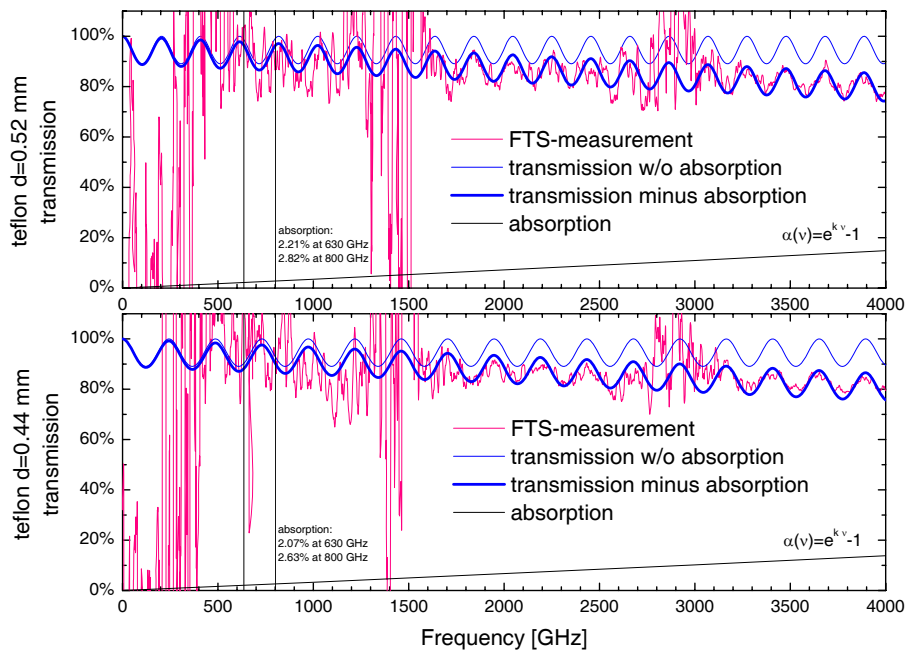


Fig. C.3: Measurement and calculation of Teflon transmission with thickness of 0.52 mm (top, raw material) and 0.44 mm (bottom, reduced thickness).

The measurement data for the dewar windows of the test-dewar and the FM-dewar are given as the dashed lines in Fig. C.4 (left). These data first have been applied to evaluate the corrected mixer noise temperature from the measured receiver performance. But for mixers, which have been characterized in both heterodyne setups (“test-dewar” and “FM-dewar”) significant discrepancies appeared. In the center of the band the discrepancies in corrected mixer noise temperature have been 40-50 K, while at the band edges the corrected mixer noise temperatures complied well.

The discrepancies in corrected mixer noise have been observed for three mixers. Thus this effect has not been assumed to be a real change in mixer performance during the storage between the two measurements¹. But the discrepancies must be explained from differences in the correction for the noise contributions of the other components.

The transmission data for the dewar-windows have been identified as the source of these discrepancies, because their strong frequency dependency explains the frequency dependent deviations in corrected mixer noise. In the center of the band for the test-dewar an absorption of 16% at 720 GHz (compare Fig. C.4, left) has been evaluated from the FTS-measurements. This results in a large correction for the optics contribution and thus a very low corrected mixer noise temperature. At the same frequency for the FM-dewar an absorption of 2.5% has been applied, which results in a much larger

¹This conclusion is verified by the fact, that the mixer performance data after this revision have been verified by the HIFI consortium. Here the mixers have been characterized in a complete different setup.

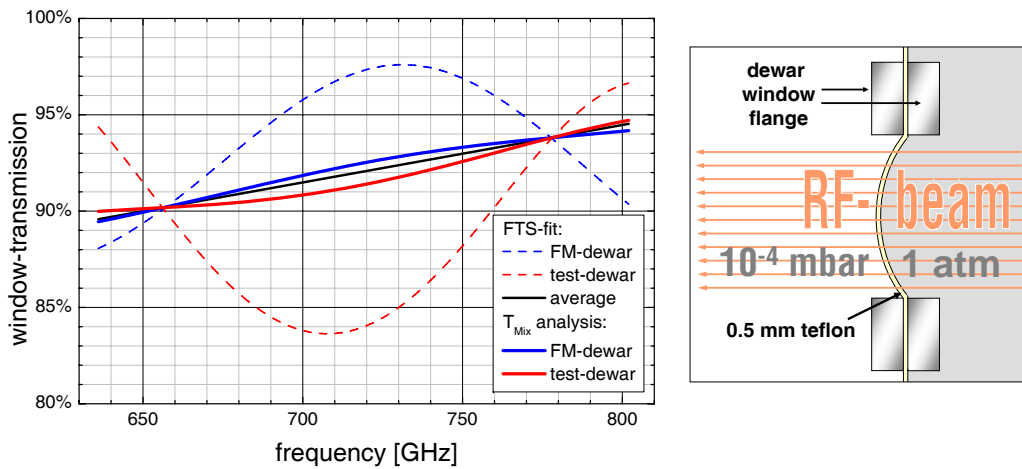


Fig. C.4: Left: Transmission data for teflon dewar window in test-dewar and FM-dewar. The dashed lines denote the fit to the transmission data obtained with the FTS. The black line is the average of both transmissions. The solid lines represent the transmission data after correction incorporating noise measurements of the three FM mixers in both setups. Right: The curvature of the dewar-window because of the difference in pressure of 1 atm produces angles of incidence different from 0° for the RF-radiation. The order of magnitude for the curvature is as given in the sketch.

corrected mixer noise temperature.

Thus it has been assumed that the average correction data have been reliable, but the variations of the transmission over the frequency range have been too large. The transmission data for both dewar windows have been corrected to the data, which are given in Fig. C.4 (left) as solid blue and red lines, in order to obtain consistent data for the corrected mixer noise. With these data for the noise correction because the deviations in corrected mixer noise have been 10-20 K maximum. This is within the typical accuracy of the mixer noise correction.

The change of the window transmission data can be justified by the curvature of the dewar window (Fig. C.4, right). Since the beam does not overall hit the dewar window at the exact angle of 0° , the interference pattern is assumed to flatten out and thus smaller variations in transmission are justified.

C.4 Transmission measurements of the radiation shield at 77 K-stage

The radiation shield at the 77 K stage is necessary to shield the cold-plate and the components connected to it from the room-temperature radiation

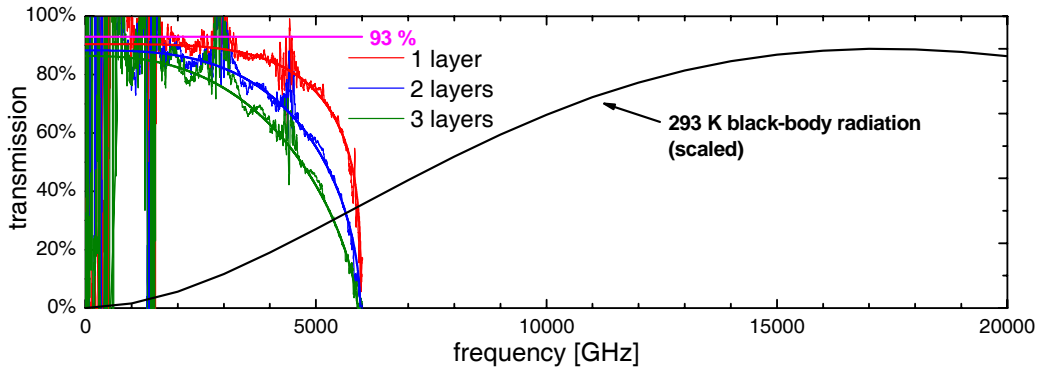


Fig. C.5: Zitex G 108 transmission measured with FTS for 1, 2 and 3 layers. For comparison the room temperature black-body radiation added.

of the dewar-window, the dewar wall and diffuse radiation from outside the dewar. It extends the hold time of the dewar and prevents the small devices in the focus of the mirror inside the dewar from a possible heating because of the radiation.

In the test-dewar a thin teflon shield has been used to absorb the diffuse RF-radiation from the dewar-window and the other surrounding warm components. For the de-embedding calculations a transmission of 100% has been assumed to be sure not to overestimate the optics-contribution to the receiver noise temperature.

For the FM-tests Zitex G 108 [99] with a nominal thickness of 0.20 mm has been investigated and finally used. The same material has been also measured in reference [100], but does not have exactly the same transmission as the material in the FM-dewar. The material has been analyzed in the FTS in one, two and three layers. The data are shown in Figure C.5. Again the data quality below 1500 GHz is quite poor. For comparison the black-body radiation according to Plancks equation is plotted in a scaled form. The measurements show the same tendency seen in [100] that the effect of multiple layers is lower for longer wavelengths, implying stronger scattering in this frequency-region, not merely absorption.

In reference [100] there is given a frequency dependence for the transmission and absorption of another type of the material (Zitex G 125), which is not suitable for the measured type G 108. To extrapolate the data to lower frequencies and to estimate the absorption of the room temperature radiation the empirical function for the transmission, given in Eq. C.5 has been applied.

$$T(\nu) = (1 - a_0) \cdot \left[1 - \left(\frac{\nu}{\nu_{\max}} \right)^{n_1} \right]^{\frac{1}{n_2}}. \quad (\text{C.5})$$

The fit parameters for the different layers are given in Table C.1. The functions are also plotted as lines in Figure C.5.

	a_0	ν_{max}	n_1	n_2
1 layer	0.095	5.97 THz	4.0	3.4
2 layers	0.117	5.96 THz	3.0	1.9
3 layers	0.136	5.90 THz	2.5	1.5

Tab. C.1: Fit-parameters for one, two and three layers of Zitex G 108 in Eq. C.5.

In order to justify whether 1, 2 or more layers of Zitex are required as N-shield, the relative absorption of the room temperature black-body radiation has been evaluated. For the transmission function of Zitex below ν_{max} the function, given in Eq. C.5, is assumed. Above ν_{max} it is assumed to be zero. For the total room temperature radiation the integral $\int_{\nu} P_{\text{Planck}}(\nu) d\nu$ has been evaluated by numerical integration with steps of $\Delta\nu = 1$ GHz from 0 to 120 THz. For the relative transmission the convolution integral

$$t_{\text{rel}} = \frac{\int_{\nu} P_{\text{Planck}}(\nu) \cdot T(\nu) d\nu}{\int_{\nu} P_{\text{Planck}}(\nu) d\nu}$$

has been evaluated by numerical integration with the same frequency limits and integration steps.

The results for the relative absorption ($a_{\text{rel}} = 1 - t_{\text{rel}}$) of room-temperature radiation by the Zitex layers are given in the last column of Table C.2. Here also the transmission of the Zitex layers is given for the HIFI frequency band 2 edges.

	transmission at		a_{rel} : absorption of 293 K black-body
	636 GHz	802 GHz	
1 layer	90.45 %	90.45 %	97.6 %
2 layers	88.24 %	88.18 %	98.1 %
3 layers	86.16 %	85.99 %	98.4 %

Tab. C.2: Transmission of one, two and three layers of Zitex G 108 (column 2 and 3) and theoretical absorption of the room-temperature black-body radiation (column 4).

It is obvious from this estimation that already one layer of Zitex G 108 absorbs the major part of the room-temperature radiation, while the use of more layers would have small relative impact on the overall room-temperature black-body absorption, but would increase the optics losses from 9.5 % to 11.8 % or 13.8 %. Thus one layer of Zitex G 108 is used as heat-shield at the 77 K-stage.

Incorporating the absolute error of 3% in measured Zitex transmission quantified by the inaccuracy of the fit to the data a transmission value of 93% is applied, since no higher correction than 7% for losses can be justified.

Appendix D

DC- and RF-characterization of devices and wafers

D.1 Tabular overview of RF-characterized devices

In the first column the name of the fabricated wafer is given with the fabrication date from the first DC-measurements in column 2. In the third column the name of the mask design is given. The three mask designs NbTiN3, CCN8 and NbTiN4 are already described in Chap. 3. The other designs NbTiN1, NbTiN2 and CCN5 are previously existing iterations of mask sets. In the fourth column the names of the devices which are characterized in RF-measurements are given. These names consist of a letter to designate the column (B,C,D at KOSMA or U,V at DIMES) and a number for the row of the device. The fifth and sixth columns show the measured or estimated DC-quality parameters of the involved NbTiN-layer [13],[80](*),[101]. The seventh column gives some comments on the fabrication scheme. Some wafers have been fabricated with UV-photolithography utilizing a monochromatic light source of a wavelength of $\lambda=193$ nm. The mask aligner is specified to work with an accuracy of 10% down to structures with linear dimensions of 800 nm. For smaller dimensions the inaccuracy increases. For newer wafers the technique of electron beam lithography (EBL) combined with chemical-mechanical polishing (CMP) [14] has been applied to achieve a higher accuracy in the junction definition. For details see [13].

FM-devices are underlined. The wafers in bold typeface are presented in detail in Sec. 4.3.

batch name	fabr. date	mask design	RF-characterized devices	NbTiN param.		comments
				T_c [K]	ρ_n [$\mu\Omega\text{cm}$]	
j10		NbTiN1	C19 D32	14.5	125	UV batch, no CMP
j12		NbTiN2	B23 B17 D27	15.1	100	UV batch, no CMP
j13	03/01	CCN5	D43 D42	15.0	105	UV batch, CMP-clean, CMP-supported lift-off
j14	04/01	CCN5	D54 D41	—" (*)	—" (*)	UV, CMP clean
j15	05/01	NbTiN2	D49 D50 D40 D42 B23 D46	—" (*)	—" (*)	UV, CMP clean
ps1	08/01	NbTiN2	D07 D16	—" (*)	—" (*)	EBL, CMP
ps2	12/01	NbTiN2	B52	—" (*)	—" (*)	EBL, CMP
ps4	04/02	NbTiN3	D11 D22 D33	—" (*)	—" (*)	EBL, CMP
ps8	07/02	NbTiN3	D01 D07 D18 B40 B53 B47 B65 D40 D63 D42 B50 B39 C25 <u>C19</u> B57 C17 C18 C20 C26 C28 B31 <u>B61</u> <u>B45</u> B52	13.8	80	EBL, CMP
CCN8-2	10/02	CCN8	U12 U22	13.5	111	fabricated by DIMES (NL)
CCN8-5	03/03	CCN8	V20 V16	13.5	111	fabricated DIMES (NL)
ps24	07/03	NbTiN3	B53 B48	>14 (*)	80 (*)	EBL, CMP
ps34	08/03	NbTiN3	B34 B58 C07 C18	14.7	78	EBL, CMP
spk3	02/04	NbTiN3	C16 C30	15.3	90	UV, no CMP, Nb and NbTiN swapped
paks10	03/05	NbTiN4	C04	15 (*)	80 (*)	EBL, CMP

D.2 Measured noise temperatures for all characterized mixers

The noise performance of the characterized mixers in terms of $T_{\text{Mix,IF}} = T_{\text{Mix}} + 10 \text{ K}/G_{\text{Mix}}$ (for definition see Subsec. 4.1) for all devices is given in four plots (Fig. D.1 to D.4). All data have been measured in the same test-dewar setup and have been analyzed with the corresponding correction for the optics components (see Appendix C). Because of their superior RF-performance there have been tested a lot more devices of wafer PS8 than from any other wafer.

In Fig. D.1 the noise performance of the devices on wafers, fabricated prior to PS8, in Fig. D.4 of the wafers fabricated after PS8 is given. The ordinate for the receiver noise $T_{\text{Mix,IF}}$ is scaled to 1000 K. In Figures D.2 and D.3 the noise performance of the devices on PS8 is given grouped according the columns of the wafer. Here the ordinate for the receiver noise $T_{\text{Mix,IF}}$ is scaled to 500 K.

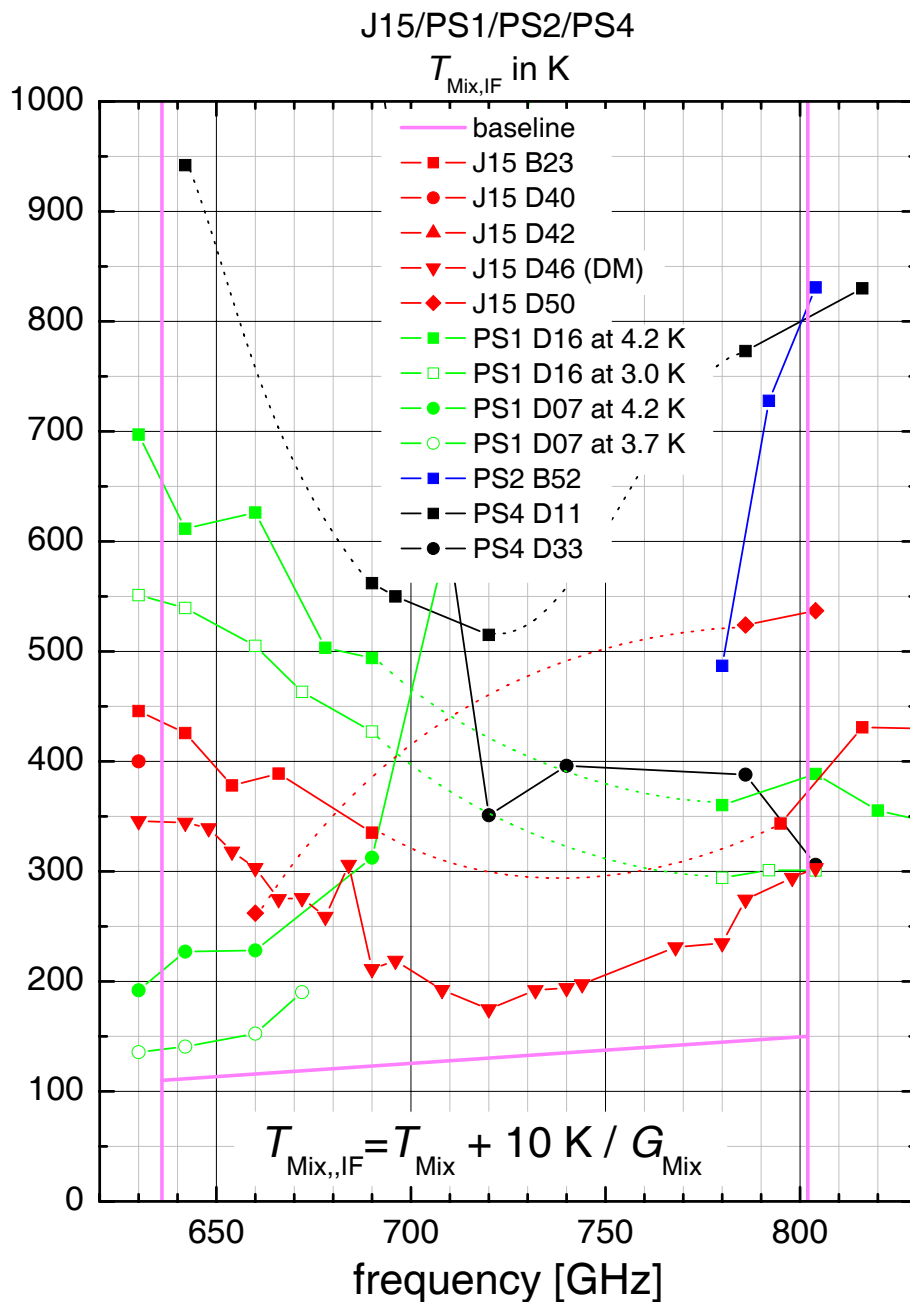


Fig. D.1: Noise performance $T_{\text{Mix,IF}}$ for the RF-measured devices of wafers J15, PS1, PS2, PS4: Two devices show a noise performance below 200 K, but do not reach the HIFI performance base-line. Device J15 D46 has been characterized as HIFI band 2 demonstration model (DM).

Seven devices of the wafer PS8 reach the performance in the center of the band already at an ambient temperature of 4.2 K, while only two devices (PS34 C18, PAKS10 C04) from all the other wafers show a performance below the base-line at some frequencies. Since these two devices show a performance of more than 350 K at 802 GHz, they have been ruled out as flight mixer devices. It is obvious, that the density of points in the Figures

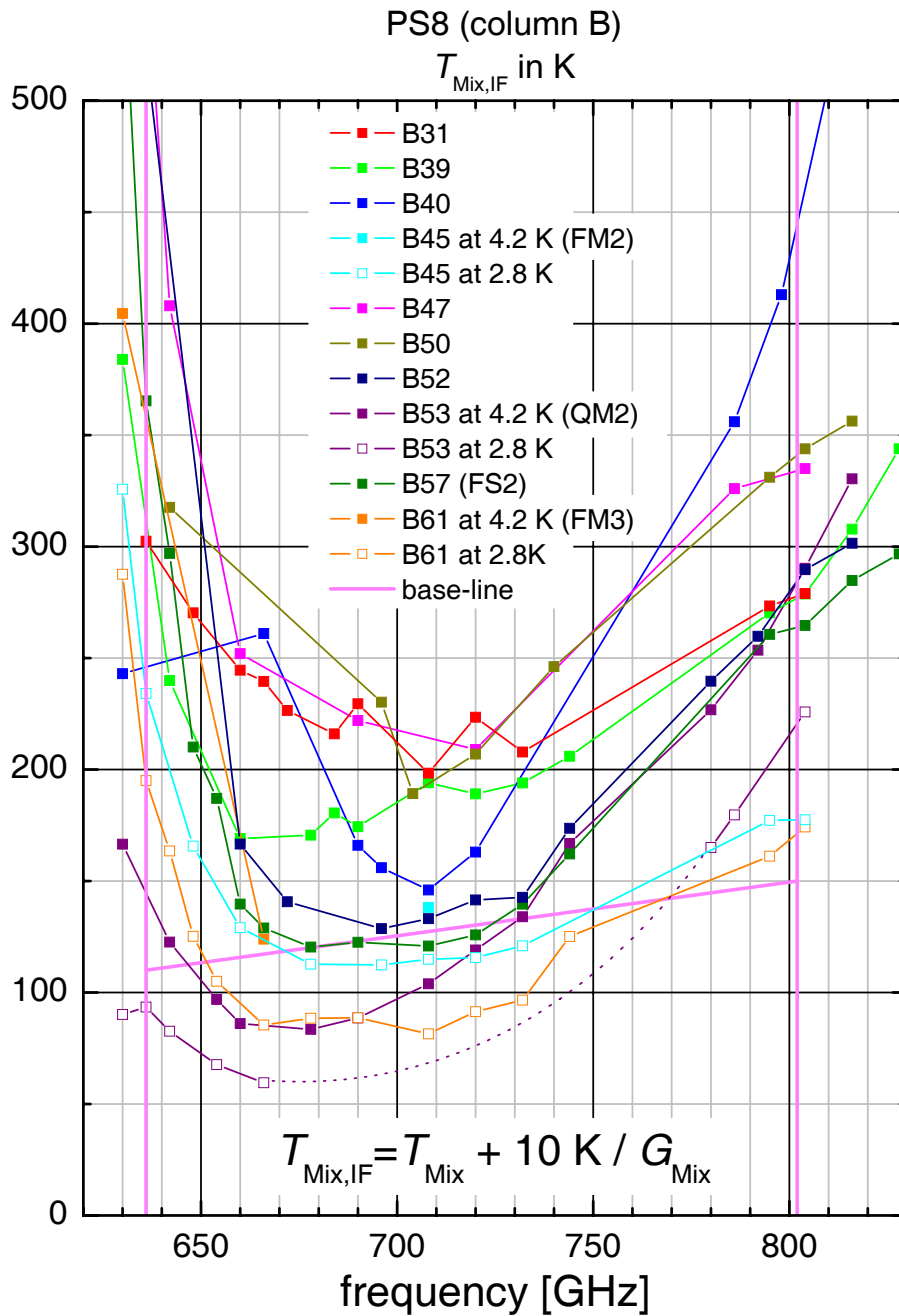


Fig. D.2: Noise performance $T_{\text{Mix,IF}}$ for the RF-measured devices of wafer PS8 column B: Four devices (B45, B53, B57, B61) show a performance below the base-line. Device B53 has been characterized as HIFI band 2 qualification model (QM). Device B61 has been delivered as flight-model mixer (FM) and integrated in the HIFI receiver for the vertical polarization. Device B45 has been characterized as FM attrition mixer. Device B57 has been characterized as flight-spare (FS) mixer.

D.2 and D.3 for PS8 around and just above the baseline is much higher than in Figures D.1 and D.4 for all the other wafers. Thus the qualification model (QM), flight model (FM) and the flight spare (FS) mixers are taken all from

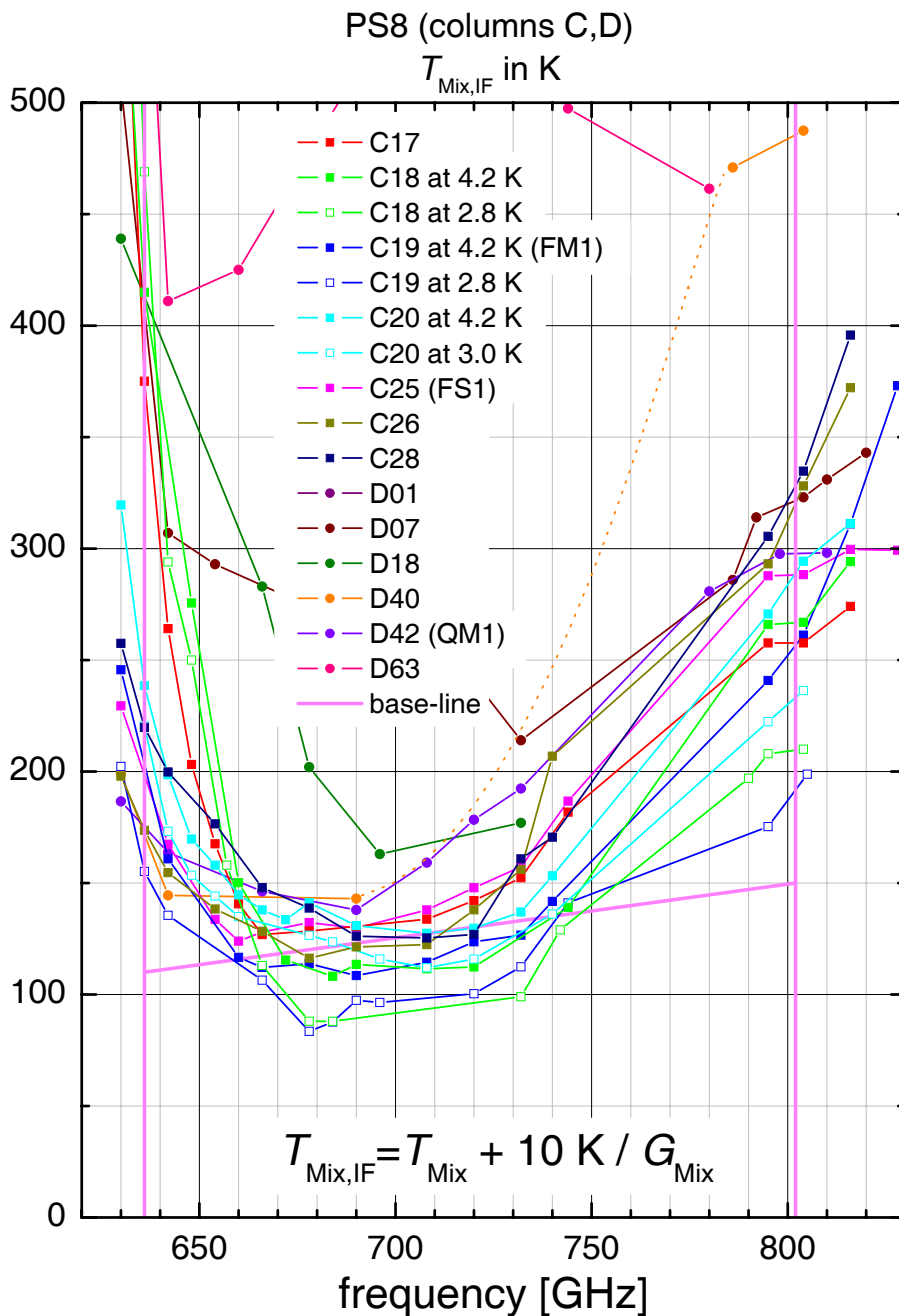


Fig. D.3: Noise performance $T_{\text{Mix,IF}}$ for the RF-measured devices of wafer PS8 columns C and D: The performance of five devices (C18-C20, C26, C28) is below the base-line for some frequencies. Device D42 has been used as mixer for the QM-program. Device C19 has been delivered as FM and is integrated in the HIFI receiver for the horizontal polarization. Device C25 has been characterized as flight-spare (FS) mixer.

PS8¹.

¹The specification of demonstration model (DM), qualification model (QM), flight model (FM) and flight-spare (FS) refers to different stages of the Herschel/HIFI project. Applied to the mixers this means that DM and QM are prototypes of the later mixers and undergo specific pre-tests. The FM mixers are integrated in the actual HIFI receiver. In the case

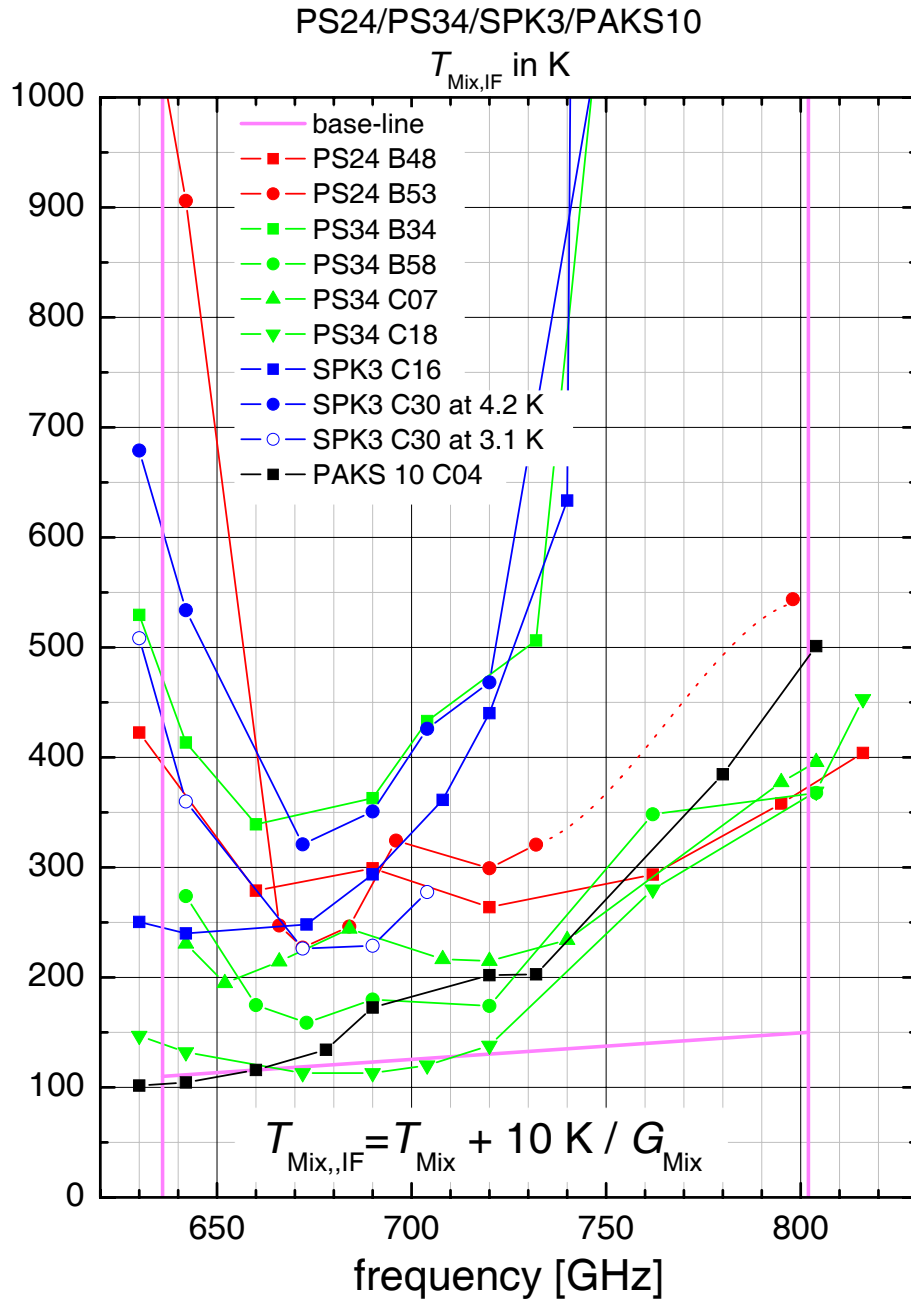


Fig. D.4: Noise performance $T_{\text{Mix,IF}}$ for the RF-measured devices of wafers PS24, PS34, SPK3 and PAKS10: Two devices show a performance below the base-line in the lower frequency band, but above 350 K at the upper frequency band.

The limits in optimum performance at 2.8 K according to these data are just below 100 K at 630 GHz and 170 K at 802 K.

serious defects occur with the FM-mixers, they can be exchanged with the FS mixers.

D.3 Selection process of devices for the flight mixers

The complete process of the characterization and selection of the mixer devices for HIFI is illustrated in Fig. D.5.

It starts with a fabricated DC-characterized wafer of SIS-devices and ends with three RF-characterized flight model mixers (two for each polarization and one attrition mixer). The main decision and selection criteria are given with the number of the respective subsection in this thesis, where the criterion is described. In the top part of the diagram the information mainly refers to the DC-measurement data of a wafer, while in the bottom part of the figure the criteria refer to the RF-measurement data of single SIS-mixers.

The pre-selection is mainly done based on the DC-measurement data (DC-quality Q , Josephson resonance frequency ν_{res}). For the optimum devices an additional analysis of the estimated band-pass is added to verify or modify the choice of device for RF-measurements in the liquid helium dewar. The results from the heterodyne and FTS-measurements are used to select the optimum mixers as flight-mixers. The RF-characterized mixers are also analyzed in order to obtain a more accurate estimate of j_c for other devices from the same wafer.

D.3.1 Selection of devices for RF-measurements based on the DC-measurements

From the DC-measurements the first information of the devices of a fabricated wafer becomes available. First two basic criteria are applied in order to select candidates for the RF-measurements.

Two basic selection criteria: From the DC-measurements first the devices have been identified, which show a Josephson resonance frequency ν_{res} in the desired frequency band and at the same time a possibly large DC-quality Q .

The DC-quality Q is the only parameter obtained from the DC-measurements which yields an information about the shot-noise contribution of a SIS-junction. A large value for Q implies a low sub-gap current. And a reduced sub-gap current results in a reduced shot-noise inside the barrier [27]. Thus devices with a possibly large DC-quality Q are selected. This concept is verified by noise calculations based on Tucker's theory for I-V-curves with variation in Q in Chap. 5.

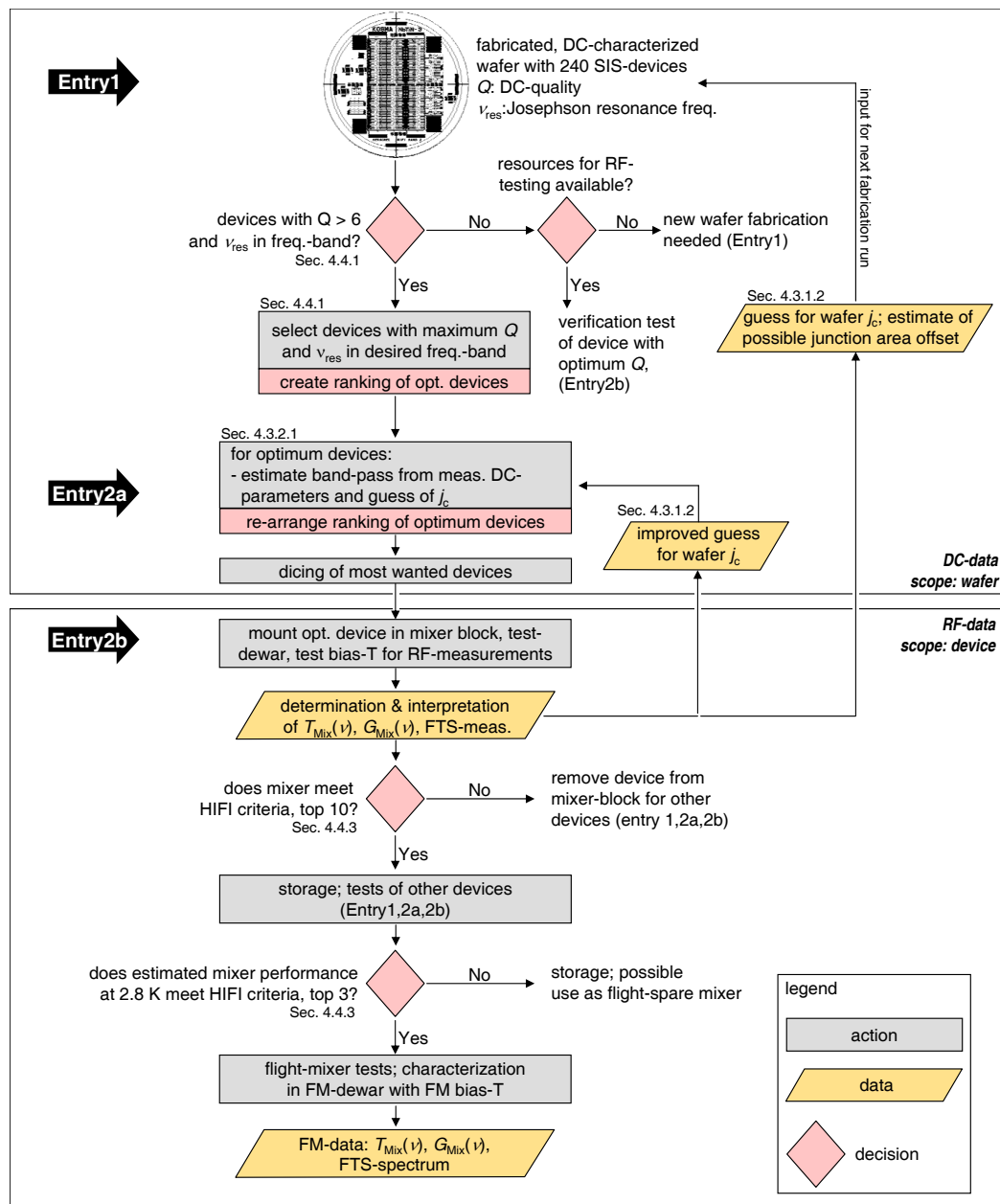


Fig. D.5: Flow chart for the selection of SIS-devices for the HIFI mixer band 2. Details of the main selection criteria are given in the subsection, which is noted at the respective item in the diagram. Criteria in the top part of the diagram refer to the DC-data of a whole wafer, while in the bottom part of the diagram the criteria refer to the RF-data of a SIS-mixer. In the standard case the process starts at "Entry1". If devices of a respective wafer are already RF-characterized, the process can start at "Entry2".

The Josephson resonance frequencies ν_{res} yield a direct estimation for the resonance frequencies of the matching circuit [102]. Experience shows that the best visible resonance usually indicates the lower edges of the frequency band. The higher resonances are sometimes also visible in the dipstick

measured IV-curve if accidentally some magnetic flux is present in the junction. The validity of this criterion is illustrated for some devices based on a comparison with later FTS-measurements in Subsec. 4.4.1.2.

From these two basic criteria a ranking for the optimum devices is created. Added to these two basic criteria is a “second” analysis, an estimation of the band-pass for the particular selected devices, as described in Subsec. 4.4.1.1. This is done in order to obtain a more consistent prediction of the band-pass, when the Josephson resonance frequencies comply with the lower band edge of the calculated band-pass. And the calculated band-pass is also evaluated to identify additional optimum devices (mainly in the direct vicinity of other optimum devices). This is done for devices, which show no clear Josephson resonance frequencies, but have a high value for Q to estimate the frequency region of optimum coupling.

From this “second” analysis the ranking for the optimum devices is re-arranged.

D.3.2 FTS-measurement interpretation

The FTS-measurement data, detection band pass $p(\nu)$ of the mixer, have been analyzed for three purposes:

- (R1) to identify the band-edges and optimum coupling regions during RF-measurements for the selection of LO-frequencies for heterodyne measurements,
- (R2) complementary data to noise measurements,
- (R3) comparison of calculated and measured band-pass in order to identify possible shifts in current density j_c and other fabrication specific parameters.

The first item is mainly relevant for the mixer selection phase. Frequency regions with strong variations in FTS-response have been characterized with a higher density in LO-frequencies ($\Delta\nu = 6$ GHz) than frequency regions with nearly constant FTS-response, unless significant discrepancies have been observed. The third item already has been described in Subsections 4.4.1.3 and 4.4.2.

FTS-measurement data as complementary data to noise measurement:

In two ways the FTS-measurement have yielded complementary information to the heterodyne data.

First, for the mixer characterization the FTS-response and the noise performance data have been used. In the relevant frequency region the intrinsic

junction noise is not strongly frequency-dependent. Thus a low noise of the mixer is related to a strong direct detection coupling. For the verification of the noise calculation it has been compared qualitatively in order to identify and remove possible errors in the measurement setup or analysis method.

Second, an important additional information of the FTS-data to the heterodyne data has been the measured conversion around 750 GHz. From the heterodyne measurements for all mixers increased noise temperatures around 750 GHz have been evaluated. But in the FTS-spectra no decrease in power conversion has been observed with the optics path evacuated, while the decrease has been observed without the evacuation of the optics path. In the heterodyne setup a major part of the optics path could not be evacuated. Thus the increased noise around 750 GHz has been identified as the absorption of the signal radiation due to several atmospheric water absorption lines (compare Table 4.1).

Bibliography

- [1] Th. de Graauw and F. P. Helmich. Herschel-HIFI: The Heterodyne Instrument for the Far-Infrared. In G. L. Pilbratt, J. Cernicharo, A. M. Heras, T. Prusti, and R. Harris, editors, *The Promise of the Herschel Space Observatory*, pages 45–51, 2001.
- [2] Th. de Graauw, N. Whyborn, E. Caux, T. Phillips, J. Stutzki, X. Tielens, R. Guesten, F. Helmich, W. Luinge, J. Pearson, P. Roelfsema, R. Schieder, K. Wildeman, and K. Wafelbakker. The Herschel-Heterodyne Instrument for the Far-Infrared (HIFI). In C. Cunningham and J. Oschmann, editors, *Astronomical Telescopes and Instrumentation 2006*, page to be published, PO Box 10, Bellingham WA 98227-0010, USA, 2006. SPIE.
- [3] G. L. Pilbratt. The Herschel mission, scientific objectives and this meeting. In *Proc. Symp. The Promise of the Herschel Space Observatory*, pages 13–20, 2000.
- [4] G. L. Pilbratt. Herschel mission: status and observing opportunities. In C. Cunningham and J. Oschmann, editors, *Astronomical Telescopes and Instrumentation 2006*, page to be published, PO Box 10, Bellingham WA 98227-0010, USA, 2006. SPIE.
- [5] A. Poglitsch, C. Waelkens, O. H. Bauer, J. Cepa, H. Feuchtgruber, T. Henning, C. v. Hoof, F. Kerschbaum, D. Lemke, E. Renotte, L. Rodriguez, P. Saraceno, and B. Vandenbussche. The Photodetector Array Camera and Spectrometer (PACS) for the Herschel Space Observatory. In C. Cunningham and J. Oschmann, editors, *Astronomical Telescopes and Instrumentation 2006*, page to be published, PO Box 10, Bellingham WA 98227-0010, USA, 2006. SPIE.
- [6] M. Griffin, A. Abergel, P. Ade, P. Andre, J.-P. Baluteau, J. Bock, A. Franceschini, W. Gear, J. Glenn, D. Griffin, K. King, E. Lellouch, D. Naylor, G. Olofsson, M. Rowan-Robinson I. Perez-Fournon, P. Saraceno, E. Sawyer, Alan Smith, B. Swinyard, L. Vigroux, and G. Wright. Herschel-SPIRE: Design, Performance, and Scientific Capabilities. In C. Cunningham and J. Oschmann, editors, *Astronomical Telescopes and Instrumentation 2006*, page to be published, PO Box 10, Bellingham WA 98227-0010, USA, 2006. SPIE.

- [7] P. L. Richards, T. Shen, R. E. Harris, and F. L. Lloyd. Quasiparticle heterodyne mixing in SIS tunnel junctions. *Appl. Phys. Lett.*, 34(5):345–347, 1979.
- [8] T. Phillips and K. Jefferts. Low-temperature bolometer heterodyne receiver for millimeter wave astronomy. *Rec. Sci. Instrum.*, 44(8):1009–1014, 1973.
- [9] P. H. Siegel. Terahertz Technology. *IEEE Trans. Microwave Theory and Techniques*, 50(3):910–928, March 2002.
- [10] J. Zmuidzinas and P. L. Richards. Superconducting detectors and mixers for millimeter and submillimeter astronomy. In *Proc. of the IEEE*, volume 92 (10), pages 1597–1616. IEEE, October 2004.
- [11] S. Haas, C. E. Honingh, D. Hottgenroth, K. Jacobs, and J. Stutzki. Low noise broadband tunerless waveguide SIS receivers for 440-500 GHz and 630-690 GHz. *Int. J. of Infrared and Millimeter Waves*, 17(3):493–506, 1996.
- [12] C. E. Honingh, S. Haas, D. Hottgenroth, K. Jacobs, and J. Stutzki. Low noise broadband fixed tuned SIS waveguide mixers at 660 and 800 GHz. *IEEE Transactions on Applied Superconductivity*, 7(2, Part 3):2582–2586, June 1997.
- [13] Stefan Glenz. *Fabrication and Characterization of Nb–Al/Al₂O₃–Nb Superconductor-Insulator-Superconductor Devices with NbTiN Based Tuning Circuits for the Herschel Space Observatory*. PhD thesis, KOSMA, 1. Physikalisches Institut der Universität zu Köln, 2005.
- [14] P. Pütz. *Fabrication of superconductor-insulator-superconductor devices for heterodyne applications with electron beam lithography*. Dissertation (PhD thesis), KOSMA, 1. Physikalisches Institut der Universität zu Köln, 2003.
- [15] CST Microwave Studio from CST GmbH, Bad Nauheimer Str. 19, D-64289 Darmstadt, Germany. Internet: www.cst.de.
- [16] T. Tils. *Design and 3-D Electromagnetic Modeling of Terahertz Waveguide Mixers and Components*. Dissertation (PhD thesis), KOSMA, 1. Physikalisches Institut der Universität zu Köln, 2006.
- [17] A. R. Kerr. Some fundamental and practical limits on broadband matching to capacitive devices, and the implications for SIS mixer design. *IEEE Trans. Microwave Theory Techniques*, 43(1):2–13, January 1995.
- [18] J. R. Tucker and M. J. Feldman. Quantum detection at millimeter wavelengths. *Rev. Mod. Phys.*, 57(4):1055–1113, 1985.

- [19] C. Gal. *Development of a Wide Bandwidth Array Acousto-Optical Spectrometer for the Herschel Satellite Mission*. Dissertation (PhD thesis), KOSMA, 1. Physikalisches Institut der Universität zu Köln, 2005.
- [20] A.R. Kerr and S.K. Pan. Design of planar image separating and balanced sis. *Proc. 7th Int. Symp on Space Terahertz Technology*, 1996.
- [21] A. Karpov, J. Blondel, D. Billon-Pierron, and K.-H. Gundlach. A 200–300 GHz single sideband SIS mixer for radio astronomy. *IEEE Transaction on Applied Superconductivity*, 11(1(1)):844–847, March 2001.
- [22] O. Hachenberg and B. Vowinkel. *Technische Grundlagen der Radioastronomie*. B.I.-Wissenschaftsverlag, 1982.
- [23] J. D. Kraus. *Radio Astronomy*. Cygnus-Quasar Books, 2nd edition, 1986.
- [24] A. R. Kerr. Saturation by noise and cw signals in sis mixers. *Proceedings of the Thirteenth International Symposium on Space Terahertz Technology*, page 11, 2002.
- [25] S. Withington, P. Kittara, and G. Yassin. Multitone quantum simulations of saturating tunnel junction mixers. *J. Appl. Phys.*, 93(12):9812–9822, June 2003.
- [26] Carlton M. Caves. Quantum limits on noise in linear amplifiers. *Phys. Rev. D*, 26(8):1817–1839, Oct 1982.
- [27] J. R. Tucker. Quantum limited detection in tunnel junction mixers. *IEEE J. Quant. Electron.*, QE-15(11):1234–1258, 1979.
- [28] H. B. Callen and T. A. Welton. Irreversibility and Generalized Noise. *Phys. Rev.*, 83(1):34–40, July 1951.
- [29] A. R. Kerr. Suggestions for revised definitions of noise quantities, including quantum effects. *Microwave Theory and Techniques, IEEE Transactions on*, 47(3):325–329, Mar 1999.
- [30] M. Tinkham. *Introduction to Superconductivity*. McGraw-Hill International Editions, second edition edition, 1996.
- [31] T. van Duzer and C. W. Turner. *Principles of Superconductive Devices and Circuits*. Prentice Hall PTR, 2nd edition, 1999.
- [32] K. H. Gundlach and M. Schicke. SIS and bolometer mixers for terahertz frequencies. *Supercond. Sci. Technol.*, 13(12):R171–R187, 2000.
- [33] B. D. Josephson. Possible new effects in superconductive tunneling. *Phys. Lett.*, 1(7):251–253, July 1962.

- [34] S. Shapiro. Josephson currents in superconducting tunneling - Effect of microwaves and other observations. *Phys. Rev. Lett.*, 11(2):81–82, July 1963.
- [35] Jörg Stodolka. *Fabrikation und Analyse supraleitender diffusionsgekühlter Hot-Electron-Bolometer als Terahertz-Heterodyn timer*. Dissertation (PhD thesis), KOSMA, 1. Physikalisches Institut der Universität zu Köln, 2003.
- [36] B. Bumble, H. G. LeDuc, and J. Stern. Fabrication of Nb/Al-N_x/NbTiN junctions for SIS mixer applications above 1 THz. In *Proc. 9th Int. Symp. on Space Terahertz Technology*, pages 295–304, 1999.
- [37] B. Bumble, H. G. LeDuc, J. A. Stern, and K. G. Megerian. Fabrication of Nb/Al-N_x/NbTiN junctions for SIS mixer applications. *IEEE Trans. Appl. Supercond.*, 11(1):76–79, 2001.
- [38] S. Kohjiro, S. V. Shitov, Z. Wang, Y. Uzawa, S. Miki, A. Kawakami, and A. Shoji. Wide-band operation of quasi-optical distributed superconductor/insulator/superconductor mixers with epitaxial NbN/AlN/NbN junctions. *Supercond. Sci. and Techn.*, 17(5):5295–5300, 2004.
- [39] J. W. Kooi, J. A. Stern, G. Chattopadhyay, H. G. LeDuc, B. Bumble, and J. Zmuidzinas. Low-loss NbTiN films for THz SIS mixer tuning circuits. In *Proc. 8th Int. Symp. on Space Terahertz Technology*, pages 310–319, 1997.
- [40] B. Leone, B. D. Jackson, J. R. Gao, and T. M. Klapwijk. Geometric heat trapping in niobium superconductor-insulator-superconductor mixers due to niobium titanium nitride leads. *Appl. Phys. Lett.*, 76(6):780–782, February 2000.
- [41] T. M. Klapwijk, G. E. Blonder, and M. Tinkham. Explanation of subharmonic energy-gap structure in superconducting contacts. *Physica B+C*, 109, 110B:1657, 1982.
- [42] P. Dieleman and T. M. Klapwijk. Shot noise beyond the tucker theory in niobium tunnel junction mixers. *Appl. Phys. Lett.*, 72(13):1653–1655, 1998.
- [43] A. W. Kleinsasser, R. E. Miller, W. H. Mallison, and G. B. Arnold. Observation of multiple Andreev reflections in superconducting tunnel junctions. *Phys. Rev. Lett.*, 72(11):1738–1741, 1994.
- [44] J. Bardeen, L. N. Cooper, and J. R. Schrieffer. Theory of superconductivity. *Phys. Rev.*, 108:1175–1204, 1957.
- [45] V. Ambegaokar and A. Baratoff. Tunneling between superconductors. *Phys. Rev. Lett.*, 10:486–489, 1963.

- [46] V. Ambegaokar and A. Baratoff. Tunneling between superconductors (erratum). *Phys. Rev. Lett.*, 11:104, 1963.
- [47] J. W. Kooi, J. Kawamura, J. Chen, G. Chattopadhyay, J. R. Pardo, J. Zmuidzinas, T. G. Phillips, B. Bumble, J. Stern, and H. G. LeDuc. A low noise NbTiN-based 850 GHz SIS receiver for the Caltech sub-millimeter observatory. *Int. J. of Infrared and Millimeter Waves*, 21(9):1357–1373, Sept 2000.
- [48] D. Hottgenroth. *Superconductor-Insulator-Superconductor Heterodyne Mixers on Niobium Basis above the Gap Frequency of Niobium and their use in an Astronomical Receiver*. Dissertation (PhD thesis), KOSMA, 1. Physikalisches Institut der Universität zu Köln, 1997.
- [49] W. Shan, T. Noguchi, S. Shi, and Y. Sekimoto. Design and Development of SIS Mixers for ALMA Band 8. *IEEE Transactions On Applied Superconductivity*, 15(2):503–506, June 2005.
- [50] W. R. McGrath, P. L. Richards, D. W. Face, D. E. Prober, and F. L. Lloyd. Accurate experimental and theoretical comparison between superconductor-insulator-superconductor mixers showing weak and strong quantum effects. *J. Appl. Phys.*, 63(8):2479–2491, April 1988.
- [51] Sybille Haas. *Low Noise Fixed-Tuned SIS Mixers For Astronomical Observations in the Submm Wave Region*. Dissertation (PhD thesis), KOSMA, 1. Physikalisches Institut der Universität zu Köln, 1998.
- [52] P. K. Tien and J. P. Gordon. Multiphoton process observed in the interaction of microwave fields with the tunneling between superconductor film. *Phys. Rev.*, 129(2):647–651, Jan 1963.
- [53] P. Dieleman, H. G. Bukkems, T. M. Klapwijk, M. Shicke, and K. H. Gundlach. Observations of andreev reflection enhanced shot noise. *Phys. Rev. Lett.*, 79(18):3486–3489, Nov 1997.
- [54] B. D. Jackson. *NbTiN-based THz SIS Mixers for the Herschel Space Observatory*. PhD thesis, Technische Universiteit Delft, NL, 2005.
- [55] R. Teipen, M. Justen, T. Tils, M. Schultz, S. Glenz, Pütz, K. Jacobs, and C.E. Honingh. Results and analysis of hifi band 2 flight mixer performance. In *Proc. 16th Int. Symp. on Space Terahertz Technology*, 2005.
- [56] RPG Radiometer Physics GmbH, D-53340 Meckenheim, Germany, Internet: www.radiometer-physics.de.
- [57] A. Murk and A. Magun. Characterization of corrugated horn antennas for HIFI. In *25th ESA Workshop on Satellite Antenna Technology*, pages 159–164. ESTEC, Noordwijk, NL, Sept. 2002.

- [58] T. Tils, A. Murk, D. Rabanus, C. E. Honingh, and K. Jacobs. High performance smooth-walled horns for THz waveguide applications. In *Proc. 16th Int. Symp. on Space Terahertz Technology*, 2005.
- [59] W. Janssen. *Streifenleiter und Hohlleiter*. Hüthig Buch Verlag, Heidelberg, Germany, 1992.
- [60] R. L. Kautz. Miniaturization of normal-state and superconducting stripline. *J. Res. Nat. Bureau of Standards*, 84(3):247–259, May–June 1979.
- [61] K. C. Gupta, R. Garg, I. J. Bahl, and P. Bhartia. *Microstrip Lines and Slotlines*. Artech House, Norwood, MA, USA, second edition, 1996.
- [62] R. K. Hoffmann. *Integrierte Mikrowellenschaltungen*. Springer Verlag, Berlin, 1983.
- [63] F. London and H. London. The electromagnetic equations of the superconductor. *Proc. Roy. Soc. (London)*, A149, 1935.
- [64] C. Kittel. *Einführung in die Festkörperphysik*. Oldenbourg Verlag, fifth edition, 1980.
- [65] C. E. Honingh, K. Jacobs, S. Haas, D. Hottgenroth, and J. Stutzki. Niobium SIS mixers at 490 GHz, 690 GHz and 810 GHz. *IEEE Transactions on Applied Superconductivity*, 5(2, Part 3):2216–2219, Jun 1995.
- [66] S. Glenz, M. Justen, P. Pütz, R. Teipen, T. Tils, C.E. Honingh, and K. Jacobs. Broadband NbTiN based SIS mixers for HIFI band 2. In *Digest 27th Int. Conf. on Infrared and Millimeter Waves*, pages 257–258. IEEE, September 2002.
- [67] D. C. Mattis and J. Bardeen. Theory of the anomalous skin effect in normal and superconducting materials. *Phys. Rev.*, 111(2):412–417, 1958.
- [68] David M. Pozar. *Microwave Engineering*, chapter 9, pages 535–537. John Wiley & Sons, Inc., New York, second edition, 1998.
- [69] T. Matsunaga, C.E. Tong, T. Noguchi, and R. Blundell. Fabrication and Characterization of a 600 GHz Resonant Distributed SIS Junction for Fixed-tune Waveguide Receiver. In *Proc. 12th Space THz Tech. Symp.*, San Diego, CA, Feb 2001.
- [70] M. Takeda and T. Noguchi. A 200–285-GHz Waveguide SIS Mixer With an Inhomogeneous Distributed Junction Array. *IEEE Trans. Microwave Theory Techniques*, 50(11):2618–2623, November 2002.

- [71] C. E. Tong, R. Blundell, K. G. Megerian, J. A. Stern, P. Shing-Kuo, and M. Pospieszalski. A distributed lumped-element SIS mixer with very wide instantaneous bandwidth. *IEEE Transactions on Applied Superconductivity*, 15(2 (Part 1)):490–494, Jun 2005.
- [72] DIMES. Delft Institute of Microelectronics and Submicron-technology, PO Box 5031, 2600 GA Delft, NL (internet: www.dimes.tudelft.nl).
- [73] Fa. Rose, Neue Nussbaumer Str. 3, D-51469, Bergisch Gladbach, Germany.
- [74] D. Teyssier and M. Gerin. HIFI most wanted frequencies. Technical report, SRON, Postbus 800, 9700 AV GRONINGEN, NL, June 2003.
- [75] Fourier Transform Spectrometer "IFS 66v/S" from Bruker Optik GmbH, Rudolf-Plank-Str. 27, D-76275 Ettlingen, Germany, Internet: www.brukeroptics.de.
- [76] M. Justen. *Design and Realization of Broadband IF Circuits for Advanced Sub-mm SIS-Mixers*. Dissertation (PhD thesis) in preparation, KOSMA, 1. Physikalisches Institut der Universität zu Köln, 2006.
- [77] PamTech, Passive Microwave Technology Inc, 4053 Calle Tesoro, Suite A, Camarillo, CA.
- [78] D. P. Woody, R. E. Miller, and M. J. Wengler. 85-115 GHz receivers for radio astronomy. *IEEE Trans. Microwave Theory Tech.*, 33(2):90–95, February 1985.
- [79] R. Teipen, M. Justen, T. Tils, S. Glenz, C. E. Honingh, K. Jacobs, B. D. Jackson, T. Zijlstra, and M. Kroug. Influence of junction-quality and current density on HIFI band 2 mixer performance. In *Proc. 14th Int. Symp. on Space Terahertz Technology*, pages 55–62, 2003.
- [80] S. Glenz. private communication, 2005.
- [81] P. Dieleman. private communication, 2005.
- [82] A. Karpov, D. Miller, F. Rice, J. A. Stern, B. Bumble, H. G. LeDuc, and J. Zmuidzinas. Low noise SIS mixer for far infrared astronomy. In J. Zmuidzinas, W. S. Holland, and S. Withington, editors, *Proc. SPIE*, pages 616–621, Bellingham, WA, USA, June 2004. SPIE—The International Society for Optical Engineering.
- [83] B.D. Jackson, G. de Lange, T. Zijlstra, M. Kroug, J.W. Kooi, J.A. Stern, and T.M. Klapwijk. Low-noise 0.8-0.96- and 0.96-1.12-thz superconductor-insulator-superconductor mixers for the herschel space observatory. *IEEE Trans. Microw. Theory Tech.*, 54(2 (1)):547–558, Feb 2006.

- [84] S. Withington and Erik L. Kollberg. Spectral-domain analysis of harmonic effects in superconducting quasiparticle mixers. *IEEE Trans. Microwave Theory Tech.*, 37(1):231–238, Jan 1989.
- [85] S. Withington and P. Kennedy. Numerical procedure for simulating the large-signal quantum behaviour of superconducting tunnel-junction circuits. *IEE Proceedings*, 138:70–76, 1992.
- [86] J. Ward, F. Rice, G. Chattopadhyay, and J. Zmuidzinas. Supermix: A flexible software library for high-frequency circuit simulation, including sis mixers and superconducting elements. In *Proc. 10th Int. Symp. Space Terahertz Technology*, pages 268–281, 1999.
- [87] F. Rice, J. Ward, J. Zmuidzinas, and G. Chattopadhyay. Fast harmonic balance of sis mixers with multiple junctions and superconducting circuits. In *Proc. 10th Int. Symp. Space Terahertz Technology*, pages 282–297, 1999.
- [88] P. K. Grimes, S. Withington, G. Yassin, and P. Kittara. Quantum multitone simulations of saturation in sis mixers. In J. Zmuidzinas, W. S. Holland, and S. Withington, editors, *Millimeter and Submillimeter Detectors for Astronomy II*, pages 158–167, Bellingham, WA, June 2004. SPIE.
- [89] M. Klinkmann. *Entwicklung von supraleitenden Tunnelementen hoher Stromdichte mit AlN-Barrieren*. Diplomarbeit (degree in physics), University of Cologne, 2005.
- [90] Advanced Design System (ADS) from Agilent Technologies, Inc., 395 Page Mill Rd., Palo Alto, CA 94306, US. Internet: www.agilent.com.
- [91] MEFiSTo-3D from Faustus Scientific Corporation, 1256 Beach Drive, Victoria, BC, V8S 2N3, CANADA. Internet: www.faustcorp.com.
- [92] R. Pöpel. Surface impedance and reflectivity of superconductors. *Journal of Applied Physics*, 66(12):5950–5957, Dec 1989.
- [93] P. Kittara. *The development of a 700 GHz SIS mixer with Nb finline devices: Nonlinear mixer theory, design techniques and experimental investigation*. PhD-Thesis, University of Cambridge, GB, Nov 2002.
- [94] H. A. Wheeler. Transmission-line properties of a strip on a dielectric sheet on a plane. *IEEE Transactions on Microwave Theory and Techniques*, 25(8):631–647, Aug 1977.
- [95] W. H. Chang. The inductance of a superconducting strip transmission line. *J. Appl. Phys.*, 50(12):8129–8134, 1979.

- [96] G. Yassin and S. Withington. Electromagnetic models for superconducting millimeter-wave and submillimeter-wave microstrip transmission lines. *J. Phys. D: Appl. Phys.*, 28, 1995.
- [97] M. Bin, M. C. Gaidis, and J. Zmuidzinis. THz SIS mixers with normal-metal Al tuning circuits. *Supercond. Sci. Tech.*, 9(4A):A136–A139, 1996.
- [98] M. Abramowitz and I. A. Stegun. *Handbook of Mathematical Functions*, volume 55 of *Applied Mathematics Series*. National Bureau of Standards, Washington, D.C. 20402, tenth edition, Dec 1972.
- [99] Vendor: Saint-Gobain Performance Plastics GmbH, Delmenhorster Strasse 20, D-50735 Cologne, Germany, Internet: www.saint-gobain.de.
- [100] D.J. Benford, M.C. Gaidis, and J.W. Kooi. Transmission properties of Zitex in the infrared to submillimeter. In *10th International Symposium on Space Terahertz Technology*, 1999.
- [101] B. Jackson, G. de Lange, L. de Jong, W. Laauwen, D. v. Nguyen, T. Zijlstra, M. Krouga, B. de Lange, M. Zuiddam, and T. Klapwijk. CCN8 Progress Meeting. Progress meeting, SRON / DIMES (NL), KOSMA, Cologne, Germany, Jan 2003.
- [102] A. Larsen, H. Dalsgaard Jensen, and J. Mygind. Self-induced steps in a small Josephson junction strongly coupled to a multimode resonator. *Phys. Rev. B*, 43(13):10179–10190, 1991.

Abstract

In this thesis the design and analysis of SIS-mixers (SIS: superconductor-isolator-superconductor) for the use as low-noise and broad-band detectors in the submm-region for astronomical observations is described. The SIS-mixers have been developed for the frequency band 2 (636-802 GHz) of the Heterodyne Instrument for the Far Infrared (HIFI) on ESA's space-observatory Herschel [4, 2]. The required performance baseline has been defined by the HIFI-consortium in terms of the estimated noise temperature contribution of the mixer to be 110 K at 636 GHz and 150 K at 802 GHz. This implies a noise temperature less than $4 \times$ the fundamental quantum noise limit over a relative bandwidth of 23%.

In the frequency region between between 80 GHz and 900 GHz Heterodyne SIS-mixers are established as the best devices for low noise mixing with a high spectral resolution. In the heterodyne method the detectable signal (radio-frequency, RF) is superposed with a signal of a well-known frequency (local oscillator, LO) and the signal in the difference frequency (intermediate frequency, IF) is further analyzed. For the HIFI band 2 mixers, the technology of Nb/Al-Al₂O₃/Nb-junctions has been used with junction areas of 0.5 – 1.0 μm^2 , a target value for the current density j_c of 15 kA/cm² and a gap-voltage of 2.75-2.77 mV.

In general, for the compensation of the junction's intrinsic capacitance and an optimized power coupling to the tunnel junction, integrated resonant microstrip matching circuits are used. To achieve the desired broad-band coupling two types of matching circuits have been theoretically modeled and experimentally studied: (1) three-step transformer single junction devices and (2) double-junction devices. This has been done for two material combinations: for an all-superconductive microstrip NbTiN/SiO₂/Nb, and for the superconductor/normal-conductor combination NbTiN/SiO₂/Al. With Nb as top-wiring the high-frequency conductivity is very inhomogeneous, because above its gap-frequency at 700 GHz the micro-strip losses significantly increase. Al as top-wiring allows a more homogenous power coupling over the frequency band, but shows larger micro-strip losses than Nb .

For the maximized power coupling of the incoming radiation to the junction over the whole frequency band a tool for the numerical optimization of the micro-strip geometry has been developed and applied. For a set most probable micro-strip material parameters the matching circuits have been optimized. Based on these optimizations the lithography masks for the fabrication of the thin-film devices in the KOSMA micro-fabrication laboratories have been designed.

The fabricated SIS-devices have been selected based on a detailed analysis of the DC-data for the more time-consuming RF-measurements in a liquid helium dewar: the heterodyne characterization and the frequency band-pass characterization with a Fourier-transform-spectrometer (FTS). In the scope of this thesis these measurements have been performed, the measurement setup has been characterized and the data have been analyzed. The single-junction devices with Nb top-wiring have shown the optimum noise performance as predicted by the coupling calculations. The optimum measured mixer noise contribution for a SIS-mixer has been determined to depend on the DC-quality Q ; a higher Q is a measure for a low leakage current and an indication for a low device shot-noise.

Only one wafer among eleven RF-characterized wafers in the device development sequence for HIFI has been identified with a sufficient number of devices showing a noise performance below the baseline at least for some frequencies. In order to understand these performance results on the characterized wafers the relative spread in junction area $\Delta A_J/A_J$, the average and optimum DC-quality Q , the Josephson resonance frequencies ν_{res} and the optimum measured noise and their impact on the measured band-pass and mixer performance have been studied.

The wafer with a superior noise performance in the desired frequency range shows a relatively large spread in junction area of $\Delta A_J/A_J = 67\%$ and medium DC-qualities Q . But the crucial properties for the superior performance of this wafer are the relatively large current density of $j_c = 13 - 14 \text{ kA/cm}^2$ and the zero average shift in absolute junction area A_J . A_J via the intrinsic capacitance and the normal resistance of the tunnel junction mainly determines the resonance frequency of the whole device. Based on a comparison of the noise results of several very similar devices the required has to be better than 5% to meet the HIFI performance requirements.

The noise performance of the flight-mixers is compliant with the HIFI baseline over 80% of the band, as has been confirmed in the HIFI integration tests. For other wafers than the wafer with the flight-mixers a significant shift of the band-pass to lower frequencies has been found to result from a significant offset in junction area. For another wafer the shift is explained with a lower effective NbTiN-quality, which is attributed to variations in the etching-process. This even outweighs the optimum properties of a relatively small spread in junction area (15-17%) and optimum DC-qualities around 12.

For a more complete theoretical analysis of a SIS-mixer a numerical tool has been developed which allows the calculation of the noise- and gain band-pass based on the three-frequency approximation of the Quantum Theory of Mixing [18]. This tool has been used to verify the power coupling calculation, used during the design process, and to evaluate the optimum fabrication parameters for future designs of SIS-devices. The effect of four fabrication parameters (NbTiN-quality, gap-voltage V_{Gap} , current density j_c and DC-quality Q) on the mixer performance has been evaluated. Based on the calculated data j_c and Q have been identified as the most critical fabrication parameters for the mixer performance. Since these two parameters partly depend on the same fabrication step, in the fabrication process they can not be optimized independently and a trade-off has to be found, which depends on the fabrication facility. A second result of the simulation is a significant reduction in mixer noise for an increased DC-quality up to $Q = 8 - 10$, but less improvement for a larger Q . And finally, for large micro-strip losses (30-40%) as for NbTiN/SiO₂/Nb-microstrips around 800 GHz an increase in j_c has resulted in a significant reduction of the calculated mixer noise contribution. This suggests a strong potential to reduce the noise temperatures in this frequency region with AlN-barriers, which are currently developed at KOSMA and promise current densities around and above 30 kA/cm^2 .

For the comparison of the measured flight-mixer performance with these simulated noise data the calculation has been expanded by including Multiple Andreev-Reflection (MAR)-enhanced shot noise as specified in [42]. The existence of MAR is indicated by the increased measured sub-gap current and the existence of sub-gap structures in the measured differential resistance. The absolute calculated noise data deviate with a factor 2 from the measured data. But the calculated results show a

good agreement with the measured noise data regarding the frequency-, bias-voltage and LO-power dependence. Thus the theory is expected to give reliable estimates for relative variations in noise performance.

Zusammenfassung

In dieser Arbeit wird das Design und die Analyse von SIS-Mischern (SIS: Supraleiter-Isolator-Supraleiter) für den Einsatz als rauscharme und breitbandige Detektoren für astronomische Beobachtungen im Submm-Bereich beschrieben. Die SIS-Mischer wurden für das Frequenzband 2 des "Heterodyne Instrument for the Far Infrared" auf dem Satellit-Observatorium der ESA Herschel entwickelt [4, 2]. Vom HIFI-Konsortium wurde eine Empfindlichkeit der Mischer mit Rauschtemperatur-Beiträgen von 100 K bei 636 GHz und 150 K bei 802 GHz vorgegeben ("HIFI-Baseline"). Diese Werte sind nur knapp das Vierfache des fundamentalen Quantenlimits bei einer relativen Bandbreite von 23%.

Für den Nachweis elektro-magnetischer Strahlung im Frequenzbereich zwischen 80 GHz und 900 GHz bei gleichzeitiger hoher spektraler Auflösung sind SIS-Heterodyn mischer derzeit die empfindlichsten Detektoren. Dabei wird das zu detektierende Signal ("Radio-Frequency", RF) mit einem Signal bekannter Frequenz ("Local Oszillator", LO) überlagert und das Signal in der Differenzfrequenz ("Intermediate Frequency", IF) nachgewiesen. Die Mischer für das HIFI Frequenzband 2 wurden in Nb/Al-Al₂O₃/Nb-Technologie realisiert, wobei die Flächen der Tunnelkontakte ("SIS-Junction") 0.5 – 1.0 μm^2 betragen, bei einer kritischen Stromdichte j_c von 15 kA/cm² und einer Gapspannung von 2.75-2.77 mV.

Um die intrinsische Kapazität der Junction zu kompensieren und die Leistungseinkopplung zu optimieren, werden die Junctions üblicherweise in eine Anpassstruktur in Mikrostreifenleitertechnik integriert. Um die geforderte breitbandige Leistungseinkopplung zu erreichen, wurden zwei Arten von Anpassstrukturen theoretisch modelliert und experimentell untersucht: (1) Einzeljunctions mit Dreistufen trafo-Anpassstruktur und (2) Doppeljunctions. Dabei wurden zwei Materialkombinationen für die Mikrostreifenleiter verwendet: die Kombination aus zwei Supraleitern NbTiN/SiO₂/Nb und die Supraleiter-Normalleiter-Kombination NbTiN/SiO₂/Al. Mit Nb als oberer Streifenleiterschicht erhält man eine sehr inhomogene Hochfrequenz-Leitfähigkeit, da oberhalb der Gapfrequenz bei 700 GHz erhebliche Streifenleiterverluste auftreten. Der Normalleiter Al garantiert zwar eine homogenere Leistungsanpassung, die Streifenleiterverluste liegen jedoch insgesamt höher als bei Nb.

Um die maximal mögliche Leistungsankopplung der zu detektierenden Strahlung in die Junction über das gesamte Frequenzband zu garantieren, wurde eine numerische Optimierung für die Geometrie der Streifenleiter entwickelt und eingesetzt. Die Anpassstrukturen wurden für einen Satz von wahrscheinlichen Materialparametern der Streifenleiter optimiert. Aufgrund dieser Rechnungen wurde das Design für die Lithographiemasken erstellt, die für die Herstellung der Dünnschicht-Elemente in den KOSMA Mikrostruktur-Labors benötigt wurden.

Von den hergestellten SIS-Elementen wurden aufgrund der DC-Kennlinien einige für die aufwändigeren Höchstfrequenzmessungen im Tieftemperatur-Dewar mit Flüssig-helium ausgewählt: für die Heterodynmessungen zur Bestimmung des Mischerrauschens und Mischergains und für die Charakterisierung des Frequenz-Bandpasses mit einem Fourier-Transform-Spektrometer (FTS). Diese Messungen wurden im Rahmen dieser Arbeit durchgeführt, der Messaufbau charakterisiert und die Messdaten ausgewertet. Die Einzeljunctions mit Nb als oberer Streifenleiterschicht zeigten dabei in

Übereinstimmung mit den Kopplungsrechnungen die niedrigsten Rauschtemperaturen. Es konnte ein Zusammenhang zwischen der optimalen Rauschtemperatur eines SIS-Mischers und dem Quality-Faktor Q der gemessenen DC-Kennlinie nachgewiesen werden, wobei ein höheres Q ein Maß für einen niedrigeren Leckstrom und somit ein Indiz für niedrigeres Schrotrauschen im Tunnelelement ist.

Nur einer von elf RF-charakterisierten SIS-Wafern aus der Device-Entwicklung für HIFI wies mehrere SIS-Elemente mit Rauschtemperaturen unterhalb der geforderten HIFI-Baseline auf. Um die Ursachen dafür zu identifizieren, wurden für einige charakterisierte Wafer vier Kenndaten, die relative Streuung in der Junctionfläche $\Delta A_J/A_J$, der durchschnittliche und optimale Quality-Faktor Q , die Josephson-Resonanzfrequenzen ν_{res} und die optimale gemessene Rauschtemperatur in Abhängigkeit von der RF-Frequenz verglichen und die Zusammenhänge mit dem Frequenz-Bandpass und dem Mischerrauschen untersucht.

Der Wafer mit mehreren sehr empfindlichen SIS-Elementen im gewünschten Frequenzbereich wies eine relativ hohe Streuung der Junction-Fläche auf ($\Delta A_J/A_J = 67\%$) und zeigte durchschnittliche Werte für den Quality-Faktor Q . Aber als entscheidend für die optimale Empfindlichkeit stellten sich die relativ hohe Stromdichte $j_c = 13 - 14 \text{ kA/cm}^2$ heraus und die Tatsache, dass die Streuung der Junctionflächen ohne einen systematischen Offset um die gewünschten Werte zentriert war. Die Junctionfläche ist der Hauptfaktor, der über die intrinsische Kapazität und den Normalwiderstand der Junction die Resonanzfrequenz des ganzen SIS-Elements definiert. Durch den Vergleich der Rauschmessungen mehrerer sehr ähnlicher SIS-Elemente wurde eine Flächengenauigkeit von unter 5% bestimmt, die notwendig ist, um mit den verwendeten Technologien die HIFI-Baseline zu erreichen.

Die Rauschtemperaturen für die Mischer, die in HIFI integriert werden ("Flight-Models", FM) erfüllen die HIFI Baseline für 80% des Frequenzbandes. Diese Ergebnisse wurden während der HIFI-Integrationstests bestätigt. Für zwei andere Wafer, die teilweise optimale DC-Charakteristika aufwiesen (geringe relative Streuung in der Junctionfläche von 15-17% und ein optimaler Quality-Faktor Q um 12), lag der Frequenzbereich optimaler Kopplung unter dem gewünschten Frequenzbereich. In einem Fall ist dafür ein merklicher systematischer Offset in der Junctionfläche verantwortlich, in dem anderen Fall eine reduzierte NbTiN-Qualität, die auf eine Änderung im Fabrikationsprozess zurückzuführen ist.

Für eine weitergehende theoretische Analyse der SIS-Mischer wurde auf der Basis der Dreiport-Näherung von Tucker's Quantenmischertheorie [18] ein Numerikprogramm entwickelt, mit dem der Rausch- und Gain-Bandpass eines Mischers berechnet wird. Damit wurden die Methode der berechneten Leistungseinkopplung in die Junction, die für das Design der Mischer verwendet wurde, verifiziert und darüber hinaus für zukünftige Mischer-Designrechnungen die optimalen Fabrikationsparameter analysiert. In diese Analyse wurden vier Fabrikationsparameter eingeschlossen: die NbTiN-Qualität, die Gapspannung V_{Gap} , die kritische Stromdichte j_c und der Quality-Faktor Q . Die Rechnungen ergaben, dass j_c und Q für die Rauschbeiträge des Mischers die kritischen Fabrikationsparameter sind. Da diese beiden Parameter zum Teil von demselben Fabrikationsschritt abhängen, können sie nicht unabhängig voneinander optimiert werden, so dass eine optimale Kombination bestimmt werden muss, die von der jeweiligen Fabrikation abhängt. Ein zweites Ergebnis der Simulationen ist eine deutliche Reduzierung des Mischerrauschens für einen verbesserten

Quality-Faktor Q bis etwa $Q = 8 - 10$; darüber wird das Mischerrauschen für weiter verbessertes Q nur wenig optimiert. Und schließlich ergaben die Rechnungen, dass für deutliche Mikrostreifenverluste, wie sie in NbTiN/SiO₂/Nb-Streifenleitern im Bereich von 800 GHz auftreten, eine Erhöhung von j_c eine deutliche Reduzierung des berechneten Mischerrauschens bewirkt. Dies Ergebnis verspricht eine merkliche Reduzierung der Rauschtemperaturen in diesem Frequenzbereich, wenn man die SIS-Junctions mit AlN-Barrieren realisieren kann, die derzeit bei KOSMA entwickelt werden und für die in anderen Fabrikationslabors Stromdichten um und oberhalb von 30 kA/cm² gemessen wurden.

Für einen besseren Vergleich der gemessenen Rauschdaten mit den berechneten Ergebnissen wurde zusätzlich der Effekt der "Multiple Andreev-Reflection" (MAR) berücksichtigt (siehe [42]). Aufgrund der vergleichsweise hohen gemessenen Leckströme und des Auftretens von periodischen Strukturen unterhalb der Gapspannung im differentiellen Widerstand ist darauf zu schließen, dass MAR in den hergestellten SIS-Junctions auftritt. Die Absolutwerte der berechneten Rauschtemperaturdaten weichen um einen Faktor 2 von den gemessenen Daten ab. Aber die Ergebnisse stimmen mit den gemessenen Rauschdaten hinsichtlich ihrer Frequenz-, Biasspannungs- und LO-Leistungsabhängigkeit gut überein. Daher lässt sich die Verwendung der Rechnung für die Analyse relativer Variationen in den Rauschtemperaturen rechtfertigen.

Danksagung

Ich danke Herrn Prof. Dr. Jürgen Stutzki, dass er es mir ermöglicht hat, an seinem Lehrstuhl die Promotion in Rahmen des Weltraumprojekts Herschel durchzuführen. Außerdem danke ich Herrn Prof. Dr. Peter Reiter, dass er sich bereit erklärt hat, das Zweitgutachten zu erstellen, und Herrn Prof. Dr. Michael Kerschgens für die Übernahme des Prüfungsvorsitzes.

Frau Dr. Netty Honingh danke ich für die Betreuung der Arbeit, für die Einweisung in die Tuningstruktur- und Mischerrechnungen, für die Koordination des Mischerprojekts für HIFI, die Korrektur der Arbeit und die geduldige Beantwortung vieler Fragen. Herrn Dr. Karl Jacobs danke ich für die Koordination der SIS-/HEB-Gruppe und die Unterstützung in vielen theoretischen und experimentellen Fragen.

Ich danke den Mitarbeitern, die alle zu der Entwicklung der HIFI-Mischer beigetragen haben, Herrn Dr. Patrick Pütz für die Entwicklung der E-Beam-Belichtung und des CMP, Herrn Dr. Stefan Glenz für die Entwicklung der NbTiN-Filme und die Herstellung zahlreicher Batches, vor allem des Wafers PS8 mit der richtigen Korrektur für das Unterätzen. Ich danke Herrn Stephan Wulff für die Herstellung und DC-Charakterisierung zahlreicher Wafer und Herrn Michael Schultz für den gewissenhaften Einbau der haardünnen SIS-Devices in die Mischerblöcke. Herrn Dr. Thomas Tils danke ich für die gute Zusammenarbeit an der Schnittstelle zwischen Tuningstruktur und Waveguide-Probe und Herrn Matthias Justen für die Entwicklung des Bias-T's und der ESD- und EMC-Schaltungen. Frau Dr. Honingh, Herrn Dr. Tils und Herrn Justen gilt mein Dank für die gut funktionierenden Schichtdienste während der Flight-Model- und Flight-Spare-Tests.

Den übrigen Mitgliedern und Assoziierten der Gruppe Dr. Sven Bedorf, Pedro Munoz Pradas, Martin Klinkmann und Gundolf Wieching danke ich für den regen Austausch in physikalischen und nichtphysikalischen Fragen. Besonders fruchtbar waren die sog. "Expertenrunden" im KOSMA-Raum und außer Haus.

Darüber hinaus danke ich den Kollegen aus der AOS-Gruppe, Dr. Michael Olbrich, Dr. Frank Schmülling, Dr. Frank Schlöder, Volker Mittenzwei und Dr. Oliver Siebertz für die Aufnahme in ihren Trakt während der Endphase der Arbeit. Hilfreich waren für mich die Unterstützung in Linux-Fragen und die Überlassung von Rechnerleistung für die Simulationsrechnungen.

Außerhalb des Instituts gilt mein Dank für die gute Zusammenarbeit bei einigen Hornmessungen Herrn Dr. Axel Murk in Bern, Schweiz, und Herrn Dr. Pieter Dieleman, Herrn Willem Jellema und Herrn Dr. Gert de Lange während der Integrationstests in Groningen, NL.

Schließlich gilt mein Dank meinen Eltern für die Unterstützung meines Studiums und meiner Frau Stephanie für den starken Rückhalt während der gesamten Promotionszeit.

Förderungen

Diese Arbeit wurde von der Deutschen Forschungsgemeinschaft über den Sonderforschungsbereich SFB 494 und von dem Deutschen Zentrum für Luft- und Raumfahrt (Förderkennzeichen 50 OF 9902 4 und 50 OF 0001 2) finanziert.

Acknowledgment

This work was supported by the Deutsche Forschungsgemeinschaft (grants Sonderforschungsbereich SFB 494) and by the Deutsches Zentrum für Luft- und Raumfahrt (grants 50 OF 9902 4 und 50 OF 0001 2).

Erklärung

Ich versichere, dass ich die von mir vorgelegte Dissertation selbständig angefertigt, die benutzten Quellen und Hilfsmittel vollständig angegeben und die Stellen der Arbeit - einschließlich Tabellen, Karten und Abbildungen -, die anderen Werken im Wortlaut oder dem Sinn nach entnommen sind, in jedem Einzelfall als Entlehnung kenntlich gemacht habe; dass diese Dissertation noch keiner anderen Fakultät oder Universität zur Prüfung vorgelegen hat; dass sie - abgesehen von unten angegebenen Teilpublikationen - noch nicht veröffentlicht worden ist sowie, dass ich eine solche Veröffentlichung vor Abschluss des Promotionsverfahrens nicht vornehmen werde. Die Bestimmungen dieser Promotionsordnung sind mir bekannt. Die von mir vorgelegte Dissertation ist von Prof. Dr. Stutzki betreut worden.

Köln, Dezember 2006

Teilpublikationen:

[I] R. Teipen, M. Justen, T. Tils, S. Glenz, C.E. Honingh, K. Jacobs, B.D. Jackson, T. Zijlstra and M. Kroug. Influence of junction-quality and current density on HIFI band 2 mixer performance. In Proc. 14th Int. Symp. on Space Terahertz Technology, pages 55-62, 2003.

[II] R. Teipen, M. Justen, T. Tils, M. Schultz, S. Glenz, Pütz, K. Jacobs and C.E. Honingh. Results and analysis of HIFI band 2 flight mixer performance. In Proc. 16th Int. Symp. on Space Terahertz Technology, 2005.

[III] C.E. Honingh, M. Justen, R. Teipen, T. Tils and K. Jacobs. Mixer development for HIFI band 2 (640-800 GHz). In Proc. 13th Int. Symp. on Space Terahertz Technology, 2002.

[IV] S. Glenz, M. Justen, P. Pütz, R. Teipen, T. Tils, C.E. Honingh and K. Jacobs. Broadband NbTiN based SIS mixers for HIFI band 2. In Digest 27th Int. Conf. on Infrared and Millimeter Waves, pages 257-258. IEEE, September 2002.

[V] M. Justen, T. Tils, S. Glenz, P. Pütz, M. Schultz, R. Teipen, C.E. Honingh and K. Jacobs. Broadband NbTiN based SIS mixer for band 2 of the HIFI instrument for the Herschel spacecraft. In Proc. of the 6th European Conference on Applied Superconductivity, pages 2994-3001. Institute of Physics Publishing, 2003.

[VI] M. Justen, M. Schultz, T. Tils, R. Teipen, S. Glenz, P. Pütz, C.E. Honingh and K. Jacobs. SIS flight mixers for band 2 of the HIFI instrument of the Herschel Space Telescope. In M. Thumm and W. Wiesbeck, editors, Digest 29th Int. Conf. on Infrared and Millimeter Waves and 12th Int. Conf. on Terahertz Electronics, pages 437-438, September 2004.

[VII] P. Pütz, S. Glenz, R. Teipen, T. Tils, N. Honingh, K. Jacobs, A. Hedden, C. Kulesa, C.E. Groppi and C.K. Walker. High sensitivity 810 GHz SIS receiver at AST/RO. In Proc. SPIE Astronomical Telescopes and Instrumentation, volume 5498, pages 509-516, 2004.

Lebenslauf

Persönliche Daten		Rafael Theodor Alfred Teipen Agricolastraße 24 10555 Berlin geb. 21. August 1969 in Münster/Westf.
Familienstand		verheiratet
Staatsangehörigkeit		Deutsch
Schulbildung	1975-1979 1979-1981 1981-1988 1988	Katholische Grundschule Bad Bentheim Orientierungsstufe Bad Bentheim Burggymnasium Bad Bentheim Abitur (Allgemeine Hochschulreife)
Hochschulstudium	1989-1997 Okt. 1997	Physikstudium an der Universität zu Köln Abschluss: Diplom
Promotion	seit Sep. 2000	Promotionsstudium am I. Physikalischen Institut der Universität zu Köln
Berufliche Tätigkeit	1995-1996 1996-1997 1997-1998 1998-2000 2000-2006	Studentische Hilfskraft bei der ExperTeam GmbH, Köln Studentische Hilfskraft am II. Physikalischen Institut der Universität zu Köln Mitarbeiter der SK ONLINE GmbH, Köln Unternehmensberater bei der ExperTeam AG, Köln Wissenschaftlicher Mitarbeiter am I. Physikalischen Institut der Universität zu Köln

Köln, Dezember 2006